WORLD METEOROLOGICAL ORGANIZATION

LECTURE NOTES ON THE APPLICATIONS OF METEOROLOGICAL SATELLITE SERVICES AND DATA

Prepared by
T. H. Vonder Haar and D. W. Hillger

EDUCATION AND TRAINING PROGRAMME
ETR-1

WMO/TD - No. 152

Secretariat of the World Meteorological Organization - Geneva - Switzerland

V6
1986

WORLD METEOROLOGICAL ORGANIZATION

LECTURE NOTES ON THE APPLICATIONS OF METEOROLOGICAL SATELLITE SERVICES AND DATA

LIBRARY

JUL 17 2008

National Oceanic &
Atmospheric Administration
U.S. Dept. of Commerce

Prepared by

T. H. Vonder Haar and D. W. Hillger

EDUCATION AND TRAINING PROGRAMME
ETR-1

WMO/TD - No. 152

Secretariat of the World Meteorological Organization - Geneva - Switzerland
1986

NOTE

The designations employed and the presentation of material in this publication do not imply the expression of any opinion whatsoever on the part of the Secretariat of the World Meteorological Organization concerning the legal status of any country, territory, city or area, or of its authorities, or concerning the delimitation of its frontiers or boundaries.

National Oceanic and Atmospheric Administration
TIROS Satellites and Satellite Meteorology

ERRATA NOTICE

One or more conditions of the original document may affect the quality of the image, such as:

Discolored pages
Faded or light ink
Binding intrudes into the text

This has been a co-operative project between the NOAA Central Library and the Climate Database Modernization Program, National Climate Data Center (NCDC). To view the original document contact the NOAA Central Library in Silver Spring, MD at (301) 713-2607 x124 or Library.Reference@noaa.gov.

HOV Services
Imaging Contractor
12200 Kiln Court
Beltsville, MD 20704-1387
January 26, 2009

CONTENTS

		Page
PREFACE		1
INTRODUCTION		3
SECTION I -	BASIC PRINCIPLES	5
CHAPTER 1 -	POLAR AND GEOSYNCHRONOUS SATELLITES	7
	1.1 Overview of the Meteorological Satellite Program; History	7
	1.2 Basic Orbits of Satellites	13
	1.3 The Direct Readout Capabilities from the Satellites; Exercises	53
CHAPTER 2 -	SATELLITE INSTRUMENTS	89
	2.1 Cloud Imaging Systems: Infrared and Visible Scanners; Spin-scan Radiometers	94
	2.2 Scanning Radiometers for Remote Sensing of Ocean and Land; Temperature and Moisture Sounding; Microwave Systems	99
	2.3 Data Collection Platforms and Platform Location Systems	104
CHAPTER 3 -	SATELLITE RECEIVING SYSTEMS	145
	3.1 APT, WEFAX, GOES-TAP	146
	3.2 High Resolution Sun-synchronous and Geostationary Imagery	150
	3.3 Quantitative Atmospheric Sounding Data	152
CHAPTER 4 -	IMAGE AND DATA DISPLAY SYSTEMS	163
	4.1 Facsimile Machines; Movie Loops	164
	4.2 Interactive Display Systems; Digital Imaging	166
CHAPTER 5 -	FUNDAMENTALS OF RADIATIVE TRANSFER USED IN MEASUREMENTS FROM SATELLITES	181
	5.1 Basic Radiometric Quantities	182
	5.2 Definitions	182
	5.3 Basic Radiation Laws	185
	5.4 The Equation of Radiative Transfer	189
SECTION II -	PRACTICAL APPLICATIONS	193
CHAPTER 6 -	ATMOSPHERIC TEMPERATURE AND MOISTURE SOUNDINGS FROM SATELLITES	195
	6.1 Fundamental Principles (Theory)	196
	6.2 Mathematical	198
	6.3 Results	203
	6.4 Impact	204
	6.5 Direct Sounder Broadcast	204

Page

CHAPTER 7 - WIND ESTIMATION FROM CLOUD MOTION 209
7.1 Methods 209
7.2 Problems 211
7.3 Solution 212
7.4 An Application 213

CHAPTER 8 - CLOUD IDENTIFICATION FROM SATELLITES 219
8.1 Definition of Cloud Types 219
8.2 Meteorology Associated with Different Cloud Types 222
8.3 Need for Accurate Cloud Type Information 223
8.4 Parameters Affecting Satellite Measurements of Clouds 224
8.5 Problem Areas in Cloud Type Identification .. 225
8.6 Single FOV Techniques 226
8.7 Multiple FOV Techniques 228

CHAPTER 9 - MID-LATITUDE SYNOPTIC FEATURES AS SEEN FROM SATELLITES 233
9.1 Basic Weather Features; Fronts; "Lows"; Jetstreams; Blocking Features 233
9.2 Views of Cyclogenesis or Stages of Weather Development 237

CHAPTER 10 - TROPICAL STORMS AND WEATHER SYSTEMS 249
10.1 The InterTropical Convergence Zone 249
10.2 Other Tropical Weather Systems 252
10.3 Tropical Storms, Hurricanes and Typhoons 254

CHAPTER 11 - SMALL-SCALE WEATHER FEATURES 269
11.1 Fog 269
11.2 Orographic (wave) Clouds 270

CHAPTER 12 - SEVERE MESOSCALE STORMS 275
12.1 Analysis and Interpretation of Thunderstorm Images 275
12.2 Thunderstorm Research Techniques 279

CHAPTER 13 - RAINFALL ESTIMATION TECHNIQUES 289
13.1 Visible-IR Approach 289
13.2 Microwave Estimates 293
13.3 Towards a Multi-spectral Satellite-measured Rainfall Technique Justification 295

CHAPTER 14 - COMBINED SATELLITE/RADAR ANALYSES 303
14.1 Simple Satellite/Radar Comparisons 303
14.3 Satellite Rainfall Techniques Using Radar/Satellite Compositing 304

Page

CHAPTER 15 - OTHER FEATURES VIEWED FROM WEATHER SATELLITES 309
15.1 Tropospheric Dust 310
15.2 Haze Layers Over the Ocean 313
15.3 Air-pollution Observations by Weather Satellites 313
15.4 Observations of Forest Fires 315

CHAPTER 16 - SATELLITE SUPPORT TO WEATHER MODIFICATION PROGRAMS 323
16.1 Satellite Support to Winter Orographic Weather Modification 323

CHAPTER 17 - SATELLITE OBSERVATION RELATED TO AIR-SEA INTERACTION 329
17.1 Sea-surface Temperature Measurements from Satellites 329
17.2 Other Oceanographic Parameters 331
17.3 Non-oceanographic Products 332

CHAPTER 18 - ASPECTS OF CLIMATOLOGY STUDIES FROM SATELLITE DATA 343
18.1 Radiation Budgets 343
18.2 Clouds 353
18.3 Other Parameters 354

SECTION III - FUTURE DEVELOPMENTS 363

CHAPTER 19 - FUTURE DEVELOPMENTS IN METEOROLOGICAL SATELLITES AND DATA-PROCESSING SYSTEMS 365
19.1 Future Satellite Capabilities 365
19.2 New Instruments 365
19.3 Data-processing Systems and Communications .. 367

CHAPTER 20 - SPECIAL DISCUSSION OF PRACTICAL APPLICATIONS FOR METEOROLOGICAL SATELLITES IN THE 1980's 369
20.1 Examples of Practical Applications 372
20.2 Examples of Scientific/Industry Cooperation 378

ANNEX LIST OF ABBREVIATED TITLES OF SLIDES ON SOME APPLICATIONS OF METEOROLOGICAL SATELLITE DATA 383

PREFACE

The world meteorological community supports and uses new and larger numbers of weather satellites for gathering various types of meteorological information. At least five geostationary and five near-polar orbiting satellites gather operational and research data and provide weather forecasters with information several times each day. All areas of the Earth are covered and new ways to use and interpret the satellite data are constantly being developed. It is the purpose of these Lecture Notes on Satellite Meteorology to assist with the training of weather scientists and forecasters in basic areas related to the practical applications of the weather satellite data.

This set of notes is neither intended to provide a full spectrum of satellite photographs of weather features nor an up-to-date review of research results from the use of weather satellite data. The reader is referred to special publications by national space agencies and the scientific literature for reviews of these topics.

These lecture notes were developed and tested in four international WMO sponsored training events, and one national training course in the U.S.A.. The first, and largest, international session directed by the first author was held in Fort Collins in 1979, followed by others in Mexico City in 1980 and Lisbon in 1981. The national session was held in Fort Collins in 1982 and was followed by another course there in 1983. It is important to acknowledge the contributions and questions from the participants at these training events. They provided the stimulation and focus for these lecture notes.

We are grateful to the WMO Secretariat for its assistance in sponsoring and organizing the several courses and the notes. Early curriculum ideas for training-course objectives were provided by Mr. David Johnson and Mr. Vincent Oliver of NOAA/NESDIS. Dr. Stanley Kidder of the University of Illinois (formerly from CSU) reviewed my early notes and made substantial contributions. Our associates at Colorado State University and other organizations, especially Mr. K. Robert Morris, provided time and material to help assemble the lecture notes. Organization of these notes and word-processing service were provided by Dee M. Vonder Haar with technical typing assistance for the equations from Patricia Wright.

Special recognition is due to those scientists listed below who made major contributions to certain sections or chapters:

E. A. Smith	Section 1.2
D. W. Reynolds	Section 8.6
R. Weldon	Chapters 9 and 10
R. A. Maddox	Chapter 12
S. Q. Kidder	Chapter 13

Thomas H. Vonder Haar
Professor and Head
Department of Atmospheric Science
Colorado State University
Fort Collins, Colorado
U. S. A.

Blank page retained for pagination

INTRODUCTION

Meteorological satellites have taken their place as a standard observing platform from which to measure the weather. The purpose of the Lecture Notes on Meteorological Satellites is to provide basic education and training for meteorologists involved in both research and forecasting. The text is directed toward the training of Class I meteorological personnel. It is intended for use by those directly involved in meteorology and climatology as well as related fields.

During the last ten years, the World Meteorological Organization has published a number of documents about satellites and their applications. Some of these are listed in the suggested reading which follows this introduction. Unlike the earlier publications, these lecture notes do not review the capabilities and plans of meteorological satellite services of the various nations. They do not provide specialized information on research topics that are closely related to satellite meteorology, nor do they provide an extensive summary of the many satellite photographs of the Earth and atmosphere already in the archives. During the course of these lecture notes, extensive references are provided to other documents to meet these specialized needs. In addition, references are made to the regular scientific literature and to special WMO publications, so the reader is thus directed to a wealth of source material. Reference is also made in the Annex to an extensive set of 395 color slides, which have been compiled by the principal author and his associates as a separate project for the World Meteorological Organization. This set of satellite training-course slides is available from the World Meteorological Organization, Geneva, at cost. The slide set can be used by instructors who also choose to use these lecture notes as part of a course in the use of meteorological satellites. However, it is important to note that the text is designed for use without the slide set.

Throughout the course of the lecture notes, the practical applications of meteorological satellites are emphasized. The notes are divided into three sections.

Section I describes the basic principles that must be mastered before discussion of the various applications. These principles involve fundamentals of orbital geometry, the nature and capacity of the satellites themselves, aspects of satellite instrumentation, and a special understanding of satellite data-receiving systems, as well as image and data display systems. The basic principles also include fundamentals of radiative transfer used in measurements from satellites.

Section II is entitled "Practical Applications". This is the largest section and describes the use of satellites to obtain measurements or estimates of the basic state parameters of the atmosphere, including temperature, moisture and winds. A discussion of cloud observation and identification from satellites includes those features associated with synoptic, tropical, and small-scale weather features. Special chapters are provided to deal with small mesoscale storms and flash floods as well as estimates of rainfall from satellite data. Some special applications of satellite data to weather modification and cloud physics studies, as well as satellite observations related to air-sea interaction and climatology, conclude this section.

Section III discusses the future developments that are anticipated in meteorological satellites and data-processing systems and concludes with a summary discussion of some of the practical applications of meteorological satellites that are envisaged to grow in the 1980's and beyond.

As is the case in any compilation of lecture notes, no attempt has been made to cover all aspects of the written literature in this area. Certain references and examples are chosen to convey information to the reader but no attempt has been made to give equal coverage to all good work in a particular area. For a particularly fine introduction and over-view to the use of satellites in meteorology, oceanography and hydrology, the reader is referred to WMO publication No. 585 - Satellites in Meteorology, Oceanography and Hydrology, 1982.

* *
*

References and Suggested Additional Reading:

WMO-411 Information on Meteorological Satellite Programmes Operated by Members and Organizations, 1975;

WMO-531 Quantitative Meteorological Data from Satellites, Technical Note No. 166, 1984 (second reprint);

WMO-585 Satellites in Meteorology, Oceanography and Hydrology, 1982

SECTION I

BASIC PRINCIPLES

The normal review of basic physics and mathematics is required for those using these lecture notes on meteorological satellites. This section is intended to provide background information and the basic principles of operation of the polar and geosynchronous meteorological satellites. This includes a discussion of satellite orbits and the so-called navigation problem. We also cover aspects of satellite instrumentation important to the user. An outline of the satellite data receiving systems is provided in Chapter 3, again with the user or meteorologist interested in practical applications in mind rather than from an engineering prospective. Chapter 4 discusses the image and data display systems which are often the interface point between the user and the vast array of technology deployed in the satellite systems. Finally, Chapter 5 provides a review of radiative transfer fundamentals. It is through the natural radiation streams measured by the satellite instruments that we obtain, detect, and infer information about the weather and the underlying surface of the earth.

Blank page retained for pagination

CHAPTER 1

POLAR AND GEOSYNCHRONOUS SATELLITES

The study of basic operating principles begins with a discussion of the fundamental satellite platforms used for observing the weather. We then cover the principles of the orbits of these satellites and conclude Chapter 1 with a discussion of tracking the "direct readout" weather satellites.

1.1 Overview of the Meteorological Satellite Program; History

In 1984 it is particularly noteworthy that we compile a Compendium, because it was just over 20 years ago, in October, 1959, when the first satellite to carry a meteorological experiment, Explorer VII, was launched into a successful orbit. We will study the Earth Radiation Budget Experiment on this satellite as well as the many other successful experiments that have been carried out by several countries during the last 20 years.

What can we learn by looking at the history of the meteorological satellite program? Well, certainly it will help us to understand the steady progression of instruments and satellite capabilities that leave us where we are today with the current operational and research systems. In addition, by some extrapolation, we can begin to think about future satellite capabilities that we might anticipate in the years to come. Of course, in the later parts of these notes on polar and geostationary meteorological satellites, we will definitely be talking about such new systems as the space shuttle and space lab. Nevertheless, the operational

meteorologist, researcher, or instructor of today can only properly understand, use and teach the principles of meteorological satellites by having a thorough understanding of the past systems.

1.1.1 Satellites

Both the Soviet Union and the United States carried meteorological experiments on their research satellites in the early 1960's. These soon developed into regular meteorological satellite systems that carried the imaging systems to take pictures of the clouds and the basic radiation measurement systems to measure the Earth's radiation budget. After the Sputnik and Explorer class satellites, the United States began its TIROS series, an acronym that stands for Television and Infrared Operational Satellites. Beginning in 1960, the TIROS extended through 1965. One of the figures shows the typical TIROS satellites. Table 1.1.1 (Johnson, 1961) shows the specific launch dates of some of these early TIROS within the context of the other artificial earth satellites and significant launchings from the late 1950's up through the launch of Vostok in 1961 that placed the first man, Cosmonaut Gagarin, into space.

Figures 1.1.1 and 1.1.2 show that the TIROS series was soon augmented in the United States by an experimental satellite program to test new meteorological devices. It was called NIMBUS and the first NIMBUS satellite was launched in 1963. NIMBUS was a test bed and has continued through 1978 with the launch of NIMBUS-7. The same figures show that the second generation operational meteorological satellites called ESSA were interspersed through the late 1960's with the experimental NIMBUS. The NIMBUS test bed allowed many new experiments to be pioneered and we shall learn about them in this Compendium.

The third series of meteorological satellites for operational purposes in the United States were named NOAA (see Table 1.1.2). Figure 1.1.3 shows the early version of NOAA (the present spacecraft is shown in Chapter 2). The NOAA series and METEOR series of the USSR were essentially the immediate forerunners of the present-day near-polar orbiting operational weather satellites system. In the USSR the METEOR satellites were preceded by experiments on COSMOS spacecraft.

In the late 1960's the launch vehicle capabilities had allowed us to place communication satellites into geostationary orbits. Such an orbit is an excellent one for meteorological satellites as we shall learn in the next two chapters. It allows an observing radiometer or camera to take continuous pictures of the developing and moving weather patterns, in contrast to the snapshot view that the polar-orbiting satellites could provide. Thus, in 1966 the United States launched one of its experimental Applications Technology Satellites (ATS-1). This satellite carried a special experiment called a spin-scan cloud camera (SSCC). The camera used the satellite's rotation to sweep across the Earth and gather a line that would be added together with many other such sweeps to form an image of the Earth's weather patterns from a distance of approximately 35,800 kilometers. ATS-1 was followed by ATS-3 (Figure 1.1.1) which had a color camera capability and together these two satellites became the forerunner of the operational geostationary satellite programs of the United States, Japan, the European Space Agency and soon India and the Soviet Union. Figure 1.1.4 displays the present day GOES (Geostationary Operational Environmental Satellite).

A list of current references to these various satellite systems are included at the end of this section. These references do not cover the

earliest beginnings of the satellite program, but rather emphasize the present situation. Prospects for the future are noted in Chapter 19. For more information about the early history the reader is referred to Hubert and Lehr (1967), NASA (1980), NASA (1982a) and to WMO-No.585. Chapter 2 of these notes discusses the instrumentation on the satellites in more detail.

1.1.2 Satellite Documents

General

Hoppe, E. R. and A. L. Ruiz, 1974: Catalog of operational satellite products. NOAA Technical Memorandum, NESS 53, NOAA-NESS, Washington, DC, 91 pp.

Houghton, J. T., 1979: The future role of observations from Meteorological Satellites. Quart. J. Roy. Meteor. Soc, 105, 443, 1-23.

Hubert, L. F. and P. E. Lehr, 1967: Weather Satellites. Blaisdell Publishing Co., Waltham, MA, 120 pp.

Johnson, J. D., F. C. Parmenter, and R. Anderson, 1975: Environmental satellites: Systems, data interpretation and application. NOAA-NESS, Washington, DC, 66 pp.

NASA, 1982a: Meteorological satellites -- past, present, and future, NASA Conference Publication 2227, AIAA 20th Aerospace Sciences Meeting, 11-14 January, Orlando, FL, 63 pp.

NASA, 1982b: The conception, growth, accomplishments and future of meteorological satellites, NASA Conference Publication 2257, American Meteorological Society's 62nd Annual Meeting, 11-15 January, San Antonio, TX, 101 pp.

NOAA Polar Orbiting Satellites (NOAA-2 to NOAA-5)

Fortuna, J. J., and L. N. Hambrick, 1974: The operation of the NOAA polar satellite system. NOAA Technical Memorandum NESS 60, NOAA-NESS, Washington, DC 127 pp.

TIROS-N and NOAA A-G Series

Hussey, J. W., 1977: The TIROS-N polar orbiting environmental satellite system. Technical Report, NOAA-NESS, Washington, DC, 35 pp.

Hussey, J. W., 1979: The TIROS-N/NOAA operational satellite system. Technical Report, NOAA-NESS, Washington, DC, 95 pp.

Kidwell, K. B., 1979: NOAA polar orbiter data (TIROS-N) users guide. Technical Report, National Climatic Center-SDSD, Washington, DC.

Lauritson, L., G. J. Nelson, and F. W. Porto, 1979: Data extraction and calibration of TIROS-N/NOAA radiometers. NOAA Technical Memorandum, NESS-107, 73 pp.

Schwalb, A., 1978: The TIROS-N/NOAA A-G satellite series, NOAA Technical Memorandum, NESS-95, 75 pp.

Schwalb, A., 1982: Modified version of the TIROS-N/NOAA A-G satellite series (NOAA E-J)-Advanced TIROS-N (ATN). NOAA Technical Memorandum, NESS-116, 23 pp.

Defense Meteorological Satellite Program (DMSP)

Dickinson, L. G., S. E. Boselly, and W. S. Burgmann, 1974: Defense meteorological satellite program (DMSP) user's guide. Technical Report AWS-TR-74-250, Air Weather Service, USAF.

SEASAT

NOAA, 1977: NOAA Program Development Plan for SEASAT-A Research and Applications. Report, NOAA-NESS, Washington, DC.

NIMBUS

NIMBUS Project, 1965: NIMBUS I User's Catalog. Goddard Space Flight Center, Greenbelt, MD.

_____, 1966: NIMBUS II Users' Guide. Goddard Space Flight Center, Greenbelt, MD, 229 pp.

_____, 1969: The NIMBUS III Users' Guide. Goddard Space Flight Center, Greenbelt, MD, 238 pp.

_____, 1970: The NIMBUS IV Users' Guide. Goddard Space Flight Center, Greenbelt, MD, 214 pp.

_____, 1972: The NIMBUS V Users' Guide. Goddard Space Flight Center, Greenbelt, MD, 112 pp.

_____, 1975: The NIMBUS VI Users' Guide. Goddard Space Flight Center, Greenbelt, MD, 227 pp.

_____, 1978: The NIMBUS VII Users' Guide. Goddard Space Flight Center, Greenbelt, MD, 263 pp.

SMS-GOES

Clark, J. D., 1983: The GOES User's Guide. NOAA/NESDIS, Washington, DC, 169 pp.

Corbell, R. P., C. J. Callahan, and W. J. Kotsch, 1976: The GOES/SMS User's Guide. NOAA-NESS, Washington, DC, 118p

METEOSAT

Ensor, G. J., 1978: The NOAA Geostationary Satellite System. NOAA-NESS, Washington, DC, 101 pp.

ESA, 1978: METEOSAT Image Bulletin. European Space Operation Center, Darmstadt, FRG.

ESA, 1981: Introduction to the METEOSAT system, ESA SP-1041, 54 pp.

METEOSAT Operations Division, 1978: Users' Guide to the METEOSAT Archive. Meteorological Data Management Department, European Space Agency, Darmstadt, FRG.

NCC, 1978: VISSIR Digital Archive Users' Guide. National Climatic Center, SDSD, Applications Branch, Washington, DC.

GMS

Meteorological Satellite Center, 1978: Monthly report of Meteorological Satellite Center. Monthly Summaries, MSC, Tokyo, Japan.

These documents, together with the more general references included at the end of this chapter, provide extensive background material for those interested in specific satellites.

1.2 Basic Orbits of Satellites

The purpose of this section is to demonstrate that for proper use of the data from satellites we must:

a) Define an orbit,

b) locate it in space,

c) locate the satellite in the orbit,

d) determine the attitude of the satellite,

e) know the optical axis relative to the satellite coordinate system, and

f) determine the pointing vector along the optical axis, and its intersection with the earth.

1.2.1 The Satellite Navigation Problem

The topic of this investigation is orbital mechanics and its relationship to the satellite navigation problem. Since the term "satellite navigation" denotes a variety of concepts, it is important to refine a definition for purposes of this study. We say, in general, that satellite navigation is a process of identifying the space and time coordinates of satellite data products (in this case meteorological satellites). Note that this characterization departs somewhat from the classical usage of navigation which implies the definition and maneuvering of the position of ships, aircraft, satellites, etc. A more exact definition is given in Section 1.2.2. A fundamental component of any satelite navigation system is a model of the satelite's orbital properties. This investigation is

primarily concerned with the mathematical and physical nature of near-earth meteorological satellite orbits and thus meteorological satellite navigation requirements. The study also considers the basic nature of the coordinate systems and the various measures of time.

There are two very general orbital application areas insofar as meteorological satellites are concerned. The first and more traditional application of orbital analysis is the process of tracking the position and motion of satellites, by the space agencies, so as to provide ephemeris and antenna pointing information to ground readout stations and operations command facilities. Considering that in this process, the actual characteristics of an orbital plane are defined, this can be referred to as a navigation process. However, for our purposes, we shall consider this process as an "orbital tracking" problem.

The second application is the analytic treatment of orbital motion in a model designed for processing the meteorological data, generated by spacecraft instrumentation. In this case, there are very different computational and operational restraints than in the case of orbit tracking. Primarily we are concerned with developing efficient and quick computational routines that retain a relatively high degree of orbital position accuracy, but are not bogged down with the multiplicity of external forces that orbit tracking models must consider.

The practical outcome of the study is a set of orbital computer models which are adaptable in a very general fashion, to a variety of analytic near-earth satellite navigation systems. The usability of these models is insured because they are based on the conventional orbital elements availabel from the primary meteorological satellite agencies, i.e., the National

Environmental Satellite, Data, and Information Service (NESDIS), the National Aeronautics and Space Administration (NASA), the European Space Agency (ESA), and the National Space Development Agency (NASDA) of Japan.

Meteorological satellites, whether they are of the experimental or operational type, are classified as either geosynchronous (≃ 24 hour period) or polar low orbiter (≃ 100 minute period) by the above agencies. The low orbiters may be placed in either sun-synchronous or non-sun-synchronous orbit. All of these satellites are in nearly circular orbit, and in general, are at altitudes at which atmospheric drag is not a significant factor over the prediction time scale under consideration (≃ 1-2 weeks). This investigation will address these types of orbits.

A principle reference used in this analysis is the very fine compendium on Orbit Mechanics by Pedro Ramon Escobal (1965), hereinafter EB. This work stands alone as an aid to solving orbital mechanics problems faced by satellite workers and scientists. Other very helpful references used in this study were the handbook on practical navigation by Bowditch (1962) and a translation of a Russian text on orbit determination by Dubyago (1961). The latter work provides a very interesting historical sketch of the development of orbital mechanics and man's understanding of the motion of celestial bodies.

1.2.2 Basic Concepts

1.2.2.1 Orbit mechanics and satellite Navigation

The following definitions are essential to an understanding of the ensuing analysis:

Orbital Mechanics: A branch of celestial mechanics concerned with orbital motions of celestial bodies or artificial spacecraft.

Celestial Mechanics: The calculation of motions of celestial bodies under the action of their mutual gravitational attractions.

Astrodynamics: The practial application of celestial mechanics, astro-ballistics, propulsion theory, and allied fields to the problem of planning and directing the trajectories of space vehicles.

Navigation (General): The process of directing the movement of a craft so that it will reach its intended destination: subprocesses are position fixing, dead reckoning, pilotage, and homing.

Navigation (Satellite): The process of determining a set of unique transformations between the coordinates of satellite data points in a satellite frame of reference and their associated terrestrial or planetary coordinates. (This definition should be contrasted with "Satellite Image Alignment", which is a non-analytic, mostly subjective process in which the two or more images to be aligned often have different aspect ratio characteristics.)

The major areas of Orbital Mechanics are:

1. Satellite Orbit Injection
    a. Thrust (Ballistic, Propulsion) forces
    b. Drag forces
    c. Lift forces

2. Determination of Orbital Elements

   a. Position vector, velocity vector, and initial time

      $(\vec{r}, \dot{\vec{r}}, t_0)$

   b. Two position vectors and times $(\vec{r}_1, t_1, \vec{r}_2, t_2)$

   c. Three pairs of azimuth-elevation angles and times
      $[(\Phi_1, H_1, t_1), (\Phi_2, H_2, t_2), (\Phi_3, H_3, t_3)]$

   d. Slant-range, range-rate, and time observations
      $[(d_1, \dot{d}_1, t_1), (d_2, \dot{d}_2, t_2)...]$

   e. Mixed observations (angles, ranges, range-rates, times)

3. Orbital Properties and Tracks

   a. Orbital elements

   b. Velocities and periods

   c. Position vectors

   d. Direct and retrograde orbits

   e. Equator crossing data

   f. Orbital revisit frequencies

4. Orbital Analytics

   a. Nodal passages

   b. Satellite rise and set times

   c. Line of sight periods and eclipses

   d. Orbital architecture

The ensuing analysis will be primarily concerned with the topics outlined in parts 3 and 4. Since meteorological satellite navigation methods are generally not affected by how satellites are placed in orbit nor how the various space agencies track these satellites so as to produce orbital elements (other than the associated errors), we will put aside any further discussion of parts 1 and 2, and instead concentrate on the material outlined in parts 3 and 4.

1.2.2.2 Satellite Navigation Modeling

Satellite navigation modeling can be considered to be a five-part problem:

1. The time dependent determination of the spacecraft orbital position in an inertial coordinate system.

2. The time dependent determination of the spacecraft orientation (attitude) in an inertial coordinate system.

3. The specification or determination (time dependent) of the optical paths of the imaging or sounding instrument with respect to the spacecraft.

4. The integration of the above static and dynamic aspects of the spacecraft into a model which can provide measurement point vectors in the inertial frame of reference.

5. The transformation of the inertial pointing vectors to pointing vectors in the preferred (non-inertial) coordinate system.

The first requirement of an analytic navigation technique is a model which can solve for satellite position at any specified time. In fact, the determination of spacecraft orientation is absolutely dependent on knowledge of satellite position if ground-based or star-based attitude determination techniques are applied. A discussion of this topic can be found in Smith and Phillips (1972) and is presently being extended by Phillips (1979). With the knowledge of spacecraft position and orientation, the dynamics of the actual on-board instrumentation can then be considered. Finally, upon integration of these three dynamic aspects of an orbiting satellite into an appropriate model, pointing vectors can be obtained which fix the relationship between an instrument field-of-view and a terrestrial coordinate (latitude, longitude, height).

1.2.2.3 Satellite Orientation

It is important to distinguish between the effect of varying satellite position and varying satellite orientation on the apparent earth scene. First of all, it is instructive to define the various terms associated with satellite orientation.

Attitude: Orientation of the principal axis of a spacecraft, e.g., the spin axis, with respect to the principal axis (spin axis) of the earth, usually given in terms of declination and right ascension with respect to a celestial frame of reference.

Precession: The angular velocity of the axis of spin of a spinning rigid body, which arises as a result of steady uneven external torques acting on the body.

Nutation: A high frequency spiral, bobbing, or jittering motion of a spinning rigid body about a mean principal axis, due to asymmetric weight distribution or short period torque modulation.

Wobble: An irregular vacillation of a body about its mean principal axis due to non-solid body characteristics.

Figure 1.2.1 has been provided to illustrate these definitions.

Variation in the orientation of a meteorological satellite can lead to both translations and rotations of earth fields with respect to a fixed satellite field-of-view. These apparent motions are superimposed on real motions due to variation in the orbital position. A requirement of any satellite navigation model is the inclusion of procedures to separate the apparent motions from the real motions which are essentially independent processes. Therefore, this investigation will be devoted to the deter-

mination of orbital position as these calculations generally preface the determination of the remaining navigational parameters.

1.2.2.4 Applications of a Satellite Navigation Model

Finally, an important question concerning satellite navigation is: "What does a navigation model provide?" Essentially, it provides the following three capabilities:

1. The capability of placing grid and/or geographic-topographic annotation information in or on the data. This process should be called a "Gridding" process.

2. A means to specify the terrestrial or planetary coordinate of a given data point coordinate, or conversely, to specify the data point coordinate corresponding to a given terrestrial or planetary coordinate. This process should be called a "Navigational Interrogation" process.

3. A framework for transforming the raw satellite imagery into alternate cartographic (map) projections. The actual process of reorganizing the raw data into a new projection should be called a "Mapping" process.

Note the actual navigation process only involves specifying, calculating, or determining the appropriate parameters inherent to the navigation model and utilizing them to calculate coordinate transformations.

1.2.3 The Two Body Problem

1.2.3.1 The Inverse Square Force Field Law

We continue the analysis by considering the two body problem, ignoring all of the perturbative influences (i.e., thrust, drag,

lift, radiation pressure, proton bombardment or solar wind, asymetrical electromagnetic forces, auxillary bodies and any aspherical gravitational potential of either body); that is, we consider only the mutual attractions of a body A with a body B and the resultant motions. Furthermore, we assume that the motion under consideration is that of a satellite or planetary body B (secondary body of mass m_2) with respect to a central body A (primary body of mass m_1).

For closed solutions we will utilize the inverse square force field law:

$$\frac{d^2\vec{r}}{dt^2} = \ddot{\vec{r}} = -\frac{K^2\mu\vec{r}}{r^3} \qquad (1.1)$$

First, we determine the origin of the above equation, Essentially, Equation 1.1 embodies the laws of Kepler and Newton. To review:

<u>Kepler's Laws</u> (Empirical-aided by astronomical observations)

I. Within the domain of the solar system all planets describe elliptical paths with the sun at one focus.

II. The radius vector from the sun to a planet generates equal areas in equal times.

III. The squares of the periods of revolution of the planets about the sun are proportional to the cubes of their mean distances from the sun.

<u>Newton's Laws of Motion</u>

I. Every body will continue in its state of rest or of uniform motion in a straight line except insofar as it is compelled to change that state by an impressed force.

II. Rate of change of momentum (mv) is proportional to the impressed force and takes place in the line in which the force acts.

$$F = ma = m(dv/dt)$$

III. Action and reaction are equal and opposite.

<u>Newton's Law of Universal Gravitation</u>

Any two bodies in the universe attract one another with a force (F_{12}) which is directly proportional to the product of thier masses (m_1, m_2) and inversely proportional to the square of the distance (r_{12}) between them:

$$F_{12} = Gm_1m_2/r_{12}^2 \qquad (1.2)$$

$$= K^2m_2/r_{12}^2$$

where:

$K^2 = Gm_1$

G = Universal Gravitational Constant

$= 6.373 \cdot 10^{-8}$ dyne.cm^2.g^{-2}

m_1 = large mass (e.g., the earth)

m_2 = smaller mass (e.g., a satellite)

We can derive the inverse square force field law from Newton's second law and his law of universal gravitation. Adopting the notation in Chapter 2 of EB, the Universal Law of Gravitation states:

$$F_{12} = \frac{Gm_1m_2}{r_{12}^2} \qquad (1.3)$$

Now consider an <u>arbitrary</u> inertial reference frame shown in Figure 1.2.2.

The force in the x direction F_{1x} is:

$$F_{1x} = F_{12}\cos\theta = F_{12}.(x_2 - x_1)/r_{12} \qquad (1.4)$$

therefore:

$$F_{1x} = \frac{Gm_1m_2}{r_{12}^2} \cdot \frac{x_2 - x_1}{r_{12}} \qquad (1.5)$$

and finally:

$$F_{1x} = \frac{Gm_1m_2}{r_{12}^3} (x_2 - x_1) \qquad (1.6)$$

= force on body 1

Newton's second law states that the unbalanced force on a body in the x direction is given by:

$$F_{1x} = m_1 \frac{d^2x_1}{dt^2} \tag{1.7}$$

therefore:

$$M_1 \frac{d^2x_1}{dt^2} = Gm_1m_2 \frac{(x_2 - x_1)}{r_{12}^3} \tag{1.8}$$

Now repeating the analysis for the y and z components we find:

$$m_1 \frac{d^2\vec{r}_1}{dt^2} = Gm_1m_2 \frac{(\vec{r}_2 - \vec{r}_1)}{r_{12}^3} \tag{1.9}$$

or:

$$\frac{d^2\vec{r}_1}{dt^2} = K^2 \frac{m_2}{m_1}(\vec{r}_2-\vec{r}_1)/r_{12}^3 \tag{1.10}$$

Now transform to a <u>relative</u> inertial coordinate system as shown in Figure 1.2.3. From above:

$$m_1 \frac{d^2\vec{r}_1}{dt^2} = Gm_1m_2 \frac{\vec{r}_{12}}{r_{12}^3} \tag{1.11}$$

where:

$$\vec{r}_{12} = \vec{r}_2 - \vec{r}_1 \tag{1.12}$$

Now considering only the x component:

$$x_{12} = x_2 - x_1 \tag{1.13}$$

we note that:

$$\underline{d^2x_{12}} = \underline{d^2x_2} - \underline{d^2x_1} \tag{1.14}$$

$$dt^2 \qquad dt^2 \qquad dt^2$$

which is the desired expression for the acceleration of body 2 with respect to body 1.

From our arbitrary inertial analysis:

$$m_1 \frac{d^2x_1}{dt^2} = Gm_1m_2 \frac{x_{12}}{r_{12}^3} \tag{1.15}$$

$$m_2 \frac{d^2x_2}{dt^2} = Gm_2m_1 \frac{x_{21}}{r_{21}^3} \tag{1.16}$$

Now since $r_{12} = r_{21}$, and cancelling masses, then:

$$\frac{d^2x_1}{dt^2} = Gm_2 \frac{x_{12}}{r_{12}^3} = Gm_2 \frac{(x_2-x_1)}{r_{12}^3} \tag{1.17}$$

$$\frac{d^2x_2}{dt^2} = Gm_1 \frac{x_{21}}{r_{12}^3} = Gm_1 \frac{(x_1-x_2)}{r_{12}^3} \tag{1.18}$$

and subtracting the two equations yields:

$$\frac{d^2x_2}{dt^2} - \frac{d^2x_1}{dt^2} = \frac{d^2x_{12}}{dt^2} = Gm_1 \frac{(x_1-x_2)}{r_{12}^3} - Gm_2 \frac{(x_2-x_1)}{r_{12}^3} \tag{1.19}$$

$$\frac{d^2x_{12}}{dt^2} = -G(m_1 + m_2) \frac{(x_2-x_1)}{r_{12}^3} \tag{1.20}$$

Now repeating the analyses for the y and z components we find:

$$\frac{d^2\vec{r}_{12}}{dt^2} = -Gm_1 \frac{(m_1 + m_2)}{m_1} \frac{\vec{r}_{12}}{r_{12}^3} \tag{1.21}$$

and finally:

$$\frac{d^2\vec{r}}{dt^2} = \ddot{\vec{r}} = \frac{-K^2\mu\vec{r}}{r^3} \tag{1.22}$$

where:

$$\mu = (m_1 + m_2)/m_1$$
$$= \text{normalized mass sum}$$

We generally apply (1.22) to a system where the primary mass (m_1) is much greater than the secondary mass (m_2), yielding μ approximately 1.0.

Often in the study of orbital mechanics, an n-body system arises in which the desired origin of the coordinate system is the mass center or barycenter; that is, motion is relative to the barycenter and not any single central body (see Figure 1.2.4). We refer to such a reference system as a <u>Barycentric Coordinate System</u> (see a review in Chapter 2 of EB). The utility of this frame of reference can be seen in the event that the trajectory of a space vehicle would undergo <u>less disturbed</u> motion if referred to as a barycenter. Since we are primarily concerned with near-earth satellites we will forego an examination of the barycentric coordinate system. It is useful to examine the governing equation, however:

$$\frac{d^2\vec{r}_{B2}}{dt^2} = -G\left(\sum_{i=1}^{n} m_i\right) \frac{\vec{r}_{B2}}{r_{B2}^3} + G \sum_{\substack{i=1 \\ i \neq 2}}^{n} m_i \vec{r}_{i2} \left(\frac{1}{r_{B2}^3} - \frac{1}{r_{i2}^3}\right) \tag{1.23}$$

where:

n = 1 (the primary mass of the system)

$n = 2$ (the space vehicle under consideration)

and B represent the barycenter.

1.2.3.2 Coordinate Systems and Coordinates

We first define the celestial sphere:

Celestial Sphere: An imaginary sphere of indefinitely large radius, having the earth as the origin and the fundamental plane being an infinite extension of the Earth's equatorial plane (see Figure 1.2.5). To define the celestial sphere we first extend a line along the fundamental plane to a point fixed by the vernal equinox (γ), which is the reference meridian, and let that be the x-axis. The z-axis is given by the earth's spin axis or principal axis. An orthogonal coordinate system is finally established by defining the y-axis as the cross product of the z and x axes (see Figure 1.2.6).

This celestial reference frame is often termed a right ascension-declination inertial coordinate system, in which declination (δ) is analogous to latitude (ϕ) (or as the case may be - colatitude), and right ascension (ρ) is analogous to longitude (λ) or hour angle (HA). Note that we refer to the equatorial plane as the fundamental plane, the z-axis as the principal axis, the vernal equinox as the reference meridian. Also note that the celestial coordinate system is not truly an inertial system since it utilizes the terrestrial spin axis as the principal axis. Since the earth's spin axis precesses (giving rise to the westward precession of the equinoxes) we are left with a non-inertial reference frame if we consider very long time periods. There is also a lunar influence on the

earth's spin axis which causes a nutation having a periodicity of approximately 18.5 years. Superimposed on these motions is the so-called Chandler Wobble, which has a period of approximately 14 months and is due to the non-solid nature of the earth itself. For our purposes, the non-inertial variation in the terrestrial spin axis is ignored.

It should be noted that we can define our coordinate system in any way we choose, however, simplicity and convenience are the watchwords. In designing coordinate systems for the various orbiting bodies or vehicles contained in the solar system, the same basic principles that are used for the earth centered (geocentric) celestial coordinate system are applied. Examples of various coordinate systems adopted for orbital analysis are referred to as follows (see EB):

Reference Body	Coordinate System
Earth	Geocentric
Sun	Heliocentric
Moon	Selenographic
Mars	Arcocentric
Satellite	Orbit Plane

It should also be pointed out that there are a choice of coordinates to be used once the coordinate system is defined. Again, the choice is arbitrary, however, the chosen coordinate parameters should have a natural relationship between the observer and the observed depending on whether measurement, calculation, or description is the nature of the problem on hand. Again, there are a variety of choices:

1. Declination (δ) - right ascension (ρ) - radial distance (r)
2. Declination (δ) - hour angle (HA) - radial distance (r)

3. Latitude (ϕ) - longitude (λ) - height (h)
4. Elevation (H) - azimuth (ϕ) - slant range (d)
5. Zenith (θ) - azimuth (ϕ) - altitude (h)
6. Cartesian (x,y,z)

The solution of the governing equation (1.22) given in an earth-relative celestial coordinate system will yield three constants after the first integration (of the three component equations), and three constants after the second. Since (1.22) is an acceleration form of a linear, second order, ordinary differential equation, the first set of constants are initial velocity terms ($\dot{x},\dot{y},\dot{z}$) and the second set of constants are initial position terms (x_0, y_0, z_0). Thus, if we are given a position vector and a velocity vector at an epoch time t_0 (six orbital elements and an epoch), we have a means to solve the governing equation.

Usually, this set of initial elements is not available since observation of the secondary body B are made from a rotating primary body A (that is a coordinate system that is different from that in which the analysis will be performed). That is why elevation-azimuth angle observations or range-range rate signals must first be transformed to a set of convenient orbital elements in the preferred coordinate system. Since this problem comes under the more general problem or orbital determination we will not consider it any further.

1.2.3.3 Selection of Units

Simplicity and computation efficiency can be achieved with the proper selection of units, based on the particular orbital problem. The proper choice of physical units for length, mass, and time is

primarily determined by the dimensionality of the primary body A. We shall discuss two systems of units; the Heliocentric (solar origin) and Geocentric (terrestrial origin) systems.

1. Heliocentric Units

Length: Astromical Unit (A.U.)

The mean distance between the sun and a fictitious planet, subjected to no perturbations, whose mass and sidereal period are the values adopted by Gauss in his determination of K_0 (we will discuss K_0 later).

1 A.U. = $1.496 \cdot 10^8$ km per A. U.

Mass: Mass of Sun (m_0)

$m_0 = 1.9888822 \cdot 10^{33}$ g per solar mass (s.m.)

Now if we use our previous definition:

$$G(m_0 + m_p) = k^2\mu \tag{1.24}$$

where:

m_0 = mass of sun

m_p = mass of planet

$K^2 = Gm_0$,

$\mu = (m_0 + m_p)/m_0$,

we can define normalized mass factors for the nine planets. Note that the mass of a planet in the heliocentric system would also include the mass of its moons. Table 1.2.1 provides normalized mass factors for the nine planets.

Table 1.2.1: Solar System Normalized Mass Factors

Planet	Normalized Mass Factor (μ)
Mercury	1.0000001
Venus	1.0000024
Earth-Moon	1.0000030
Mars	1.0000003
Jupiter	1.0009547
Saturn	1.0002857
Uranus	1.0000438
Neptune	1.0000512
Pluto	1.0000028

2. Geocentric Units

Length: Earth equatorial radius (e.r.)

1 e.r. = 6378.214 km per e.r.

Mass: Mass of earth (m_e)

$m_e = 5.9733726 \cdot 10^{27}$ g per earth mass (e.m.)

Note the mass of the moon (m_m):

$m_m = 7.3473218 \cdot 10^{25}$ g per moon mass (m_m)

must be considered as part of the planetary mass when considering the earth orbit in a heliocentric system, but is ignored when considering a satellite in a geocentric system.

1.2.3.4 Velocity and Period

We need to define the velocity and period of an orbiting body. Consider first the circular orbit of a satellite at height

h (mass m_s) above the earth (radius R_e). Therefore, the geocentric radius r is given by

$$r = R_e + h \tag{1.25}$$

and:

$$m_s \ddot{\vec{r}} = - m_s \cdot K^2 \mu \vec{r}/r^3 \tag{1.26}$$

However, the magnitude of $m_s r$ is a centrifugal force $-m_s \cdot V^2/r$ where V is the circular velocity at orbital altitude. Therefore in scalar form:

$$m_s \frac{V^2}{r} = \frac{m_s \cdot K^2 \cdot \mu}{r^2} \tag{1.27}$$

$$V^2 = \frac{K^2 \cdot \mu}{R_e + h} \tag{1.28}$$

$$V = (K^2 \mu/(R_e + h))^{\frac{1}{2}} \tag{1.29}$$

$$V = K (\mu/(R_e + h))^{\frac{1}{2}} \tag{1.30}$$

Therefore V is the required orbit velocity for a circular orbit at height h.

Since the circular orbital track would be a distance of $2\pi(R_e + h)$, for a single revolution, the orbital period (P) would be $2\pi\cdot(R_e + h)/V$, or:

$$P = \frac{2\pi\cdot(R_e + h)^{3/2}}{K\mu^{\frac{1}{2}}} \tag{1.31}$$

Note that as the height of a satellite <u>increases</u>, the velocity required to maintain it in circular orbit <u>decreases</u>. See Figure 1.2.7 for an illustration. Note, however, from a propulsion point of view, more energy is expended in lifting a satellite against gravity to reach a higher orbit, than is gained in the reduction or the forward speed required for orbit injection.

If we solve $P = \pi\cdot(R_e + h)^{3/2}/(K\mu^{1/2})$ for h using a period P of 24 hours, we have solved for the required height of a geosynchronous satellite; that is, an orbital configuration in which the period is that of a single rotation of the earth. The required height for a geosynchronous satellite in a circular orbit is thus approximately 35,863 km (42241.214 km from geocentric origin).

Now since we know the orbital period P, we can determine the ground speed (V_{gs}) of a circular orbit, i.e., the velocity at radius R_e. Since the path of one revolution is $2\pi \cdot R_e$, then

$$V_{gs} = 2\pi R_e/P$$

$$= \frac{R_e}{R_e + h} \cdot K \cdot \left(\frac{\mu}{R_e + h}\right)^{\frac{1}{2}} \tag{1.32}$$

and applying equation (5.29):

$$V = \frac{R_e}{\quad} \cdot V \tag{1.33}$$

$$gs \quad (R_e + h)$$

Table 1.2.2 tabulates various orbital characteristics as a function of satellite altitude.

1.2.3.5 Elliptic Orbits

In the consideration of elliptic orbits governed by our principle equation, the radius r, of the second body from the primary body, can be given by

$$r = p/(1 + e \cdot \cos v) \tag{1.34}$$

which is simply the equation describing conic section (see Figure 1.2.8), where:

e = eccentricity

v = true anomaly

p = semi-parameter of conic

= ed

Thus we see that if $p \neq 0$, then:

$0 < e < 1$ the conic is an ellipse

$e = 1$ the conic is a parabola

$1 < e < \infty$ the conic is a hyperbola

In the following disccussions the term semi-major axis (a) will be used. It is defined as half the maximum diameter of the conic. Note that (see Dubyago, 1961):

$a = 0$ for parabolic motion

$0 < a < \infty$ for elliptic or circular motion

$-\infty < a < 0$ for hyperbolic motion

For an ellipse, a and p are related through e by $p=ed=a(1-e^2)$.

As an aside, it is interesting to note that for any arbitrary position of a vehicle, within the influence of the terrestrial gravitational field, there is a given escape velocity (V_{esc}). The magnitude of the initial velocity vector r determines the type of path, that is:

elliptic if $\| \dot{\vec{r}} \| < v_{esc}$

parabolic if $\| \dot{\vec{r}} \| = V_{esc}$

hyperbolic if $\| \dot{\vec{r}} \| > V_{esc}$

The escape velocity from a celestial body is given by:

$$V_{esc} = (2gR)^{1/2} \tag{1.35}$$

where:

g = gravitational constant of body

R = radius of body

For the earth and noon, the escape velocities of a missile launched from the surface are:

Body	V_{esc}
Earth	$\simeq 11\ km \cdot s^{-1}$
Moon	$\simeq 2.5\ km \cdot s^{-1}$

Contrast the above to the velocity of an air parcel at the earth's surface (no wind):

$$V_{par} = \Omega R_e = 7.292 \cdot 10^{-5} \cdot 6371\ km \cdot s^{-1} \tag{1.36}$$

$$\doteq 0.46\ km \cdot s^{-1}$$

where Ω is the earth's angular velocity and R_e is the earth radius.

The equation for an ellipse, in polar coordinates with the origin at a focus, is given by:

$$r = a(1 - e^2)/(1 + e \cdot \cos v) = p/(1 + e \cdot \cos v) \tag{1.37}$$

Noting that $p \neq 0$, $0 < e < 1$, and $0 < a < \infty$ for the planets, constitutes a proof of Kepler's First Law.

A proof of Kepler's Second Law requires an integration of the area swept out by the radius vector $\vec{r}$. This results in the definition of the orbital period P in the relative inertial coordinate system which we have established. The period is then given by:

$$P = \frac{2\pi}{K\mu^{\frac{1}{2}}}\, a^{3/2} \tag{1.38}$$

which corresponds to equation (1.31). A proof of equation (1.38) is given in Chapter 3 of EB.

This is the appropriate form in a relative inertial coordinate system. Note that for circular orbits:

$$V = K\,(\mu/a)^{\frac{1}{2}} \tag{1.39}$$

which corresponds to equation (5.30). For elliptic orbits V is not constant.

Now since the period P of a body is:

$$P = \frac{2\pi}{K\mu^{\frac{1}{2}}}\,a^{3/2} \tag{1.40}$$

we can square both sides to get Kepler's Third Law:

$$P^2 = \frac{4\pi^2}{K^2\mu}\,a^3 \tag{1.41}$$

(The squares of the periods of revolution of the planets about the sun are proportional to the cubes of their mean distances from the sun.)

It is interesting that Kepler derived his laws empirically, involving many years of laborious data reduction. His 3rd law did not include the mass factor μ since the accuracy in his data simply did not allow the detection of the secondary mass effect (see EB).

1.2.3.6 The Gaussian Constant

We can now define the Gaussian constant K_0, noting that:

$$P^2 = \frac{(2\pi)^2}{\mu K^2}\,a^3 \tag{1.42}$$

and choosing a heliocentric system of characteristic units. It is a simple matter to compute the numberical value of K^2 or the Gaussian constant:

$$K_0 = (K^2)^{\frac{1}{2}} \tag{1.43}$$

thus:

$$K_0 = \frac{2\pi}{P\mu^{\frac{1}{2}}} \; a^{3/2} \tag{1.44}$$

Now since the period of the Earth is 365.256365741 mean solar days (celestial period), and if the semi-major axis of the earth's orbit is taken to be 1 A.U. and $\mu^{\frac{1}{2}} = 1.0000015$, then $K_0 = 0.017202099$ A.U.$^{3/2}$·day^{-1}.

This was the procedure Gauss used to determine K_0 in his 1809 publication "Theoria Motus Corporum Coelestium In Sectionibus Conicis Solem Ambientium", i.e., Theory of the Motion of Heavenly Bodies Revolving Round the Sun in Conic Sections (see EB). Similar procedures are used to obtain the gravitational constants of the other planets. Table 1.2.3 provides gravitational constant data for the planets.

Table 1.2.3: Gravitational Constants of the Major Planets

(From Escobal, 1965)

Planet	Semimajor Axis (km)	Gravitational Constants (K_p) (A.U.$^{3/2}$/Mean Solar Day)
Mercury	2,424	6.960×10^{-6}
Venus	6,100	2.691×10^{-5}
Earth	6,378.15	2.99948×10^{-5}
Mars	3,412	9.786×10^{-6}
Jupiter	71,420	5.3153×10^{-4}
Saturn	60,440	2.908×10^{-4}
Uranus	24,860	1.136×10^{-4}
Neptune	26,500	1.240×10^{-4}
Pluto	4,000	2.700×10^{-5}

Note that for Table 1.2.3, 1 A.U. = 149,599,000 km and K_p is related to K_o by $K_p = K_o\,(m_p/m_o)^{\frac{1}{2}}$. Also note that in the geocentric system, the present value of K_e (earth gravitational constant) is 0.07436574 e.r.$^{3/2}$ · min^{-1}.

1.2.3.7 Modified Time Variable

It is often convenient in the treatment of orbital problems to transform the time dimension to the so-called modified time variable (τ). The transformation involves a gravitational constant (e.g., K_θ or K_e) and an epoch time t_o. In Heliocentric units:

$$\tau = K_o(t-t_o) \tag{1.45}$$

whereas in Geocentric units:

$$\tau = K_e(t-t_o) \tag{1.46}$$

The advantage of using this quantity can be seen if we recast the governing equation in terms of τ. Since:

$$d^2\tau = K^2 d^2t \tag{1.47}$$

then:

$$\frac{d^2\vec{r}}{dt^2} = -K^2\ \mu\vec{r}/r^3 \tag{1.48}$$

transforms to:

$$\frac{d^2\vec{r}}{d\tau^2} = -\ \mu\vec{r}/r^3 \tag{1.49}$$

and K^2 does not appear.

Use of characteristics units, leads to a new unit of velocity (V_{csu}), the circular satellite unit velocity (see Chapter 3 of EB):

$$v_{csu} = K(\ \frac{\mu}{a}\ )^{\frac{1}{2}} \tag{1.50}$$

In The Heliocentric System:

$$v_{csu} = K_\theta\ (\frac{1}{1\ A.U.})^{\frac{1}{2}} = 0.017202099 \quad \frac{A.U.^{3/2}}{day}\ (\frac{1}{1\ A.U.})^{\frac{1}{2}} \tag{1.51}$$

$$v_{csu} = 0.017202099\ \frac{A.U.}{day} \cdot 1.496 \cdot 10^{11}\ \frac{m}{A.U.} \cdot \frac{1\ day}{86400\ sec} \tag{1.52}$$

$$= 29,785\ m \cdot s^{-1}$$

In the Geocentric System:

$$V_{csu} = K_e \left(\frac{1}{1\ e.r.}\right)^{\frac{1}{2}} = 0.07436574\ \frac{e.r.^{3/2}}{min} \left(\frac{1}{1\ e.r.}\right)^{\frac{1}{2}} \qquad (1.53)$$

$$V_{csu} = 0.07436574\ \frac{e.r.}{min} \cdot 6.378214 \cdot 10^6\ \frac{m}{e.r.} \cdot \frac{1\ min}{60\ sec} \qquad (1.54)$$

$$= 7{,}905\ m \cdot s^{-1}$$

1.2.3.8 Classical Orbital Elements

Let us first establish an elliptic frame of reference in which we consider coordinates along x_ω, y_ω axes in a plane containing the orbit (see Figure 1.2.9).

We have already defined:

e = eccentricity

$= (a^2 - b^2)^{\frac{1}{2}}/a$

a = semi-major axis

b = semi-minor axis

p = semi-parameter of cnic

$= a(1-e^2)$

v = true anomaly

In addition, the positions where $dr/d\tau$ are zero are called apsis (plural for apse). Elliptical orbits possess two points where the above condition is satisfied, i.e., the minimum radius position (perifocus) and the maximum radius position (apofocus). In discussing the sun in its ecliptic, we refer to the apsis as perihelion and aphelion (see Figure 1.2.10).

A complete set of orbital elements sufficient to describe an orbit are the "Classical Orbital Elements".

They are as follows:

1. Epoch Time (t_0): Julian day and GMT time for which the following elements are defined.

2. Semi-major Axis (a): Half the distance between the two apsis of perifocus and apofocus.

3. Eccentricity (e): Degree of ellipticity of the orbit.

4. Inclination (i): Angle between the orbit plane and the equatorial plane of the primary body.

5. Mean Anomaly (M_0): Angle in orbital plane with respect to the center of a mean circular orbit, having a period equivalent to the anomalistic period, from perifocus to the satellite position.

6. Right Ascension of Ascending Node (Ω_0): Angle in orbital plane between vernal equinox (reference meridian) and northward equator crossing.

7. Argument of Perigee (ω_0): Angle in orbit plane from ascending node to perifocus.

The above set of elements satisfies the requirement of defining six constants and an epoch time noted in Section 1.2.3.2. Note that if the epoch time were to correspond to perifocus, the mean anomaly would be zero and thus would be an unnecessary parameter. This is generally not the case with either NASA, NESS, ESA, or JMS orbital element transmissions. Of the 7 parameters, the threer angular quantities (M_0, Ω_0, ω_0) are subscripted similar to t_0 indicating that they are time dependent quantities. The European Space Agency has used true anomaly rather than mean anomaly in their orbital transmissions for the Meteosat and GOES-1 satellites.

First we recall the essential angles:

i ▪ Orbital inclination

Ω_0 ▪ Right ascension of ascending node

ω_0 ▪ Argument of perigee

Following the approach given in Chapter 3 of EB, the angles i, Ω_0, ω_0 (the "Classical Orientation Angles") are used to define the orbit plane in celestial space, defined by an orthogonal (I, J, K) coordinate system (as shown in Figure 1.2.11).

Note that:

$$0 \leq i < \pi$$

$$0 \leq \Omega_0 < 2\pi$$

$$0 \leq \omega_0 < 2\pi$$

From Figure 1.2.11 it is convenient to define retrograde and direct orbits:

1. Retrograde: Orbits whose motion is in the direction of y to x.
2. Direct or Prograde: Orbits whose motion is in the direction of x to y.

Compare the above with the classic definition of a retrograde orbit:

> Motion is an orbit opposite to the usual orbital direction of celestial bodes within a given system; e.g., a satellite motion, in a direction opposite to the motion of the primary body.

Finally, adding the satellite to the orbit, as in Figure 1.2.12, allows display of the mean anomoly M_0 (angle v in the figure). The mean anomaly is the angle from the perifocus to the satellite position, completing the set of orbital elements needed to define the position of a satellite in space.

1.2.4 Perturbation Theory

1.2.4.1 Concept of Gravitational Potential

We will now consider the deviation of an orbit from the ideal, two body, inverse square-force field law. In order to do so, we must distinguish the concepts of empirically correctly orbit calculation due to a non-perfect two body system, and the actual prediction of orbit positions based on a physical model which accounts for forces that perturb a body from perfect two body motion. The first technique has received a good deal of study under the general heading of "Differential Correction". A discussion of this topic is given in Chapter 9 of EB, by Dubyago (1961), and by Capellari et al. (1976). The method consists of bringing a predicted orbit position into agreement with a set of actual orbit measurements in such a way so as to adjust a set of constant orbital elements to satisfy a new local time period. Thus the methodology does not necessarily consider the physical reasons why an orbit is perturbed.

The general area of "Perturbation Theory" consists of developing a set of reasonable, time dependent quantities which arise due to various perturbation forces, which in turn lead to time dependent expressions for the orbital elements themselves. This theory, although not necessarily adaptable to analytic techniques, has a physical basis in fact. Since the satellite navigation problem is not really compatible with the required procedures used in Differential Correction techniques, we shall address the following discussion to perturbation techniques.

1.2.4.2 Perturbative Forces and the Time Dependence of Orbital Elements

A satellite, under the influence of a perfect inverse square force field law, would have a set of constant orbital elements:

$$[a, e, i, M_0, \Omega_0, \omega_0]$$

devoid of any time dependence. However, due to perturbative forces, the orbital elements are acted upon leading to shifts or oscillations. There are a number of effects which can be considered as perturbative forces:

1. Aspherical gravitational potential
2. Auxillary bodies (e.g. sun, moon, planets)
3. Atmospheric drag
4. Atmospheric lift
5. Thrust
6. Radiation Pressure (shortwave and longwave radiation)
7. Galactic particle bombardment, e.g. protons (e.g. solar wind)
8. Electromagnetic field asymmetry

The most important of these effects on earth satellites is due to the first factor; the aspherical gravitational potential of the earth itself. Atmospheric drag becomes significant for the lower orbit satellites (heights less than 850 km).

The aim of general perturbation theory is to develop closed expression for the time dependence of the orbital elements. It has been shown that perturbations possess different characteristics (see Chapter 10 of EB and Dubyago (1961) for a review):

1. Secular variations
2. Long term periodic variations
3. Short term periodic variations

In working with meteorological satellite orbits, we are primarily concerned with non-oscillatory secular perturbations which cause ever increasing or decreasing changes of particular orbital elements away from their values at an epoch t_0 as shown in Figure 1.2.13

The aspherical gravitational potential of the earth primarily effects M, Ω, and ω (where we understand that M, Ω, and ω without subscripts are no longer constant). The other elements (a, e, i) undergo minor periodic variations about their mean values due to the aspherical gravitational potential, but in terms of meteorological satellite orbits, are not considered significant. In general, long period variations are caused by the continuous variance of ω whereas short period variations are caused by linear combinations of variations in M and ω.

In terms of meteorological satellites we are generally considering nearly circular, free flying orbits with altitudes greater than 800 km. In addition, updated orbital parameters from the satellite agencies can be expected at a frequency of no greater than two weeks. Given these boundary conditions, most of the above perturbation terms can be ignored. The major perturbation effect, of course, is the non-sphericity of the earth and the resultant effect on the gravitational potential field. The minor terms insofar as meteorological satellites are concerned, are the lunar effect, atmospheric drag, and solar radiation pressure. In general the minor terms need not be included in orbit propagations that take place over a one to

two week period, if we consider the allowable error bars associated with satellite navigation requirements. That is to say, ignoring the effect of the minor perturbations does not lead to position or ephemeris errors significantly greater than the resolution of the data fields under analysis.

It is important to note that the space agencies responsible for tracking satellites often include the minor terms in retrieving orbital elements. This is due to the fact that generalized orbit retrieval packages have been developed for the extensive variety of operational and experimental satellites, and missiles rather than retrieval packages individually tailored to specific types of satellites. The primary difficulty with treating the minor terms in a satellite navigation model is that the required mathematics does not lend itself to streamlined analytic calculations, a principle requirement for processing the vast amounts of data produced by most meteorological satellite instruments. This is the principle reason for retaining only the major perturbation effect (asymmetric gravitational potential) which can be handled in a direct analytic fashion.

If we ignore the oscillatory components (in a, e, and i) we can then develop secular perturbation expressions for any selected order of the gravitational potential expansion. It is this process, for satellite applications, which elements the time dependence in a, e, and i while including it in M, Ω, and ω. Next note that the time dependence of an arbitrary orbital element (x) can be expressed as a Taylor series expansion:

$$x = x_0 + \dot{x}(t - t_0) = \ddot{x}(t - t_0)^2/2! + \ldots \qquad (1.55)$$

where x_0 is the initial value at an epoch t_0, and $\dot{x}$, $\ddot{x}$, ..., are time

derivatives. Now, if we ignore all but first order time derivatives and consider only the first order variations of the aspherical gravitational potential, we can express the time dependence of M, Ω, and ω in simple finite difference form with adequate accuracy:

$$
\begin{aligned}
M &= M_o + \dot{M}(t - t_o) \\
\Omega &= \Omega_o + \dot{\Omega}\,(t - t_o) \\
\omega &= \omega_o + \dot{\omega}(t - t_o)
\end{aligned}
\tag{1.56}
$$

where $\dot{M} = \bar{n}$ is defined as the Anomalistic Mean Motion and $\dot{\Omega}$, $\dot{\omega}$ are the first derivatives of Ω and ω. These expressions, derived in Chapter 10 of EB, are given by:

$$\dot{M} = \pi = n \left[1 + \frac{3}{2} J_2 \frac{(1-e^2)^{\frac{1}{2}}}{p^2} (1 - \frac{3}{2} \sin^2 i) \right] \tag{1.57}$$

$$\dot{\Omega} = - (\frac{3}{2} \frac{J_2}{p^2} \cos i)\, \pi \tag{1.58}$$

$$\dot{\omega} = (\frac{3}{2} \frac{J_2}{p^2} \left[2 - \frac{5}{2} \sin^2 i \right])\pi \tag{1.59}$$

which are all function of a, e, and i. It is important to note that as long as the latter 3 parameters remain nearly constant with time, it is not necessary to apply implicit numerical techniques to the solutions of equations (1.57), (1.58), and, (1.59). However, a principal effect of atmospheric drag on low orbit satellites is to modify the values of a, e, and i as a function of the eccentric anomaly. This is due to the fact that the essential effect of drag is to de-energize a satellite orbit and thus

reduce the dimension (semi-major axis) of the orbit ellipse. In addition, if the initial orbit is highly non-circular, the variation in the drag effect due to the elliptic path leads to modification of the orbit inclunation. If a low-flying satellite (small period or high eccentricity) were being considered, time dependent expressions for the semi-major axis, eccentricity, and inclination should be included. EB provides a set of expressions for drag induced derivatives of a, e, and i in Chapter 10 of his text, however, to include these expressions in an orbital solution would require a multiple step iterative approach to the calculation of the six derivative quantities. With respect to the satellite navigation problem, drag induced perturbations need not be considered for meteorological satellites until orbital altitudes start falling below 850 km.
Note that the sign of the expression for $d\Omega/dt$ (see Equation 1.57) indicates why orbits must retrograde to achieve a sun synchronous configuration (eastward precession of ascending node). Since $d\Omega/dt$ must be positive and the expression is of the form $-[\text{positive constant}] \cdot \cos i$, then the cosine of i must be negative. This requires $i > 90$.

1.2.4.3 Required Inclination for a Sun-Synchronous Orbit

Another problem which we can address, is the determination of the required inclination angle for sun synchronous orbits for a given

orbital period (P). This is simply a matter of requiring $\dot{\Omega}$ to be 360 degrees per mean solar year. Now since:

$$\frac{d\Omega}{dt} = -\left(\frac{3}{2}\frac{J_2}{p^2}\cos i\right)\pi \tag{1.60}$$

$$\pi = n\left[1 + \frac{3}{2}J_2\frac{(1-e^2)^{\frac{1}{2}}}{p^2}\left(1 - \frac{3}{2}\sin^2 i\right)\right] = 2\pi/\bar{p} \tag{1.61}$$

$$p = a(1 - e^2) \tag{1.62}$$

$$n = \frac{\mu^{\frac{1}{2}}}{a^{3/2}} K = 2\pi/p \tag{1.63}$$

We simply require that i satisfies:

$$\frac{360 \text{ degrees}}{365.24219879 \text{ days}} = -\frac{3}{2}\left(\frac{J_2}{p^2}\cos i\right) n\left[1 + \frac{3}{2}J_2\frac{(1-e^2)^{\frac{1}{2}}}{p^2}\left(1 - \frac{3}{2}\sin^2 i\right)\right] \tag{1.64}$$

or

$$0.985647336 \text{ deg}\cdot\text{day}^{-1} = -\frac{3}{2}\left(\frac{1082.28\cdot 10^{-6}}{p^2}\cos i\right) n$$

$$\left[1 + \frac{3}{2}\,1082.28\cdot 10^{-6}\frac{(1-e^2)^{\frac{1}{2}}}{p^2}\left(1 - \frac{3}{2}\sin^2 i\right)\right]$$

Note that a is assumed to be in cannonical units:

$a(\text{e.r.}) = a(\text{km})/R_e\ (\text{km})$

This equation is easily solved numerically. Since the right hand side

of equation (1.64) is monotonically increasing as i goes from 90° to 180°, we can use a Newton's method approach in the interval ($90^o \leq i \leq 180^o$) to isolate, to a specified tolerance, a solution matching the left hand side. By applying this procedure, Table 1.2.4 has been generated which gives the required satellite height and inclination for a sun synchronous orbit, given the satellite period. A circular orbit (e=0) is assumed.

Table 1.2.4 Required Orbital Inclination for a Sun Synchronous Satellite Given a Satellite Period (e=0)

Period (minutes)	Height (km)	Inclination (Deg)
90	274.36	96.5893
100	758.44	98.4366
110	1226.62	100.5585
120	1680.80	102.9718

1.2.5 Summary

This section has been directed toward the study of the orbit properties of near-earth meteorological satellites, and in particular, the application of the results to the satellite navigation problem. Beginning with some basic definitions of time and coordinate systems, the basic foundation for the solution of the two body Keplerian orbit was outined. This solution was adapted to the conventional orbital element parameters available from the meteorological satellite agencies. This is a fundamental requirement for any analytic satellite navigation model. Perturbations to orbits and their effects (some useful) were discussed.

1.3 The Direct Readout Capabilities from the Satellites; Exercises

Direct readout for the weather satellites brought satellite imagery of clouds within reach of small forecast and research units around the world. ERT (1979), describes the history of this noteworthy addition to the basic satellite system - one unique in the 1960's to the world's meteorological services. The so-called "APT" (Automatic Picture Transmission) systems need special explanation and study. They were first tested on TIROS-8 in 1963 and on NIMBUS-1 in 1964, and became a continuing service beginning with ESSA-2 in 1966.

The remaining portion of this section describes the details of the procedures to be followed in obtaining these "APT" satellite data. (The equipment requirements are discussed in Chapter 3). The sequence is:

a) receive the teletype APT PREDICT message

b) decode the message

c) track the satellite; record the data

d) display the data as a photograph

e) earth-locate (grid) the photograph.

After the descriptive sections illustrating procedures, several exercises to demonstrate the APT procedures conclude the section. Several references are then listed, including one in the scientific literature (Madden and Parsons, 1973) which describes computer generation of the grids and display of the APT data when it is digitized. For an excellent overview of not only the satellite location and tracking topics, but also "amateur" engineering and equipment, see Taggart (1981), the New Weather Satellite Handbook.

Digression:

Before proceding through the general exercises regarding the decoding of the information from the teletype and the conversion of that information into a satellite location and then satellite tracking data, let us pause for a moment to recall from the previous section what satellite orbits look like. Figure 1.3.0.1 shows three satellite orbits in a right-ascension-declination coordinate system. The near-polar orbit and the geosynchronous orbit are the ones most commonly used. If we convert these two orbits into an earth-coordinate system and plot against earth coordinates, latitude and longitude, we have the pictures of orbits shown in Figure 1.3.0.2 and 1.3.0.3. The near polar orbiter (like a sun-synchronous orbit) has an oscillatory motion which moves as the earth moves or rotates. The geosynchronous orbit shows almost no motion with a slow eliptical path resulting from a non-perfect orbit (e.g., inclination not exactly equal to zero degrees and orbit not a perfect circle). These pictures of "what satellite orbits look like" are good to visualize as we move through the remainder of this section and learn how to locate satellites in both kinds of orbits.

1.3.1 General Information on APT PREDICT Messages (TBUS 1 and TBUS 2)

APT information listed on the world weather teletype circuit under the TBUS 1 heading is for satellites which are NIGHT-ASCENDING (northbound at night). NOAA-6 is an example of such an orbit. Information under the TBUS 2 heading is for DAY-ASCENDING satellites; for example, TIROS-N is northbound on the sunlit side of its orbit.

A new orbit number is assigned when the satellite crosses the equator northbound. The reference orbit is the orbit to which the satellite sub-point information applies for the times after the equator crossing. The equator crossing times and longitudes are for northbound equator crossings only.

For TBUS 1, NIGHT PART II is the northern hemisphere, northbound leg of the reference orbit following the equator crossing, PART III is the southern hemisphere, northbound leg of the previous numbered orbit that connects to it, where the time is in minutes before the northbound equator crossing. Both are for while the satellite is over the darkened portion of the earth. For TBUS 1, DAY PART II is the northern hemisphere, southbound leg of the reference orbit and DAY PART III is the southern hemisphere, southbound leg of the reference orbit while the satellite is over the sunlit side of the earth.

In TBUS 2 messages, DAY PART II is the northern hemisphere, northbound leg of the orbit following the northbound equator crossing and on the sunlit portion of the earth. DAY PART III is the northbound, southern hemisphere portion of the previous numbered orbit before the given equator crossing time and connects to DAY PART II at the equator crossing. NIGHT PART II is the southbound, northern hemisphere part of the reference orbit and NIGHT PART III is the southbound, southern hemisphere part where both are for the darkened portion of the earth.

1.3.2 Addition of Orbital Elements to APT Predict (TBUS) Messages (Part IV)

Orbital elements for polar orbiting satellites have been added to Part IV of the APT Predict (TBUS) message transmitted by teletype and via ATS WEFAX. These elements appear in each daily message, and are updated periodically. The format of both the teletype and WEFAX messages are identical. (See end of chapter).

Example -- For NOAA-6 Parts II and III

TBUS 1 NIGHT-ASCENDING NOAA-6

		Time GMT	Latitude	Longitude
	Eq. Crossing	20:43:03	0°N(S)	17.81°W
PART II	+02 min	20:47:03	7.0°N	19.4
NIGHT	+04	20:47:03	14.1	21.0
N. Hemisphere;	+06	20:49:03	21.2	22.7
Northbound	+08	20:51:03	28.2	24.5
	+10	20:53:03	35.3	26.5
	+12	20:55:03	42.3	28.8
	+14	20:57:03	49.3	31.5
	+16	20:59:03	56.1	35.0
	+18	21:01:03	62.9	39.7
	+20	21:03:03	69.5	47.0
	+22	21:05:03	75.6	59.9
PART III	-02 min	20:41:03	7.0°S	16.2°W
NIGHT	-04	20:30:03	14.1	14.6
S. Hemisphere;	-06	20:37:03	21.2	12.9
Northbound	-08	20:35:03	28.2	11.0
	-10	20:33:03	35.2	9.1
	-12	20:31:03	42.2	6.8
	-14	20:29:03	49.1	4.1
	-16	20:27:03	56.0	0.6
	-18	20:25:03	62.7	3.9°E
	-20	20:23:03	69.3	11.0
	-22	20:21:03	75.3	23.6
	-24	20:19:03	80.1	49.4
	-26	20:17:03	81.0	93.5
	-28	20:15:03	77.2	126.5
	-30	20:13:03	71.5	142.4
	-32	20:11:03	65.0	150.9

		Time GMT	Latitude	Longitude
PART II	+24 min	21:07:03	80.2°N	86.9°W
DAY	+26	21:09:03	80.8	131.6
N. Hemisphere;	+28	21:11:03	76.9	163.5
Southbound	+30	21:13:03	71.0	178.8
	+32	21:15:03	64.5	172.9°E
	+34	21:17:03	57.8	167.7
	+36	21:19:03	50.9	164.0
	+38	21:21:03	44.0	161.2
	+40	21:23:03	37.0	158.8
	+42	21:25:03	30.0	156.7
	+44	21:27:03	23.0	154.9
	+46	21:29:03	16.0	153.2
	+48	21:31:03	8.9	151.5
	+50	21:33:03	1.9	149.9
PART III	52	21:35:03	5.1°S	148.4°E
DAY	54	21:37:03	12.1	146.7
S. Hemisphere;	56	21:39:03	19.2	145.1
Southbound	58	21:41:03	26.2	143.3
	60	21:43:03	33.2	141.4
	62	21:45:03	40.1	139.2
	64	21:47:03	47.1	136.7
	66	21:49:03	53.9	133.5
	68	21:51:03	60.7	129.3
	70	21:53:03	67.3	123.1
	72	21:55:03	73.6	112.8

With the aid of a satellite-tracking chart (Figure 1.3.2.1) or small computer program for a small computer (Taggart, 1981) you convert the satellite location information to antenna tracking information appropriate to a particular station. The following general example is for illustration. Always refer to the specific users' guide for an example related to the actual satellite of interest to you.

Example -- Satellite Tracking

TBUS 1 APT PREDICT 27 Sept 1975 NOAA-6

PART I Reference orbit = 1311
Equator crossing time = 20:57:41 (GMT), 14:57:41 (local)
Equator crossing longitude = 21.44°W, Octant = 0
Period = 101 min, 18 sec
Orbital increment = 25.32°

Find the next orbit that gives the best picture coverage (closest orbital track) to Fort Collins.

Fort Collins latitude = 40.58°N, longitude = 105.8°W

Step 1: Find the range of equator crossing longitudes which give an antenna elevation of at least 20°.

Step 2: Determine from the orbital increment which orbits fall into the range found in Step 1.

Step 3: Determine the times of the equator crossings for the orbits found in Step 2.

You should now have the necessary information (equator crossing, longitude and time) to be able to graphically determine the antenna positions and satellite subpoints minute-by-minute.

Range: S - N 77.5°W to 111.0°W
N - S 59.7°E to 93.0°E

Orbits: only #1314 falls within 20° elevation range
for S - N orbits 97.4°W eq. crossing.

Time	Orbit 1315	=	03:42:55 GMT
			- 1:41:18
	Orbit 1314	=	02:01:37 GMT eq. crossing

1st Horizon 3 min 45 sec after eq. crossing

02:05:22 GMT

The final step after reception of the satellite data at your tracking station is its display (Chapter 4) and gridding (earth location). Because each direct readout satellite system today has special data sample averaging procedures refer to the appropriate users' guide. Some engineering information about the APT and HRPT (High Resolution Picture Transmission) is included in Chapter 3 and in Taggart (1981).

References and Suggested Additional Reading:

Abramowitz, M. and I. A. Stegun, 1972: Handbook of Mathematical Functions, Dover Publications, Inc., New York, 1046 pp.

Allison, L. J., R. Wexler, C. R. Laughlin and W. R. Bandeen, 1977: Remote sensing of the atmosphere from environmental satellites, GSFC Preprint X-901-77-132, 111 pp.

American Ephermis and Nautical Almanac, 1978: Issued by the Nautical Almanac Office, U. S. Naval Observatory and Her Majesty's Nautical Almanac Office, Royal Greenwich Observatory, U. S. Government Printing Office, Washington, DC, 573 pp.

Barnes, J. C. and M. D. Smallwood, 1982: TIROS-N Series Direct Readout Services Users' Guide, NOAA-S/T 82-86, NOAA/NESS, Washington, DC, 132 pp.

Bowditch, N., 1962: American Practical Navigator - An Epitomie of Navigation. U. S. Navy Hydrographic Office, H.O. Pub. No. 9, U. S. Government Printing Office, 1524 pp.

Brouwer, D. and G. M. Clemence, 1961: Methods of Celestial Mechanics. Academic Press, New York, 598 pp.

Campbell, G. G. and T. H. Vonder Haar, 1978: Optimum satellite orbits for accurate measurement of the earth's radiation budget, summary. Atmospheric Science Paper No. 289, Department of Atmospheric Science, Colorado State University, Fort Collins, CO, 61 pp.

Cappellari, J. O., C. E. Velez and A. J. Fuchs, 1976: Mathematical theory of the Goddard trajectory determination system. Technical Report X-582-76-77, Goddard Space Flight Center, Greenbelt, MD, 599 pp.

Dubyago, A. D., 1961: The Determination of Orbits (translated from Russian), The MacMillan Co., New York, 434 pp.

ERT, 1979: TIROS-N series direct readout services users' guide, Doc. No P-7378, 696 Virginia Rd, Concord, MA, 60 pp.

Escobal, P. R., 1965: Methods of Orbit Determination. John Wiley and Sons,Inc., New York/London/Sydney, 463 pp.

Escobal, P. R., 1968: Methods of Astrodynamics. John Wiley and Sons, Inc., New/London/Sydney, 342 pp.

Hubert, L. F. and P. E. Lehr, 1967: Weather Satellites, Blaisdell Publishing Co., Waltham, MA, 120 pp.

Johnson, F. S., 1961: Satellite Environment Handbook, Stanford University Press, Stanford, CA, 155 pp.

Kozai, Y., 1959: The motion of a close earth satelite. The Astronomical Journal, 64, 9.

McGraw-Hill, 1974: Dictionary of Scientific and Technical Terms. McGraw-Hill Book Co., New York/St. Louis/San Francisco, 1634 pp.

Madden, R. and C. Parsons, 1973: A technique for real-time, quantitative display of APT scanning radiometer data, J. Appl. Meteor., 12, 381-385.

Makemson, M. W., R. L. M. Baker and G. B. Westrom, 1961: Analysis and standardization of the astrodynamic constants. J. Astronautical Sciences, 8, 1-13.

NASA, 1980: Meteorological satllites, Technical Memorandum 80704, L. J. Allison (Ed.), 71 pp.

NASA, 1982a: Meteorological Satellites - Past, Present and Future. Conference Publication 2227, 63 pp.

NASA, 1982b: The conception, growth, accomplishments and future of meteorological satellites, Conference Publication 2257, 101 pp.

Phillips, D. R., 1979: Incorporation of star measurements for the determination of orbit and attitude parameters of a geosynchronous satelite. Presented at the 4th Annual Flight Mechanics/Estimation Theory Symposium, 15-18 Oct, NASA Goddard Space Flight Center, Greenbelt, MD.

Smith, E. A. and D. R. Phillips, 1972: Automated cloud tracking using precisely aligned digital ATS pictures. IEEE Trans. on Comp., C-21, 715-729.

Smith, E. A., 1980: Orbital mechanics and analytic modeling of meteorological satellite orbits, CSU Atmosheric Science Paper No. 321, Fort Collins, CO, 161 pp.

Spiegel, M. R., 1968: Mathematical Handbook of Formulas and Tables. McGraw-Hill Book Co., New York/St. Louis/San Francisco/Toronto/Sydney, 271 pp.

Sterne, T. E., 1960: An Introduction to Celestial Mechanics. Interscience Publishers, New York, 206 pp.

Taggart, R. E., 1981: The New Weather Satellite Handbook, Wayne Green Inc., Peterborough, NH, 132 pp.

Widger, W. K., 1966: Orbits, altitudes, viewing geometry, coverage and resolution pertinent to satelite observations of the earth and its atmosphere. Technical Report for Contract No. N-61339-66-C-0031, U. S. Naval Training Device Center, Port Washington, NY, 489-537.

WMO-No. 585, 1982: Satellites in meteorology, oceanography, and hydrology. 56 pp.

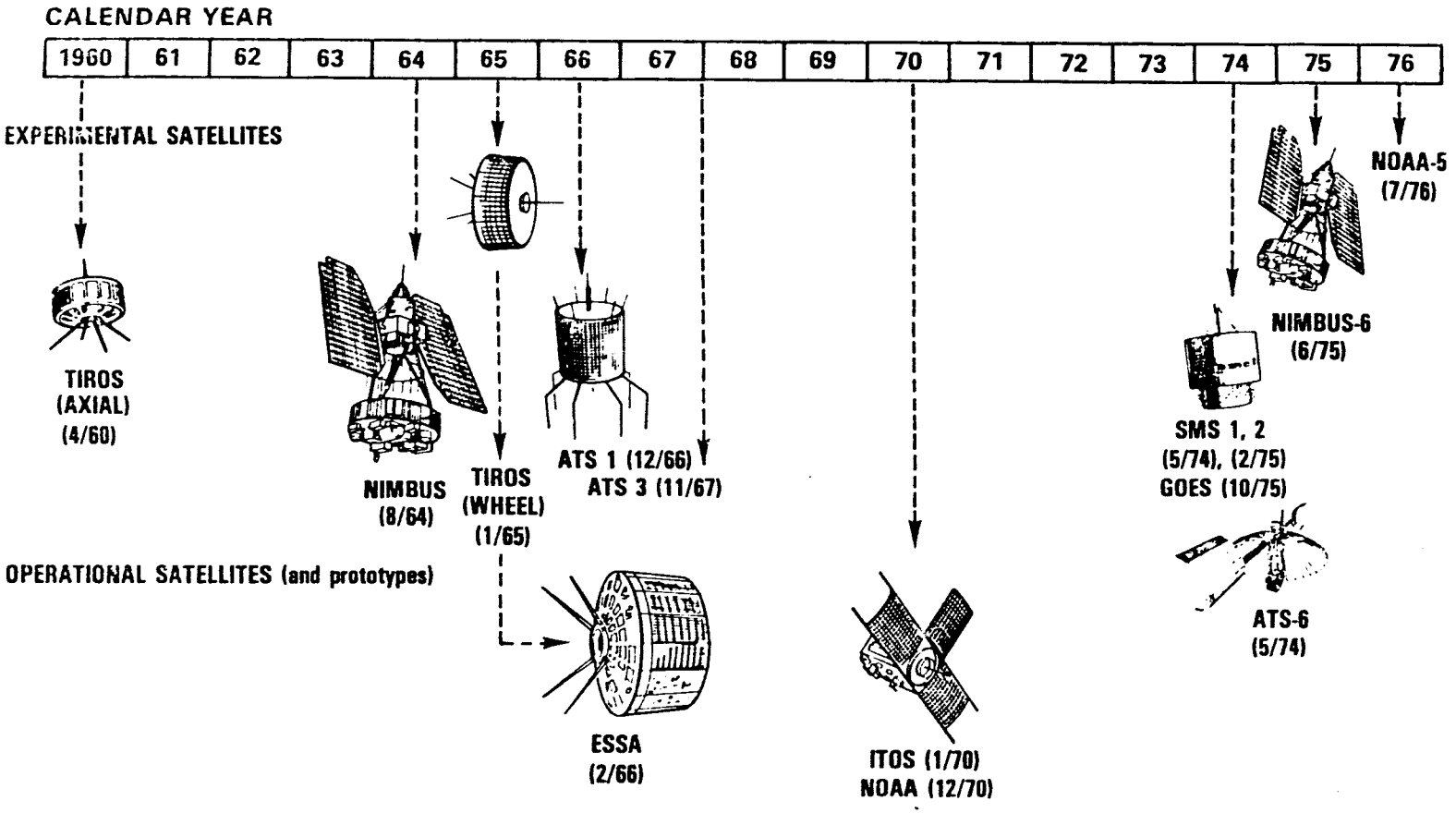

Figure 1.1.1 U.S. Meteorological Satellite Program from 1960 to 1967 (Allison, 1977)

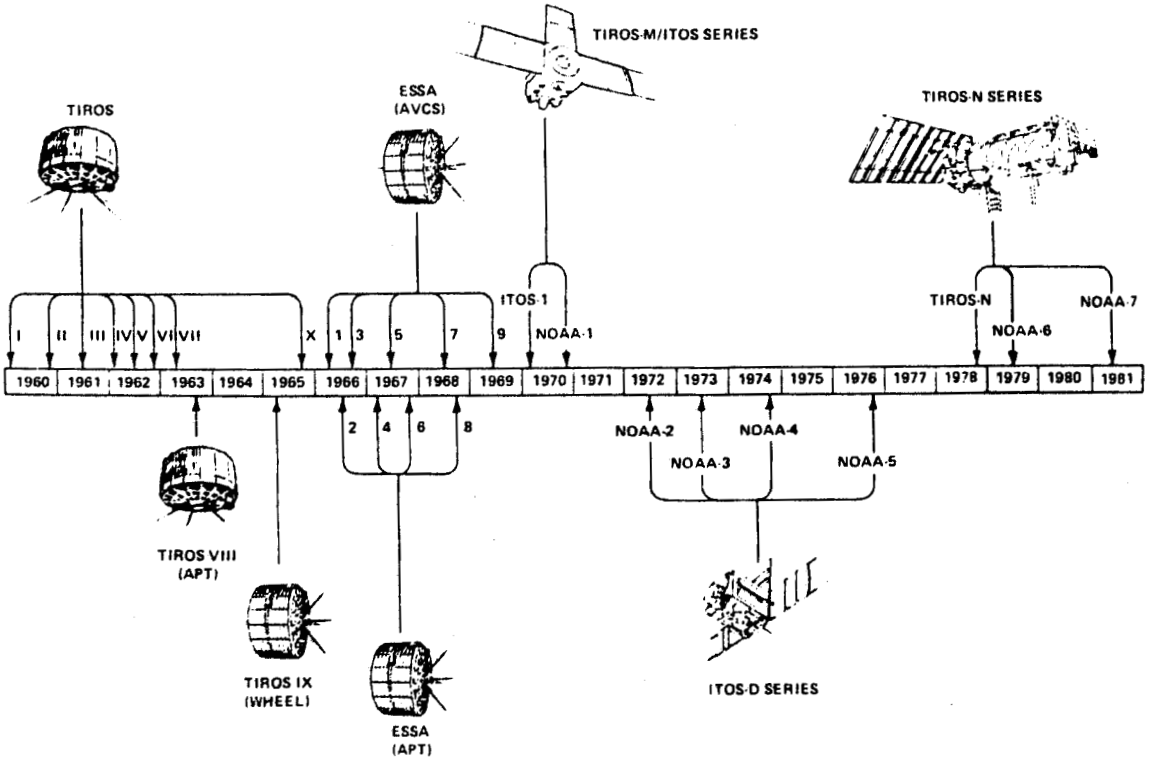

TIROS Polar-Orbiting Global Operational Meteorological Satellite System Evolution

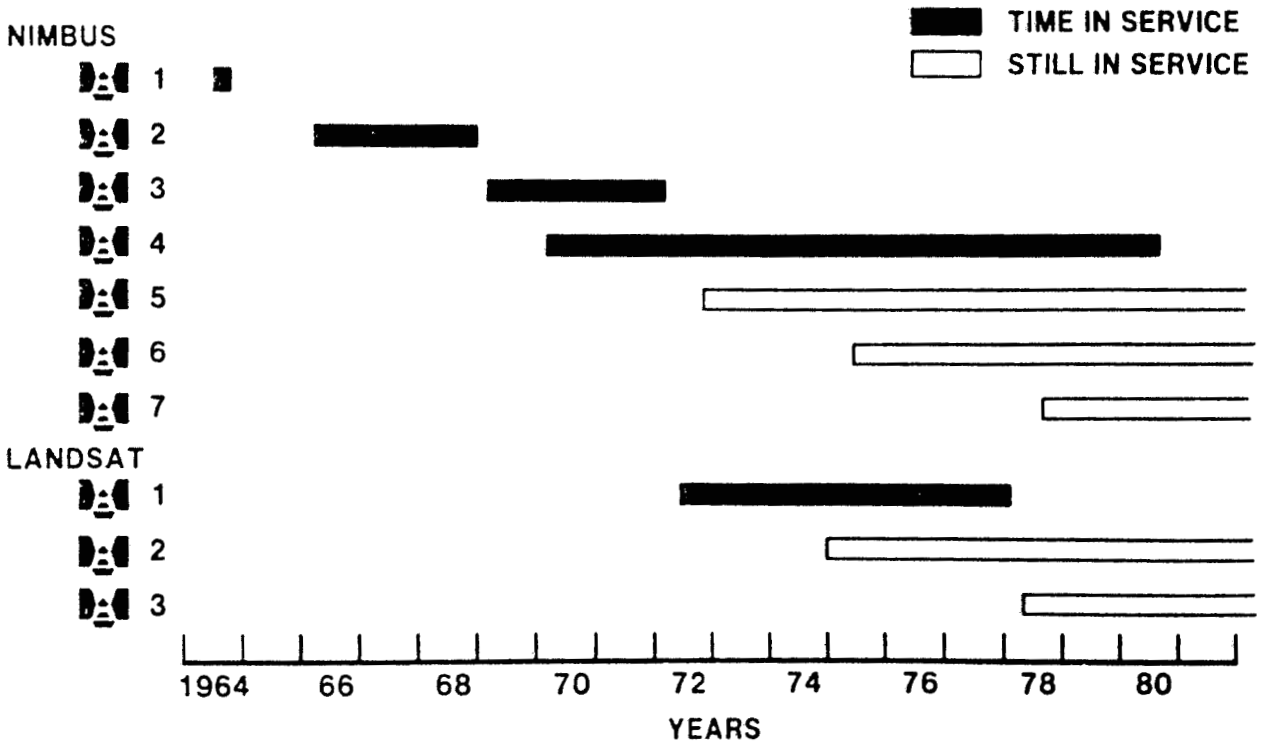

Decades of Experimental Performance, Nimbus/Landsat

Figure 1.1.2 U.S. Polar-Orbiting Meteorological Satellite Program (NASA, 1982a)

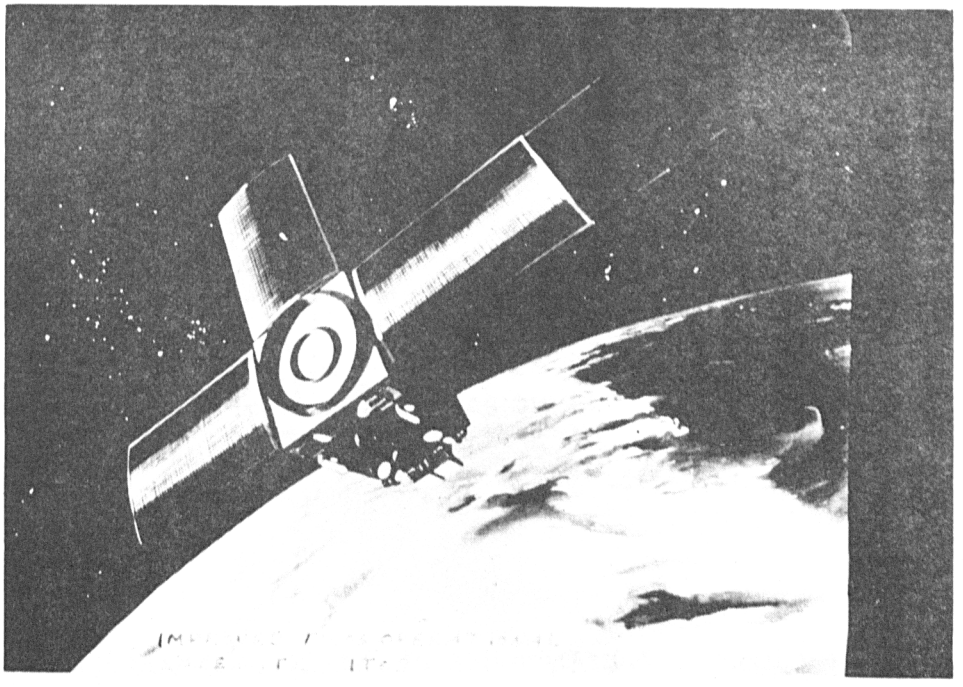

Figure 1.1.3 Improved TIROS Operational Satellite (ITOS) (Slide Set #27)

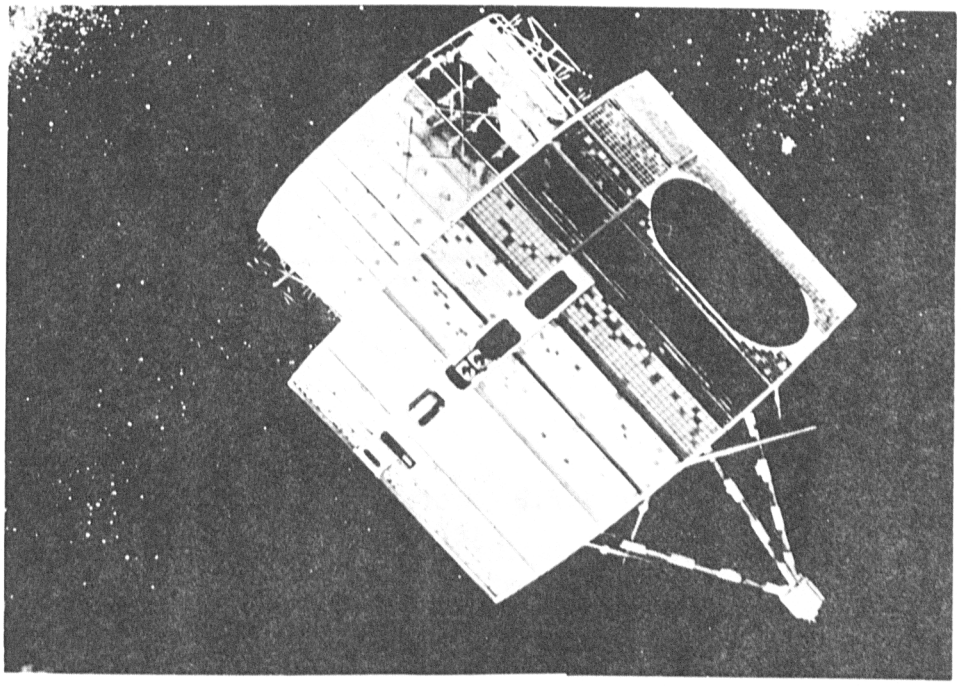

Figure 1.1.4 Geostationary Operational Enviornmental Satellite (GOES) (Slide Set #25)

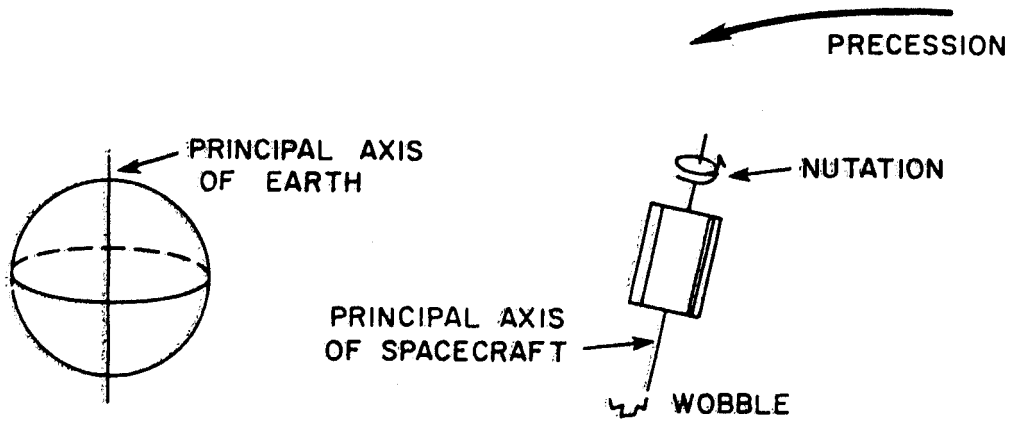

Figure 1.2.1 Dynamics of Satellite Orientation

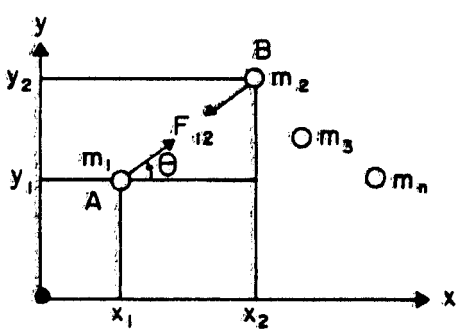

Figure 1.2.2 Arbitrary inertial coordinate reference frame

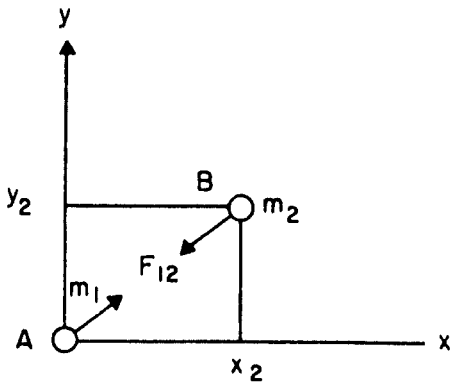

Figure 1.2.3 Relative inertial coordinate reference frame.

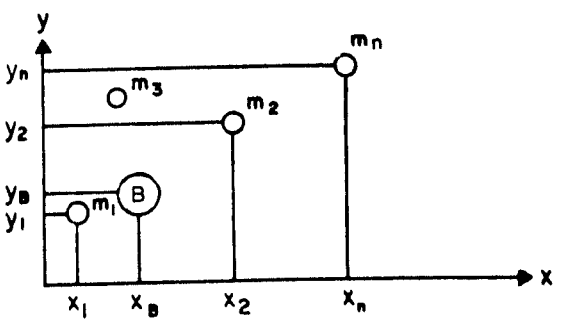

Figure 1.2.4 Barycentric coordinate reference frame.
(Based on a figure from EB, 1965)

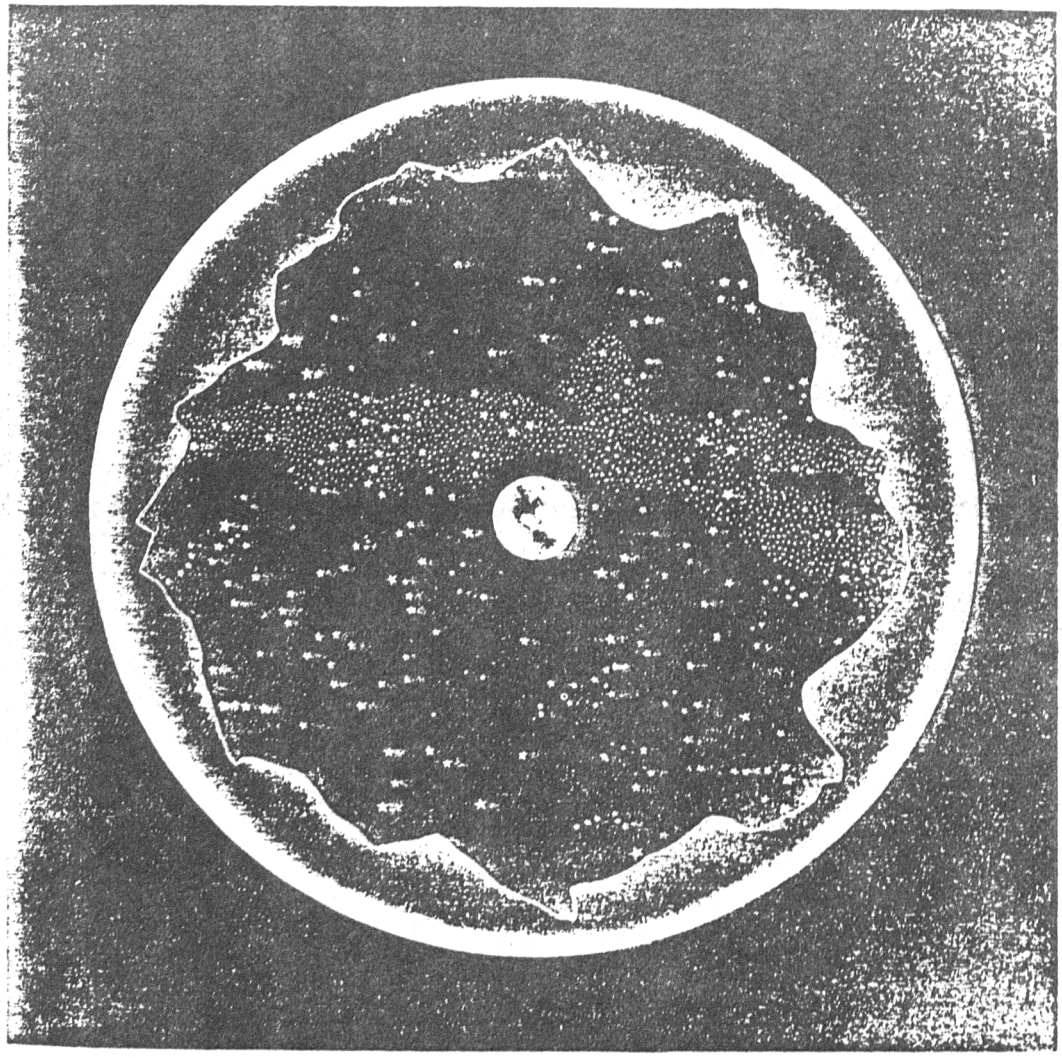

Figure 1.2.5 The celestial sphere (From Bowditch, 1962)

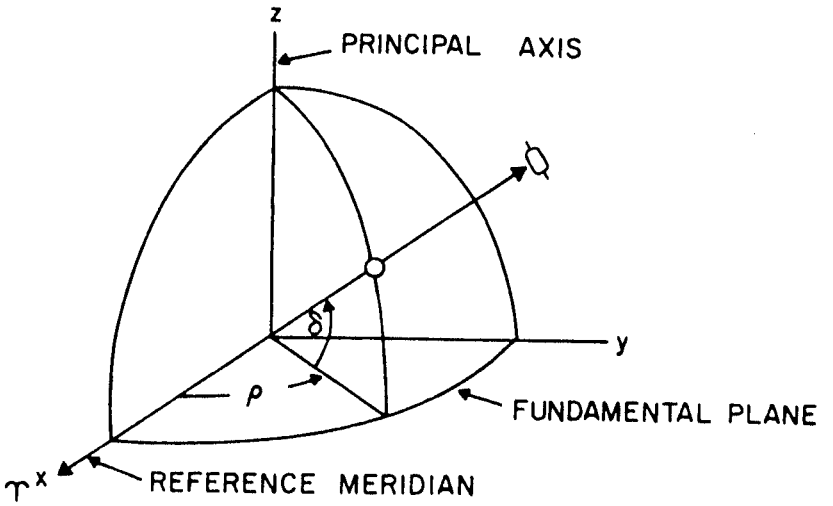

Figure 1.2.6 The right ascension - declination inertial coordinate system.

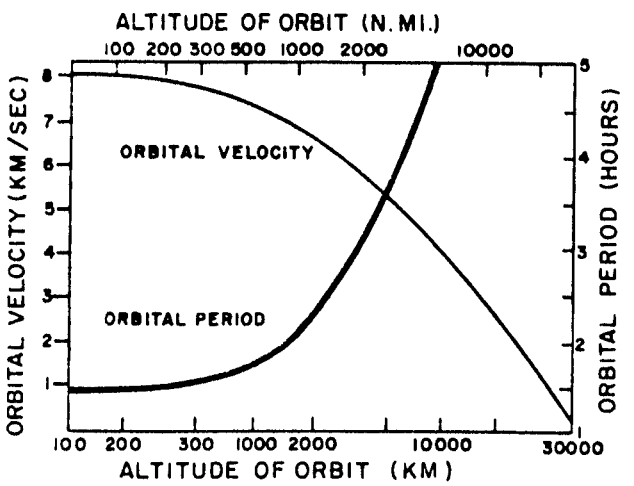

Figure 1.2.7 Velocity and period of a satellite in circular orbit as a function of altitude (From Widger, 1966)

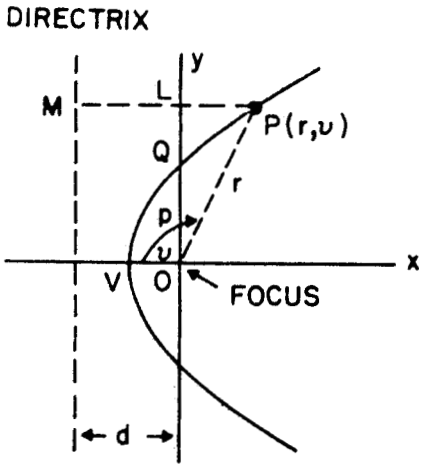

If a point P moves so that its distance from a fixed point (called the focus) divided by its distance from a fixed line (called the directrix) is a constant e (called the eccentricity), then the curve described by P is called a conic (so-called because such curves can be obtained by intersecting a plane and a cone at different angles). If the focus is chosen at origin O the equation of a conic in polar coordinates (r,ν) is, if OQ = p and LM = d:

$$r = \frac{p}{1 + e\cos\nu} = \frac{ed}{1 + e\cos\nu}$$

Figure 1.2.8 Conic sections (Based on a figure from Spiegel, 1968).

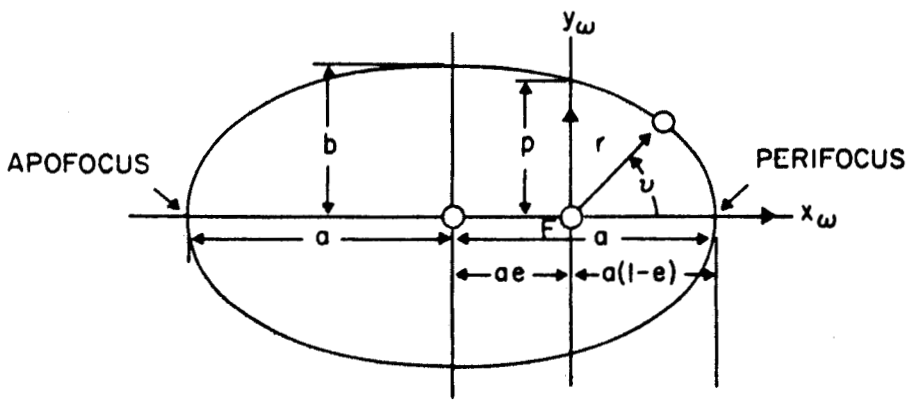

Figure 1.2.9 Elliptic frame of reference
(Based on a figure from EB, 1965)

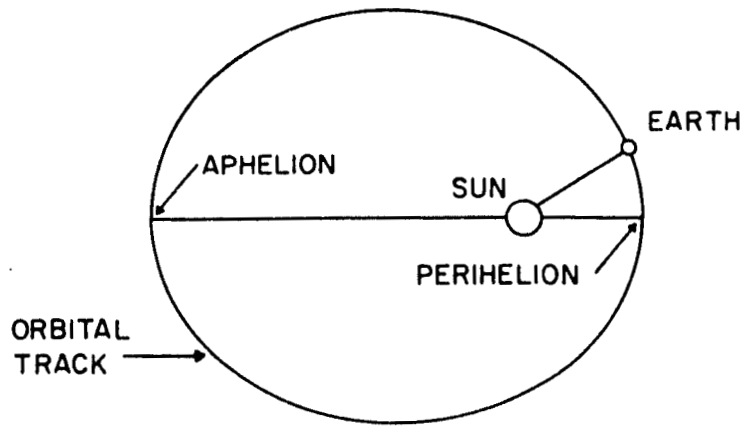

Figure 1.2.10 Perihelion and aphelion of earth in solar orbit (Not exact scale)

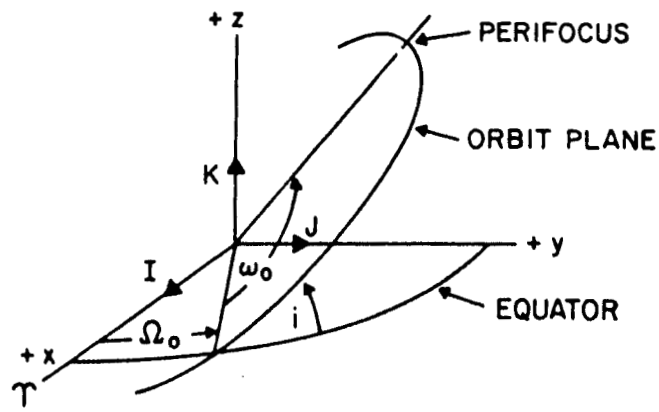

Figure 1.2.11 The Classical Orientation Angles and the Orthogonal I, J, K Coordinate System (Based on a figure from EB, 1965)

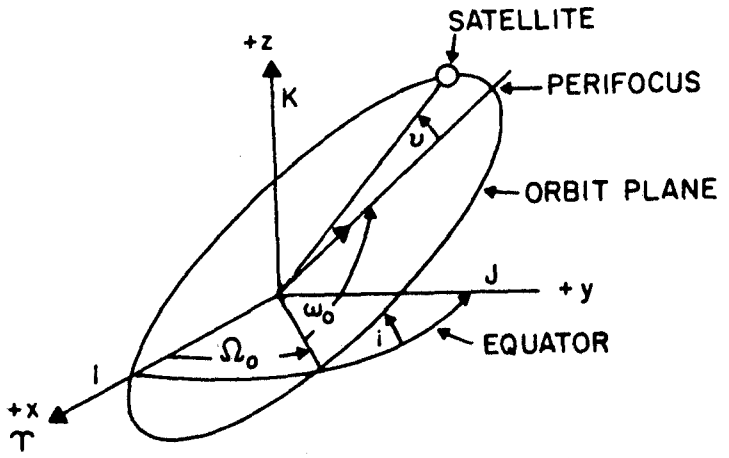

Figure 1.2.12 Adding the satellite to Figure 1.2.11
(Based on a figure from EB, 1965)

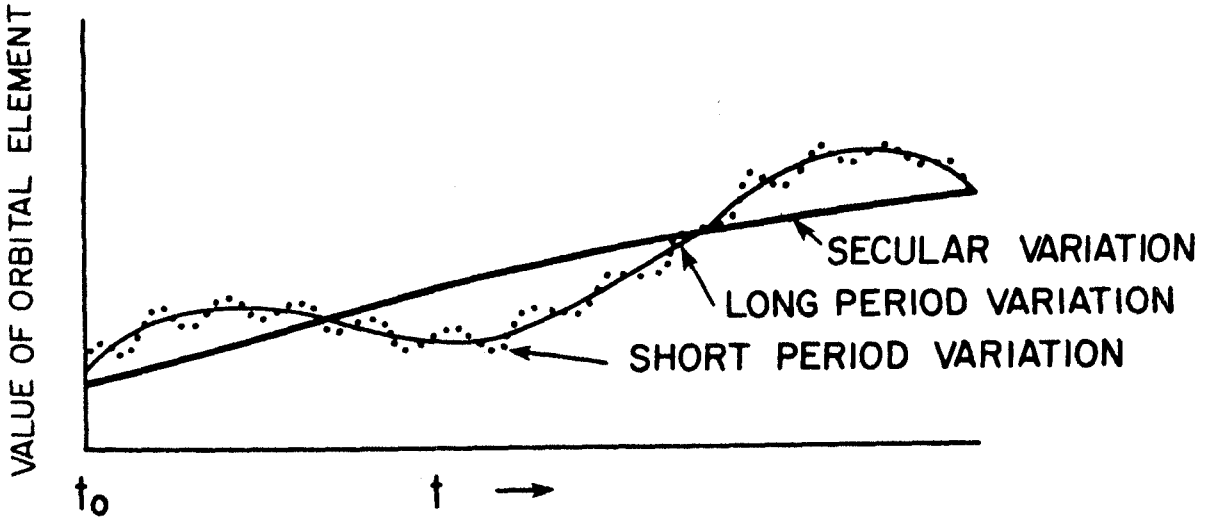

Figure 1.2.13 Three principle types of orbital perturbations

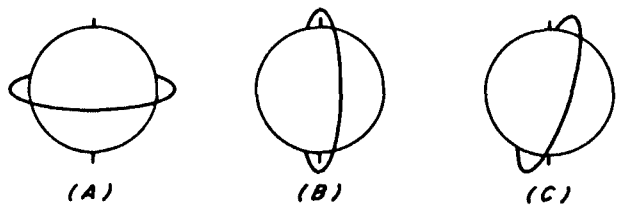

Figure 1.3.0.1 Three Satellite Orbits (Taggart, 1981)

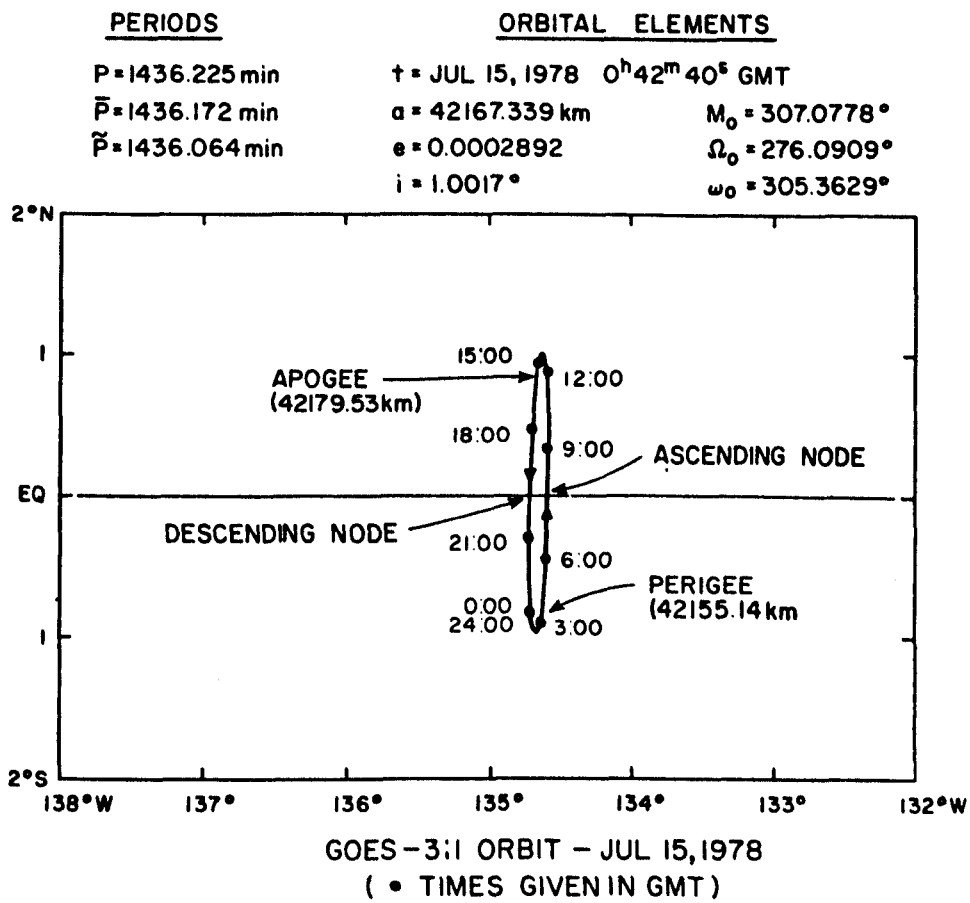

Figure 1.3.0.2 Geosynchronous Orbit in Earth Coordinates (Smith, 1980)

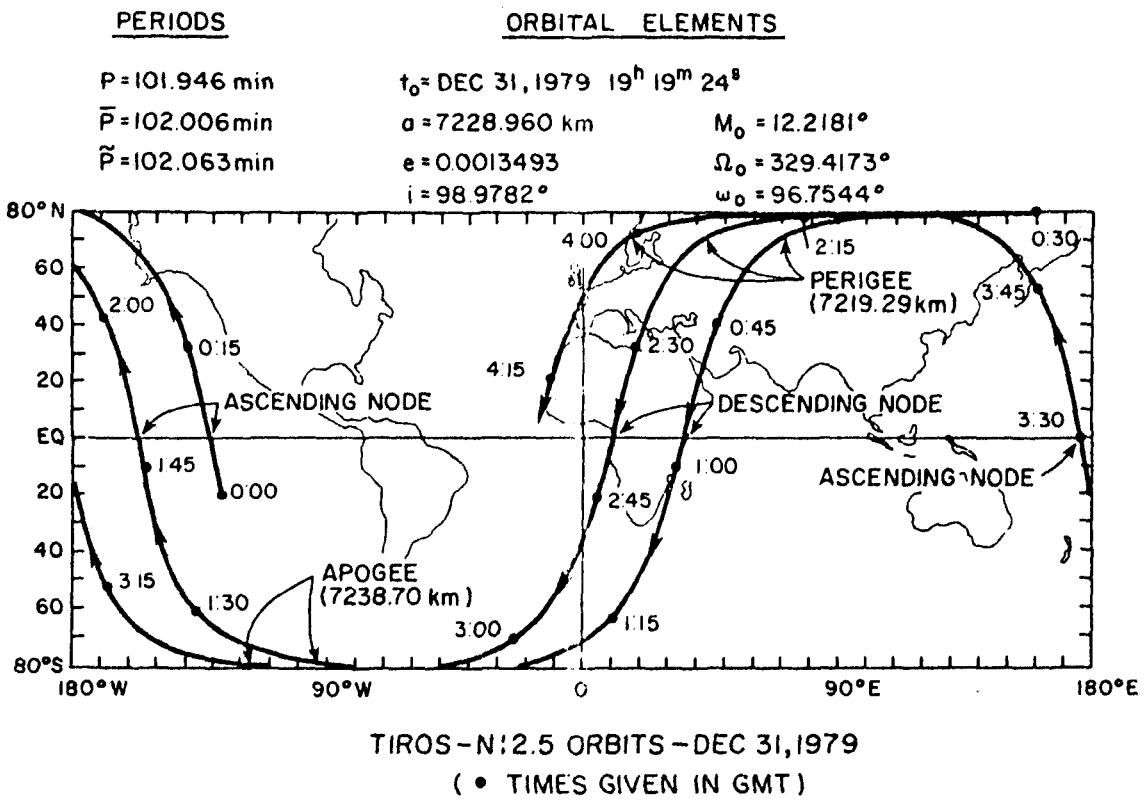

Figure 1.3.0.3 Polar Orbit in Earth Coordinates (Smith, 1980)

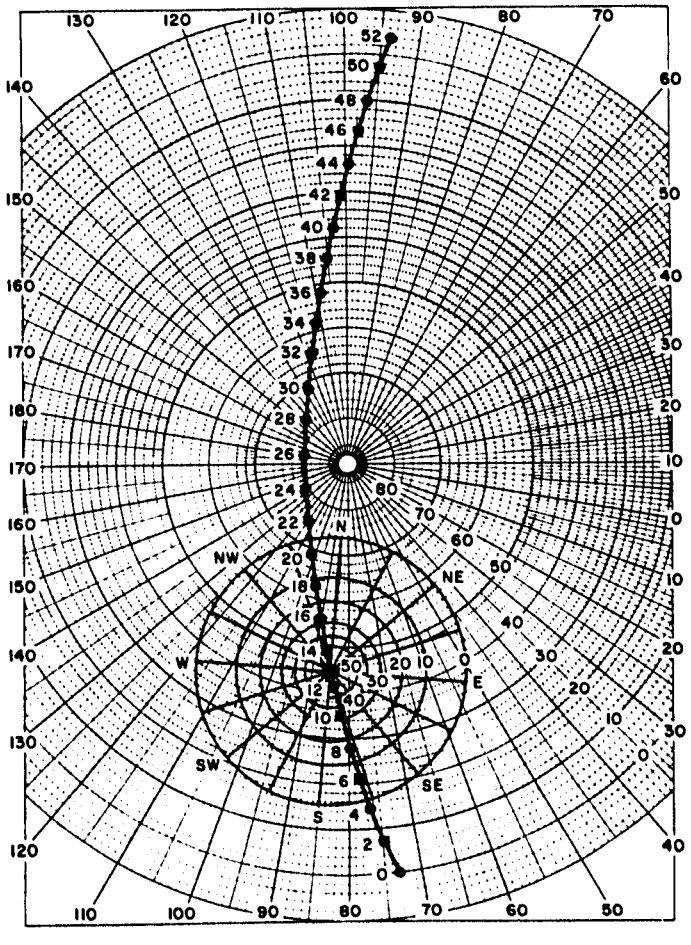

Figure 1.3.3.1 Polar-Orbiting Satellite Tracking Chart (Taggart, 1981)

Table 1.1.1 Early List of Artificial Earth Satellites (Johnson, 1981)

EARTH SATELLITES AND SPACE PROBES—APRIL 24, 1961

Designation	Name	Weight (kg)	Launch Date	Initial Altitude Perigee (km)	Initial Altitude Apogee (km)	Decay Date	Major Purpose
1957 Alpha 1	——	3500	10-4-57	280	950	12-1-57	Sputnik I launcher
1957 Alpha 2	Sputnik I	84	10-4-57	230	950	1-4-58	Earth orbit
1957 Beta	Sputnik II	3600	11-3-57	230	1670	4-14-58	Radiation measurement (contained dog, no recovery attempted)
1958 Alpha	Explorer I	14	1-31-58	370	2540	~1966	Cosmic-ray measurement (discovered Van Allen belt)
1958 Beta 1	——	23	3-17-58	660	3950	~2500	Vanguard I launcher
1958 Beta 2	Vanguard I	1.47	3-17-58	660	3950	~3000	Geodesy, atmospheric density
1958 Gamma	Explorer III	14	3-26-58	190	2810	6-28-58	Radiation-belt measurement
1958 Delta 1	——	...	3-17-58	660	3950	~2500	Sputnik III launcher
1958 Delta 2	Sputnik III	1327	5-15-58	240	1880	4-6-60	General geophysical measurement
1958 Epsilon	Explorer IV	17.4	7-26-58	260	2200	10-23-59	Radiation-belt measurement
——	Pioneer I	38.3	10-11-58	...	180,000	10-12-58	Space probe (did not escape from Earth)
——	Pioneer III	5.87	12-6-58	...	160,000	12-7-58	Radiation measurement (did not escape from Earth)
1958 Zeta	Score	3969	12-18-58	180	1480	1-21-59	Radio-relay tests (Eisenhower's voice message)
——	Lunik I (Mechta)	1472	1-2-59	(0.98)[a]	(1.29)[b]	...	Lunar and space probe
1959 Alpha 1	Vanguard II	9.41	2-17-59	560	3320	~2150	Cloud-cover measurement
1959 Alpha 2	——	23	2-17-59	560	3320	~2100	Vanguard II launcher
1959 Beta	Discoverer I	590	2-28-59	160	970	3-5-59	System checkout
——	Pioneer IV	6.08	3-3-59	(0.99)[a]	(1.15)[b]	...	Space probe
1959 Gamma	Discoverer II	730	4-13-59	230	350	4-26-59	Attempted capsule recovery
1959 Delta	Explorer VI	64.4	8-7-59	250	42,400	Uncertain	General geophysical measurement
1959 Epsilon 1	Discoverer V	771	8-13-59	220	720	9-28-59	Attempted capsule recovery
1959 Epsilon 2	——	88	8-13-59	220	720	Uncertain	Discoverer V capsule
1959 Zeta	Discoverer VI	771	8-19-59	220	860	10-20-59	Attempted capsule recovery
——	Lunik II	389.4	9-12-59	...	...	9-13-59	Lunar probe (impact)
1959 Eta	Vanguard III	45	9-18-59	510	3750	~2060	Magnetometer
1959 Theta	Lunik III	278.5	10-3-59	40,000	470,000	4-20-60	Lunar probe (far-side photograph)
1959 Iota 1	Explorer VII	41.5	10-13-59	550	1130	~2000	General geophysical measurement
1959 Iota 2	——	26.8	10-13-59	550	1130	~1990	Explorer VII launcher
1959 Kappa	Discoverer VII	771	11-7-59	160	840	11-26-59	Attempted capsule recovery
1959 Lambda	Discoverer VIII	771	11-20-59	210	1670	3-8-60	Attempted capsule recovery
1960 Alpha	Pioneer V	42.9	3-11-60	(0.81)[a]	(0.99)[b]	...	Space probe (magnetic and radiation measurements)
1960 Beta 1	——	23	4-1-60	700	750	~2050	Tiros I launcher
1960 Beta 2	Tiros I	122	4-1-60	700	750	~2050	Cloud-cover measurement (photographs)
1960 Gamma 1	——	570	4-13-60	370	800	1962	Transit 1B launcher
1960 Gamma 2	Transit 1B	120	4-13-60	370	800	~1966	Navigation system
1960 Delta	Discoverer XI	771	4-15-60	130	340	4-26-60	Attempted capsule recovery
1960 Epsilon 1	Sputnik IV	2500	5-15-60	300	370	1963	Attempted capsule recovery
1960 Epsilon 2	——	2100	5-15-60	300	370	7-17-60	Sputnik IV launcher
1960 Zeta 1	Midas II	2270	5-24-60	480	520	~1972	Rocket-launch detector
1960 Eta 1	Transit IIA	101.1	6-22-60	620	1060	~2050	Navigation system
1960 Eta 2	Greb	19	6-22-60	620	1060	~2050	Solar radiation (piggy-back satellite)
1960 Eta 3	——	...	6-22-60	620	1060	~2050	Launcher
1960 Theta	Discoverer XIII	771	8-10-60	260	700	11-14-60	Capsule recovery
1960 Iota 1	Echo I	68	8-12-60	1400	1800	~1965	Global-communication test
1960 Iota 2	——	...	8-12-60	1400	1800	~6000	Echo I launcher
1960 Kappa	Discoverer XIV	771	8-18-60	190	810	9-16-60	Capsule recovery (capsule recovered in air)
1960 Lambda 1	Sputnik V	4590	8-19-60	300	340	8-20-60	Capsule recovery (contained dogs)
1960 Lambda 2	——	...	8-19-60	300	340	9-23-60	Sputnik V launcher
1960 Mu	Discoverer XV	771	9-13-60	200	610	10-18-60	Capsule recovery
1960 Nu 1	Courier IB	227	10-4-60	970	1240	~2250	Communication system
1960 Nu 2	——	...	10-4-60	970	1240	2250	Courier IB launcher
1960 Xi 1	Explorer VIII	40.89	11-3-60	490	2290	~2000	Radio-wave measurement
1960 Xi 2	——	26.8	11-3-60	490	2290	2000	Explorer VIII launcher
1960 Omicron	Discoverer XVII	771	11-12-60	180	990	12-29-60	Capsule recovery (capsule recovered in air)
1960 Pi 1	Tiros II	127	11-23-60	640	710	~2250	Cloud-cover measurement
1960 Pi 2	——	...	11-23-60	640	710	2250	Tiros II launcher
1960 Rho 1	Sputnik VI	4563	12-1-60	180	250	12-2-60	Capsule recovery
1960 Rho 2	——	...	12-1-60	180	250	12-2-60	Sputnik VI launcher
1960 Sigma	Discoverer XVIII	771	12-7-60	280	740	4-2-61	Capsule recovery (capsule recovered in air)
1960 Tau	Discoverer XIX	771	12-20-60	210	650	1-23-61	Infrared-radiation measurement
1961 Alpha 1	Samos II	1860	1-31-61	480	560	...	System check-out
1961 Beta 1	Sputnik VII	7214	2-4-61	220	380	2-26-61	General geophysical measurement
1961 Gamma 1	(Venus probe)	642	2-12-61	(0.72)[a]	(1.02)[b]	...	Space probe
1961 Gamma 3	Sputnik VIII	7214	2-12-61	240	480	2-25-61	Launch base for Gamma 1
1961 Delta 1	Explorer IX	6.6	2-16-61	640	2580	...	Drag measurement (Scout booster)
1961 Epsilon	Discoverer XX	1111	2-17-61	320	640	...	Capsule recovery
1961 Zeta	Discoverer XXI	1111	2-18-61	260	1080	...	Engine-restart test
1961 Eta 1	Transit IIIB	113	2-22-61	190	990	3-30-61	Navigation system
1960 Eta 2	Lofti	24.5	2-22-61	190	990	3-30-61	Radio-wave measurement (piggy-back satellite; did not separate from Transit IIIB)
1961 Theta 1	Sputnik IX	4700.9	3-9-61	240	250	3-9-61	Capsule recovery (dog recovered)
1961 Iota 1	Sputnik X	4695	3-25-61	179	248	3-25-61	Capsule recovery (dog recovered)
1961 Kappa	Explorer X	35.4	3-25-61	177	181,000	...	Magnetic-field and solar-wind measurement
1961 Lambda 1	DiscovererXXIII	1111	4-8-61	299	647	...	Capsule recovery
1961 Mu 1	Vostok	4715	4-12-61	175	302	4-12-61	First man in space (man recovered)
1961 Mu 2	...	...	4-12-61	175	302	4-16-61	Vostok launcher

[a] Perihelion in astronomical units (1.49×10^8 km).
[b] Aphelion in astronomical units.

Table 1.1.2 U.S. Meteorological Satellites (NASA, 1982a)

THE TIROS/ESSA/ITOS/NOAA SATELLITES IN ORBIT

Name	Launched	Weight (lbs)	Period (min)	Perigee (km)	Apogee (km)	Inclination (deg)	Life (days)	Remarks
TIROS I	01APR60	263	99.2	796	867	48.3	89	1 TV-WA and 1 TV-NA
TIROS II	23NOV60	278	98.3	717	837	48.5	376	1 TV-WA, 1 TV-NA, passive & active IR scan
TIROS III	12JUL61	285	100.4	854	937	47.8	230	2 TV-WA, HB, IR, IRP
TIROS IV	08FEB62	285	100.4	817	972	48.3	161	2 TV-WA, IR, IRP, HB
TIROS V	19JUN62	287	100.5	680	1119	59.1	321	1 TV-WA, 1 TV-MA
TIROS VI	18SEP62	281	98.7	783	822	58.2	389	1 TV-WA, 1 TV-MA
TIROS VII	19JUN63	299	97.4	713	743	58.2	1809	2 TV-WA, IR, IP, HB
TIROS VIII	21DEC63	260	99.3	796	878	58.5	1287	1st APT TV direct readout & 1 TV-WA
TIROS IX	22JAN65	320	119.2	806	2967	96.4	1238	First "wheel"; 2 TV-WA global coverage
TIROS X	02JUL65	320	100.6	848	957	98.6	730	Sun synchronous, 2 TV-WA
ESSA 1	03FEB66	320	100.2	800	965	97.9	861	1st operational system, 2 TV-WA, FPR
ESSA 2	28FEB66	290	113.3	1561	1639	101.0	1692	2 APT, global operational APT
ESSA 3	02OCT66	350	114.5	1593	1709	101.0	738	2 AVCS, FPR
ESSA 4	26JAN67	290	113.4	1522	1656	102.0	465	2 APT
ESSA 5	20APR67	350	113.5	1556	1635	101.9	1034	2 AVCS, FPR
ESSA 6	10NOV67	290	114.8	1622	1713	102.1	763	2 APT TV
ESSA 7	16AUG68	350	114.9	1646	1691	101.7	571	2 AVCS, FPR, S-Band
ESSA 8	15DEC68	290	114.7	1622	1682	101.8	1103	2 APT TV
ESSA 9	26FEB69	350	115.3	1637	1730	101.9	1030	2 AVCS, FPR, S-Band
ITOS 1	23JAN70	683	115.1	1648	1700	102.0	510	2 APT, 2 AVCS, 2 SR, FPR, 3-axis stabilization
NOAA 1	11DEC70	683	114.8	1422	1472	102.0	252	2 APT, 2 AVCS, 2 SR, FPR
NOAA 2	15OCT72	750	114.9	1451	1458	98.6	837	2 VHRR, 2 VTPR, 2 SR, SPM
NOAA 3	06NOV73	750	116.1	1502	1512	101.9	1029	2 VHRR, 2 VTPR, 2 SR, SPM
NOAA 4	15NOV74	750	114.9	1447	1461	101.6	1463	2 VHRR, 2 VTPR, 2 SR, SPM
NOAA 5	29JUL76	750	116.2	1504	1518	102.1	1067	2 VHRR, 2 VTPR, 2 SR, SPM
TIROS-N	13OCT78	3127	98.92	849	864	102.3	868	AVHRR, HIRS-2, SSU, MSU, HEPAD, HEPED, DCS, TED
NOAA 6	27JUN79	3127	101.26	807.5	823	98.74	857*	AVHRR, HIRS-2, SSU, MSU, HEPAD, HEPED, DCS, TED
NOAA 7	23JUN81	3127	101.9	845	879	98.9	731*	AVHRR-2, HIRS-2, SSU, MSU, HEPAD, HEPED, TED, DCS

APT	Automatic Picture Transmission TV
AVCS	Advanced Vidicon Camera System (1" Vidicon)
AVHRR	Advanced Very High Resolution Radiometer - 4 ch.
AVHRR-2	Advanced Very High Resolution Radiometer - 5 ch.
DCS	Data Collection System
FPR	Flat Plate Radiometer
HB	Heat Budget Instrument
HEPAD	High Energy Proton and Alpha Particle Detector
HIRS-2	High Resolution Infrared Sounder
IP	Ion Probe
IR	Infrared 5 Channel Scanner
IRP	Infrared Passive
HEPED	Medium Energy Proton and Electron Detector
MSU	Microwave Scanner Unit
SEM	Solar Environmental Monitor, TED, HEPED, HEPAD
SPM	Solar Proton Monitor
SR	Scanning Radiometer
SSU	Stratospheric Sounding Unit
TED	Total Energy Detector
TV	Television Cameras (1/2" vidicon)
	NA Narrow Angle - 12°
	MA Medium Angle - 78°
	WA Wide Angle - 104°
VHRR	Very High Resolution Radiometer
VTPR	Vertical Temperature Profile Radiometer

*Still Operational

Table 1.2.2: Orbital Characteristics as a Function of Altitude - R_e = 6370 km (From Widger, 1966).

Orbit Altitude Km	Orbit Altitude N. Miles	$R_e + h$ Km	$R_e + h$ N. Miles	$\left(\frac{R_e+h}{R_e}\right)$	$\left(\frac{R_e}{R_e+h}\right)$	Orbital Velocity km/hr	Orbital Velocity knots	Ground Velocity (Non-Rotating Earth) km/hr	Ground Velocity (Non-Rotating Earth) knots	Orbital Period hours	Orbital Period min.	Westward Displace. Per Orbit Deg.Long.
150	81	6520	3516	1.024	.9770	28111	15245	27464	14894	1.458	87.48	21.87
185	100	6555	3535	1.029	.9717	28080	15203	27285	14773	1.468	88.08	22.02
200	108	6570	3543	1.031	.9695	28004	15188	27150	14725	1.476	88.56	22.14
250	135	6620	3570	1.039	.9622	27901	15130	26846	14558	1.492	89.52	22.38
278	150	6648	3585	1.044	.9582	27839	15099	26675	14468	1.502	90.12	22.53
300	162	6670	3597	1.047	.9550	27795	15074	26544	14396	1.509	90.54	22.64
350	189	6720	3624	1.055	.9478	27690	15017	26245	14233	1.526	91.56	22.89
371	200	6741	3635	1.058	.9450	27649	14994	26128	14169	1.533	91.98	23.00
400	216	6770	3651	1.063	.9408	27589	14962	25956	14076	1.543	92.58	23.15
450	243	6820	3678	1.071	.9339	27488	14905	25671	13920	1.560	93.60	23.40
463	250	6833	3685	1.073	.9322	27462	14893	25600	13883	1.565	93.90	23.48
500	270	6870	3705	1.079	.9271	27386	14851	25390	13768	1.578	94.68	23.67
550	297	6920	3732	1.086	.9204	27287	14798	25115	13620	1.595	95.70	23.93
556	300	6926	3735	1.087	.9197	27277	14793	25087	13605	1.597	95.82	23.96
600	324	6970	3759	1.094	.9138	27189	14745	24845	13474	1.612	96.72	24.18
649	350	7019	3785	1.102	.9075	27095	14694	24589	13335	1.629	97.74	24.44
650	351	7020	3786	1.102	.9073	27092	14692	24581	13330	1.629	97.74	24.44
700	378	7070	3813	1.110	.9009	26995	14640	24320	13189	1.647	98.82	24.71
741	400	7111	3835	1.116	.8957	26919	14597	24111	13075	1.661	99.66	24.92
750	405	7120	3840	1.118	.8945	26902	14588	24064	13049	1.664	99.84	24.96
800	432	7170	3867	1.126	.8883	26807	14536	23813	12912	1.682	100.92	25.23
834	450	7214	3885	1.131	.8842	26725	14503	23630	12824	1.697	101.82	25.46
850	459	7220	3894	1.134	.8821	26715	14487	23565	12779	1.699	101.94	25.49
900	486	7270	3921	1.141	.8761	26624	14436	23325	12647	1.717	103.02	25.76
927	500	7297	3935	1.146	.8729	26575	14411	23197	12579	1.727	103.62	25.91
950	513	7320	3948	1.149	.8701	26531	14388	23085	12519	1.735	104.10	26.03
1000	540	7370	3975	1.157	.8642	26441	14338	22850	12391	1.753	105.18	26.30
1019	550	7389	3985	1.160	.8620	26408	14320	22764	12344	1.760	105.60	26.40
1050	567	7420	4002	1.165	.8583	26352	14290	22618	12265	1.771	106.26	26.57
1100	594	7470	4029	1.173	.8526	26264	14243	22393	12144	1.788	107.26	26.82
1112	600	7482	4035	1.175	.8513	26243	14232	22341	12116	1.793	107.58	26.90
1150	621	7520	4056	1.181	.8469	26179	14194	22171	12021	1.806	108.36	27.09
1200	648	7570	4083	1.189	.8413	26089	14147	21949	11902	1.825	109.50	27.38
1205	650	7575	4085	1.189	.8409	26083	14145	21933	11895	1.826	109.56	27.39
1250	674	7620	4109	1.196	.8360	26005	14103	21740	11790	1.842	110.52	27.63
1297	700	7667	4135	1.204	.8307	25925	14059	21536	11679	1.860	111.60	27.90
1300	701	7670	4136	1.204	.8305	25919	14057	21526	11674	1.861	111.66	27.92
1350	728	7720	4163	1.212	.8251	25834	14011	21316	11560	1.879	112.74	28.19
1390	750	7760	4185	1.218	.8208	25769	13974	21151	11470	1.894	113.64	28.41
1400	755	7770	4190	1.220	.8198	25752	13966	21111	11449	1.897	113.82	28.46
1450	782	7820	4217	1.228	.8146	25670	13921	20911	11340	1.915	114.90	28.73
1483	800	7853	4235	1.233	.8111	25615	13891	20776	11267	1.928	115.68	28.92
1500	809	7870	4244	1.236	.8094	25589	13876	20712	11231	1.934	116.04	29.01
1550	836	7920	4271	1.243	.8043	25508	13833	20516	11126	1.952	117.12	29.28
1575	850	7945	4285	1.247	.8016	25468	13810	20415	11070	1.961	117.66	29.42
1600	863	7970	4298	1.251	.7992	25428	13789	20322	11020	1.971	118.26	29.57
1650	890	8020	4325	1.259	.7942	25349	13747	20132	10918	1.989	119.34	29.84
1668	900	8038	4335	1.262	.7924	25321	13730	20064	10880	1.996	119.76	29.94
1700	917	8070	4352	1.267	.7893	25267	13703	19943	10816	2.008	120.48	30.12
1750	944	8120	4379	1.275	.7844	25191	13662	19760	10716	2.027	121.62	30.41
1761	950	8131	4385	1.277	.7834	25175	13651	19722	10694	2.031	121.86	30.47
1800	971	8170	4406	1.283	.7796	25113	13619	19578	10617	2.046	122.76	30.69
1850	998	8220	4433	1.291	.7749	25039	13578	19403	10522	2.064	123.84	30.96
1853	1000	8223	4435	1.291	.7745	25033	13574	19388	10513	2.066	123.96	30.99
35815	19326	42185	22761	6.622	.1510	11052	5992	—	—	24.000	1440.00	—

PART IV

AAAAAAAAA BBBBB CCCCCCCCCCC DDEEFFGGHHIIIII JJJJJJJ

KKKKKKKK LLLLLLLL MMMMMMMM NNNNNNNN OOOOOOOO PPPPPPPP

QQQQQQQQ RRRRRRRR SSSSSSSSSS TTTTTTTTTT UUUUUUUUUU VVVVVVVVV

WWWWWWWWW XXXXXXXXX YYYYYYYYY ZZZaaabbb cccc dddddddddd

eeeeeeeee fffffffff ggggggggg SPARESPARE

APT TRANSMISSION FREQUENCY XXX.XX MHz
HRPT TRANSMISSION FREQUENCY XXXX.XX MHz
BEACON (DSB) TRANSMISSION FREQUENCY XXX.XX MHz
APT DAY X/X APT NIGHT X/X
DCS CLOCK TIME DAY XXX XXXXX.X
(ADDITIONAL PLAIN LANGUAGE REMARKS WHEN NEEDED)

TABLE 1.3.1

Numbers used in TBUS, SATOB, SATEM, SAREP bulletins to identify satellites:

10 - 19	ITOS series satellites
20 - 29	SMS/GOES series satellites
30 - 39	TIROS-N series satellites

PART IV - (Contains high precision orbital elements, transmission frequencies, and remarks).

Symbol	Explanation
AAAAAAAAA	Spacecraft identification (International designator- see "COSPAR Guide to Rocket and Satellite Information and Data Exchange Information Bulletin #9, July 1962).
BBBBB	Orbit number at epoch.
CCCCCCCCCCC	Time of ascending node (days from January 1 at 00Z, to nine decimal places.
DD	Epoch year
EE	Epoch month
FF	Epoch day
GG	Epoch hour
HH	Epoch minute
IIIII	Epoch second, to three decimal places
JJJJJJJ	Greenwich Hour Angle at Aries at epoch, to four decimal places.
KKKKKKKK	Anomalistic period (minutes), to four decimal places.
LLLLLLLL	Nodal period (minutes), to four decimal places.
MMMMMMMM	Eccentricity, to eight decimal places.
NNNNNNNN	Argument of perigee (degrees), to five decimal places.
OOOOOOOO	Right Ascension of the ascending node (degrees), to five decimal places.
PPPPPPPP	Inclination (degrees), to five decimal places.
QQQQQQQQ	Mean anomaly (degrees), to five decimal places.
RRRRRRRR	Semi-major axis (km), to three decimal places.
SSSSSSSSSS	Sign and epoch X position component (km), to four decimal places.
TTTTTTTTTT	Sign and epoch Y position component (km), to four decimal places.

Symbol (Cont.)	Explanation (Cont)
UUUUUUUUUU	*Sign and epoch Z position component (km), to four decimal places.
VVVVVVVVV	*Sign and epoch X velocity (Xdot) component (km/sec), to six decimal places.
WWWWWWWWW	*Sign and epoch Y velocity (Ydot) component (km/sec), to six decimal places.
XXXXXXXXX	*Sign and epoch Z velocity (Zdot) component (km/sec), to six decimal places.
YYYYYYYYY	Ballistics coefficient CD-A/M (m^2/kg), to eight decimal places.
ZZZ	Daily solar flux value (10.7 cm) (10^{-7} watt/m^2).
aaa	90-day running mean of solar flux (10^{-7}watts/m^2).
bbb	Planetary magnetic index ($2x10^{-5}$ gauss).
cccc	Drag modulation coefficient, to four decimal places.
dddddddddd	Radiation pressure coefficient (m^2/kg), to ten decimal places.
eeeeeeeee	Sign and perigee motion (deg/day), to five decimal places.
fffffffff	Sign and motion of Right Ascension of the ascending node (deg/day), to five decimal places.
ggggggggg	Sign and rate of change of mean anomaly at epoch (deg/day), to two decimal places.
SPARESPARE	spares

- -

*-- All signed values in PART IV are preceeded by a "P" or "N" to denote a plus (+) or minus (-)value.

- -

APT TRANSMISSION FREQUENCY XXX.XX MHz
HRPT TRANSMISSION FREQUENCY XXXX.XX MHz
BEACON (DSB) TRANSMISSION FREQUENCY XXX.XX MHz
APT DAY X/X APT NIGHT X/X where X will identify channels being used.
DCS CLOCK TIME DAY XXX XXXXX.X
Followed by PLAIN LANGUAGE messages when necessary.

SAMPLE APT PREDICT (TBUS) BULLETIN

The following encoded APT Predict (TBUS) Bulletin example is referred to throughout the remaining appendices. The major features of the message are decoded on the following pages.

```
TBUS2 KWBC 211900
APT PREDICT
062430 TIROS N


PART I
08749 02416 01653 01146 T0202 L2550
87532 30503 11349
87570 55311 24446
87611 24121 34243
DAY   PART II
02840 070132 04840 140149 06840 21066
08840 28084 10840 350204 12840 419227
14840 488255 16840 55689 18840 623336
20840 688407 22840 749529 24840 796776
26841 808200 28841 774538 30841 717705
32851 654794 34842 588749 36842 520710
38842 452679
DAY   PART III
02845 070100 04855 140083 06855 210066
08855 280048 10855 350028 12845 419005
14868 488022
NIGHT PART II
40852 383655 42852 313633 44842 244614
46842 174596 48842 104580 50852 034563
NIGHT PART III
52857 035547 54857 105531 56857 175514
58857 244497 60857 314478 62857 383456
64857 452431 66857 520401 68857 588362
70857 654306 72857 717217 74857 773050
76858 808714 78858 797290 80858 749043
82855 689079 84845 624150 86845 557197
88845 489232 90845 420259
PART  IV
1979 057A 09345 105066560150 810414203210007 1509616
01011681 01012254 00124732 17142454 13773458 09867899
18869440 07189253 M053313427 P048448725 M000019396
P00759127 P00825300 P07350534 003263350 245206018 9449
0000499998 M00290091 P00098722 P00512415 SPARESPARE

APT TRANSMISSION FREQUENCY 137.62 MHZ
HRPT TRANSMISSION FREQUENCY 1707 MHZ
BEACON (DSB) FREQUENCY 137.77 MHZ
APT DAY/NIGHT 1/4 APT IR CHANNEL 4 (10.5 to 11.5 MICROMETERS)
AND VIS CHANNEL 1 (0.55 to 0.90 MICROMETERS)
WILL BE TRANSMITTED CONTINUOUSLY.
DCS CLOCK TIME DAY 088 41126.4
```

Decoding Excercise

TBUS2 KWBC 211900

TBUS2	- Bulletin heading--identifies bulletin for satellite southbound in daylight
KWBC	- Bulletin source--Washington, D. C. Communications Center
211900	- 21 -Day of the month--21st - 1900 -Bulletin broadcast time--1900z
APT PREDICT	- Bulletin identifier
062430	- Message serial number 06 --month -- June 24 --Day for which bulletin applies -- 24th 30 --Satellite identifier (see code table 1.3.1).
TIROS N	- Plain language satellite identifier
PART I	- Identifies reference orbit information and the orbital height, equator crossing, longitude and equator crossing time for the fourth, eighth, and twelfth orbits after the reference orbit.

08749 02416 01653 01146 T0202 L2550

08749	0 - Group indicator 8749 - Reference orbit number
02416	0 - Group indicator 24 - Day of month of equator crossing 16 - Hour
01653	0 - Group indicator 16 - Minutes 53 - Seconds (time of equator crossing 16:16:53z)
01146	0 - Octant 0 (0° to 90°), N. Hemisphere 1146 - 011.46°W (equator crossing longitude for orbit 8749 in octant 0)
T0202	T - Group indicator 0202 - Orbital period 102 minutes 02 seconds
L2550	L - Group indicator 2550 - Nodal longitudinal increment 25.50°

87532 30503 11349

87532 30503	8753	- Orbit number 8753 (4th orbit after reference orbit)
	2 30503	- Time (23:05:03z) of ascending node for orbit 8753
11349	1	- Octant 1 (90°W to 180°)
	1349	- 113.49°W (equator crossing for orbit 8753 in octant 1)
87570 55311 24446 87611 24121 34243		- Decoded in same manner as previous underlined line of data
DAY PART II		- Contains satellite altitude and subpoint coordinates at two-minute intervals after time of Northbound (ascending) equator crossing.

02840 070132 04840 140149 ....

02840	02	- Minute 02 after Northbound equator crossing
	84	- Spacecraft height 840km
	0	- Octant 0 (0° to 90°W), N. Hemisphere
070132	070	- Latitude 07.0°N
	132	- Longitude 013.2°W
04840	04	- Minute 04 after Northbound equator crossing
	84	- Spacecraft height 840 km
	0	- Octant 0 (0° to 90°W), N. Hemisphere
140149	140	- Latitude 014.0°N
	149	- Longitude 14.9°W

Remainder of DAY PART II decoded in same manner. Data for DAY PART II are continuous at 2-minute intervals from equator North to Northern terminator.

DAY PART III - Contains satellite altitude and subpoint coordinates at two-minute intervals South of the equator. satellite Northbound in the Southern Hemisphere (Points are plotted Southward from the equator).

02845 070100 04855 140083 ....

02845	02 - Minute 02 before Northbound equator crossing 84 - Spacecraft height 840 km 5 - Octant 5 (0 to 90°W, S. Hemisphere)
070100	070 - Latitude 07.0°S 100 - Longitude 010.0°W
04855	04 - Minute 04 after equator crossing 85 - Spacecraft height 850 km 5 - Octant 5 (0 to 90°W, S. Hemisphere)
140083	140 - Latitude 14.0°S 083 - Longitude 08.3°W

Remainder of DAY PART II decoded in same manner

NIGHT PART II - Satellite altitude and subpoint coordinates at two-minute intervals beginning at the day/night terminator in the N. Hemisphere and continuing southward toward the equator.

40862 383655 42862 313633 ....

40852	- 40 - Minute 40 after Northbound equator crossing - 85 - Spacecraft height 860 km - 2 - Octant 2 (90°E to 180°, N. Hemisphere)
383655	- 383 - Latitude 38.3°N - 655 - Longitude 165.5°E
42852	- 42 - Minute 42 after equator crossing - 85 - Spacecraft height 860 km - 2 - Octant 2 (90°E e to 18 ', N. Hemisphere) - 313 - Latitude 31.3°N - 633 - Longitude 163.3°E

Remainder of NIGHT PART II decoded in same manner. Data continuous at 2-minute intervals.

NIGHT PART III - Satellite altitude and subpoint coordinates at two-minute intervals south of the equator on the descending side of the orbit.

52867 035547 54867 105531..... .....

52857	- 52	- Minute 52 after Northbound equator crossing
	- 85	- Spacecraft height 860 km
	- 7	- Octant 7 (90°E to 180°, S. Hemisphere)
035557	- 035	- Latitude 03.5°S
	- 547	- Longitude 154.7°E
54857	- 54	- Minute 54 before equator crossing
	- 85	- Spacecraft height 860 km
	- 7	- Octant 7 (90°E to 180°, S. Hemisphere)
105531	- 105	- Latitude 10.5°S
	- 531	- Longitude 153.1°E

Remainder decoded in same manner. Data continuous at 2-minute intervals from first point South of equator to Southern terminator.

PART IV - Indicator -- orbital elements, transmission frequencies, and remarks follow.

AAAAAAAAA	1979-057A	1979-057A International designator
BBBBB	09345	revolution 9345
CCCCCCCCCCC	105066560150	105.066560150 days
DDEEFFGGHHIIIII	810414203210007	81--1981 year 04--04 months 14--14 days 20--20 hours 32--32 minutes 10007--10.007 seconds
JJJJJJJ	1509616	150.9616 degrees
KKKKKKKK	01011681	101.1681 minutes
LLLLLLLL	01012254	101.2254 minutes
MMMMMMMM	00124732	0.00124732 no units
NNNNNNNN	17142454	171.42454 degrees
OOOOOOOO	13773458	137.73458 degrees
PPPPPPPP	09867899	98.67899 degrees
QQQQQQQQ	18869440	188.69440 degrees
RRRRRRRR	07189253	7189.253 km

SSSSSSSSSS	M053313427	-5331.3427 km
TTTTTTTTTT	P048448725	+4844.8725 km
UUUUUUUUUU	M000019396	-1.9396 km
VVVVVVVVV	P00759127	+0.759127 km/sec
WWWWWWWWW	P00825300	+0.825300 km/sec
XXXXXXXXX	P07350534	+7.350534 km/sec
YYYYYYYYY	003263350	0.03263350 m2/kg
ZZZaaabbb	245206018	245--245 x 10^{-7} watt/m^2 206--206 x 10^{-7} watt/m^2 018--36 x 10^{-5} gauss
cccc	9449	0.9449 no units
dddddddddd	0000499998	0.000499998 m^2/kg
eeeeeeeee	M00290091	-2.90091 degrees/day
fffffffff	P00098722	+0.98722 degrees/day
gggggggg	P00512415	+5124.15 degrees/day
SPARESPARE	SPARESPARE	No information at this time

APT TRANSMISSION FREQUENCY 137.62 MHZ
HRPT TRANSMISSION FREQUENCY 1707 MHZ
BEACON (DSB) FREQUENCY 137.77 MHZ
APT DAY/NIGHT 1/4 APT IR CHANNEL 4 (10.5 TO 11.5 MICROMETERS)
AND VIS CHANNEL 1 (0.55 TO 0.90 MICROMETERS)
WILL BE TRANSMITTED CONTINUOUSLY.
DCS CLOCK TIME DAY 088 41126.4 - DATA COLLECTION SYSTEM CLOCK TIME RESET FOR JULIAN DAY 088, 41126.4 SECONDS

- -

NOTE: The classical elements (Keplerian) from MMMMMMMM to RRRRRRRR are (Brower) mean elements; the position and velocity components SSSSSSSSSS to XXXXXXXXX are actual. The Greenwich Hour Angle initially will be put out as mean siderial time; it is expected to eventually become apparent siderial time.

The paramenter "time of the ascending node" (i.e., CCCCCCCCCCCC) is presently being reevaluated. It may be to changed to "epoch time minus time of the ascending node crossing prior to epoch (in minutes)". Thus, the user could compute the time of the northbound equator crossing prior to epoch instead of the time for an arbitrary northbound equator crossing. Naturally any changes would be announced.

Blank page retained for pagination

CHAPTER 2

SATELLITE INSTRUMENTS

A wide range of instruments, primarily radiometers, have been flown on weather satellites. The practical user of data from these instruments must be aware of some basic instrument characteristics which will affect his interpretation and use of the data. They are:

a) field-of-view (and resulting ground resolution)

b) spectral response

c) calibration (and resulting accuracy and precision)

d) time and space sampling

Of course, there are other instrument parameters which are important for special uses and especially for consideration in the design of new instruments. In this chapter we will address the four above and a few others of special note. After an overview of these topics we will consider the categories of

a) cloud-imaging systems (Sec. 2.1)

and b) sensors for temperature and moisture sounding including microwave sensors (Sec. 2.2).

We conclude the chapter with a survey of equally important weather sensing systems, the data collection and platform location systems.

Consider a small area, A_S, on the surface of the earth (or a cloud) as shown in Figure 2.0.1. When illuminated by the sun the radiance from the surface, N_S, will be reflected solar energy (of course, emitted infrared and microwave energy also arises from A_S; this is discussed in Chapter 5).

For the purpose of this example, N_S will be reflected solar radiation and it reaches the aperature (opening) of a satellite-borne instrument having an area, A_C, of that opening. What is the radiant power, P_r, received at the satellite instrument? This is the basic signal which will be interpreted in terms of some information about the surface (e.g., cloud) or the atmosphere between the surface and the satellite. The equation is:

$$P_r = A_S \omega_S N_S(\gamma) \cos\gamma \qquad (2.0.1)$$

where γ is the angle between the local vertical through A_S and the line from A_S to A_C. The same figure shows the simpler case where the satellite is directly above A_S and thus $\gamma = 0$. Then equation (2.0.1) becomes $Pr = A_S \omega_S N_S$. Since from the definition of a solid angle,

$$\omega_S = \frac{A_C}{r_S^2} \qquad (2.0.2)$$

with r_S the distance between A_S and A_C. The solid angle, ω_S, is that subtended from the surface by the aperature of the instrument. Of course, $A_S = \pi a^2$ and for small angles, α (the "field-of-view" of the satellite sensor), we know

$$a = r_S \frac{\alpha}{2} \quad , \text{ thus } \quad A_S = \frac{\pi r_S^2 \alpha^2}{4}$$

and

$$P_r = N_S A_C \pi \frac{\alpha^2}{4} \qquad (2.0.3)$$

however, since the solid angle subtended at the sensor aperature by the

surface A_S is

$$\omega_C = \frac{\pi\alpha^2}{4} \quad , \qquad \text{then}$$

$$P_r = A_C \omega_C N_S \quad \text{(in Watts)} \qquad (2.0.4)$$

Equation 2.0.4 gives us our desired expression for the power received at the satellite sensor in terms of two known sensor parameters (A_C and ω_C) and the unknown signal from the earth-atmosphere system (N_S in Watts $\cdot$ m^{-2} steradian^{-1}).

NOTE: In the case of reflected solar radiation the radiance, N_S, on the earth is a function of the reflectance, ρ, and the incident angle, θ. Assuming atmospheric transmittance is unity,

$$N_S = S_0 \cdot \rho \cdot \cos\theta \cdot \pi^{-1}, \qquad (2.0.5)$$

where S_0 is the solar constant (in irradiance units at the distance of the earth from the sun). The π factor arises because the outgoing radiance is assumed isotropic (independent of direction). Pi (π) is the integral over a hemisphere of the cosine factor in order to change from irradiance to radiance units. (See Chapter 5 for more on radiation quantities and units).

At the satellite instrument the power received (P_r) is converted to an output voltage (V_0) and generally digitized immediately to a digital count (C). The digital count is recorded on tape at the satellite or immediately transmitted to the ground. Since

$$V_0 \propto k_1 P_r \qquad \text{and} \qquad C \propto k_2 V_0$$

sometimes satellite instrument <u>calibration</u> curves are simply shown relating

$$C \propto k_1 k_2 P_r \qquad \text{or even} \qquad C \propto k_3 N_s.$$

So long as the user has some understanding of the values A_c and ω_c as well as the relationships expressed by k_1 and k_2 he can then confidently use values of C provided to him from the satellite data center to understand the signal N_s.

User's manuals and engineering documents convey this information to the meteorologist with the aid of tables and graphs. Figure 2.0.2 is a typical calibration curve from the SMS-1 and GOES-1 visible light sensors. Here N_s is expressed as a relative reflectance from the surface, A_s; C is given as a digital "count" (in this case a number between 0 and 255). Note that the curve is non-linear. Departure from linearity across a range of earth signals important to the user is very critical information. Always inquire about this aspect of the calibration of a satellite instrument.

Of course, calibration also carries information about the absolute (and relative) accuracy of instrument. If it is possible to "re-calibrate" the satellite instrument in orbit additional information is available to the user about the stability of the sensor. This information often provides the necessary assurance that measured signals, N_s, have a high degree of reliability for the user. Discussion of details of instrument calibration is beyond the scope of these notes. Refer to publications from the space agencies, COSPAR, and the WMO. Hudson (1969) is a good textbook on engineering aspects of satellite instruments. Williamson (1977) provides a summary report on calibration technology for meteorological satellite applications.

The satellite instrument field-of-view, FOV, is shown in Figure 2.0.1 as α. For a small angle of α ($\Delta\alpha$) and nadir viewing the <u>ground resolution</u> (Δx) of the satellite sensor is:

$$\Delta x = h\Delta\alpha \qquad (2.0.6)$$

with h the height of the satellite and $\Delta\alpha$ in radians. The instrument makes a weighted measurement of radiation from the ground spot of size Δx. Features the size of Δx or smaller generally cannot be studied by use of the satellite data.

For reasons discussed further in Chapter 5, most satellite sensors are designed to measure in limited spectral regions (e.g., the visible or "window" infrared regions noted in Section 1.1). Thus, each sensor has a spectral response as is shown in Figure 2.0.3 for two infrared "channels" of an instrument carried on METEOSAT-1. In this case, the instrument spectral response curves are normalized to the peak spectral transmittance of the combined instrument system of optics, filter and detector. These are typical curves and the radiance that is actually measured is called "filtered" radiance, $N_{\Delta\lambda}$, where

$$N_{\Delta\lambda} = \sum N_\lambda \phi_\lambda \Delta_\lambda \,/\, \sum \phi_{\lambda\Delta\lambda} \qquad (2.0.7)$$

and $\Delta\lambda$ is the wavelength interval between λ_1 and λ_2; ϕ_λ is the normalized spectral response.

The time and space sampling of an instrument is determined first by the orbit of its satellite (see Section 1.2.7) and also by its scanning or pointing mechanisms. Obviously, this is an important characteristic for users.

Any user or prospective user of a specific set of data from a satellite instrument (or the reader of a paper or report using the data)

should be aware of the basic instrument characteristics discussed above. Without such knowledge it is difficult to fully understand - or properly use - data from the satellite experiment.

The user should also inquire in some cases about such instrument parameters as response time, data sample averaging or overlap, etc. Details are found in users' manuals and guides and some examples are noted in following sections.

As part of this overview of satellite instrumentation the example of the presentday operational U.S. sun-synchronous weather satellite, NOAA, is provided in Figure 2.0.4 (Schwalb, 1978) and Table 2.0.1. The data in the figure and table demonstrate typical characteristics of a 1983 meteorological satellite with its package of instruments.

Further examples of the wide range of satellite instruments flown to date for research and operational purposes are given in Figure 2.0.5 and in Tables 2.0.2 and 2.0.3 (Also see Table 1.1.2).

2.1 Cloud Imaging Systems: Infrared and Visible Scanners, Spin-scan Radiometers

We begin our study of specific types of satellite instrumentation by considering the category of sensors designed to obtain imagery of clouds. These instruments are by far the most familiar to the non-specialist and provide the largest amount of data used by the weather forecasters and research scientists. A common characteristic of these instruments is that they are designed to see through the atmoshere. They are designed to operate in so-called atmospheric "window" so that the gases in the atmosphere will not impede the view of the cloud surfaces.

Scanning radiometers are currently the primary imaging devices for both the polar-orbiting and geosynchronous operational satellites, replacing the vidicon cameras of the early TIROS and ESSA satellites, and ITOS A-C (NOAA-1 and 2). Generally speaking, the scanning radiometers sense energy simultaneously in both visible and infrared wavelengths (2 or more). In this section, we will describe two basic types of scanners — the SR (Scanning Radiometer) used for cloud and ocean surface imagery and APT on NOAA-3, 4 and 5, and the VISSR (Visible-Infrared Spin Scan Radiometer) of the SMS-GOES series of geosynchronous satellites.

The Scanning Radiometer (SR) is a two-channel scanning instrument sensitive to energy in the visible spectrum 0.5 to 0.7 μm and in the infrared (IR) window region 10.5 to 12.5 μm. The instrument was designed to operate on a sun-synchronous spacecraft in a 1464 km orbit. Further details on the SR can be obtained from Schwalb (1972).

The SR is a line scan device; global coverage is achieved from continuous horizon-to-horizon cross-track scanning by the mirror combined with the forward motion of the spacecraft (Figure 2.1.1). Since the mirror rotates at a constant angular rate, the geometric resolution on the ground changes as the distance from the subsatellite point increases; a picture produced from these signals will appear foreshortened in the area of the horizons. The 5.3 mrad IFOV of the infrared channel provides a ground resolution of approximately 7.5 km at the subpoint. Successive lines are contiguous at the subpoint and overlap as the distance from the subpoint increases. In equatorial regions, contiguous data from successive orbits will occur at a point about 1668 km from the subsatellite point. At this point the data zenith angle is 60° and the IFOV spot covers about 15 km x

22 km. The visible channel, with a 2.8 mrad IFOV produces a 4 km spot at the subpoint. This spot size increases to approximately 7.5 km by 15 km at the equatorial contiguity point. It should be noted that there will be a 4 km "gap" between visible channel data lines at the subpoint. The gap will not be apparent in the display and will disappear entirely at distances more than about 1385 km from the subpoint.

It should be noted that the SR is one of the instruments which provided a great amount of useful "APT" data as discussed in Section 1.3. The Advanced Very High Resolution Radiometer (Figure 2.1.2) is an increased resolution 4-channel instrument based on the SR.

In contrast to the SR instrument, the cross-earth scan for the Visible and Infrared Spin-Scan Radiometer (VISSR) is due to the rotation (100 rev/min) of the entire satellite, where the VISSR looks out the side of the satellite perpendicular to the satellite spin axis (the oval aperature in Figure 1.1.4). With the spin axes of the satellite and the earth being parallel, a scan line is aligned west to east across the face of the earth. Once during each revolution of the satellite, the scan mirror (Figure 2.1.3) angle is slightly changed (stepped) to give the north-south displacement between successive scan lines to form an earth image. The scan mirror is the only part of the VISSR which needs to move for an image to be taken. Note that in the VISSR configuration shown in Figure 2.1.3 that the instrument view to earth is out through the sun shade or towards the bottom of the figure. The radiation cooler shown on the VISSR radiates heat from the HgCdTe infrared detector into cold space and makes the infrared sensor much more temperature-sensitive. A linear array of eight visible sensors corresponds to the coverage of a single IR sensor. Thus, the resolution in

the visible channel is about 8 times the IR resolution. Light is guided to the visible photomultipliers by using fiber optics light guides, but reaches the IR sensor directly. Each scan is composed of one IR line, and 8 visible lines of higher resolution covering the same area (See the GOES references in Section 1.1).

The sensor scans from west to east in eight identical visible channels and two redundant infrared channels. This sensor provides visible data at 0.8 km resolution and infrared data at 8 km resolution. These are realized at satellite subpoint and deteriorate as the area viewed moves away from subpoint. With the satellite rotating at 100 revolutions per minute, the VISSR scanning mirror scans the earth for about one-twentieth of each complete 360° rotation. The radiometer performs 1821 steps in successive scans from north to south in 18.2 minutes. This provides an image of the complete earth disc or about one quarter of the earth's surface. The resulting visible images (0.55 to 0.70 μm band) contains 14,568 lines and have a resolution of nearly 0.8 km. Infrared images (10.5 to 12.6 μm band) have a total of 1821 lines with a 9.3 km resolution. In addition to this normal scan mode, the spacecraft may be placed into a limited scan mode. While in this mode, the north to south scan may be limited to a fewer number of scans. This reduces the area of coverage, but increases the frequency of imaging for special weather observation.

A special note to the user of VISSR-type infrared data deals with sensor response time. Because the IR signal from earth is low at the geostationary orbit distance and the satellite spin causes a rapid scan across the earth an instrument response time of 55 microseconds is a factor to consider. Along each scan line described above the output of the IR detector

is sampled each 7.6 microseconds. Thus, 7 samples of earth signal are taken and converted to output (count) values during the response time. A user interested in studying a sharp-edged cloud over a hot background surface will not obtain the proper infrared temperature of the cloudtop.

The VISSR launched on ATS-1 became the first successful meteorological experiment on a geostationary satellite. It was designed by V. E. Suomi and colleagues at the University of Wisconsin-Madison. The operating principles of VISSR have been used on the SMS and GOES experiments as well as GMS of Japan and METEOSAT of ESA.

Digression:

Geostationary satellite data such as that from the VISSR are extremely valuable to the meteorologist because of their high time frequency. Images are available every 30 minutes and sometimes even more frequently. One disadvantage of the geostationary orbit is the viewing of clouds and weather systems at large values of great circle arc from the subpoint of the satellite which is necessarily on the equator. However, the data at these near-horizon positions are still quite quantitative and very useful if the appropriate corrections for the viewing angle can be made.

The most obvious uncertainty that arises when using the data from GOES, METEOSAT and GMS at values of great circle arc greater than 50° from the subpoint is the apparent mislocation of the tops of high clouds relative to their actual position above a point on the earth's surface. Weiss (1979) has calculated the correction factors necessary to adjust the situation displayed in Figure 2.1.4. The geometry of the problem is shown in Figure 2.1.5. Results from Weiss' work are shown in Figures 2.1.6 and 2.1.7 and Tables 2.1.1 and 2.1.2. For example, he points out that a cloud

top at 10 km appearing over Anchorage (ANC) must be corrected by 30 km to the south-southeast to find the actual cloud location. An exercise for the reader is to reproduce Weiss' calculations with the aid of trigonometry. He used the following values for constants in Figure 2.1.5; R = 6371 km, R_e = 6378 km, A = 35,793 km.

2.2 Scanning Radiometers for Remote Sensing of Ocean and Land; Temperature and Moisture Sounding; Microwave Systems

The next category of instruments we will discuss covers those slightly more sophisticated instruments which are designed for remote sensing purposes. They may also produce image quality data, but often include channels with certain selected spectral intervals to obtain information about a particular characteristic of cloud, land surface, or atmospheric constituent. The techniques used for temperature and moisture sounding will be discussed in Chapter 6.

2.2.1 The Temperature-Humidity Infrared Radiometer (THIR)

The NIMBUS-7 meteorological satellite which was launched in 1978, carried a Temperature-Humidity Infrared Radiometer (THIR), shown in Figure 2.2.1.1. This two-channel scanning radiometer proved its reliable performance on NIMBUS-4 (1970) and -5 (1972) by recording several years of day-night cloud coverage, cloud heights, ground and sea-surface temperatures and providing a qualitative estimate of mid-tropospheric humidity under clear sky conditions.

The two THIR detectors consist of germanium-immersed thermistor bolometers which have peak spectral responses in the 10.5 - 12.5 μm "window" and the 6.3 - 7.25 μm water vapor absorption region (Figure 2.2.1.2).

[Note that NIMBUS THIR is identical to the old NOAA APT SR except the visible sensor is replaced by a 6.3 - 7.25 μm water vapor channel.] A cutaway of the radiometer, shown in Figure 2.2.1.3, includes the scan mirror, sun shield, folded optical Cassegranian telescope, a dichroic beam splitter, electronics module and two detectors.

The elliptically-shaped plane scan mirror, inclined at 45° to the optical axis of the instrument, rotates at 48 rpm and scans through a 360° angle in the plane perpendicular to the direction of motion of the satellite. Figure 2.2.1.4 shows the 7.7 by 7.7 km ground resolution (scan spot) of the 11 μm channel at zero degree nadir increasing to an elongated 14 by 31.8 km scan spot at 50° nadir, at an 1112 km orbital altitude. Similarly the ground resolution of the 6.7 μm channel at the sub-satellite point was 22.6 km while at 50° nadir, it was 41.1 km by 93.5 km.

A sample NIMBUS-5 THIR (11μm) scan sequence is shown in Figure 2.2.1.5. The two detectors simultaneously view the housing, A, at spacecraft zenith, (zero seconds). Seven synchronous pulses start at C, followed by six 1-volt calibration steps. A space scan starts at D to G, followed by an earth scan (117° wide) to I, a space scan to K, a housing scan to M, and then back to zenith. The entire sequence lasts 1.23 seconds. The space and housing-viewed parts of the scan serve as part of the in-flight check of calibration. Note the small noise ripple on the housing and space scans. The THIR design parameters and performance specifications are shown in Table 2.2.1.1. The NIMBUS-4 THIR (11 μm) calibration curve (Figure 2.2.1.6) relates the voltage output of the detector to equivalent blackbody temperature (T_{BB}) at a 293 K housing temperature while Table 2.2.1.1 relates the effective radiance (N) to the equivalent blackbody temperature (T_{BB}) for both channels.

An analog-to-digital converter on the satellite NIMBUS-7 digitizes the 11 μm and 6.7 μm channels at a minimum rate of 1200 and 400 samples per second respectively and outputs a 10-bit digital word (or "count" from 0 to 1023). Figure 2.2.1.7 shows typical THIR output. Note the moist (gray) and dry (black) areas in the 6.7 μm channel. The 11.5 μm shows the more typical infrared "window" image of clouds and surface. Allison et al. (1972) gives some applications of THIR data.

[Historical Note: The early NIMBUS experiments MRIR and THIR developed and tested the water vapor measurements from satellites. However, the most dramatic application of this method was first accomplished by the European Space Agency when METEOSAT-1 carried a water vapor channel into geostationary orbit for the first time.]

2.2.2 Microwave Instruments

Passive microwave signals emitted and reflected from portions of the earth and atmosphere provide additional remote sensing information which can be measured from satellites. Chapter 5 discusses the nature of the radiation at these millimeter and centimeter wavelengths.

In late 1969 the USSR satellite COSMOS 243 carried the first successful microwave meteorological experiment. Thus far, U. S. and USSR instruments viewing at various wavelengths have been used to determine cloud water content, atmospheric temperature and moisture, estimates of precipitation and properties of the ocean or land surfaces. Following chapters on applications will review these topics.

A good review of passive microwave sensing is provided in NASA's NIMBUS-5 Users' Guide (available from Goddard Space Flight Center,

Greenbelt, MD 20771). It describes the Electrically Scanning Microwave Radiometer (ESMR) whose antenna is shown in Figure 2.2.2.1 and the NIMBUS E Microwave Spectrometer (NEMS).

A more advanced instrument, the Scanning Multichannel Microwave Radiometer (SMMR) was flown on NIMBUS-7 launched in late 1978. The SMMR channel wavelengths are centered at 0.8 cm, 1.4 cm, 1.7 cm, 2.8 cm and 4.6 cm. Polarization components of the microwave radiation are extracted for each channel. The highest ground resolution is about 20 km for the 0.8 cm channel. The principal scientific objectives of SMMR were to obtain sea-surface winds and temperatures (See Chapter 17). In addition, other geophysical parameters are extracted from the SMMR data. These include: sea ice parameters, a mesoscale soil wetness index, snow accumulation rates over continental ice sheets, subsurface physical temperatures in snow cover, and atmospheric parameters over open ocean water of total water vapor, total non-precipitating liquid and rainfall rate.

The following description of SMMR as typical of a microwave instrument of the late 1970's is extracted from NASA's NIMBUS-7 Users' Guide. The SMMR is a ten-channel instrument delivering orthogonally polarized antenna temperature data at the five microwave wavelengths indicated in Table 2.2.2.1. A diagram of the SMMR is shown in Figure 2.2.2.2.

Six conventional Dicke-type radiometers are utilized. Those operating at the four longest wavelengths measure alternate polarizations during successive scans of the antenna; the others, at the shortest wavelength, operate continuously for each polarization. A two-point reference signal system is used, consisting of an ambient RF termination and a horn antenna viewing deep space. A switching network of latching ferrite circulators

selects the appropriate polarization or calibration input for each radiometer.

The remainder of the instrument, including the radiometers, control electronics, power supply, data and programmer subsystems, is a derivative of the NIMBUS-5 NEMS and NIMBUS-6 SCAMS instruments with minor modifications to take advantage of improved state-of-the-art components.

Physically, the SMMR instrument consists of five hardware elements:

- The antenna assembly consisting of the reflector, fabricated of graphite epoxy, and the feedhorn
- The scan mechanism, including momentum compensation devices
- An RF module containing the input and reference switching networks, the mixer-IF preamplifiers, and the Gunn local oscillators
- An electronics module containing the main IF amplifiers, all the post-detection electronics, and the power supplies for the scan and data subsystems
- A power supply module which contains the dc-to-dc converters and regulators for the rest of the instrument

The antenna, scan mechanism, RF module, and sky horn cluster are mounted on a bridge-like platform which is then installed as a preassembled, aligned and calibrated unit on the spacecraft. The electronics and power supply modules are mounted separately and are cabled to the instrument and spacecraft through connectors. Its overall size (refer to Figure 2.2.2.2) can be visualized by noting that the elliptical antenna reflector is approximately 110 cm x 80 cm. Total instrument weight is about 50 kg, its power consumption 60 watts, and its digital data output rate 2 kbs.

On NIMBUS-7, the SMMR scan pattern is forward viewing and scans

equally to either side of the orbital track so the swath is centered on that track. With a sub-satellite velocity of about 6.5 $km \cdot s^{-1}$ and a scan period of 4.096 seconds, overlap coverage is provided at all wavelengths.

To conserve power, the scan is sinusoidal. Part of the time spent at the scan extremeties is utilized for reading the radiometer internal and space horn references. The dwell time of all the SMMR channels are integral multiples of and synchronous with the 0.81 cm channel dwell time of 32 ms. Concurrent dwell time facilities multispectral data analyses on various geometric scales.

Conversion of the raw radiometric readings to microwave brightness temperatures involves correcting for actual antenna patterns, including sidelobe effects, as well as separating out the horizontal and vertical polarization components of each of ten channels of radiometric data. These equations are available from NASA.

2.3 Data Collection Platforms and Platform Location Systems

A third category of instruments connected with the satellite programs are those called data collection, relay, and location systems. In addition to probing the atmosphere with the remote sensors discussed in preceding sections, satellite platforms both on polar-orbiting and geostationary spacecraft provide new opportunities for the collection and relay of standard weather data from sites on the surface of the land or water, from moving platforms such as aircraft or ships, and even from drifting buoys and balloons.

These data collection platforms (DCP's) are coming into increasing use each day in areas of meteorology and hydrology and have also been used by

those in the biological sciences. A data collection platform is simply an automatic measuring device with a radio transmitter to provide contact with the satellite. Sizes and shapes of DCP's vary a good deal but generally, apart from the small antenna that is necessary, their dimensions are no more than those of an average sized suitcase and their weight no more than about 50 kg.

There are four basic types of platforms: self-timed, interrogated, alert and random-access. If location of a drifting platform is required an additional multiple transmission feature or other device is necessary. A typical data collection platform is shown in Figure 2.3.0.1 with a close up of its antenna and solar panel in Figure 2.3.0.2. The type shown in these figures is typical of the fixed land-based platform which sends its 100 bit per second signal for less than 1 minute to one of the geostationary satellites such as GOES, GMS, or METEOSAT.

In the remaining part of this section, we will first discuss the data collection platforms systems operating through the geostationary satellites and then discuss the platform data and location capabilities from the near-polar orbiting satellites.

2.3.1 DCP's for Geostationary Satellites

Because of the coverage of a typical geostationary satellite shown in Figure 2.3.1.1 the satellite can maintain continuous contact with all reporting platforms within approximately 77 degrees of great circle arc from the satellite subpoint on the equator. For this reason, over much of the world geostationary satellites are the primary collection platform for DCP's. Over the polar regions and for special drifting plat-

forms that do not know their own location, polar-orbiting satellites with special capabilities are necessary. A GOES data collection platform is shown in Figure 2.3.1.2. In addition to meteorological data, it can be equipped to obtain hydrological data with a stream flow gauging system and a recording precipitation gauge.

A group wishing to make use of the data collection platform capabilities should contact the operating agency for the geostationary satellite that covers their area of interest. In order in insure that the transmissions from the DCP's do not interfere with other systems, each data collection platform transmitter, timing circuits and other aspects of the engineering must pass special acceptance tests before being connected into the satellite system. In addition, permission to transmit must be obtained from the national agency having authority over radio transmission and communications.

After making these arrangements, the user is generally free to attach whatever type of meteorological, hydrological, or other sensors most appropriate to his purpose. However, the constraint in terms of 100 bits per second is a general one which places a limit on the amount of data which can be transmitted. A few examples of the different applications of data collection platforms make it easier to appreciate their usefulness: (a) standard meteorological observations, (b) environmental monitoring, (c) sea state (See Figure 2.3.1.3 for an example of a moored buoy which monitors sea-state activity, sea temperature as well as standard meteorological parameters), (d) aircraft to satellite data relay (ASDAR), (e) hydrological monitoring. Several publications are available which summarize uses of the data collection platforms connected to geostationary satellites. They include WMO Publication No. 480 and WMO Publication No. 420.

The ASDAR system mentioned above is a new and slightly different application of geostationary DCP's that deserves further discussion. During the Global Weather Experiment in 1979 a few wide-bodied commercial aircraft operating on long-haul routes were equipped with specially designed DCP which extracted details of aircraft position, flight level, air temperature, wind direction and speed from the aircraft's navigation system every 7.5 minutes (Sparkman and Gireytys, 1977). A tape recorder in the ASDAR system stores the data and transmits them for 2 minutes every hour. The last 8 data sets are transmitted. After retransmission to the ground through the geostationary satellite, these data are made available to all meteorological authorities concerned with forecasting for aviation.

The technical report NESS-78 provides detailed background information for those interested in the use of data collection platforms. In this report and in the reports from other satellite agencies, lists of vendors are available who can provide the DCP equipment that has passed the basic approval tests.

When a user places his DCP into operation he receives the data back in one of two ways. The central readout facility of the satellite agency normally collects the data and makes it available either in a digital form suitable for access by the owners' computer or terminal via telephone lines or be in a mail form with the listings or printout of data sent to the user from the central site. A second way to receive data, and also a much quicker way, is to establish connections with a secondary satellite readout station. A typical station is comprised of an antenna as shown in Figure 2.3.1.4 at Colorado State University's Department of Atmospheric Science. This is a 5 meter antenna which also has a capability to readout the ima-

gery as will be discussed in Chapter 3. Even smaller antennas down to approximately 2 meters in size can be used for the data collection platform reception.

At the present time (1982) the cost of a completely equipped secondary satellite receiving station for data collection platform (not necessarily imagery) from the GOES satellites is approximately U.S. $70,000. This should not be confused with the approximate cost of one of the data collection platforms to which one attaches instruments. A basic platform with one or two meteorological or hydrological instruments (and capabilities for the user to add other instruments) costs about U.S. $3,000 - $4,000 in 1982.

2.3.2 Data Recording and Location from Other Satellites

As noted earlier the near-polar orbiting (often sun-synchronous satellites) are required to readout data collection platform information over the polar regions which are out of range for geostationary satellites. In addition, research during the last 10 years has lead to the development of systems on the polar-orbiting satellites (with associated ground processing equipment) which can determine the location of moving or drifting platforms such as balloons or buoys, which do not know their own location.

One of the very first successful tests of the location of a drifting platform was obtained during the EOLE Experiment (Morel and Bandeen, 1973). In the southern hemisphere, balloons were released from launch sites in Argentina and completely circumnavigated the mid-latitudes of the southern hemisphere on several occasions. The balloons were used to obtain wind data at 200 mb for research purposes. During the Global Weather Experiment

an important data source in the southern hemisphere were drifting balloons and drifting buoys. Figure 2.3.2.1 shows the location on 30 May 1979 of the instrumented drifting buoys measuring sea surface temperature and sea level pressure over generally data-void regions of the southern hemisphere.

The RAMS (Random Access Measurement System) on the NIMBUS-6 and the ARGOS system on TIROS-N are two examples of platform location systems for data collection by polar satellites. RAMS on NIMBUS-6 was designed for use by the Tropical Wind Energy conversion and Reference Level Experiment (TWERLE). This experiment used drifting constant level balloons to determine winds, temperatures, and pressure gradients in the upper troposphere in the tropics. An example of the TWERLE balloon system is shown in Figure 2.3.2.2. Both the RAMS and the ARGOS use the differential-Doppler method of determining location of the platforms. The location information is computed by using data obtained from the measurement of the DCP carrier frequency as received on the satellite. When several measurements are received during a given contact (passage of the NIMBUS or TIROS/NOAA satellite within range of the platform) the location can be determined to within 3-5 kilometers. Detection of the Doppler shift (frequency change) of the transmitted frequency from the platform requires that the frequency must remain nearly constant during the time the satellite is receiving signals from the platforms during a single orbit. It is not the platform transmitter frequency itself that needs to be measured so precisely, but the change of the frequency that is due to the relative motion between the satellite and the platform during an orbit. Thus, the oscillator (frequency generator) of the platform must be fairly stable with time. A stable crystal oscillator that was insulated from temperature changes was used on the TWERLE balloon transmitters.

On the present-day NOAA satellites (as first carried out by the TIROS-N) the Data Collection and Location System (DCLS) was designed, built and furnished by the the Centre National D'Etudes Spatiales (CNES) of France. They refer to it as the ARGOS data collection and location system. The ARGOS provides a means for obtaining environmental information and earth location information for fixed or moving platforms. The environmental data messages sent by the platform through the satellite will vary in length depending on the type of platform and its purpose. As in the case of the geostationary satellites, the terrestrial DCP's that transmit to ARGOS must be accepted for entry into the system after meeting certain tests.

By international agreement, use of the ARGOS is limited to platforms requiring location service or for those situated in polar regions out of the range of the data collection system on geostationary satellites. General platform criteria are shown in Table 2.3.2.1. For the ARGOS platform, the data output rate is 720 bits per second. A final note regarding the DCLS (ARGOS) is that the satellite rebroadcasts the data collection platform information over the satellite beacon frequency along with the temperature sounder data (See Section 3.3). Location data is only available in this mode of operation if a special computer for signal processing is available at the small ground readout site. Normally, the ARGOS data is collected from the U.S. satellite by central groundstation facilities and forwarded to CNES for location determination and output processing. A user receives information from platforms of interest provided by CNES. A normal time delay occurs between platform transmission and receipt of data by the user.

References and Suggested Additional Reading:

Allison, L. J. (editor), A. Schnapf, B. C. Diesen III, P. S. Martin, A. Schwalb and W. R. Bandeen, 1980: Meteorological satellites, NASA Technical Memorandum 80704, 71 pp.

Allison, L. J., J. Steranka, G. T. Cherrix and E. Hilsenrath, 1972: Meteorological applications of the NIMBUS-4 temperature-humidity infrared radiometer, 6.7 micron channel data. Bull. Amer. Meteor. Soc., 53, 526-535.

Fleming, R. J., T. M. Kaneshige, W. E. McGovern and T. E. Bryan, 1979: The global weather experiment II. The second special observing period. Bull. Amer. Meteor. Soc., 60, 1316-1322.

Hudson, R. D., 1969: Infrared system engineering, John Wiley and Sons, New York, 642 pp.

Morel, P. and W. Bandeen, 1973: The EOLE experiment: Early results and current objectives, Bull. Amer. Meteor. Soc., 54, 298-306.

NESS (National Environmental Satellite Service, 1979: U. S. Department of Commerce, Geostationary Operational Environmental Satellite/Data Collection System, Washington, DC. NOAA Technical Report NESS-78, 86 pp.

Schwalb, A., 1978: The TIROS-N/NOAA A-G Satellite Series. NOAA Technical Memorandum, NESS-95, 75 pp.

Schwalb, A., 1972: Modified version of the improved TIROS operational satellite (ITOS D-G), NOAA Technical Memorandum NESS-35, 48 pp.

Sparkman, J. and J. Giraytys, 1977: Aircraft to satellite data relay. WMO No. 480. Geneva.

Weiss, C., 1978: Cloud-location corrections near the horizon of an SMS image, NOAA, NWS/NESS Satellite Applications Information Note. 78/8. 8 pp.

Williamson, L. E., 1977: Calibration technology for meteorological satellites, Atmospheric Science Laboratory Report, USAFEC, WSMR, NM, 88002, 139 pp.

World Meteorological Organization, 1975: Publication No. 420, Technical Conference on Automated Meteorological Systems (Teacams) Washington, DC.

World Meteorological Organization, 1977: Publication No. 480, Technical Conference on Instruments and Methods of Observation, Hamburg, FRG.

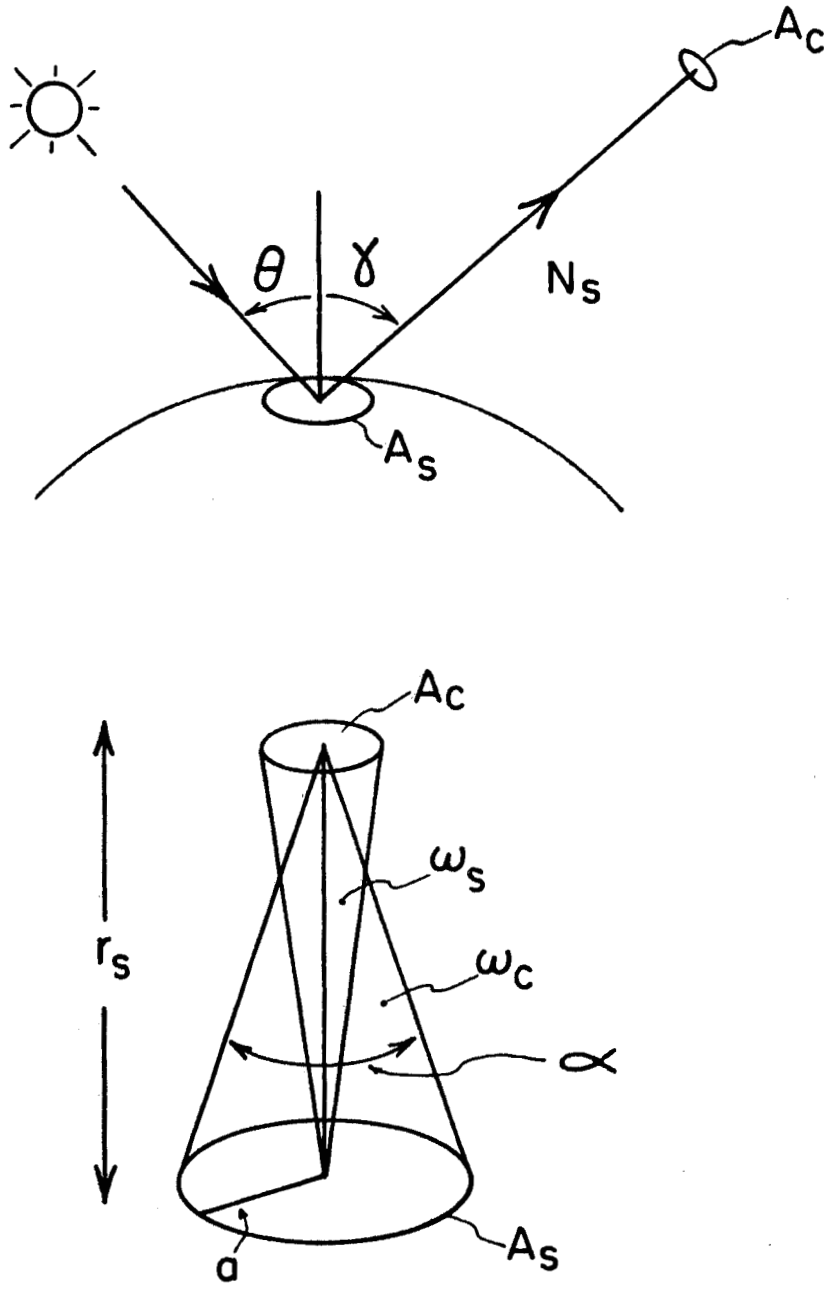

Figure 2.0.1 Viewing Area on Earth as Seen from a Satellite

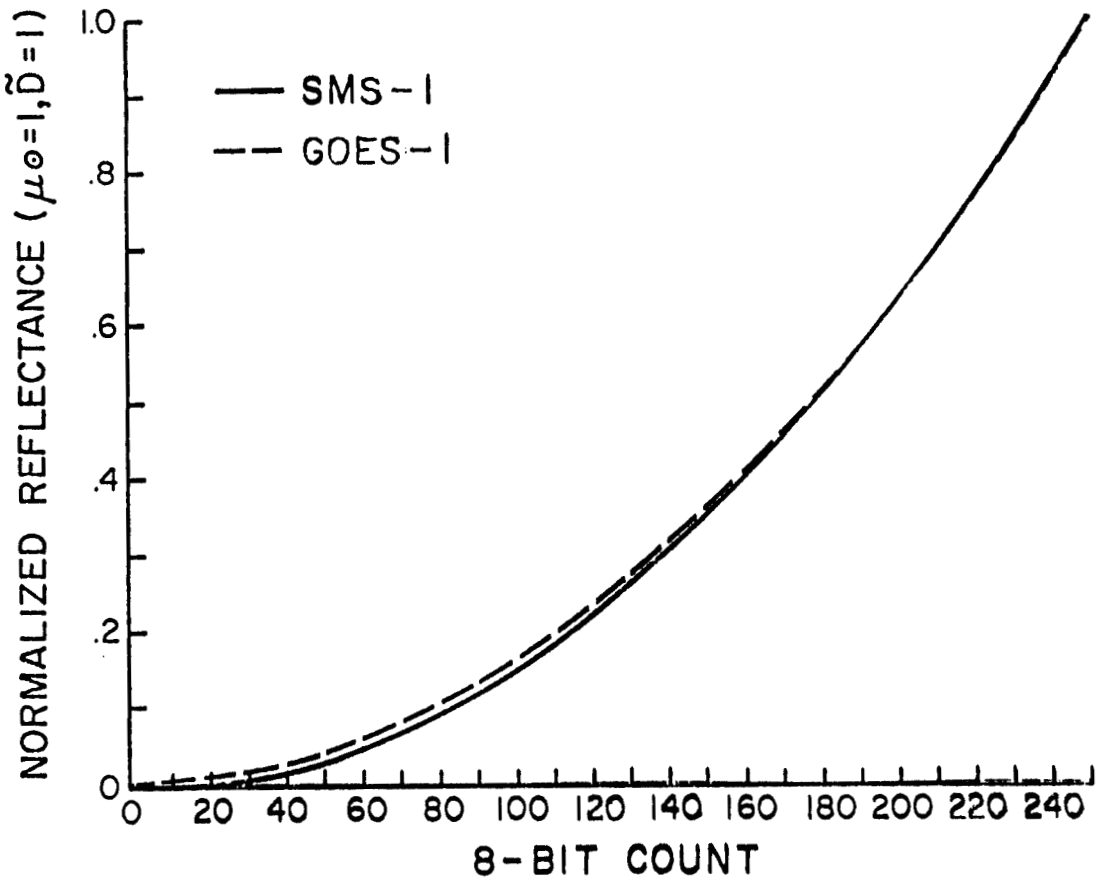

Figure 2.0.2 SMS/GOES Visible Calibration Curves

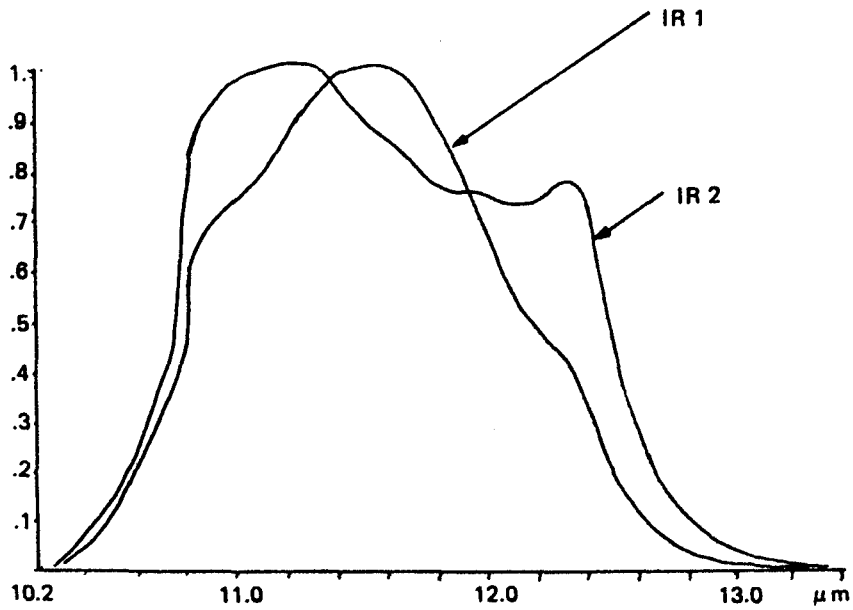

Spectral response of IR Channels.*

Normalised Spectral Response at 90° K

μm	IR1	IR2
10.0	0	0
10.13	0	0
10.26	0	0
10.39	.056	.073
10.53	.144	.188
10.76	.415	.554
10.81	.620	.830
10.96	.718	.963
11.11	.791	.994
11.27	.920	1.000
11.43	.999	.921
11.59	1.000	.856
11.76	.903	.768
11.94	.717	.742
12.12	.524	.727
12.31	.404	.765
12.5	.189	.431
12.7	.056	.147
12.9	.017	.045
13.11	.005	.013
13.33	.000	0

NOTE: The values of spectral response given on this page correspond to data from Meteosat-1. Response from Meteosat-2 is not exactly the same, and is specified in the Meteosat System Guide, Volume 6, Annex B1.

Figure 2.0.3 Spectral Response of Two METEOSAT Infrared Channels (ESA, 1981)

TIROS-N Spacecraft

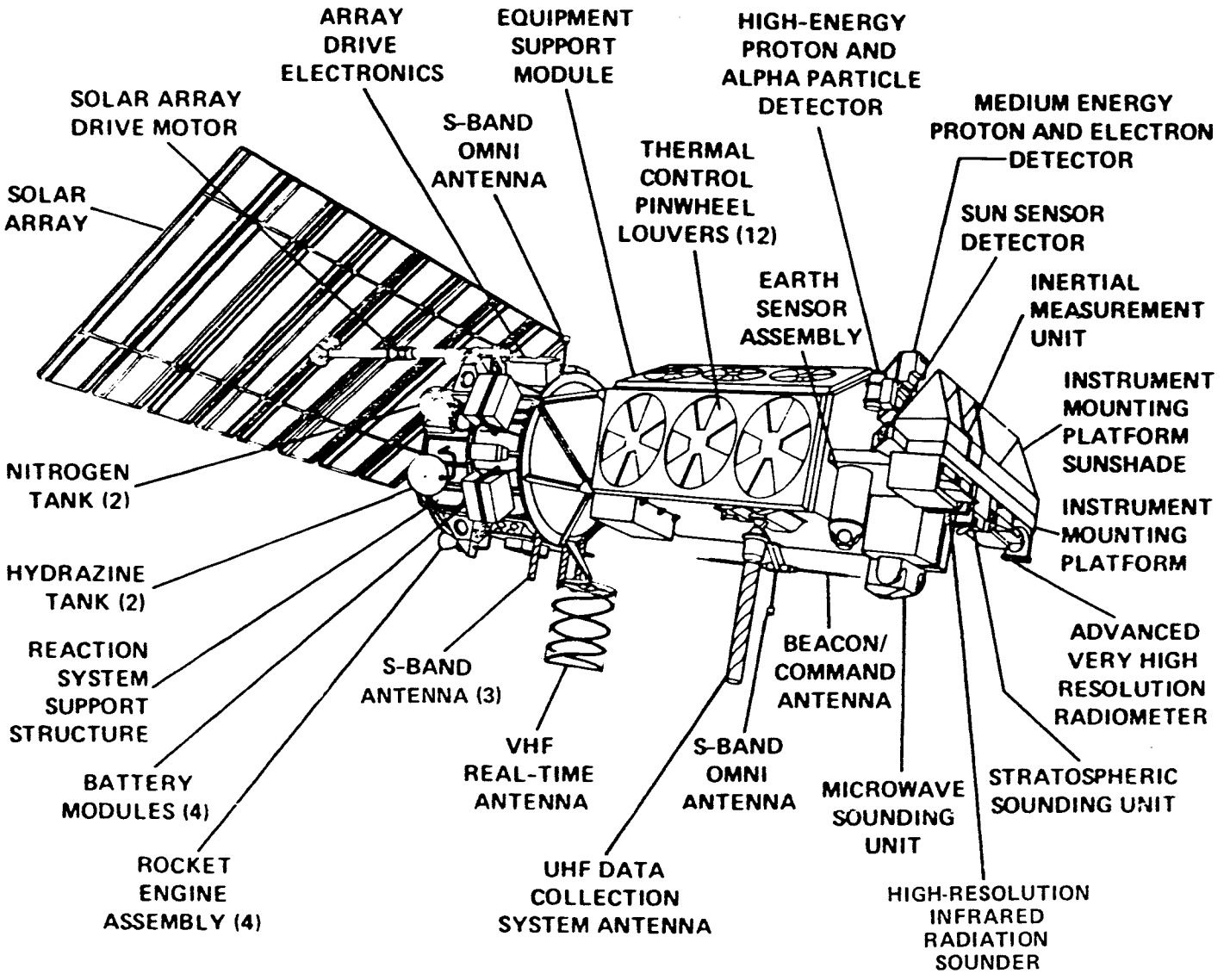

Figure 2.0.4 TIROS-N Spacecraft (Slide Set #22) (Schwalb, 1978)

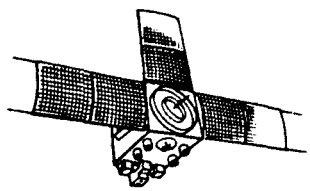

ITOS 1, NOAA 1

Payload

- 2 APT TV Cameras
- 2 AVCS TV Cameras
- 2 Scanning Radiometers
- 1 Flat Plate Radiometer
- 1 Solar Proton Monitor

3-Axis Momentum Bias Stabilization

Mission

- Global Daytime Direct Readout
- Global Daytime Stored Data
- Day & Night VIS and IR Direct and Remote Data
- Heat Budget Data
- Electron, Proton Data

ITOS-1 launched 1/23/70

NOAA-1 launched 12/11/70

ITOS-B Launch Vehicle Failure

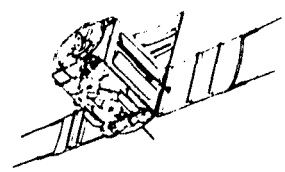

NOAA 2, 3, 4, 5

Payload

- 2 Scanning Radiometers
- 2 Very High Resolution Radiometers
- 2 Vertical Temperature Profile Radiometers
- 1 Solar Proton Monitor

Mission

- Global Visible and IR Imaging
- Medium Resolution - Real Time and Remote
- High Resolution - Real Time and Limited Remote
- Temperature Sounding Real Time and Stored Global
- Electron and Proton Flux Data

NOAA 2 - 10/15/72

NOAA 3 - 11/6/73

ITOS E Launch Vehicle Failure

NOAA 4 - 11/15/74

NOAA 5 - 7/29/76

Figure 2.0.5 ITOS/NOAA Improved TIROS Operational System, 1970-1978 (NASA, 1982a)

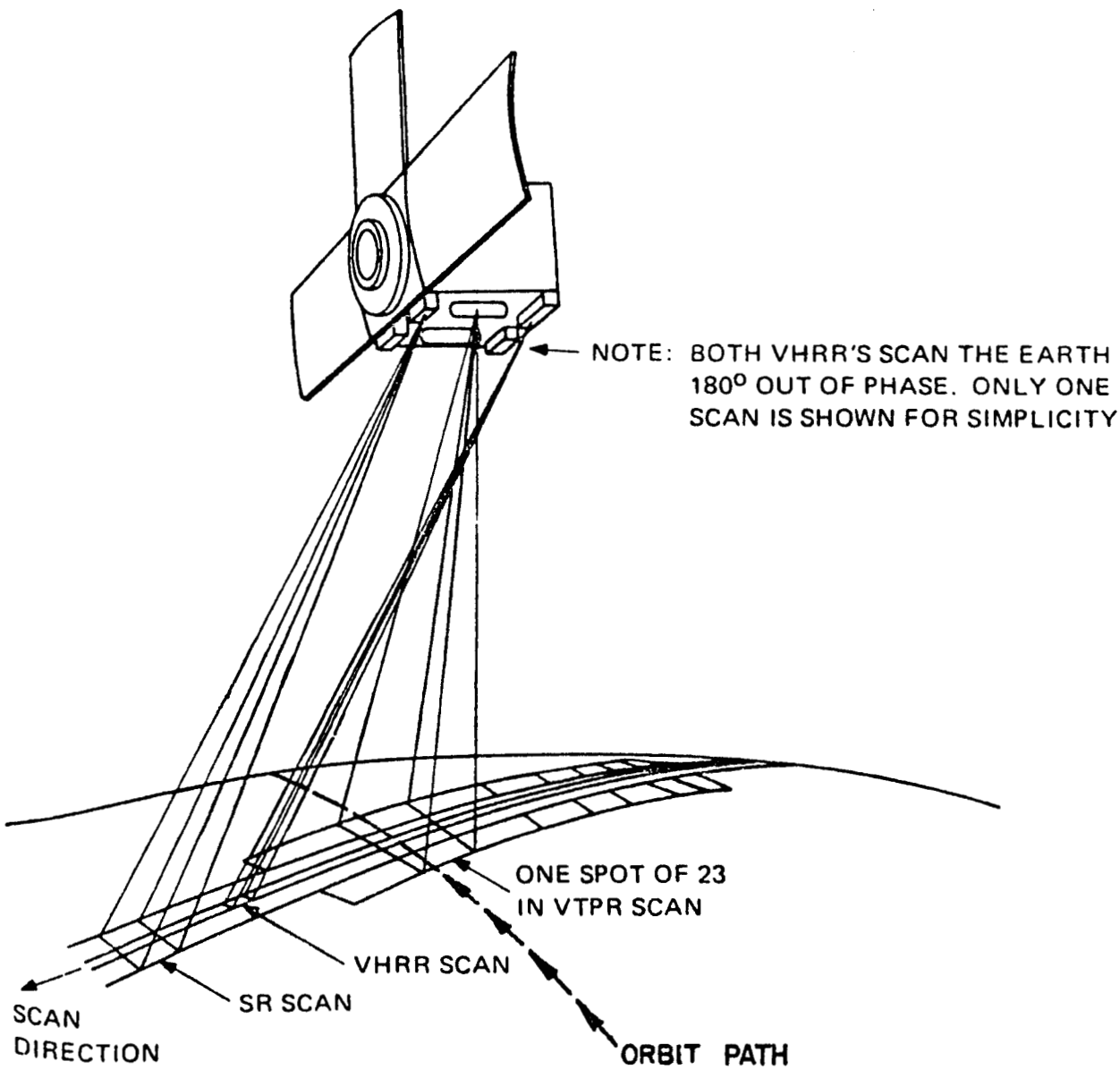

Figure 2.1.1 Scanning of Sensors Perpendicular to Orbit Path (Schwalb, 1972)

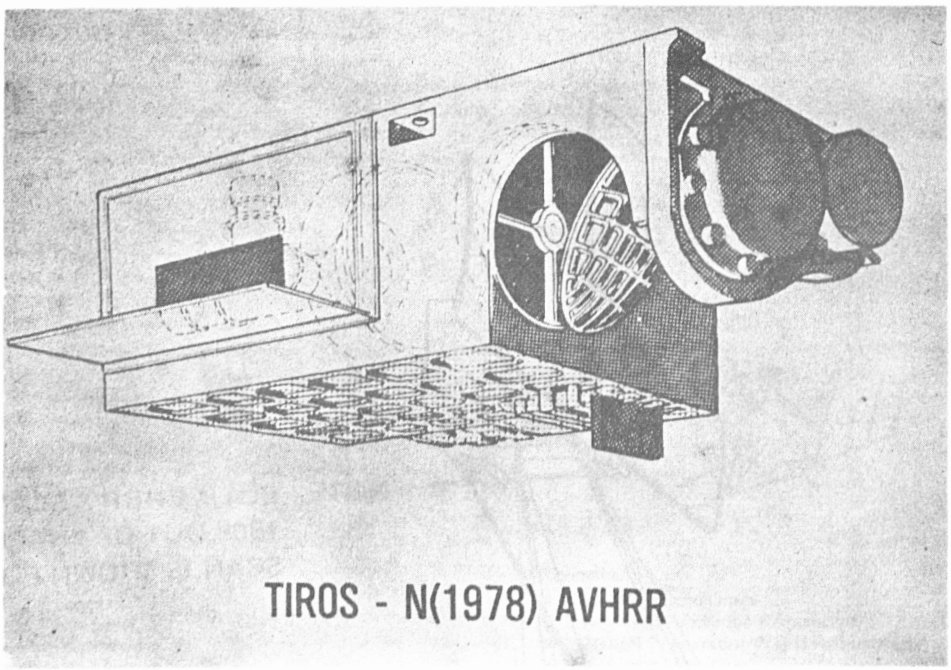

Figure 2.1.2 TIROS-N Advanced Very High Resolution Radiometer (AVHRR) (Slide Set #21)

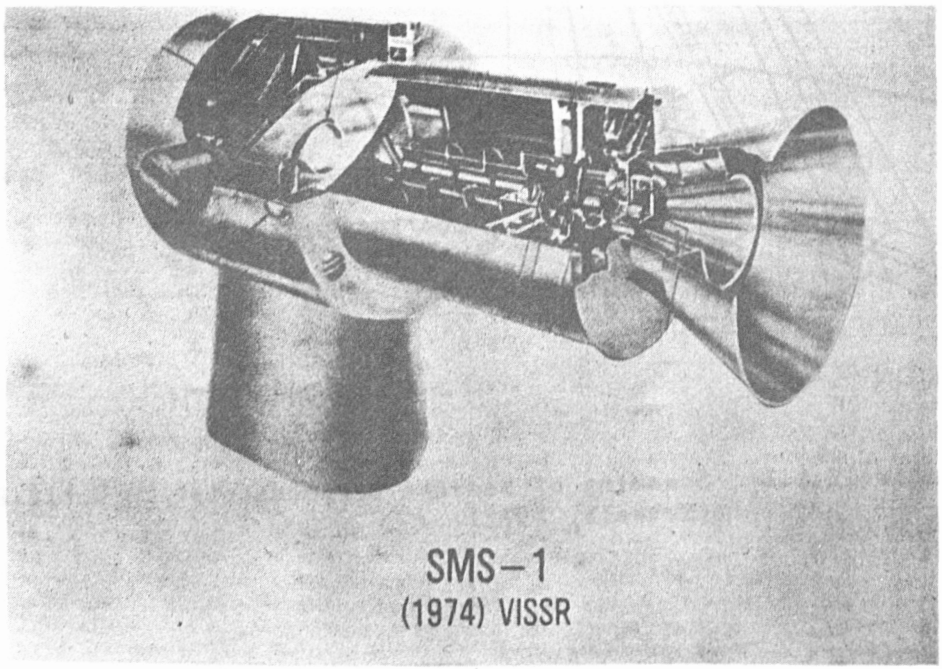

Figure 2.1.3 SMS-1 VISSR (Slide Set #24)

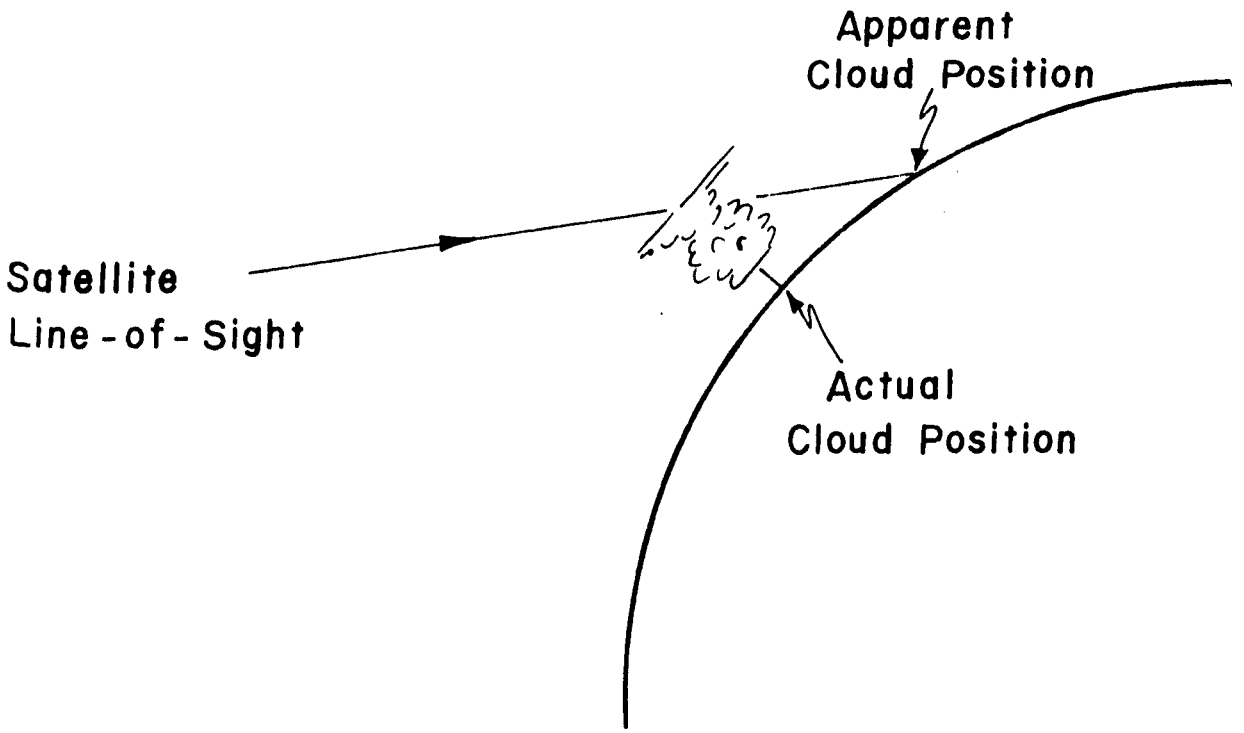

Figure 2.1.4 Actual vs. Apparent Cloud Location (Weiss, 1977)

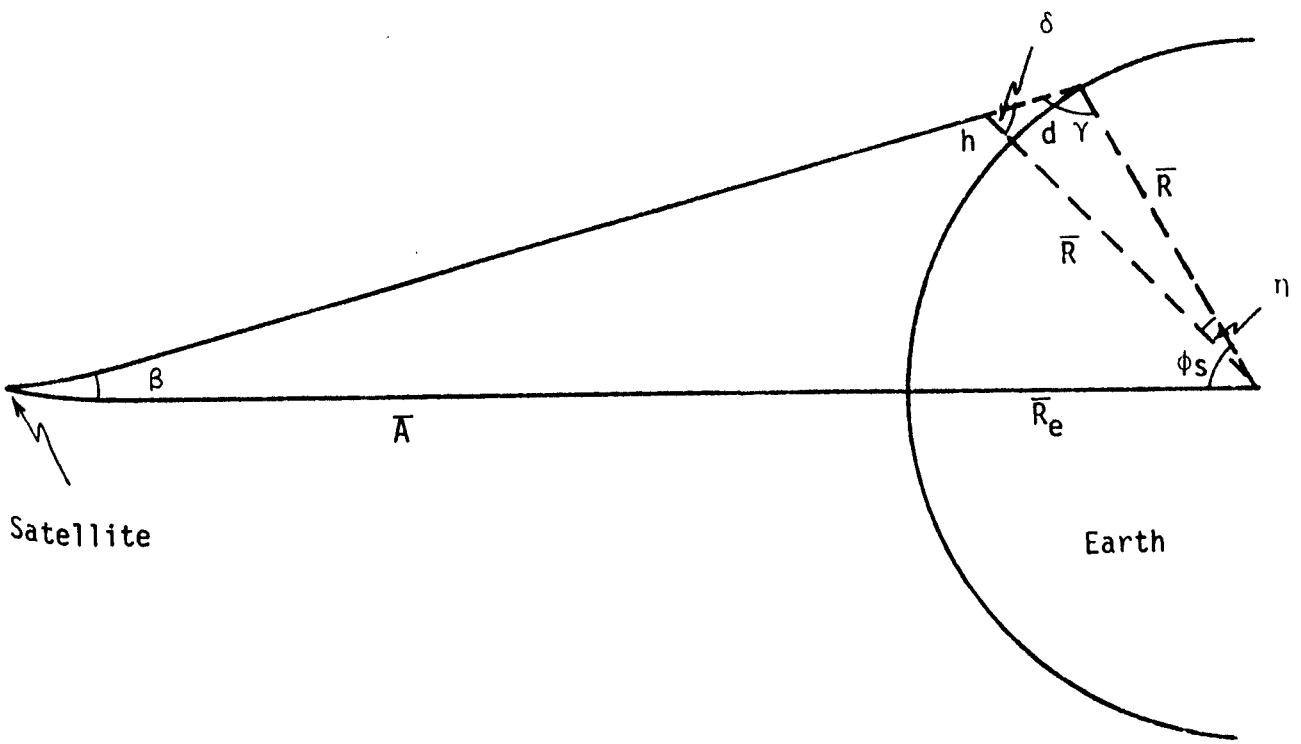

Figure 2.1.5 Geometry for Cloud Location Corrections (Weiss, 1977)

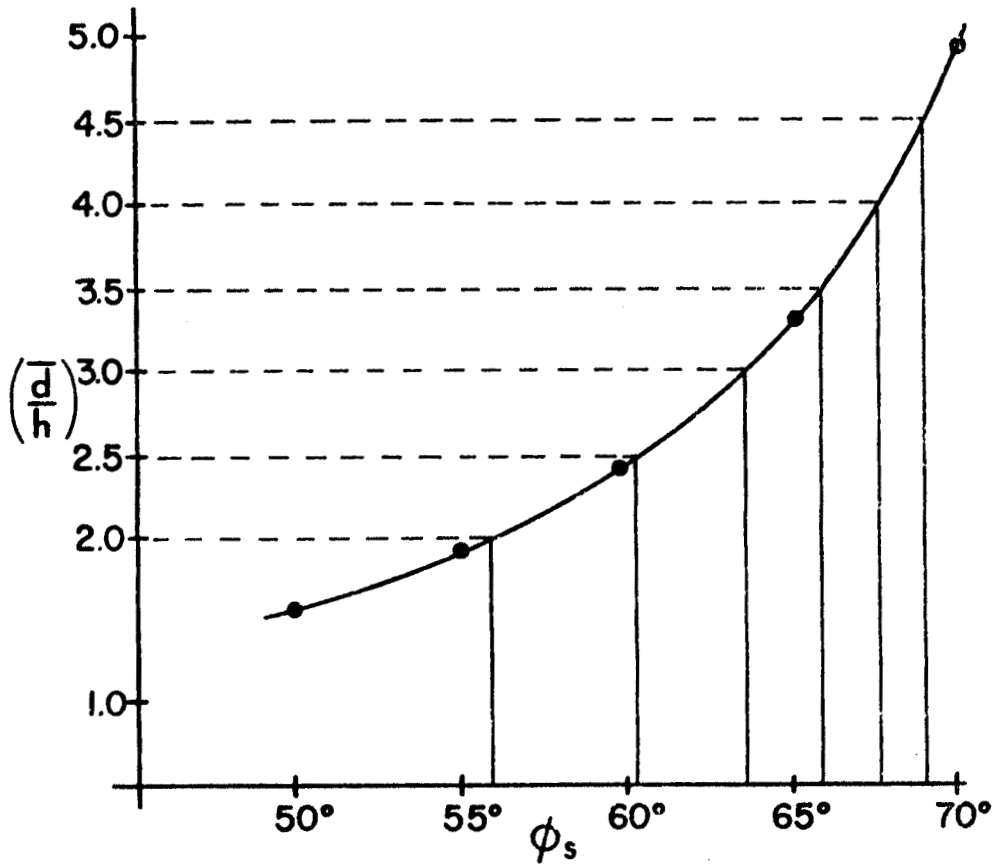

Figure 2.1.6 Graph of Mean Correction Coefficients (Weiss, 1977)

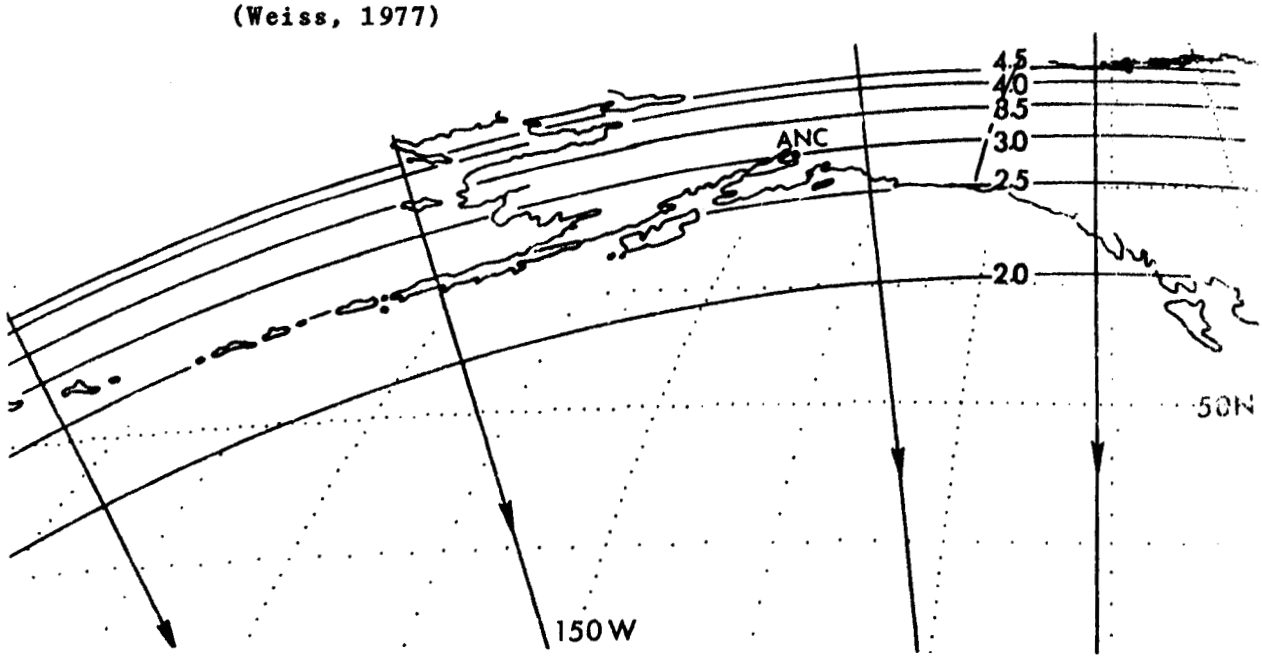

Figure 2.1.7 Plot of Mean Correction Coefficients (Weiss, 1977)

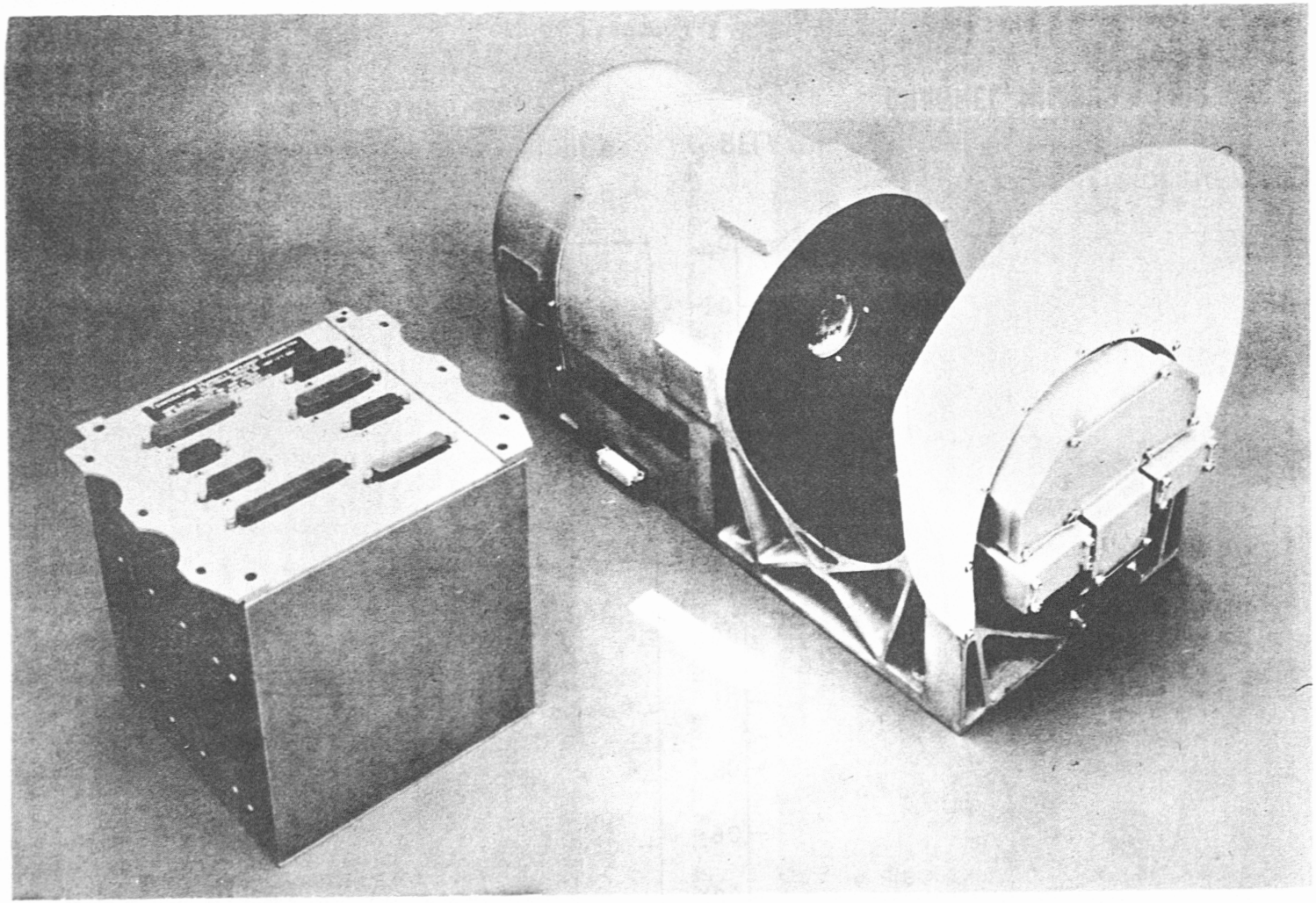

Figure 2.2.1.1 **NIMBUS G (1978)**

Temperature - Humidity Infrared Radiometer (THIR)

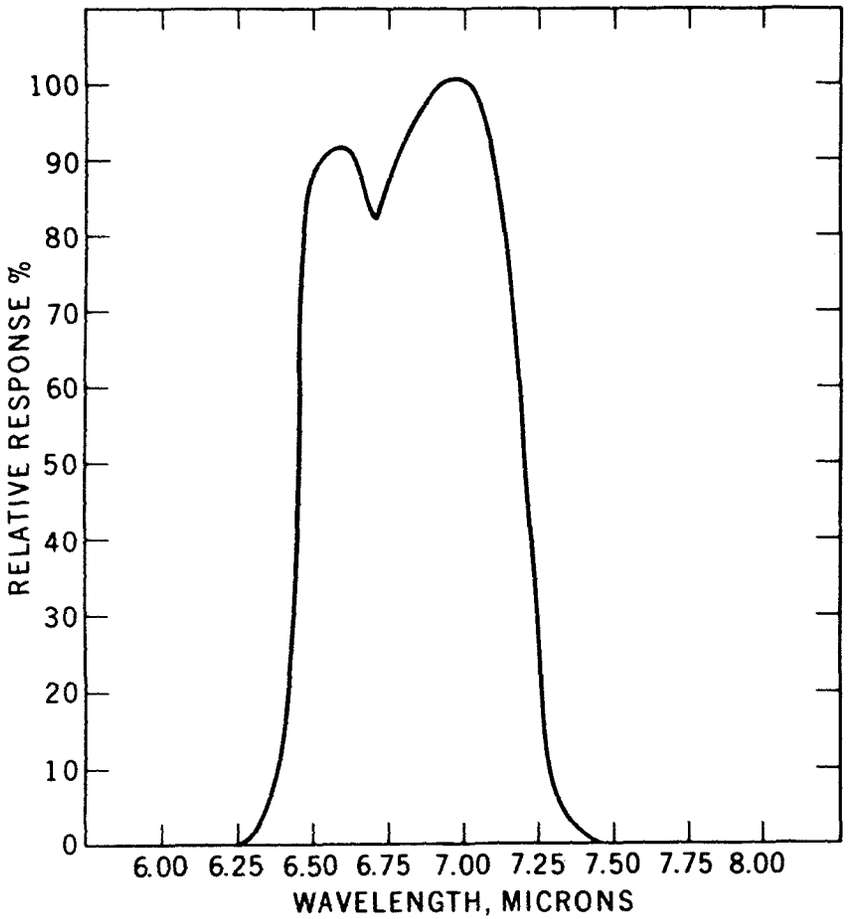

RELATIVE SPECTRAL RESPONSE OF THE 6.7 MICRON CHANNEL, NIMBUS 4 THIR

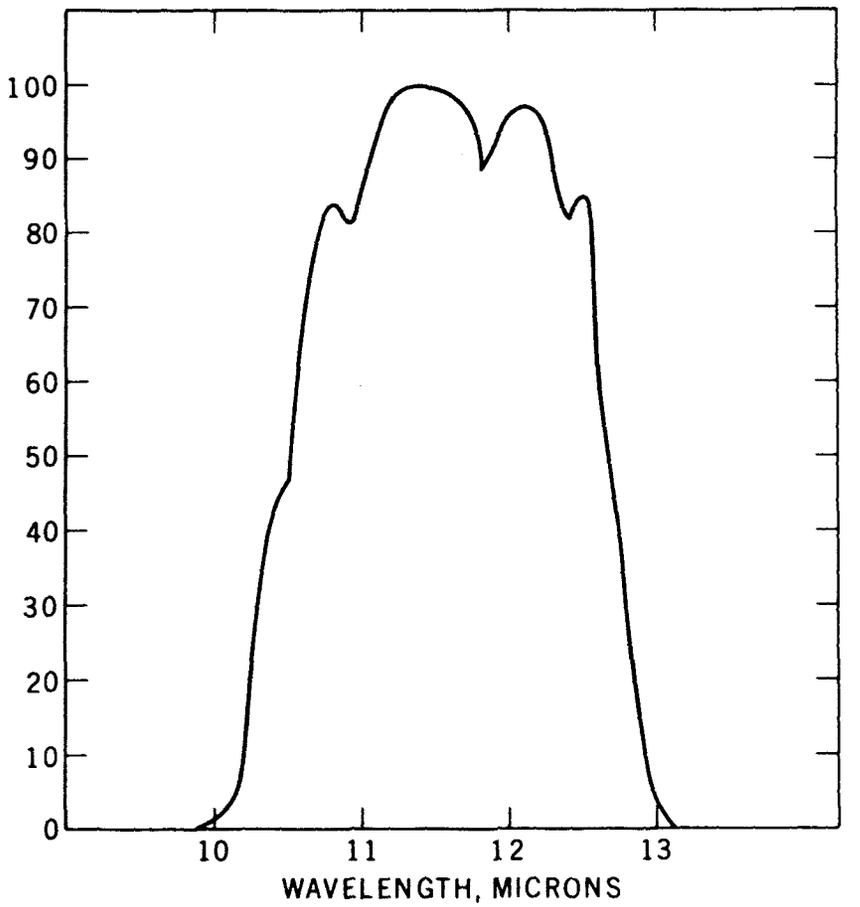

RELATIVE SPECTRAL RESPONSE OF THE 11.5 MICRON CHANNEL, NIMBUS 4 THIR

Figure 2.2.1.2

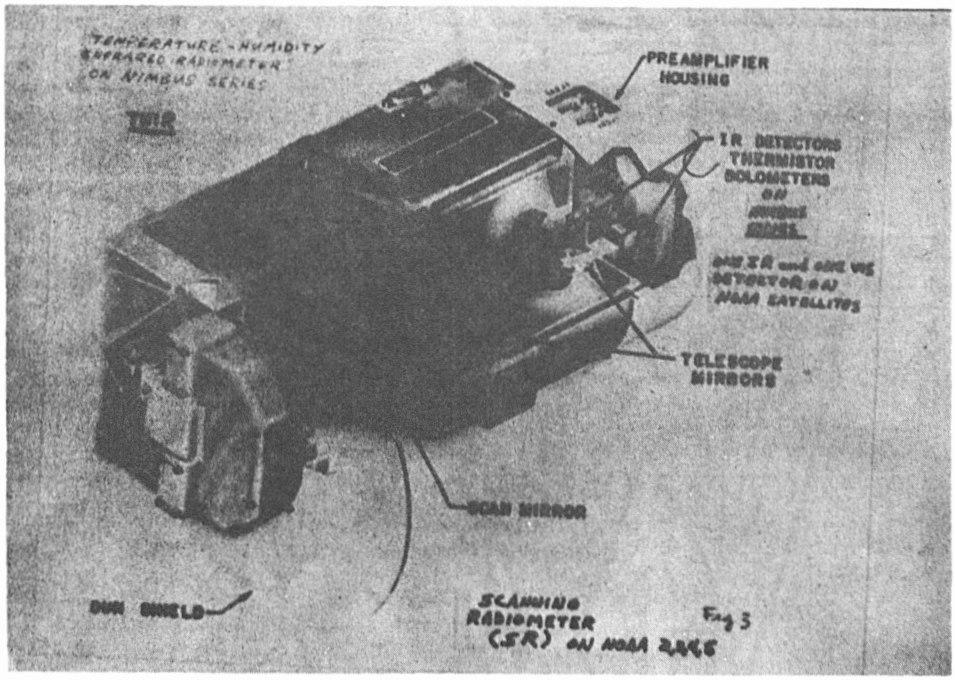

Figure 2.2.1.3 NIMBUS THIR Instrument (Slide Set #26)

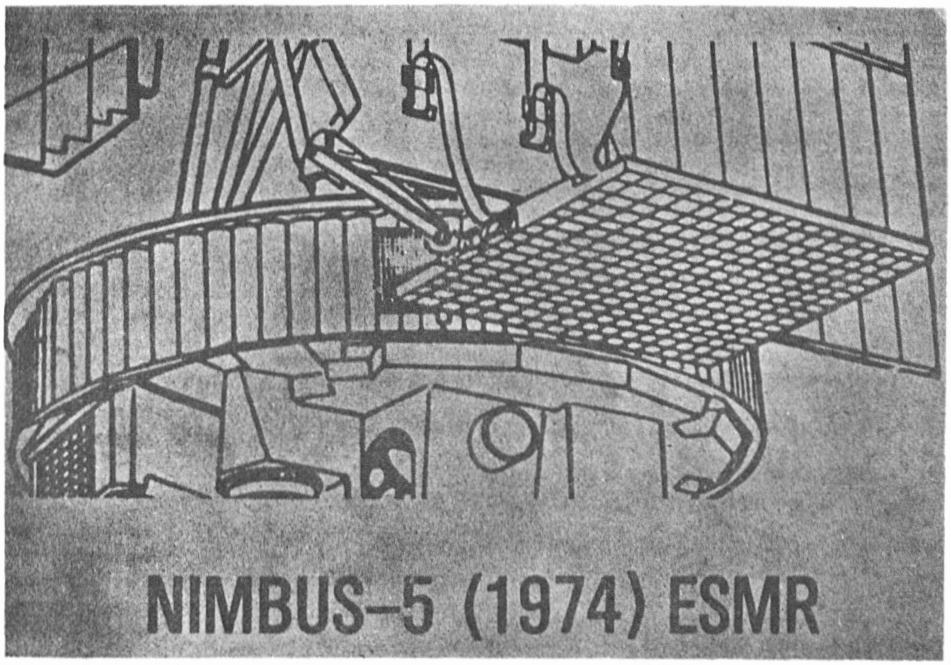

Figure 2.2.2.1 NIMBUS-5 ESMR Antenna (Slide Set #28)

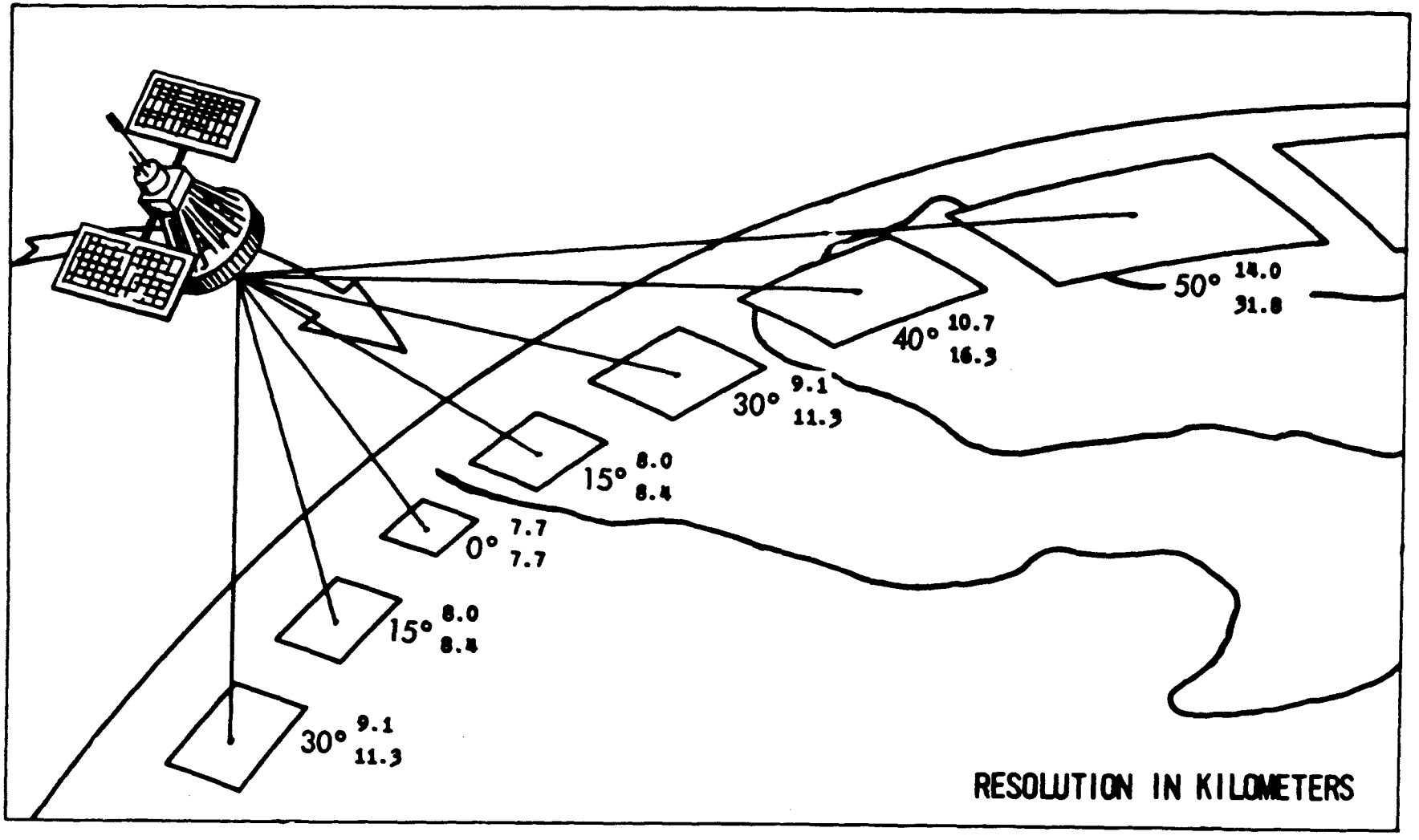

Figure 2.2.1.4 Ground Resolution of NIMBUS-5 THIR (NIMBUS-5, 1972)

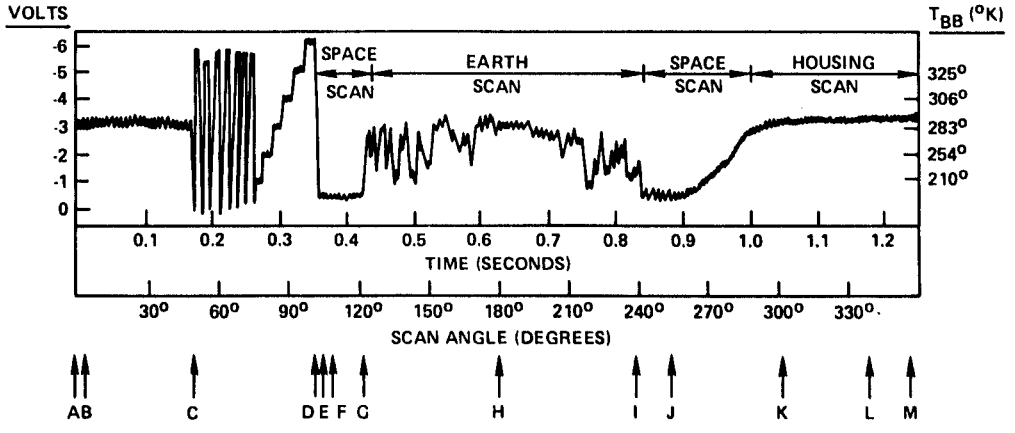

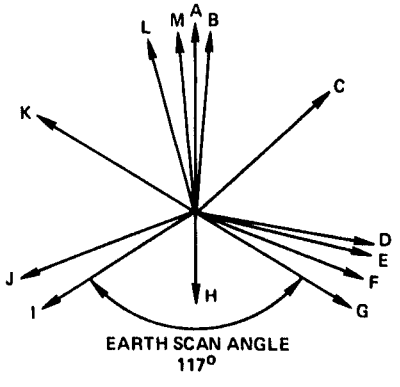

LEGEND

REFERENCE LETTER	ANGLE (DEGREES)	TIME (MSEC)	EVENT
A:	0°	0	SPACECRAFT ZENITH
B:	5°	17.4	RADIOMETER IFOV JUST STARTING TO LEAVE HOUSING.
C:	48°	166.7	SCAN MIRROR POSITION PIP NO. 1 OCCURS AND RADIOMETER SYNC WORD AND CALIBRATION SIGNAL SEQUENCE IS STARTED. 6.7 MICRON CHANNEL GAIN RETURNED TO NORMAL.
D:	100°	347.5	RADIOMETER IFOV JUST STARTING TO SEE ALL OF SPACE.
E:	103.5°	359.4	CALIBRATE SIGNAL SEQUENCE ENDS AND RESTORE PERIOD STARTS.
F:	110.7°	384.4	RESTORE PERIOD ENDS
G:	121.5°	422.2	EARTH SCAN PERIOD BEGINS (600-NMI ORIBT)
H:	180°	625.0	SPACECRAFT NADIR
I:	238.5°	828.8	EARTH SCAN PERIOD ENDS (600-NMI ORBIT)
J:	250°	868.9	RADIOMETER IFOV JUST STARTING TO SEE HOUSING
K:	302°	1048.5	SCAN MIRROR POSITION PIP NO. 2 OCCURS AND 6.7 MICRON CHANNEL GAIN IS ATTENUATED BY A FACTOR OF 3.
L:	345°	1197.9	RADIOMETER IFOV COMPLETELY FILLED BY HOUSING
M:	355°	1232.6	RADIOMETER Z-AXIS

Figure 2.2.1.5 **NIMBUS 5 THIR (11μm) SCAN SEQUENCE**

NIMBUS 4 THIR (11μm) CALIBRATION CURVE

(AT 293°K, HOUSING TEMP.)

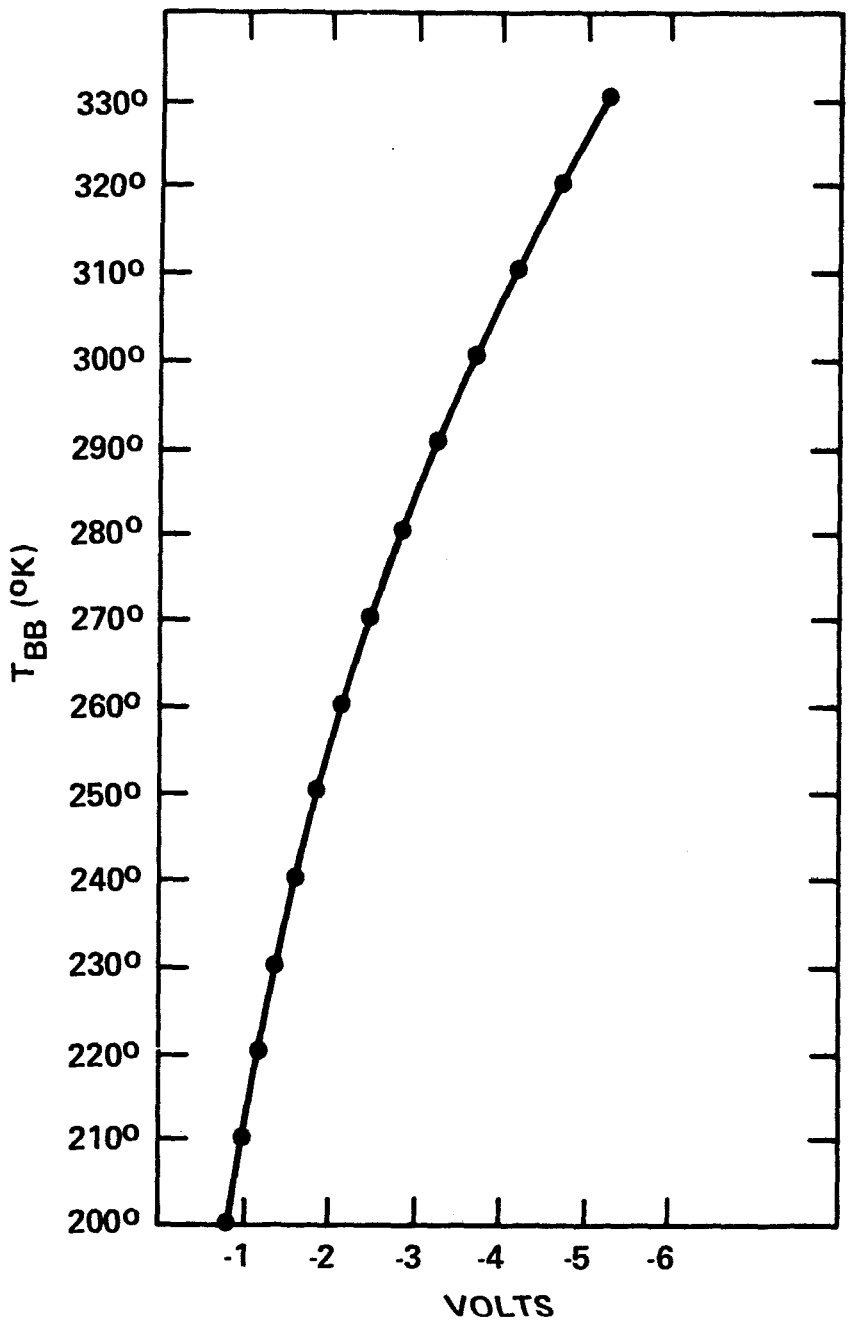

Figure 2.2.1.6

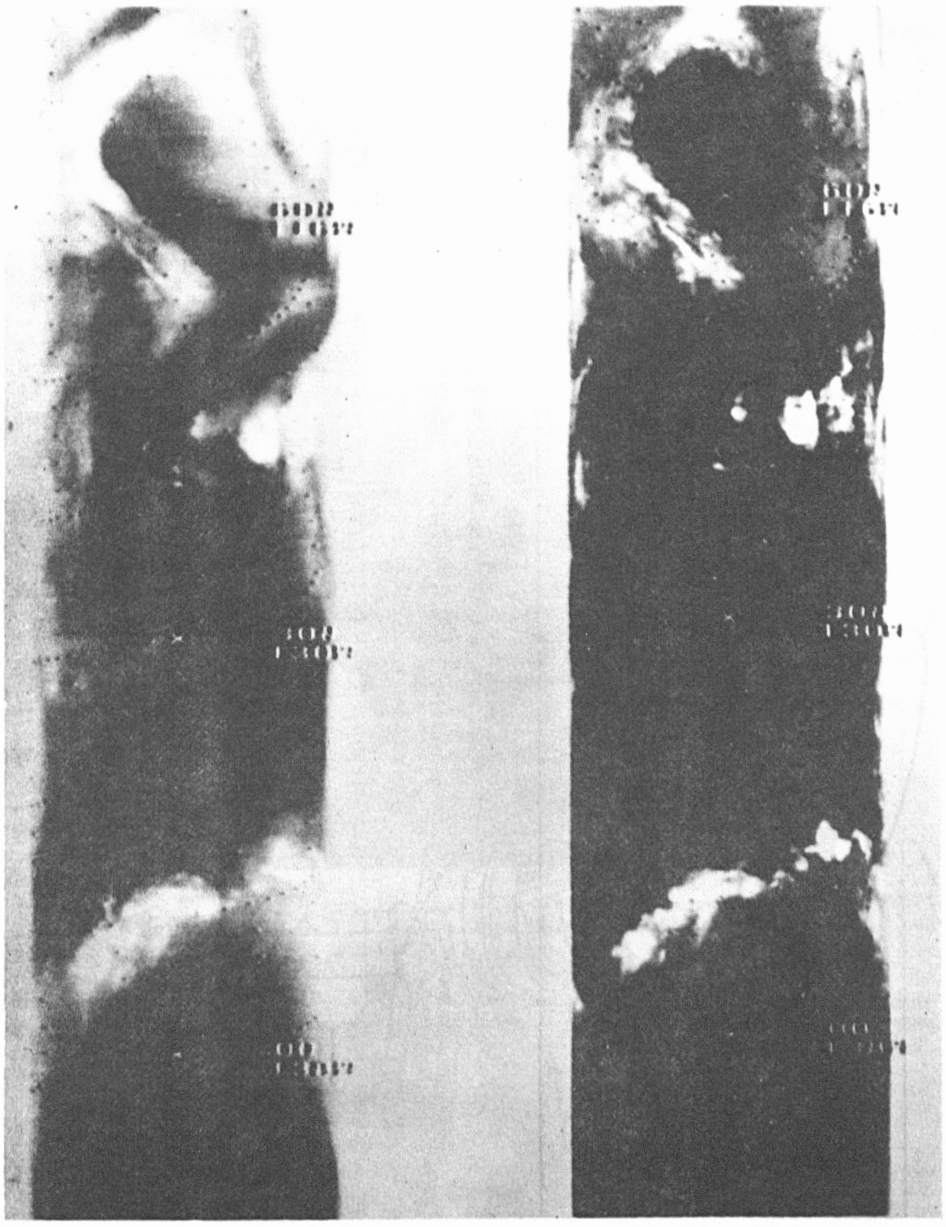

6.7μm 11.5μm

NIMBUS 4 THIR
30 AUGUST 1970
ORBIT 1934(N)

Figure 2.2.1.7

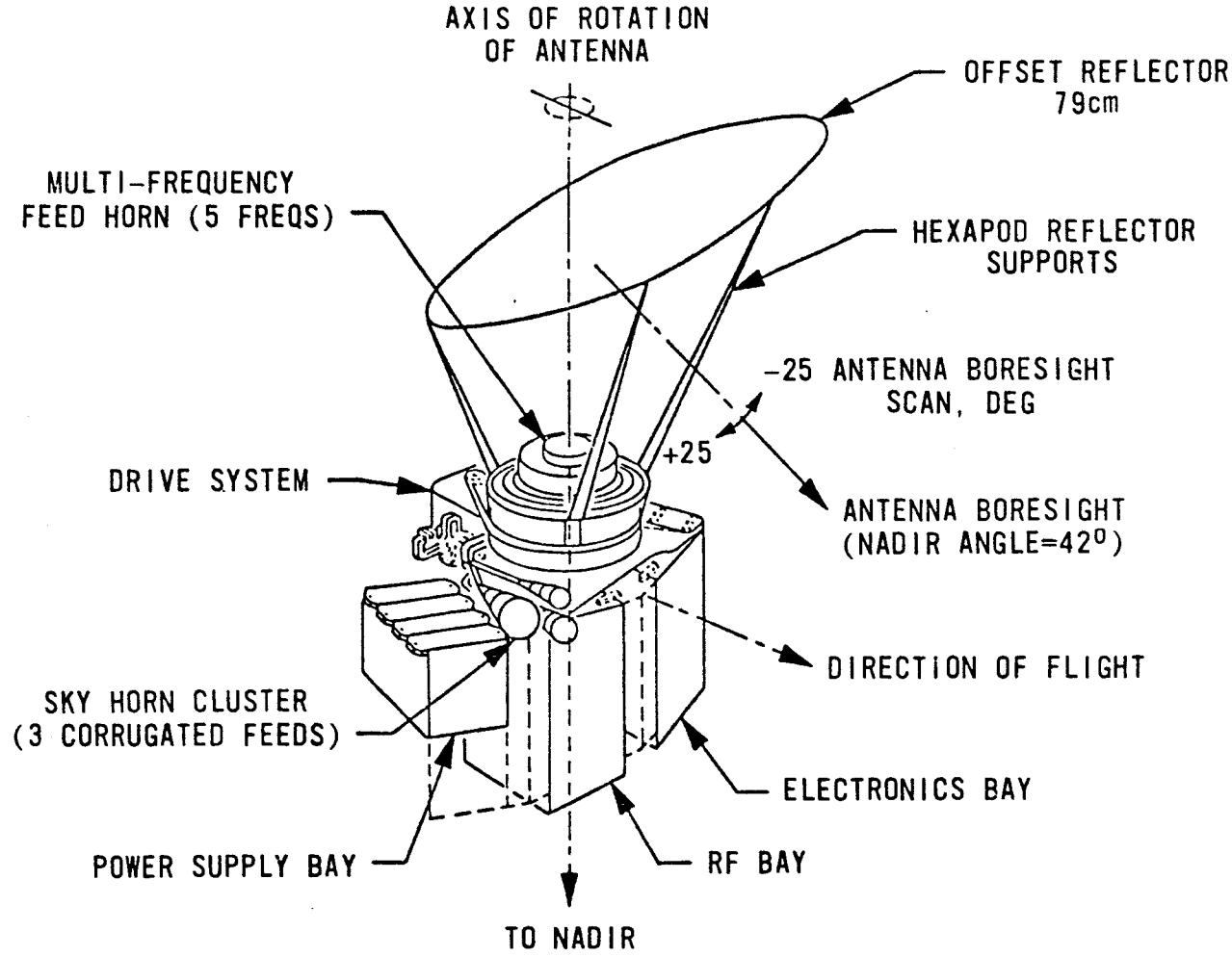

Figure 2.2.2.2 NIMBUS-7 SMMR Instrument Configuration (NIMBUS-7, 1978)

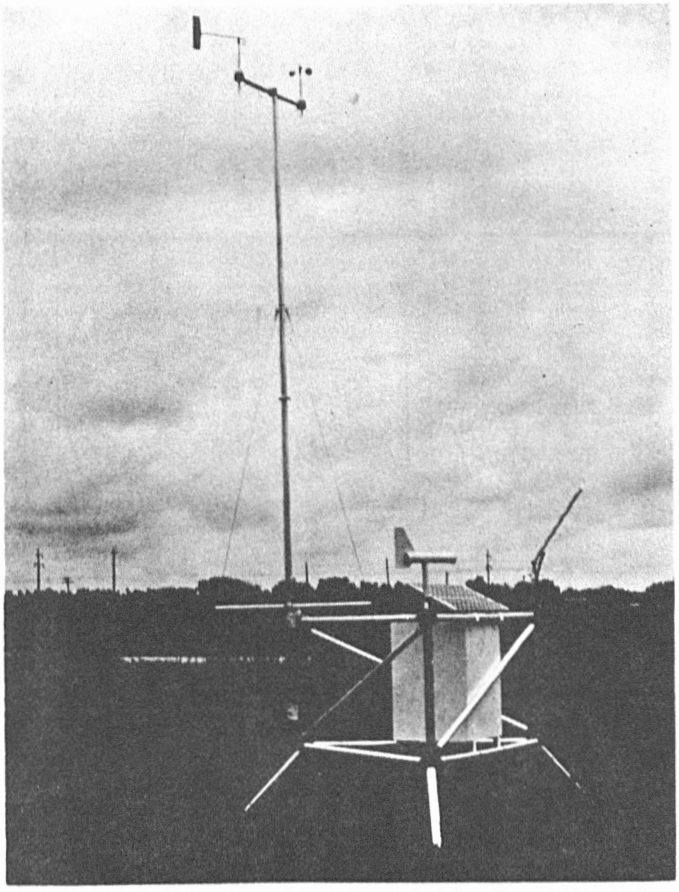

Figure 2.3.0.1 Data Collection Platform (DCP)
(Slide Set #32)

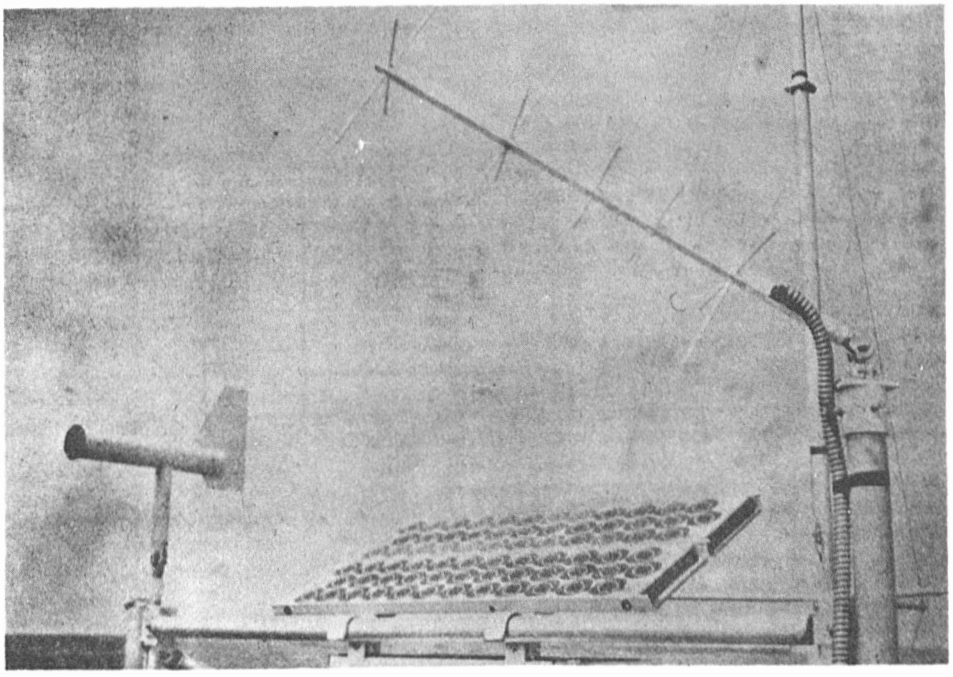

Figure 2.3.0.2 DCP Antenna and Solar Panel
(Slide Set #31)

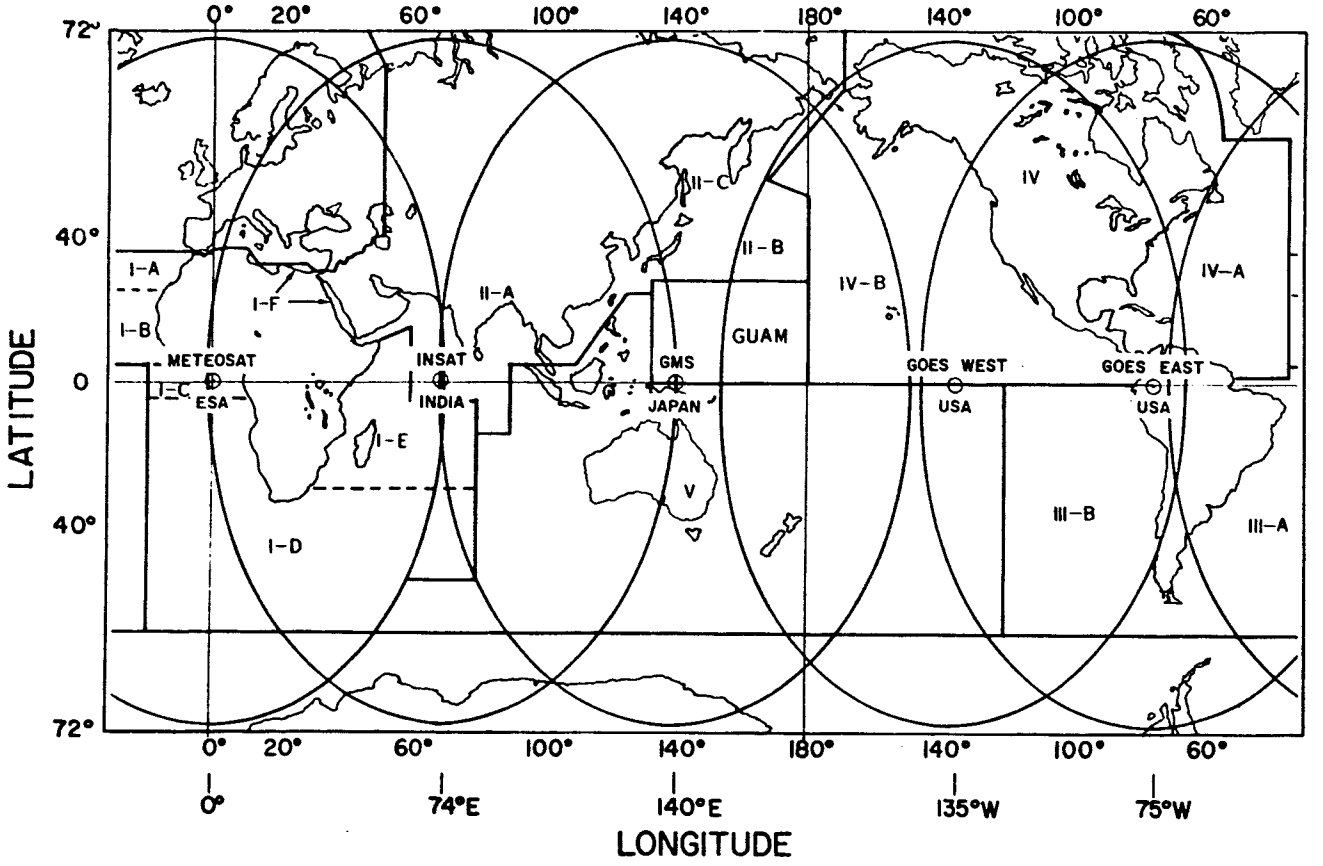

Figure 2.3.1.1 Geostationary Satellite Coverage as of early 1982 (NASA, 1982b)

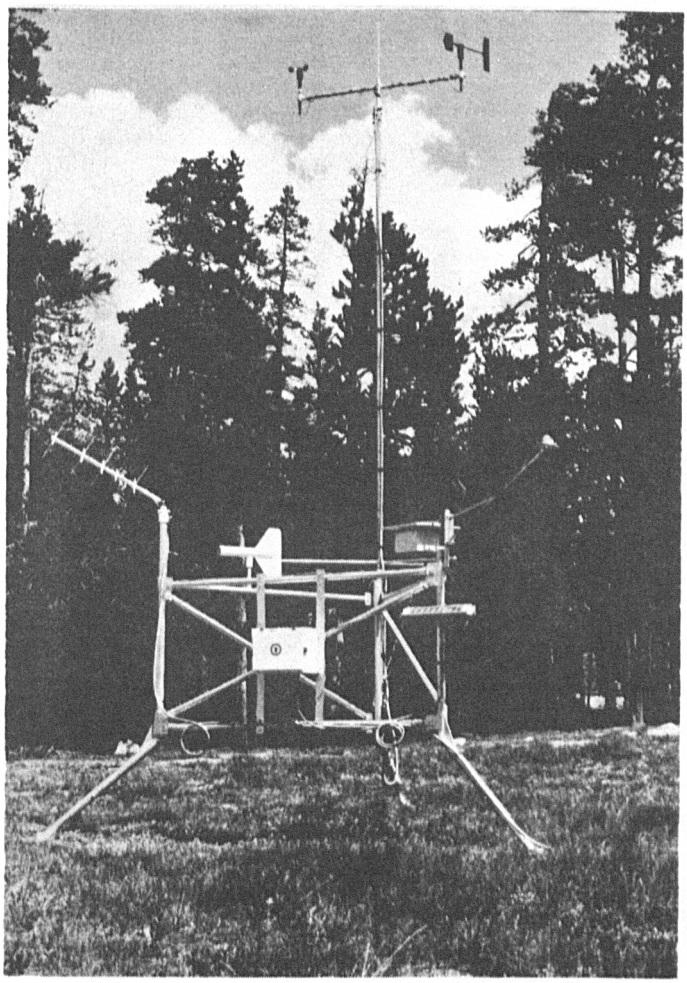

Figure 2.3.1.2 GOES DCP

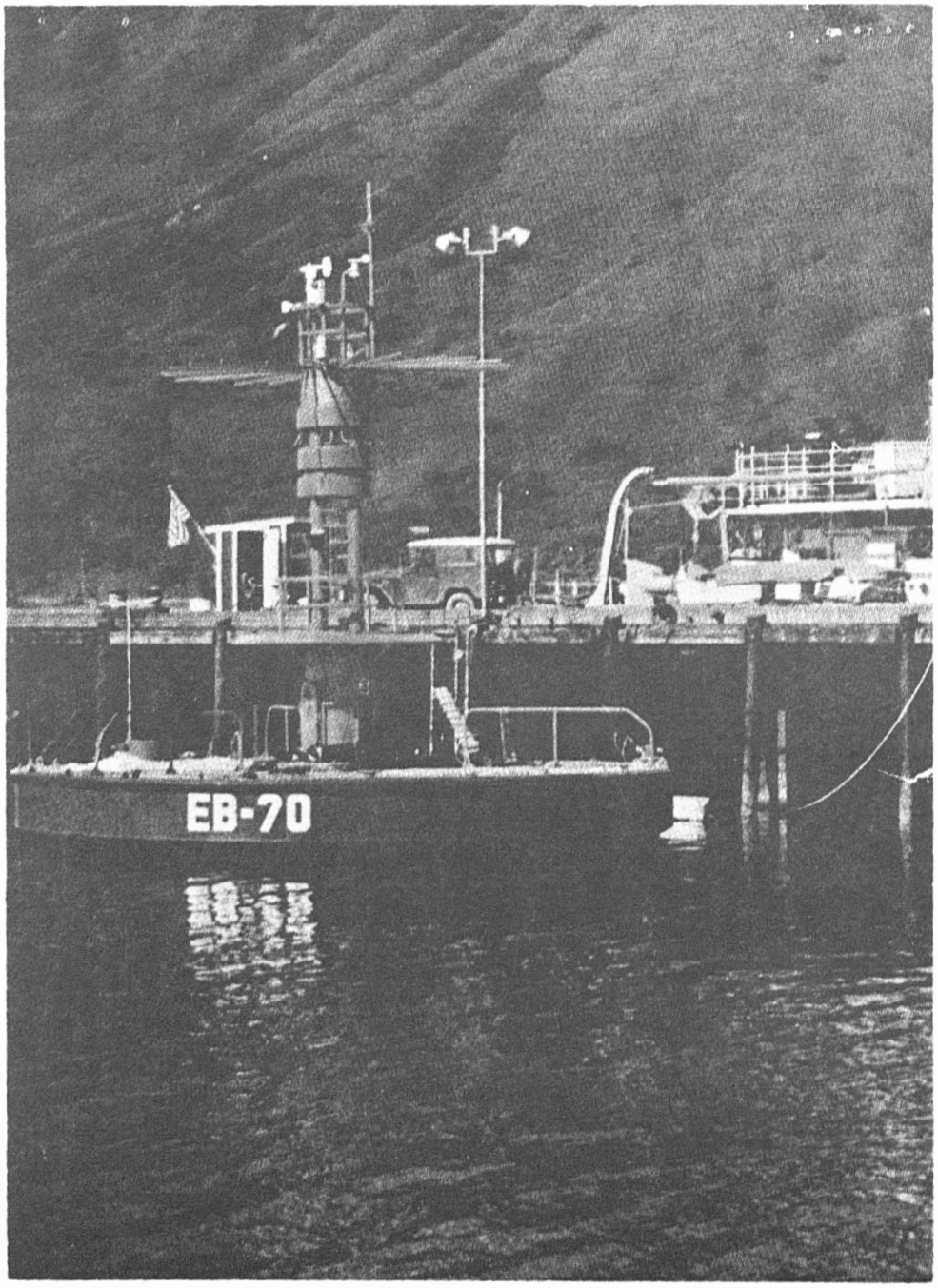

Figure 2.3.1.3 Moored Buoy DCP

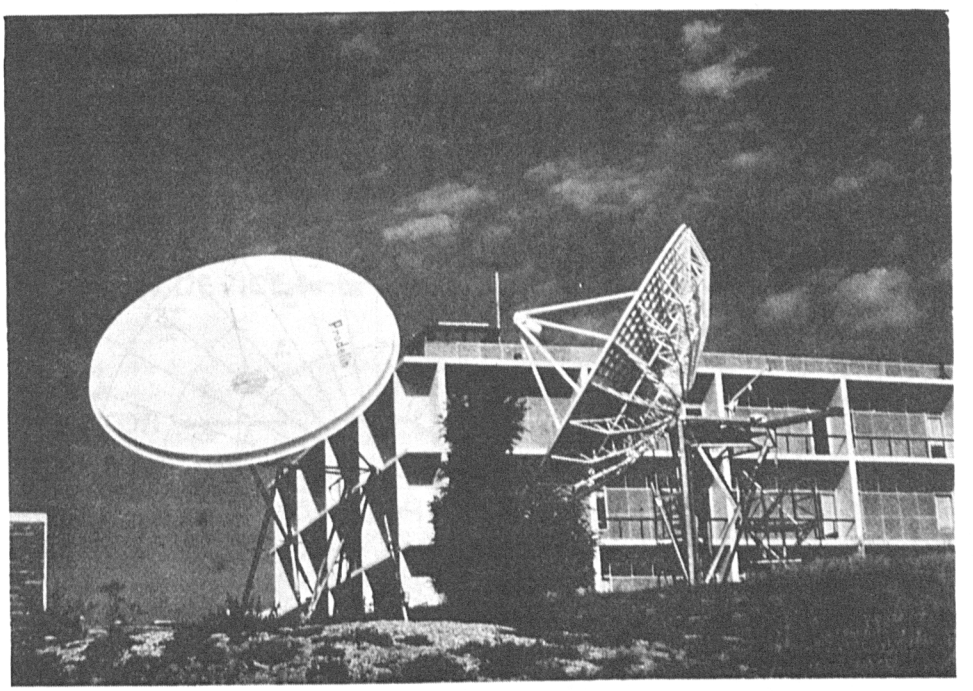

Figure 2.3.1.4 CSU's Department of Atmospheric Science Antenna Systems (5 and 10 meters) (Slide Set #36)

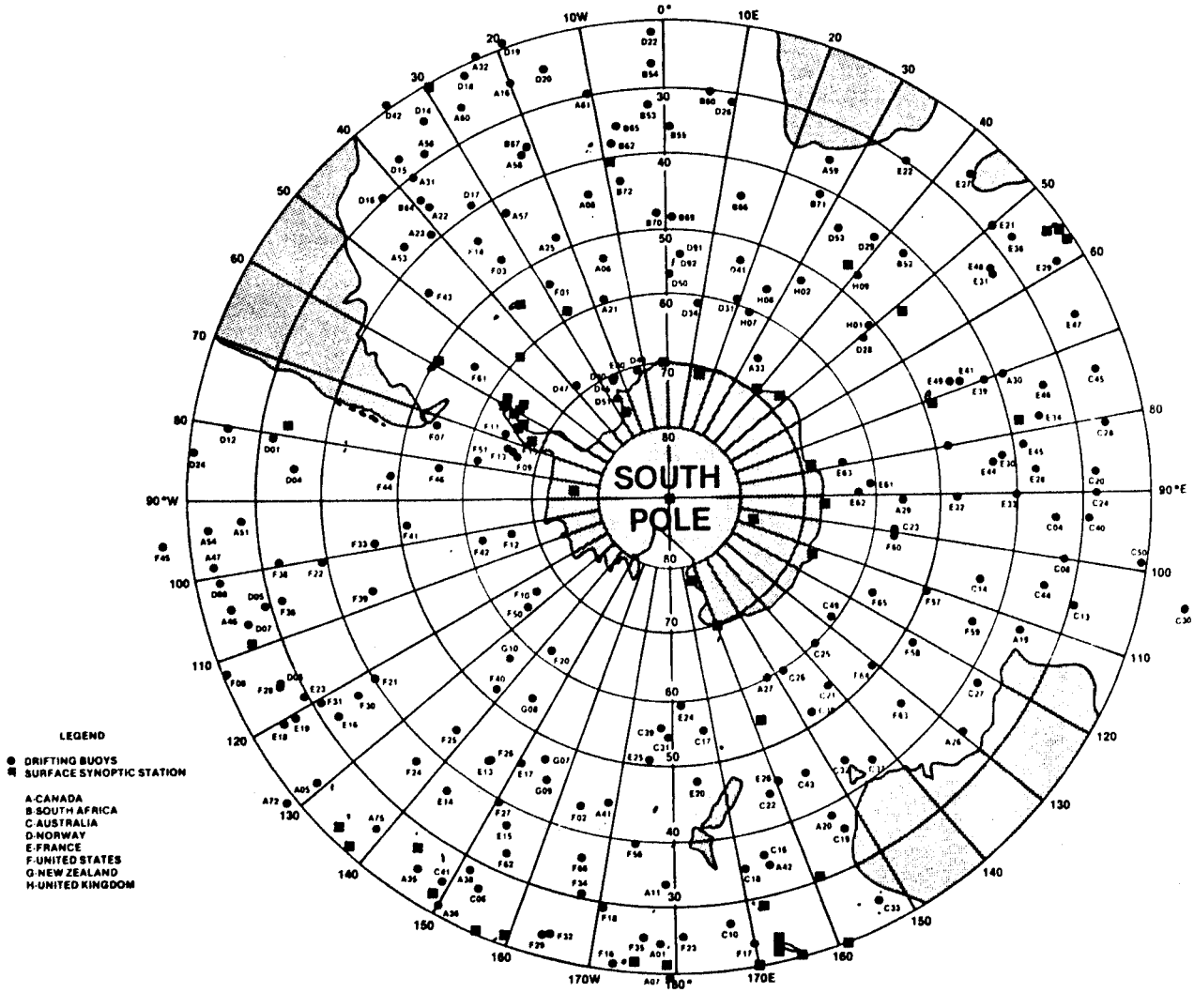

Figure 2.3.2.1 Location of Instrumented Drifting Buoys on 30 May 1979 (Fleming, et al., 1979)

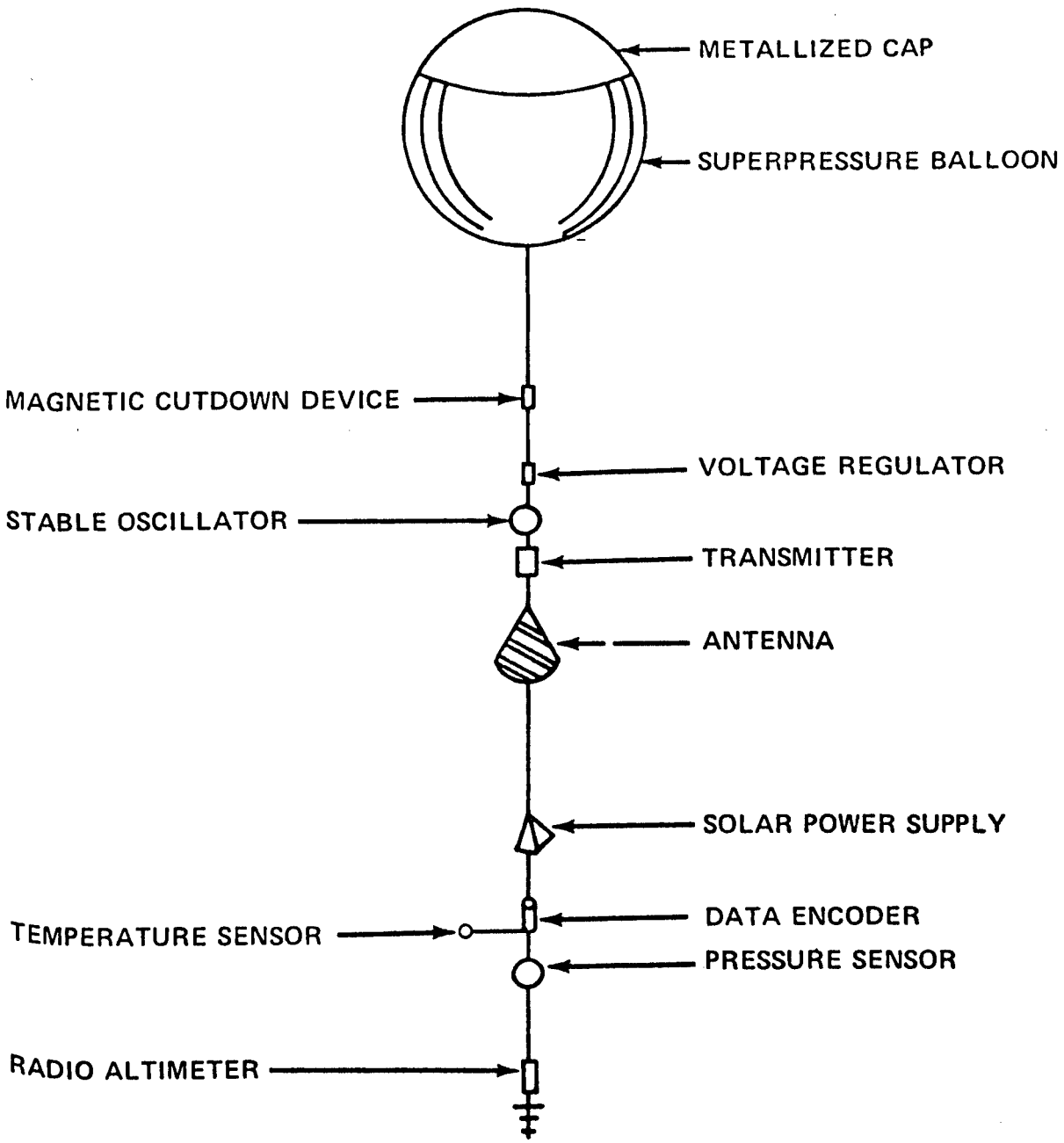

Figure 2.3.2.2 TWERLE Balloon System (NIMBUS-6, 1975)

Table 2.0.1 TIROS-N/NOAA A-G Summary Sheet (Schwalb, 1978)

Spacecraft	:	Total weight (includes expendables)	1421 Kg (3127 lbs)
Payload	:	Weight including tape recorders	194 Kg (427 lbs)
	:	Reserved for growth	36.4 Kg (80 lbs)

Instrument Complement:

Advanced Very High Resolution Radiometer (AVHRR)
High Resolution Infrared Radiation Sounder (HIRS/2)
Stratospheric Sounder Unit (SSU)
Microwave Sounder Unit (MSU)
Data Collection System-ARGOS (DCS)
Space Environment Monitor (SEM)

Spacecraft Size: 3.71 meters in length (146 inches)
1.88 meters in diameter (74 inches)

Solar Array : 2.37 m X 4.91 m : 11.6 square meters
(7.8 ft X 16.1 ft : 125 sq ft)

420 watts, end of life, at worst solar angle

Power Requirement: Full operation-330 watts
Reserved for growth-90 watts

Attitude Control System: 0.2° all axes
0.14° determination

Communications

Command Link	:	148.56 MHz
Beacon	:	136.77; 137.77 MHz
S-Band	:	1698; 1702.5; 1707 MHz
APT	:	137.50; 137.62 MHz
DCS (uplink)	:	401.65 MHz
Data Processing	:	All digital (APT; analog)
Orbit	:	833; 870 km nominal
Launch Vehicle	:	Atlas E/F
Lifetime	:	2 years planned

Table 2.0.2 U.S. Meteorological Satellite Program (Allison, et al., 1980)

Name	Launched	Period (Min)	Perigee (km)	Apogee (km)	Inclination (Deg)	Remarks
TIROS I	01APR60	99.2	796	887	48.3	1 TV-WA and 1 TV-NA
TIROS II	23NOV60	98.3	717	837	48.5	1 TV-WA, 1 TV-NA, passive & active IR scan
TIROS III	12JUL61	100.4	854	937	47.8	2 TV-WA, HB, IR, IRP
TIROS IV	08FEB62	100.4	817	972	48.3	1 TV-WA, IR, IRP, HB
TIROS V	19JUN62	100.5	680	1119	58.1	1 TV-WA, 1 TV-MA
TIROS VI	18SEP62	98.7	783	822	58.2	1 TV-WA, 1 TV-MA
TIROS VII	19JUN63	97.4	713	743	58.2	2 TV-WA, IR, ion probe, HB
TIROS VIII	21DEC63	99.3	796	878	58.5	1st APT TV direct readout & 1 TV-WA
Nimbus I	28AUG64	98.3	487	1106	98.6	3 AVCS, 1 APT, HRIR "3-axis" stabilization
TIROS IX	22JAN65	119.2	806	2967	96.4	First "wheel"; 2 TV-WA global coverage
TIROS X	02JUL65	100.6	948	957	98.6	Sun synchronous, 2 TV-WA
ESSA 1	03FEB66	100.2	800	969	97.9	1st operational system, 2 TV-WA, FPR
ESSA 2	28FEB66	113.3	1561	1639	101.0	2 APT, global operational APT
Nimbus II	15MAY66	108.1	1248	1354	100.3	3 AVCS, HRIR, MRIR
ESSA 3	02OCT66	114.5	1593	1709	101.0	2 AVCS, FPR
ATS I	06DEC66	24 hr	41,257	42,447	0.2	Spin scan camera
ESSA 4	26JAN67	113.4	1522	1658	102.0	2 APT
ESSA 5	20APR67	113.5	1556	1635	101.9	2 AVCS, FPR
ATS III	05NOV67	24 hr	41,166	41,222	0.4	Color spin scan camera
ESSA 6	10NOV67	114.8	1622	1713	102.1	2 APT TV
ESSA 7	16AUG68	114.9	1646	1691	101.7	2 AVCS, FPR, S Band
ESSA 8	15DEC68	114.7	1622	1682	101.8	2 APT TV
ESSA 9	26FEB69	115.3	1637	1730	101.9	2 AVCS, FPR, S Band
Nimbus III	14APR69	107.3	1232	1302	101.1	SIRS A, IRIS, MRIR, IDCS, MUSE, IRLS
ITOS 1	23JAN70	115.1	1648	1700	102.0	2 APT, 2 AVCS, 2 SR, FPR, 3 axis stabilization
Nimbus IV	15APR70	107.1	1200	1280	99.9	SIRS B, IRIS, SCR, THIR, BUV, FWS, IDCS, IRLS, MUSE
NOAA 1	11DEC70	114.8	1422	1472	102.0	2 APT, 2 AVCS, 2 SR, FPR
NOAA 2	15OCT72	114.9	1451	1458	98.6	2 VHRR, 2 VTPR, 2 SR, SPM
Nimbus 5	11DEC72	107.1	1093	1105	99.9	SCMR, ITPR, NEMS, ESMR, THIR
NOAA 3	06NOV73	116.1	1502	1512	101.9	2 VHRR, 2 VTPR, 2 SR, SPM
SMS 1	17MAY74	1436.4	35,605	35,975	0.6	VISSR, DCS, WEFAX, SEM
NOAA 4	15NOV74	101.6	1447	1461	114.9	2 VHRR, 2 VTPR, 2 SR, SPM
SMS 2	06FEB75	1436.5	35,482	36,103	0.4	VISSR, DCS, WEFAX, SEM
Nimbus 6	12JUN75	107.4	1101	1115	99.9	ERB, ESMR, HIRS, LRIR, T&DR, SCAMS, TWERLE, PMR
GOES 1	16OCT75	1436.2	35,728	35,847	0.8	VISSR, DCS, WEFAX, SEM
NOAA 5	29JUL76	116.2	1504	1518	102.1	2 VHRR, 2 VTPR, 2 SR, SPM
GOES 2	16JUN77	1436.1	35,800	36,200	0.5	VISSR, DCS, WEFAX, SEM
GOES 3	15JUN78	1436.1	35,600	36,200	0.5	VISSR, DCS, WEFAX, SEM
TIROS N	13OCT78	98.92	849	864	102.3	AVHRR, HIRS 2, SSU, MSU, HEPAD, MEPED
Nimbus 7	24OCT78	99.28	943	955	104.09	LIMS, SAMS, SAM II, SBUV/TOMS, ERB, SMMR, THIR, CZCS
NOAA 6	27JUN79	101.26	807.5	823	98.74	AVHRR, HIRS 2, SSU, MSU, HEPAD, MEPED

APT	Automatic Picture Transmission TV	NEMS	Nimbus E Microwave Spectrometer
AVCS	Advanced Vidicon Camera System (1" Vidicon)	PMR	Pressure Modulated Radiometer
AVHRR	Advanced Very High Resolution Radiometer	SAM-II	Stratospheric Aerosol Measurement-II
BUV	Backscatter Ultraviolet Spectrometer	SAMS	Stratospheric and Mesospheric Sounder
CZCS	Coastal Zone Color Scanner	SBUV	Solar Backscatter Ultraviolet Spectrometer
DCS	Data Collection System	SCAMS	Scanning Microwave Spectrometer
ERB	Earth Radiation Budget	SCMR	Surface Composition Mapping Radiometer
ESMR	Electrically Scanned Microwave Radiometer	SCR	Selective Chopper Radiometer
FPR	Flat Plate Radiometer	SEM	Solar Environmental Monitor
FWS	Filter Wedge Spectrometer	SIRS	Satellite Infrared Spectrometer
HB	Heat Budget Instrument	SMMR	Scanning Multichannel Microwave Radiometer
HEPAD	High Energy Proton and Alpha Particle Detector	SPM	Solar Proton Monitor
HIRS	High Resolution Infrared Radiation Sounder	SR	Scanning Radiometer
HRIR	High Resolution Infrared Radiometer	SSU	Stratospheric Sounding Unit
IDCS	Image Dissector Camera System	T&DR	Tracking and Data Relay
IR	Infrared - 5 Channel Scanner	THIR	Temperature Humidity Infrared Radiometer
IRIS	Infrared Interferometer Spectrometer	TOMS	Total Ozone Mapping Spectrometer
IRLS	Interrogation, Recording and Location Subsystem	TV	Television Cameras (½" Vidicon)
IRP	Infrared Passive		NA Narrow Angle – 12°
ITPR	Infrared Temperature Profile Radiometer		MA Medium Angle – 78°
LIMS	Limb Infrared Monitoring of the Stratosphere		WA Wide Angle – 104°
LRIR	Limb Radiance Infrared Radiometer	TWERLE	Tropical Wind Energy Conversion and Reference Level Experiment
MEPED	Medium Energy Proton and Electron Detector	VHRR	Very High Resolution Radiometer
MRIR	Medium Resolution Infrared Radiometer	VISSR	Visible Infrared Spin-Scan Radiometer
MSU	Microwave Sounder Unit	VTPR	Vertical Temperature Profile Radiometer
MUSE	Monitor of Ultraviolet Solar Energy	WEFAX	Weather Facsimile

Table 2.0.3 NIMBUS Experiement Summary (NASA, 1982a)

Abbreviation	Experiment Name	Experimenter	Equipment Contractor	Type of Sensor	Scientific Objective
APT	Automatic Picture Taking	GSFC	RCA	Slow Readout Vidicon Camera	Local Cloud Cover Images (pictures)
AVCS	Advanced Vidicon Camera	GSFC	RCA	Wide Angle Multi-vidicon Camera	High Resolution Cloud Cover Images
BUV	Backscatter Ultraviolet Spectrometer	NCAR/GSFC	Beckman	Radiometer/ Spectrometer	Spatial Distribution of Atmospheric Ozone
CZCS	Coastal Zone Color Scanner	GSFC	Ball Bros.	Multispectral Imaging Radiometer	Ocean and Coastal Area Measurement of Chlorophyll, Vegetation, Temp. and Gelbstoff
ESMR	Electrically Scanning Microwave Radiometer	GSFC	Aerojet	Scanning (imaging) Microwave Radiometer	Thermal Image of the Earth and Ocean Unobscured by Clouds
ESMR-F	Electrically Scanning Microwave Radiometer	GSFC	Aerojet	Two Polarization, Scanning Microwave Radiometer	Map Liquid Water Content of Clouds Sea-Ice Cover, Gross Characteristics of Land
ERB	Earth Radiation Budget	NOAA	Gulton	Fixed and Scanning Radiometer	Measure Planetary Heat Budget total Solar Radiation and Angular Distribution of Earth Flux
FWS	Filter Wedge Spectrometer	GSFC	ITT	Radiometer/ Spectrometer	Vertical Distribution and Temperature Profile of Water Vapor and Carbon Dioxide
HIRS	High Resolution Temperature Sounder	GSFC/NOAA	ITT	Scanning Spectral Radiometer	Vertical Temperature Profile and H_2O Distribution
HRIR	High Resolution Infrared Radiometer	GSFC	ITT	IR Imaging Radiometer	Night Cloud Cover
				Dual Channel Imaging Radiometer	Day/Night Cloud Cover
IDCS	Image Dissector Camera	GSFC	ITT	Imaging Radiometer	Day Cloud Cover
IRIS	Infrared Interferometer Spectrometer	GSFC	TI	Radiometer/ Spectrometer	Vertical Temperature & Moisture Profile and Distribution of Other Atmospheric Gases
IRLS	Interrogation, Recording, and Location System	GSFC	Radiation Inc		Locate, Interrogate and Record Data from Remote Stations (balloons and buoys)
ITPR	Infrared Temperature Profile Radiometer	ESSA	Gulton	Radiometer/ Spectrometer	Vertical Temperature Profile (CO_2)
LIMS	Limb Infrared Monitoring of the Stratosphere	LRC	Honeywell	Multispectral Scanning Radiometer	Stratospheric Measurement of Temp., Ozone, Water, Vapor, Nitric Acid, Nitrogen Dioxide
LRIR	Limb Radiance Inversion Radiometer	NCAR/U of Florida	Honeywell	Scanning Spectral Radiometer	Stratospheric Measurements of Temperatures, Water Vapor, and Ozone Profiles
MRIR	Medium Resolution Infrared Radiometer	GSFC	SBRC	Imaging Radiometer/ Spectrometer	Vertical Temperature Profile, Heat Balance, and Distribution of Atmospheric Gases
MUSE	Monitor Ultraviolet Solar Energy	GSFC	Adcole	Radiometer/ Spectrometer	Measurement of Solar Ultraviolet Energy
NEMS	Microwave Spectrometer	JPL/MIT	JPL	Radiometer/ Spectrometer	Vertical Temperature Profile Using O_2 Line, Water and Water Vapor Distribution
PMR	Pressure Modulated Radiometer	Oxford	Marconi	Scanning Spectral Radiometer	Vertical Temperature Profiles to 85 KM
RMP	Rate Monitoring Package	GSFC	Sperry		Measurement of Angular Rate by Gas Bearing Gyro
RTG	Radioisotope Thermoelectric Generator	AEC	Martin		Assess the Usefulness of Radioactive Power Supplies
SAM II	Stratospheric Aerosol Measurement II	LRC	University of Wyoming	Spectral Radiometer	Measure and Map Global Aerosol Concentration and Optical Properties in Stratosphere and Troposphere
SAMS	Stratospheric and Mesospheric Sounder	Oxford	Hawker-Siddley	Pressure Broadening Spectral Radiometer	Global Measurement of Temperature and Select Gaseous Distribution
SBUV/TOMS	Solar Backscatter UV Energy and Total Ozone Mapping Spectrometer	GSFC	Beckman	Monochro Monitor Photometer	Map Total and Vertical Distribution of Ozone Measure Solar Irradiance
SCAMS	Scanning Microwave Spectrometer	JPL/MIT	JPL	Scanning Spectral Radiometer	Vertical Temperature Using O_2 line, Water Vapor Distribution
SCMR	Surface Composition Mapping Radiometer	GSFC	ITT	Imaging Radiometer/ Spectrometer	Identification of Surface Minerals (ERS)
SCR	Selective Chopper Radiometer	Reading & Oxford University	Marconi	Radiometer/ Spectrometer	Vertical Temperature Profile and Distribution of Atmospheric Gases
SMMR	Scanning Multichannel Microwave Radiometer	GSFC	JPL	Scanning Microwave Radiometer	Seal Temp., Surface Winds, Ice Extent, Soil Moisture, Snow Cover, Continental Ice Atmospheric Moisture, Water Vapor and Rainfall
SIRS	Satellite Infrared Spectrometer	ESSA	ESSA Gulton/ SBRC	Radiometer/ Spectrometer	Vertical Temperature Profile and Distribution of Atmospheric Gases
T&DRE	Tracking and Data Relay Experiment	GSFC	GSFC/GE/ BBC	S-Band Transponder	Range and Range Rate Measurements, Data Relay
THIR	Temperature/Humidity Infrared Radiometer	GSFC	SBRC	Imaging Radiometer/ Spectrometer	Cloud Cover, and Water Vapor Mapping
TWERLE	Tropical Winds Energy Conversion Reference Level Experiment	GSFC/Univ of Wisconsin	TI	RF Receiver Balloon Transmitter	Measure Large Scale Atmospheric Motions, Conversion of Potential to Kinetic Energy, Provide 150 mb Reference Level

Nimbus Experiment Summary (Continued)

Abbreviation	Special Instrument Technique	Number of Data Channels (Sensor Only)	Spectral Interval	Pointing Direction	Angular Resolution (Degrees)	Scanning	Nimbus Spacecraft
APT	Stored Image Vidicon (slow scan)	1	0.5 to 0.75 μm	Nadir	2.5 nm**	77°	1, 2
AVCS	Vidicon Camera	3	0.5 to 0.75 μm	Nadir	1.0 nm**	107°	1, 2
BUV	Grating Spectrometer	12	2500 to 3888 Å	Nadir	12.0	None	4
CZCS	Mechanically Scanned Radiometer	6	433 to 800 μm 10.5 to 12.5 μm	Nadir	0.05	Across Track ± 40° Along Track ± 20°	7
ESMR	Electronically Scanned Phased Array Antenna Dicke Switch	1	19.35 GHz	Nadir	1.4	74°	5
ESMR-F	Electronic Conical Scanned Phased Array Antenna Measure both Horizontal and Vertical Simultaneously, Dicke	2	37 GHz	Nadir	1.1	74°	6
ERB	Two Axis Gimbal Mounted Scanning Radiometer	22	2000 Å 50 μm	Nadir and Towards the Sun	5.14 x +0.25 Scan Channels 1.5 Fixed Channels	Horizon to Horizon, Along Track and Across Track	6, 7
FWS	Continuously Variable Interference Filter Disk	1	1.2 2.4 μm 3.2 6.4 μm	Nadir	2.6	None	4
HIRS	Mechanically Scanned Radiometer with Spectral Selection by Interference Filters Radiation Cooler	17	0.7 15 μm	Nadir	1.5	72°	6
HRIR	Mechanically Scanned Imaging Radiometer Spectral Dispersion by Interference Filters	1	3.4 to 4.2 μm	Nadir	0.5	Horizon to Horizon	1, 2
		2	3.4 to 4.2 μm 0.7 to 1.3 μm	Nadir	0.4		3
IDCS	Electrically Scanned Imaging Radiometer	1	0.5 to 0.75 μm	Nadir	1.2 nm**	98.2°	3, 4
IRIS	Michelson Interferometer with Self Calibration	1	5 to 25 μm	Nadir	8.0	None	3
					5.0		4
IRLS				Nadir	120.0 (beamwidth)	None	3, 4
ITPR	Fixed Spectral Filters Mech. Step Scan	7	3.8 to 15 μm	Nadir	1.5	76°	5
LIMS	Mechanical Scanning Radiometer	6	6.1 to 15.8 μm	Earth Limb	0.03°	Horizon to Space 12°	7
LRIR	Mechanically Scanned Radiometer Interference Filters CH_3/NH_3 Cryo Cooler	4	8.7 25 μm	Towards the Horizon	0.3 x 0.03	10° Acquisition 2° Track Vertically	6
MRIR	Mechanically Scanned Radiometer with Fixed Interference Filters	5	0.5 to 29 μm	Nadir	2.7	Horizon to Horizon	2, 3
MUSE	Fixed Spectral Filter	5	1120 to 3100 Å	Towards Sun	90	None	3, 4
NEMS	Microwave Radiometer (Dicke Superheterodyne)	5	20 to 60 GHz	Nadir	10.0	None	5
PMR	Pressure Broadening Spectral Filter	2	15 μm	Nadir	4.0 x 20.0	15°	6
RMP	Hydrodynamic Gas Bearing Gyroscope					None	3
RTG						None	3
SAM II	Mechanically Scanned Radiometer	1	1 μm	Spacecraft Sunrise/Sunset	0.01°	10° Vertical Scan	7
SAMS	Mechanically Scanned Radiometer	9	2.7 to 15 μm 25 to 100 μm	Towards Horizon	1.6° x .16°	Horizon +5° to -9° ± 15° About	7
SBUV/TOMS	Fixed and Spectral Scanning Radiometers (TOMS/SBUV)	20	16 μm to 80 μm	Nadir	SBUV 11° TOMS 3°	Vertical and Cross Track	7
SCAMS	Mechanically Scanned Microwave Radiometer (Dicke Superheterodyne)	5	20 60 GHz	Nadir	7.5	86°	6
SCMR	Spectral Filters and Cooled Detector	3	0.8 to 1.1 μm 8.3 to 9.2 μm 10.5 to 11.3 μm (1 at IR & Visible)	Nadir	0.03	Horizon to Horizon	5
SCR	Selective Absorbtion of Gas	6	2 to 200 μm (Near to Very Far IR)	Nadir	3.0 & 5.0	None	4
		16			1.5 & 2.2		5
SMMR	Mechanically Scanned Radiometer	10	6.33, 10.69, 18.00, 21.00, 37.00 GHz	42° Conical Off Nadir	0.8° ~ 4.2°	Conical Forward of Nadir ± 25°	7
SIRS	Grating Spectrometer	8	11 to 15 μm (Far IR)	Nadir	12.0	None	3
		14	11 to 15 μm (Far IR)			35°	4
T&DRE	Doppler Shift			Zenith			6
THIR	Mechanically Scanned Radiometer	2	6.5 μ to 7.5 μm (Far IR)	Nadir	1.2	Horizon to Horizon	4, 5, 6, 7
			10.5 to 12.5 μm (Far IR)		0.4		
TWERLE	Antenna Receiver, and Random Access Computer	8	400 MHz				6

**In Nautical Miles for 600 NM Orbit Altitude

h \ ϕ_s	50°	55°	60°	65°	70°
3km	4.67	5.81	7.43	9.98	14.67
5km	7.78	9.67	12.37	16.60	24.36
10km	15.53	19.30	24.66	33.04	48.24
15km	23.25	28.89	36.88	49.31	71.66

Table 2.1.1 Cloud Location Corrections (Weiss, 1978)

h \ ϕ_s	50°	55°	60°	65°	70°
3km	1.56	1.94	2.48	3.33	4.89
5km	1.56	1.93	2.47	3.32	4.87
10km	1.55	1.93	2.47	3.30	4.82
15km	1.55	1.93	2.46	3.29	4.78
$(\frac{\bar{d}}{h})$	1.55	1.93	2.47	3.31	4.84

Table 2.1.2 Correction Coefficients of Cloud Location (Weiss, 1978)

Table 2.2.1.1 THIR Subsystem Specifications (NIMBUS-7, 1978)

Design Parameter	Channel 1	Channel 2
Wavelength Band of Operation (Half Power Points (microns))	6.5 to 7.0	10.5 to 12.5
Field-of-View (mrad)	20	7
Ground Resolution (Subsatellite Point at 955 Km) (Km)	20	6.7
Collecting Aperture (cm^2)	110	110
Detector (Immersed Bolometer)		
Size (mm)	0.67 x 0.67	0.22 x 0.22
Time Constant (msec)	2.7	1.8
Scan Rate (rps)	0.8	0.8
Dwell Time (msec)	4.2	1.4
Information Bandwidth (Hz)	115	345
Dynamic Range (Target Temperature) (°K)	0 to 270	0 to 330
Performance Characteristics	**Channel 1**	**Channel 2**
Noise Equivalent Irradiance (NEI) (watts/cm^2)	4.35×10^{-10}	3.0×10^{-10}
Noise Equivalent Temperature Differential (NETD) at Indicated Scene Temperature	5.0°K @ 185°K 0.26°K @ 300°K	1.5°K @ 185°K 0.28°K @ 300°K
S/N Ratio at Indicated Scene Temperature	3.8:1 @ 185°K 110:1 @ 270°K	19:1 @ 185°K 375:1 @ 330°K
Physical Characteristics	**Scanner**	**Electronics Module**
Weight (lbs)	14.0	6.0
Size (in.)	7.5 x 7.1 x 15.7 (Excluding sunshield)	7.0 x 6.8 x 6.0
Power Requirements	**Scanner**	**Electronics**
-24.5 vdc (watts)	1.8	5.8
100-Hz Two-Phase Square Wave 5.25 V (watts/phase)	0.1	
Operating Temperature Range	**0° to 45°C**	

Table 2.2.2.1 SMMR Performance Characteristics (NIMBUS-7, 1978)

Parameter	Channel				
	1	2	3	4	5
Wavelength (cm)	4.54	2.8	1.66	1.36	0.81
Frequency (GHz)	6.6	10.69	18.00	21.00	37.00
R-F Bandwidth (MHz)	250	250	250	250	250
Integration Time (ms) (approximate)	126	62	62	62	30
I-F Frequency Range (MHz)	10-110	10-110	10-110	10-110	10-110
Dynamic Range (°K)	10-330	10-330	10-330	10-330	10-330
Absolute Accuracy (°K rms)	<2.0	<2.0	<2.0	<2.0	<2.0
Temperature Resolution, ΔTrms (°K) (per IFOV)*	0.9	0.9	1.2	1.5	1.5
Antenna Beam Width (±0.2°)	4.2	2.6	1.6	1.4	0.8
Antenna Beam Efficiency (percent)	87.0	87.0	87.0	87.0	87.0
Scan Cycle ±0.4 rad (±25°)/second**	4.096	4.096	4.096	4.096	4.096
Double Sideband Noise (dB) (maximum)	5.0	5.0	5.0	5.0	5.0

*IFOV are remapped to form equal sized cells (150, 90, 50km) across the swath prior to retrieval of geophysical parameters; the ΔT rms's are correspondingly lower.

**Add 2 ms (used for integer dump) for complete IFOV cycle time.

Table 2.3.2.1

ARGOS Platform Characteristics

Carrier Frequency	401.650MHz
Aging (During Life)	±2kHz
Short Term Stability (100ms)	$1:10^9$ (Platform Requiring Location) $1:10^8$ (Platform Not Requiring Location)
Medium Term Stability (20 min)	:0.2Hz/min (Requiring Location)
Long Term (2 hr)	:±400Hz
Power Out: 34.8dbm (3W) Nominal	
Range During Transmission (Stability)	:0.5db
Antenna:: Vertical Linear Polarization	
Message Length: 360ms to 920ms	
Repetition Period for Message:	40-60 sec (Requiring Location) 60–200 sec (Not Requiring Location)
Data Sensors: 4–32 Eight-Bit Sensors for Environmental Data	
Total Number of Platforms:	4,000 global 450 Within View

Blank page retained for pagination

Chapter 3

SATELLITE RECEIVING SYSTEMS

As we have seen in earlier chapters many of the instruments flown on meteorological satellites and the satellite data transmission systems themselves have been designed to allow direct access to the data by prospective users. The reason for this emphasis on the so-called direct readout satellite capabilities comes from the very perishable nature of weather data. Old weather data has little or no use to a forecaster. While it is important to the research scientist, the opportunity to obtain data for research over regions and at times of special interest give the researcher an advantage when compared to after-the-fact acquision of data from the tremendous number of data tapes that are recorded in the archives. Thus, for both forecasting and research we will talk in this chapter about the direct readout satellite systems.

We will also discuss the so-called higher resolution data systems that allow secondary ground stations to obtain data at the same data rate and resolution at which it is placed upon the satellite tape recorders. Thus, in Section 3.2 we will consider the high resolution sun-synchronous and geostationary satellite imagery available in this form. Finally, in Section 3.3 we will discuss the receiving systems that are capable of obtaining the quantitative atmospheric sounding data. The sounding data come primarily at this time from the polar orbiting NOAA satellites but also from experiments now being flown on the geosynchronous satellites.

For more than 10 years amateur radio operators and amateur weather groups as well as a variety of hobbyists have been receiving data

from the weather satellites. Information has been provided by the satellite operators to these groups to allow them to develop some very efficient receiving sets based on surplus and home-built equipment. The new weather satellite handbook by Taggart (1981) is a fine up-to-date summary of not only what has been done but how to do it. Our discussion in this chapter will not be addressed to the amateur receiving group, but rather to those meteorologists who are involved in the reception of satellite data as part of their professional activities. Thus, we will discuss the commercially available systems that are typical of those available in the 1980's. Our reference or mention of various brand name products or companies implies absolutely no endorsement of these products or companies; the references are merely used to demonstrate typical equipment packages which are available today.

For a historical reminder Figure 3.0.1 shows a typical APT (Automatic Picture Transmission) system antenna which meteorologists began using in the late 1960's. Such VHF antennae with associated receivers and display equipment are found around the world and are put to good use by many forecasting units. The figure shows the NOAA-3 satellite, the antenna, the tracking control system and the photofascimile system to produce the small photographic prints of the satellite image over the local area. The figure was taken from Vonder Haar et al. (1974) who described the direct readout meteorological satellite data systems connected to a low-cost computer processing system.

3.1 APT, WEFAX, GOES-TAP

In the 1980's the reliable APT systems continue to obtain great amounts of weather satellite information using the data transmitted from

the scanning radiometers on both the NOAA satellites of the United States and the METEOR satellites of the Soviet Union. New, modern-day electronics and antenna systems have all but removed the need for the tracking apparatus which was common during the last 10 years.

The VHF omni-directional antenna pictured in Figure 3.1.1 together with the control panels and tape recorders show a typical modern-day system. The satellites are received at the local station on specified frequencies set aside for this use near 137.5 MHz. The system shown in Figure 3.1.1 produces the paper facsimile product and while that is the most common option, other users choose to obtain an actual photographic print from their display device or digitize the incoming analog signal (see Vonder Haar et al., 1974) to produce a computer analyzed and displayed product. The reader is referred to Chapter 1, Section 1.3 for further information about the tracking and coverage obtained from the direct readout NOAA or METEOR satellites.

Prospects for continued operation of this basic weather satellite service are good. The World Meteorological Organization has sponsored standardized formats for the APT and is in regular contact with the satellite operating agencies to represent the international community in this area. Even though the scanning radiometers on the satellites are becoming more complex with much higher data rates, they have thus far always maintained a direct readout (APT) transmission mode to meet the needs of the smaller groundstations and forecasting units. These plans will continue and the WMO Bulletin is a good source of information about future development in this area. The many companies advertise in the Bulletin and elsewhere regarding the equiment needed to readout the satellites. Contact them for direct information.

The second-most-popular direct readout satellite receiving station is the one called WEFAX (Weather Facsimile). In fact, since WEFAX is now transmitted each day by four geostationary satellites, this system is rapidly rivalling the APT as the primary direct readout system of the 1980's. These transmissions may come in either VHF or UHF frequencies. The VHF transmissions are designed to be received by the standard APT system. Using UHF frequencies near 1691.0 MHz, the WEFAX from GOES-EAST, GOES-WEST, GMS and METEOSAT are valuable in that they provide not only satellite imagery from the respective satellites but also weather information in terms of standard maps and charts.

The typical WEFAX antenna is shown in Figure 3.1.2; it is approximately 2 meters in diameter. An even smaller antenna, 1 meter size, is shown in Figure 3.1.3. By incorporating new preamplifiers and electronics, smaller antennas of approximately 1 meter can be used in receiving data from some satellites, such as METEOSAT. The acronym SDUS in Figure 3.1.3 stands for the Secondary Data User Station. This is a term used by the European Space Agency (ESA) synonymously with the WEFAX acronym used in this chapter.

Figure 3.1.4 shows assembled WEFAX sectors from the METEOSAT geostationary satellite of the European Space Agency received by the system shown in Figure 3.1.3. This display is typical in that a geostationary satellite image is transmitted in sectors and one either uses the local area sector only or primarily, or assembles a number of sectors each transmitted in sequence according to a pre-arranged schedule to assemble the entire large-scale region viewed by a geostationary satellite.

Of course, one of the advantages of the geostationary satellite is the ease with which the pictures are gridded or located with respect to

geocentric coordinates of latitude and longitude. If the orbit of the geostationary satelite is approximately circular in the equatorial plane, the satellite operating agencies often superimpose a grid which can be inspected by the meteorologists receiving the WEFAX image insofar as the fit to coast lines and other landmarks is concerned. For many operational purposes (and particularly for synoptic weather purposes), the pre-gridded WEFAX data are certainly adequate. This relieves the user of a bit a work that is involved when one must grid APT data from the near-polar orbiting satellites. For these reasons as well the WEFAX is truly an operational or automated product if the appropriate equipment is put to use. As is obvious from Figure 3.1.4 the high latitude regions and of course the polar regions cannot be viewed well from the geostationary satellite WEFAX product.

There is a special type of satellite image distribution system which is in operation in the United States. It is called the GOES-TAP to indicate that it is a tap on a transmission line that is provided by the National Environmental Satellite and Data Information Service of NOAA. Users in weather stations across the entire United States and other groups can obtain GOES sectors from this source. It is a land-line transmission system as distinct from the satellite-transmitted systems discussed earlier in this section. The GOES-TAP has brought the satellite data at nearly full resolution into the forecast offices of the National Weather Service and also to many private groups, research groups and universities. The display system that is required at the end of the leased GOES-TAP line is discussed in Chapter 4.

Since a typical user receives whatever is placed onto the GOES-TAP circuit by the NESDIS, it has limited flexibility as compared to the WEFAX

which allows users to select from a wider geographic coverage in many cases. Nevertheless, GOES-TAP has been put to very great use by those interested in regional and synoptic scale weather. It was through this system that the enhancements of the satellite imagery came into greatest use. These enhancements or special transformations of the basic satellite imagery to bring out certain meteorological features are also discussed in Chapter 4.

3.2 High Resolution Sun-Synchronous and Geostationary Imagery

As we have noted in earlier sections the present-day meteorological satellite instrumentation often produce data of high ground resolution. Ground resolutions of 1 km are not uncommon from both geostationary and near-polar orbiting satellites. The Advanced Very High Resolution Radiometer (AVHRR) on the NOAA satellites and the VISSR on the GOES satellites are just two examples of visible and infrared satellite instrumentation producing data of high ground resolution. The number of data points (pixels) which accompany such high ground resolution cause the high output data rates from these instruments. Thus, the bandwidth required to transmit the data is increased and VHF frequencies are no longer capable of carrying the high resolution data. However, the UHF or S-band frequencies are used in this case. Larger antennas, receivers and telemetry systems capable of accommodating these higher frequency data transmissions are essentially all that separates the type of satellite receiving systems discussed in this section from the APT and WEFAX systems discussed in the previous section. Figure 3.2.1 shows two antenna systems, one in the foreground, of 5 meters in diameter, the other 10 meters in diameter that

are used at Colorado State University's Department of Atmospheric Science receive the high data rate transmissions of the full-resolution visible and infrared imagery data from the GOES-EAST and -WEST satellites. Data rates received on these systems in the 1690 MHz range are approximately 1.7 million bits per second for the full resolution visual data with a ground resolution of 1 km and approximately 528,000 bits per second with the 8 km infrared data.

The European Space Agency has pioneered on-board sectorizing so that its PDUS stations can receive according to a prearranged transmission program the full resolution data (either visible or infrared or water vapor channel) from the METEOSAT over a special region of interest. This eliminates the need for one piece of equipment at the PDUS station as compared to the GOES Direct Readout Satellite Ground Station (DRSGS). In both cases the data from these geostationary satellites are retransmitted from the primary command and control station with the use of a data buffer on the ground such that they are passed back through the same satellite (or another satellite if necessary) and relayed to the PDUS or DRSGS in near real-time. The data are delayed only a few fractions of a second by the retransmission process. The retransmission does allow the addition of calibration and navigation information into the documentation records accompanying the imagery data so that the high-resolution data receiving sites are very well prepared for their own computer analysis of the visible and infrared (and sometimes water vapor) images.

The counterpart of the high resolution GOES and METEOSAT data transmission from the NOAA satellites in sun-synchronous orbits is called the High Resolution Picture Transmission (HRPT). Again, UHF frequencies

are used to transmit data from the Advanced Very High Resolution Radiometer (AVHRR) described in Chapter 2. This scanning radiometer has a ground resolution in its channels of approximately 1 km, and thus ground stations equipped with the proper antennae and precision satellite tracking systems can receive excellent high resolution images from the satellite at least two times each day. Figure 3.2.3 shows one of the high-resolution HRPT receiving stations. The equipment necessary to receive the high-resolution data is available from several vendors, and its cost and complexity is considerably greater than that necessary to receive the VHF transmissions in the APT mode. The typical data rate transmitted on the HRPT is 665,400 bits per second.

3.3 Quantitative Atmospheric Sounding Data

The sun-synchronous satellite NOAA carries the TIROS Operational Vertical Sounder (TOVS). These types of instruments were described briefly in Chapter 2, and the application of data from the TOVS for obtaining temperature soundings of the atmosphere will be discussed in Chapter 6. Insofar as receiving the data is concerned, relatively new developments have made the satellite sounding data from this instrument available to users in the direct readout mode. They are available from two separate real-time data transmission links, the VHF beacon transmission link and the link which combines the TOVS data with the output from the AVHRR. This is in fact the HRPT service mentioned above. Thus, it is possible for those with either VHF beacon reception capabilities (data rates about 8,000 bits per second) or those with the HRPT systems to receive these sounding data.

All data from the TOVS are in digital form and suitable for computer processing to obtain the temperature and moisture soundings. In the early

1980's the use of the sounding data is increasing in the direct readout mode. Several groups are sponsoring meetings to discuss and foster the use of the direct readout sounding data. When coupled with the imagery of the clouds in the visible and window infrared wavelengths, the upper-level temperature and moisture information obtained from the sounding experiments can be a special aid to weather forecasters.

References and Additional Reading

Clark, R. M. and E. W. Feigel, 1981: The WEFAX Users' Guide, NOAA-S/T 81-266, NOAA/NESS, Washington, DC, 47 pp.

Popham, R. W. and J. L. Henderson, 1982: Proceedings of the WEFAX Users' Conference for National and International User's of GOES WEFAX Services, NOAA-S/T 82-255, NOAA/NESS, Washington, DC, 102 pp.

Summers, R. J. and T. Gotwald, 1981: Teachers Guide for Building and Operating Weather Satellite Ground Stations for High School Science, NASA EP-184, NASA/GSFC, Greenbelt, MD 20771, 83 pp.

Taggart, R. E., 1981: The New Weather Satellite Handbook, Wayne Green, Inc., Peterborough, NH, 132 pp.

Vermillion, C., 1969: Weather satellite picture receiving stations, NASA Special Publication No. 5080.

Vonder Haar, T., D. Reynolds and L. Lilie, 1974: Direct readout meteorological satellite data processing with a low-cost, computer-linked system. Atmospheric Science Paper No. 227, Colorado State University, Fort Collins, CO 40 pp.

WMO, 1980: Instruments and Observing Methods, Report No. 4, Meteorological Satellite Ground Based Receiving Equipment (WMO Equipment Survey), WMO, Geneva, Switzerland, 34 pp.

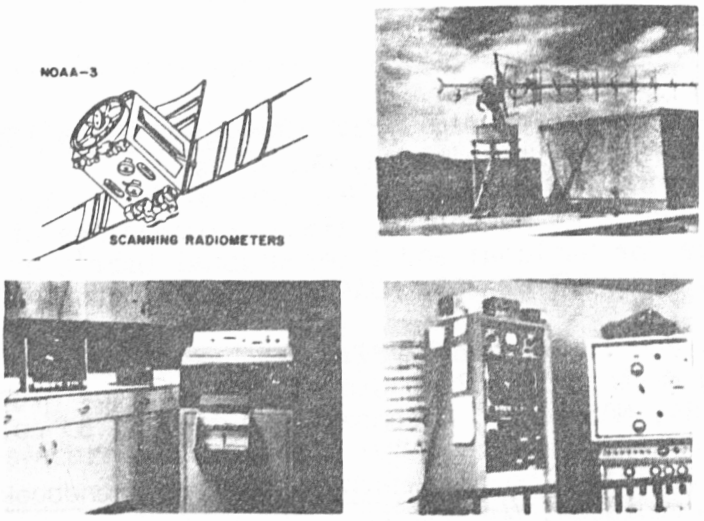

Figure 3.0.1 APT Receiving System (circa 1970)

ALDEN UNIVERSAL SATELLITE GROUND RECEIVING STATION APTS-3B WITH OPTIONS

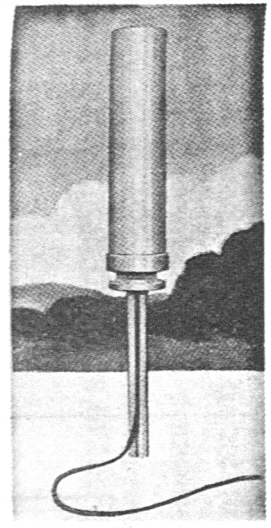

VHF Telemetry Omni-Directional Antenna with integrally installed VHF Low Noise Preamplifier, ALDEN Model 9330-9-2A.

Digital Chronometer Model 9330-9-1A to provide operator with precise, illuminated 24 hour time indication.

Facsimile Tape Recorder for simultaneous taping, or tape playback, of received APTS type signals, ALDEN CAT. NO. 903C.

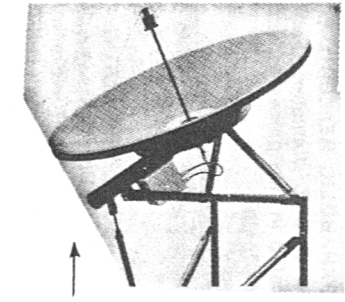

UHF Parabolic Antenna with UHF/VHF Down Converter to convert 1691.0 MHz or 1691.0/1694.5 MHz (METEOSAT) to VHF.

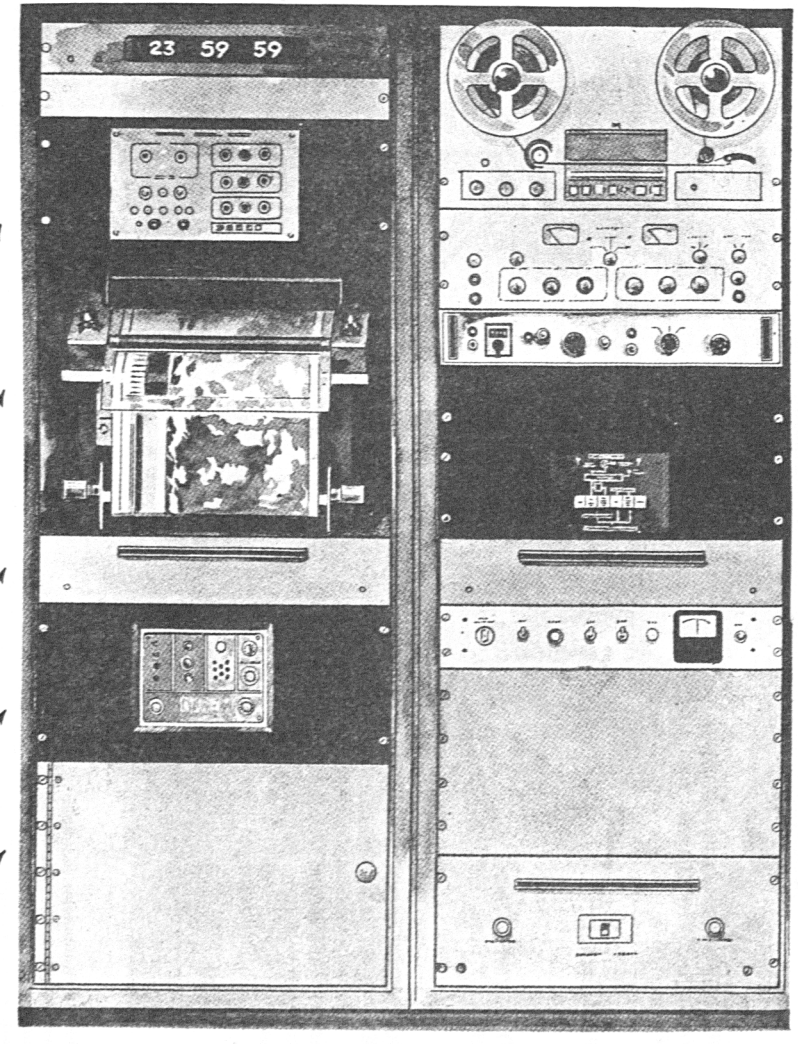

Scanning Radiometer/Satellite Signal Processor for automatic recognition of VIS and IR signals from TIROS-N satellites, ALDEN Model 9310D.

ALDEN 1100 Model 9273R APTS/Weather Chart Recorder for APTS WEFAX pictures.

Slide-out drawer with hinged steel writing surface — two provided, one in each bay.

ALDEN Model 9273R APTS/Weather Chart Recorder electronics.

Accessories/Parts Compartment with door provides convenient storage space.

VHF Satellite Telemetry Receiver — provides 4 VHF channels, 137.62, 137.50, 137.15 and 137.30 MHz.

Operator's Control Center at desk height level for ease of selection of system modes of operation.

FSK Converter Option for radiofacsimile weather chart reception, ALDEN CAT. NO. 421C.

Blank panel. Provides 19 in. RETMA rack space for customer's accessory use.

APTS-3B Power Entrance. Optional transformers provide isolation of AC mains, 115V/60 Hz or 230V/50 Hz.

Figure 3.1.1 Modern Receiving System for APT, WEFAX

TYPICAL UHF PARABOLIC ANTENNA INSTALLATIONS

As shown, the 6 ft. diameter parabolic antenna is mounted on the universal stand in the high look angle configuration. The radome is not shown so as to be able to depict antenna details.

FEED GUY WIRES. (3) Spring loaded.

PARABOLIC REFLECTOR. 6 ft. or 8 ft. diameter. (Fabricated in two pieces for easy shipping).

FEED. PLANE POLARIZED

PARABOLIC REFLECTOR MOUNT. Provides vernier adjustment of ±10° elevation, ±5° azimuth.[1]

VERTEX TUNING PLATE.

LEAD-IN CABLE. (Low Loss). From antenna feed to module A2.

MODULE A2 UHF MICROWAVE UHF/VHF DOWN CONVERTER.

ADJUSTABLE MOUNT PIVOT POINTS.

PIPE. 4½ in. O.D.

UNIVERSAL STAND. Heavy steel tubing galvanized after fabrication.

ADJUSTMENT ROD. With lock nuts.

HIGH LOOK ANGLE ADJUSTMENT ROD PAD. Provides 40° to 67° adjustment. (Installing this pad on a raised footing will provide adjustment to 90° overhead).

ADJUSTABLE GUY ROD ATTACHMENT BRACKET. For 8 ft. parabolic reflector.

RF LEAD-IN CABLE. RG214/U or equal.

MOUNTING PADS. With holes for 5/8" dia. bolts.

[1]When 8 ft. diameter parabolic reflector is provided, the vernier adjustment of this mount is ±5° elevation, ±5° azimuth.

LOW LOOK ANGLE ADJUSTMENT ROD PAD. Provides 12° to 40° adjustment.

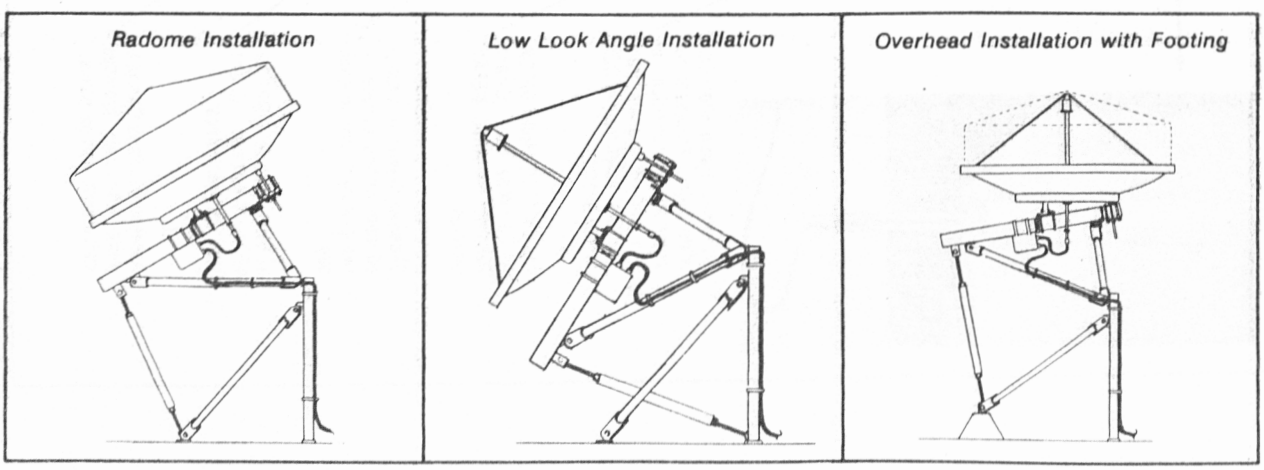

Fig. 7 *Antenna Configuratrions*

Figure 3.1.2 WEFAX Antenna

SKYCEIVER VI

SECONDARY DATA USER STATION FOR GEOSTATIONARY SATELLITES

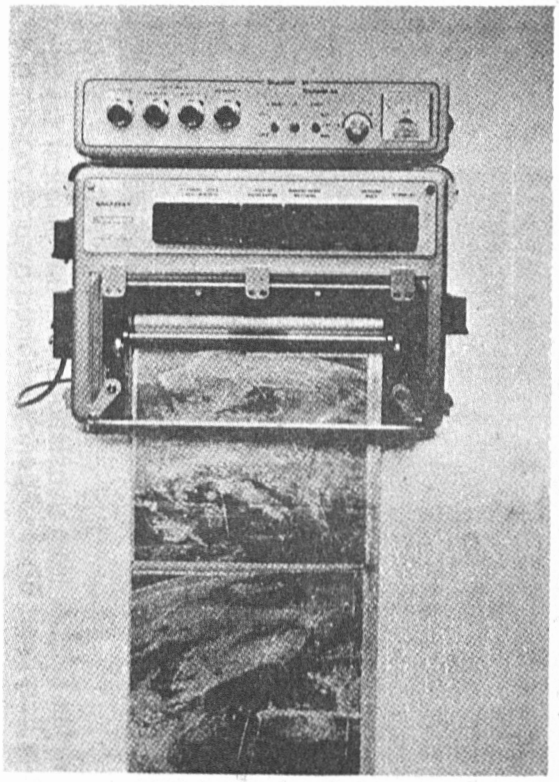

INDOOR EQUIPMENT

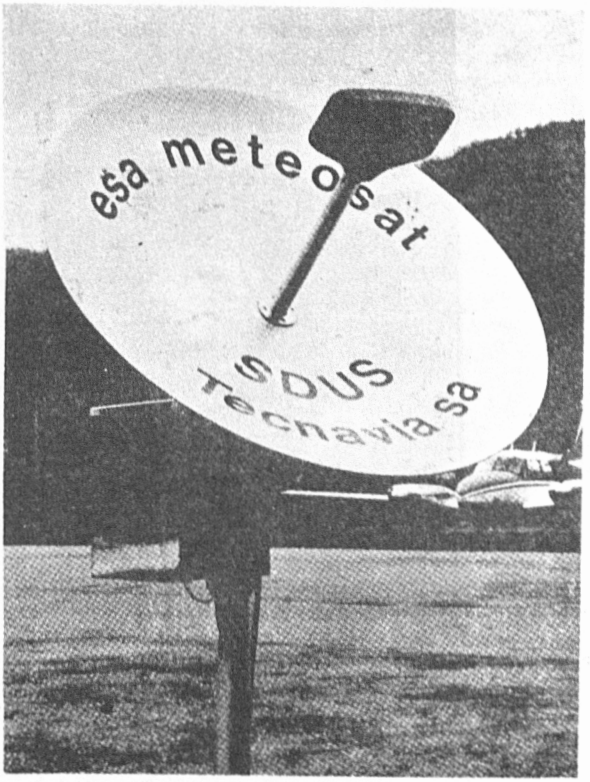

OUTDOOR EQUIPMENT

SKYCEIVER VI - SDUS - is a complete, inexpensive, professional WEFAX receiving system from geostationary satellites.

It is the most compact equipment of its type on the market.

Operation is fully automatic, reliable and inexpensive giving high quality meteorological pictures in the visible and infrared spectrum.

Figure 3.1.3 Secondary Data User Station

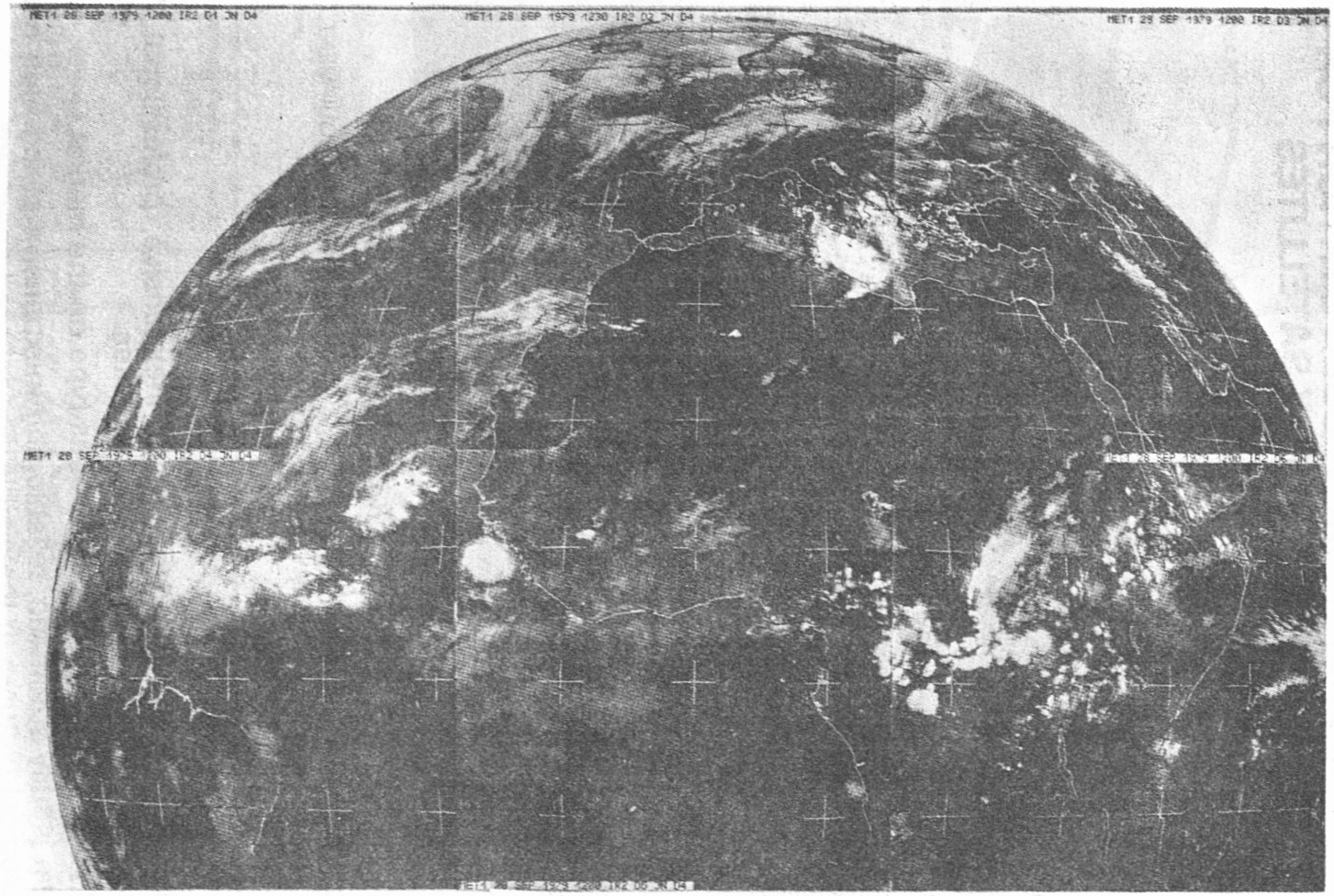

Figure 3.1.4 Assembled wefax sectors from geostationary meteorological satellite METEOSAT of the European Space Agency received by a SKYCEIVER VI - L

Figure 3.2.1 CSU's Two Antenna System (5 and 10 meters) (Slide Set #2)

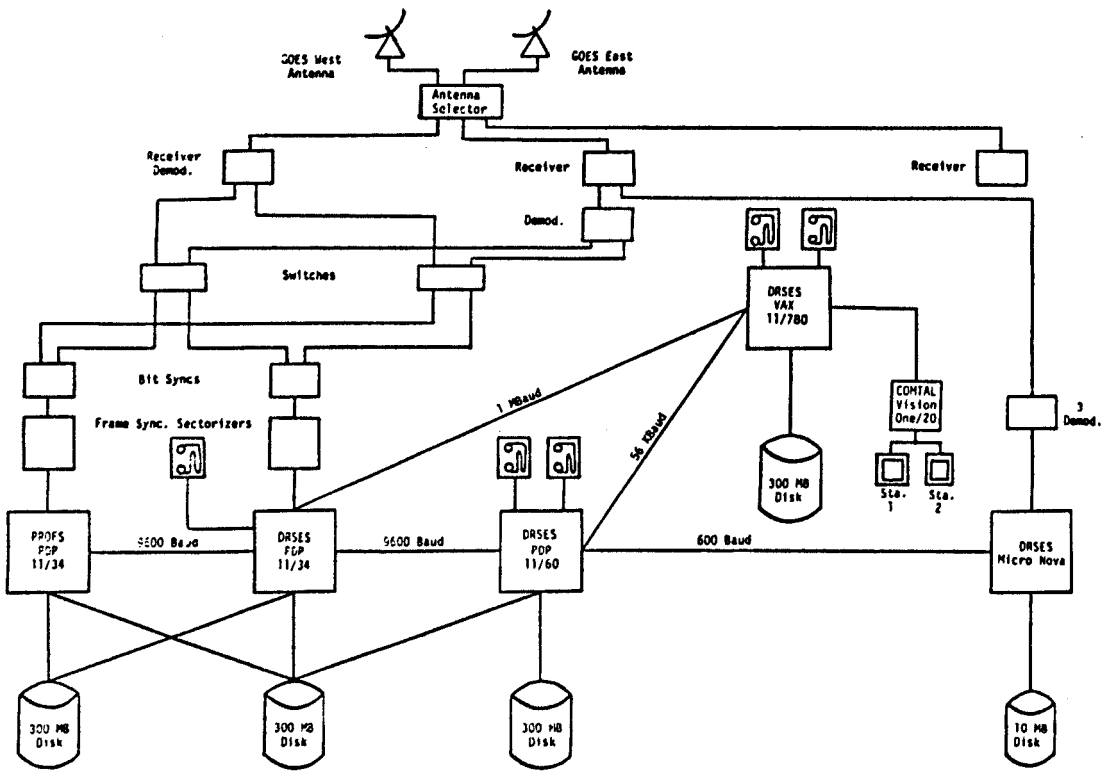

Figure 3.2.2 Block Diagram of CSU DRSGS for GOES

Meteorological Pictures from Space

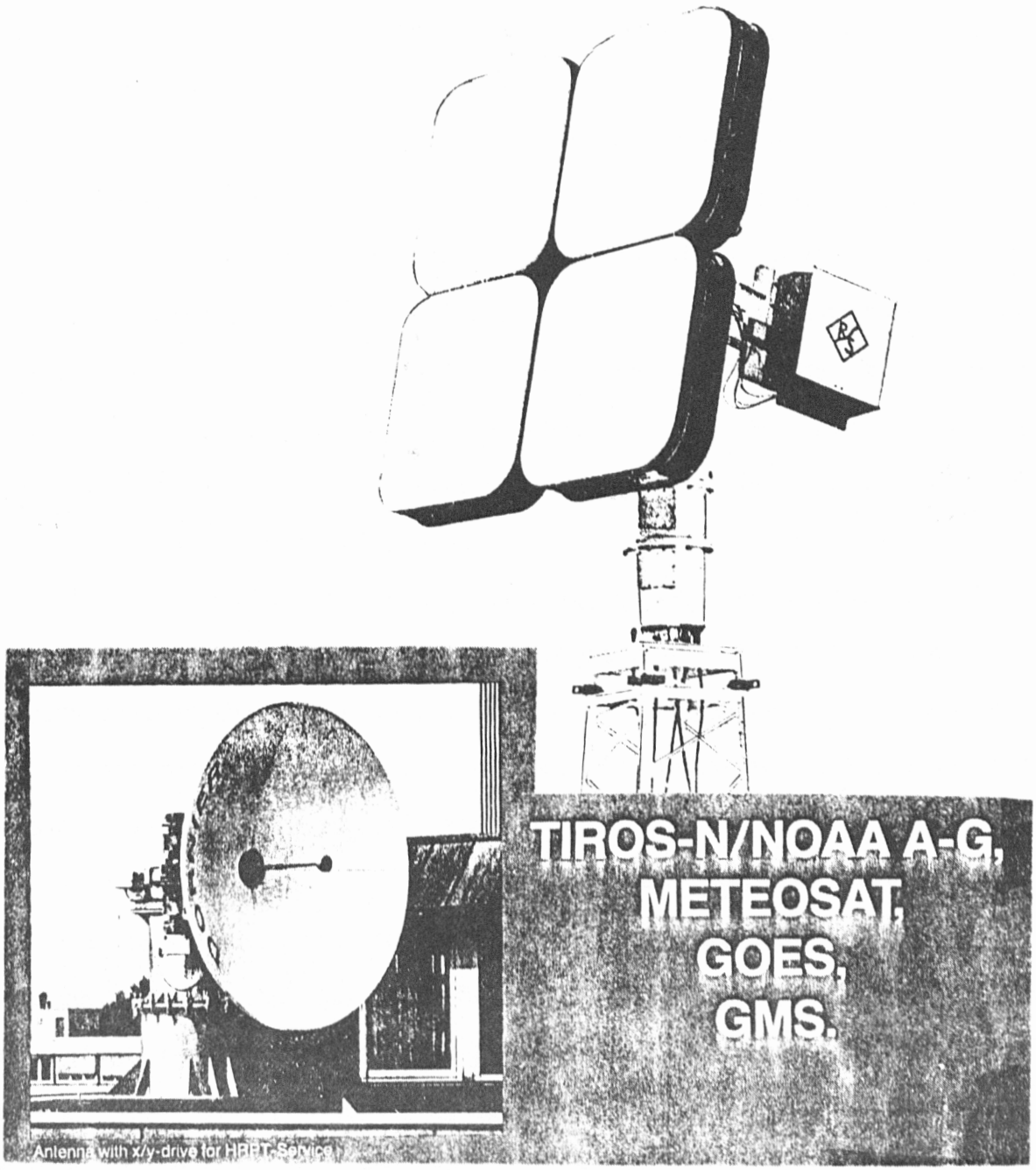

Figure 3.2.3 HRPT Receiving Station Antenna

Blank page retained for pagination

CHAPTER 4

IMAGE AND DATA DISPLAY SYSTEMS

The satellites, instruments and receiving systems described in previous chapters take us only a portion of the way necessary for full application of the meteorological data. Good image and data display devices are extremely important to the user in the forecast or research area. In this chapter we will discuss the basic image producing and image display systems, such as the facsimile machines and the movie loops used to describe sequences of satellite images. We will also investigate the new interactive image and data display systems many of which use new technology tool called "digital imaging". This means that the satellite view of the clouds in various spectral intervals as dictated by the instrument is processed in a computer and displayed on a video device under computer control. Examples of the new digital imaging are found throughout this notebook with some special examples in Chapter 14. There, the latest display devices which produce color-enhanced photographs under computer control are noted in a discussion of the application of satellite and radar data to several meteorological problems.

With the importance of proper display of the image to the meteorologist, it is not surprising that a vast array of image producing devices have been used in the course of the history of satellite meteorology. Very early photographic processes have retained some measure of use into the 1980's. They have been joined by computer plotter outputs which were very popular during the 1960's and early 1970's, and by the paper facsimile and

improved laser facsimile systems. Of course, the television [or video or sometimes cathode ray tube (CRT)] devices now abound. They can be used in either a video analog mode or linked to a computer to produce the digital images noted above.

4.1 Facsimile Machines; Movie Loops

Early satellite data from the APT satellites and from data that had been tape recorded and readout at a central receiving site were often produced on a photofacsimile device of the kind shown in Figure 3.0.1. The paper facsimile systems (for example, Figure 3.1.3) have a very common technology with the systems used to transmit weather maps and it is not surprising that they were adapted to meteorological satellite display purposes in the first 10 years of the satellite program.

Because of their relatively inexpensive operating costs and simplicity these paper facsimile systems are still in use today. The number of shades of gray that can be obtained from some of these systems varies from three or four to ten or twelve in the high quality laser facsimile systems. One of the so-called laser-fax devices is shown in Figure 4.1.1. Devices such as this one can use various speeds to handle either the APT or the WEFAX scale of data. These are typical display systems that are joined with the GOES-TAP network to bring hard copy satellite images into the National Weather Service Forcast Offices in the United States. Other companies manufacture and market very similar systems so the user is encouraged to compare systems offered by several vendors.

Some of the present-day facsimile machines have electronic modifications that allow a user to select particular enhancement curves to display

the data in order to emphasize special meteorological features. One of the enhancement curves that is used by the NOAA/NESDIS Field Services Division is shown in Figure 4.1.2. Here, the gray scale or digital count value is modified in order to obtain a displayed image of the type shown in Figure 4.1.3. In this particular kind of enhancement we are trying to emphasize the thunderstorms and the very cold cumulus cloud tops. This is done in the display device and thus is separate to a certain extent from the satellite instrumentation and calibration curves discussed in earlier chapters. Whether attached to one of the facsimile systems or used in a computer as part of the digital imaging system such enhancements can have great benefits to the user. However, it is extremely important that the user be aware of the type of enhancement being used for the image he is analysing. Interpretation varies with the knowledge of the particular enhancement curve that is used.

Most meteorologists are well aware that the geostationary satellite images are routinely obtained every 30 minutes. Thus, a sequence of photos from geostationary satellites is very amenable to use in a movie loop to give a time lapse display of the developing weather situations. These movie loops were first made using standard photographic techniques with a movie camera and registration table. Video cameras and techniques were used as well, and now the rapid refresh capabilities of digital imaging systems allows one to make a movie loop of a sequence of weather satellite pictures under computer control.

These movie loops are excellent for research (for example, in the tracking of clouds to infer winds from the cloud motion) and for training purposes. Furthermore, when loops are made in near-real time they can help

short range forecasting by allowing the meteorologist to identify rapidly developing and/or advecting regions of cloudiness and associated weather. Finally, the movie loops are excellent for providing a global view and perspective on atmospheric motions. For this reason alone, some of the films that are noted at the end of this chapter are highly recommended for use in basic meteorological classes. They serve as a reminder of the global nature of atmospheric flow and weather systems for meteorologists at all levels in their career.

4.2 Interactive Display Systems; Digital Imaging

By the mid-1970's a number of groups had developed computer-linked video display systems for processing meteorological satellite data. These systems used the rapidly developing new technology of rapid-refresh computer memories. Television monitors or CRT's attached to the output of these memories operate in the video mode and thus require refreshing at rates greater than 1/30th of a second. Under computer control the new memories were able to feed the video signals at such a rate as to produce flicker-free displays. This opportunity to use the developing high technology was recognized by a number of the groups, and thus the mini-computers and the video display systems were linked by these new memories. As a result, the meteorological user or forecaster could now manipulate and display images under computer control and make a picture as an output of the computer operations. The age of "digital imaging" was born.

Figures 4.2.1 and 4.2.2 show examples of the mini-computers and video display systems used for research at the Department of Atmospheric Science at Colorado State University. This equipment allowed the development and

test in collaboration with electrical engineering colleagues of the first 8-plane or 8-picture loop rapid-refresh digital imaging system using the new memories. Other groups rapidly developed systems of their own and today throughout the world digital imaging is continuing to develop from the research through the applications mode. A number of the references suggested for additional reading at the end of this chapter describe the history of this development.

One of the capabilities of digital imaging that is so valuable to the meteorologist is the rapid zoom capability under computer control. This is demonstrated in Figures 4.2.3 and 4.2.4 where a strong winter storm over the central United States is shown in the synoptic scale and then a zoom to a region of the Great Lakes is made using digital imaging.

The use of the computer-linked systems is not limited to pure imagery since all of the graphics (including color graphics) capability of the new mini-computer systems can be combined with the satellite data for digital imaging. Figure 4.2.5 shows a portion of a GOES satellite visible satellite image over the State of Colorado in which the major interstate highways are shown superimposed over the satellite image. (Note that the satellite image is truncated across the western part of the state since this image has been remapped from a sector of satellite data taken by the direct readout satellite ground station described in Chapter 3.) The Arkansas River is also shown on the photo along with some of the temperatures reported early in the morning hours of the 9th of December 1978, a situation that was cold and clear over the Rocky Mountain area and the High Plains to the east of the mountains.

The additional capabilities of the various systems available at the present time and the ease with which a meteorological user can take advantage of these systems varies as can be expected from one unit to the next. It is important to remember that each digital imaging system was developed to meet a particular research objective or display need. However, in recent years the National Weather Service in the United States has developed both the Automation of Field Operations and Services (AFOS) and the Prototype Regional Operational Observation and Forecast System (PROFS). These systems are designed for the weather forecaster and represent a combination of several aspects of the new technology. In contrast, the McIDAS (Man-computer Interactive Data Analysis System) and the IRIS (Interactive Research and Imaging System--formerly termed ADVISAR) were developed for research purposes.

Table 4.2.1 contrasts these four systems in terms of some common parameters. These include the number of overlays that can be displayed on a CRT, the time to load an image, the zoom capacity, the data types able to processed by this system, the reproducability of the results and the looping capacity in terms of number of frames that can be formed into an image loop. The data in the table are adapted from Kelly (1982, personnal communication).

Table 4.2.1: Intercomparison of "Digital Imaging" Systems for Parameters Listed (adapted from Kelly, 1982)

PARAMETERS	AFOS	McIDAS	PROFS	IRIS
# overlays/ CRT	(3)1	(7)4	(6)3	(5)2
Time to load image (sec)	(3/20)1	(1/30)2	(1/30)2	(1/30)2
Zoom capacity (ratio)	(25/1)4	(0)1	(16/1)3	(4/1)1
Data types able to process	1	4	3	2
Reproducibility of results	1	2	3	4
Looping Capability	1	4	3	2

The primary entries in the table are a figure of merit ranging from 1 which represents a fair capability to 4 which represents outstanding capability. Such "figures of merit" differ considerably from the kind of technical parameters that are described in the sales brochures for these devices. In many respects, however, those described in Table 4.2.1 are more important to the meteorologist/user in that they make an attempt to focus on the features of each of the digital imaging systems which add to its success in the display of meteorological satellite and other data.

There have already been tests of both the ADVISAR and PROFS systems in the real-time forecasting environment. Vonder Haar et al. (1982) described the successful test of an ADVISAR-type system installed in the National Weather Service Forecast Office in Denver, Colorado during the spring and summer of 1980. The mini-computer based system received images from the satellite ground station 100 km away and presented digital images of the

regional weather to the forecasters involved in synoptic forecasting as well as forecasts of severe storms and floods in the mountain region. Beran and McDonald (1981) and Reynolds (1982) describe the more complex PROFS system which has undergone much more extensive testing and development. It will most likely lead to the type of image display system that we will find in the weather stations of the future. In a similar manner, the mobile display unit described by Vonder Haar et al. (1982) is the forerunner of improved systems of this type which will be linked to the main satellite data processing and receiving sites and which can be extremely useful for support of research field programs as well as forecast units that might be operating away from the main center. A display of the mini-computer link-up for the mobile display unit is shown in Figure 4.2.6.

We can expect the rapidly expanding high technology area to give us continued improvements in digital imaging. For example, in the near future research on the three-dimensional display of clouds (Brubaker, 1982) will allow meteorologists more insights into the weather associated with the cloud images. Infrared imagery gives us height information yet we often display it in a two-dimensional form. Figure 4.2.7 from the work of Brubaker and his colleagues shows an original infrared GOES image which has been processed to obtain the three-dimensional representation of the clouds shown in two different graphic displays. Such displays made with the improved digital imaging capabilities will allow meteorologists to study cloud-to-cloud interaction and the evolution of individual clouds into severe weather.

Finally, for those readers interested in the more internal details of a typical digital imaging system, we provide Figure 4.2.8 which is a schematic depiction of the All Digital Video Imaging System for Atmospheric Research (ADVISAR) at Coloardo State University. This figure displays the parallel data interface from the computer to the ADVISAR and the individual image frames which are composed of the rapid refresh memories. It also shows the linkage between the output from the computer memories to the digital-to-analog converters which are used to drive the video display monitors.

References and Suggested Additional Reading

General Books:

Foley, J. D. and A. VanDam, 1982: Fundamentals of Interactive Computer Graphics. Addison-Wesley Publishing Company, Inc., Menlo Park, CA, 664 pp.

Scott, J. E., 1982: Introduction to Interactive Computer Graphics. John Wiley and Sons, Inc., New York, NY, 225 pp.

McIDAS:

Hilyard, J. (ed.), 1977: Interactive video displays for atmospheric studies. Proceedings of a workshop at the University of Wisconsin, Madison, 14-16 June.

Smith, E. A., 1975: The McIDAS System. IEEE Trans. Geosci. Elec., GE-13, 123-126.

SPADS:

Schramm, W. G., P. Zeleny, R. E. Nagle and A. I. Weinstein, 1982: The Navy SPADS, a Second Generation Environmental Display System. Preprints Ninth Conference on Weather Forecasting and Analysis, 28 June - 1 July, American Meteorological Society, Seattle, WA, 72-75.

PROFS/POWS:

Beran, D. W. and A. E. MacDonald, 1981: Design of a short-range forecasting system. IAMAP Symposium, Hamburg, Germany, 25-28 August, 347-350.

Reynolds, D. W., 1982: Prototype workstation for mesoscale forecasting: a look to the 1990's. Preprints Ninth Conference on Weather Forecasting and Analysis, 28 June - 1 July, American Meteorological Society, Seattle, WA, 65-71.

IRIS (ADVISAR):

Green, R. N. and M. Kruidenier, 1982: Interactive data processing for mesoscale forecasting applications. Preprints Ninth Conference on Weather Forecasting and Analysis, 28 June - 1 July, American Meteorological Society, Seattle, WA, 60-64.

Smith, E. A., T. H. Vonder Haar and T. A. Brubaker, 1977: All Digital Video Imaging System for Atmospheric Research (ADVISAR) Technical Report, Department of Atmospheric Science, Colorado State University, (Also in Proceedings of a Workshop on Interactive Video Displays for Atmospheric Studies, University of Wisconsin, Madison.)

OTHER:

Brubaker, T., 1982: Three-dimensional representation of clouds from satellite images. Naval Research Reviews, Vol. 34, 53-59.

Vonder Haar, T., et. al., 1982: Realtime processing and transmission of digital satellite imagery for use at a remote forecasting facility. National Weather Digest, 7/2: 32-37.

LIST OF AVAILABLE FILMS (16 mm):

WAB465 (Sound Film, 30 minutes), The Importance of Thunderstorm Outflow Boundaries in the Development of Deep Convection (GOES Imagery/Ground Based Radar). Available from the Walter A. Bohan Company, 2026 Oakton St., Park Ridge, IL 60068.

WAB409 (Sound Film, 19 minutes), The Initiation of Convection (GOES-East/GOES-West). Available from the Walter A. Bohan Company, 2026 Oakton St., Park Ridge, IL 60068.

EMR WEATHER PRODUCTS

EMR 816-02/03 LASER FACSIMILE RECORDERS

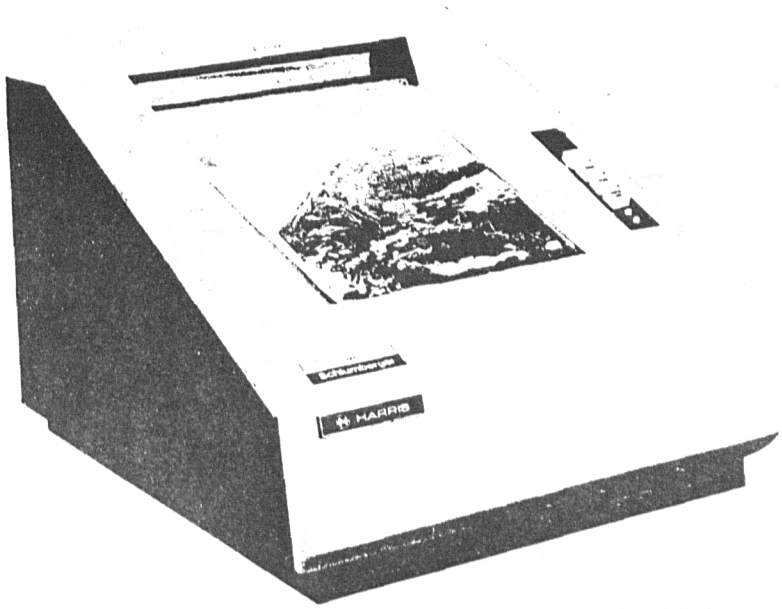

- Photographic quality images.
- Laser beam recording on dry silver paper or film — no chemicals or darkroom required for image processing.
- Automatic APT/WEFAX mode selection.
- Internal gray scale generator.
- Operator adjustable marking power.
- Simple operation — as easy as using an office copier.
- Directly compatible with the EMR Scanning Radiometer Data Manipulators (SRDM's).
- Amplitude-modulated subcarrier input in WMO APT/WEFAX format.
- Compatible with present and future weather satellites when used with the EMR SRDM's.

Through an international distribution agreement, EMR sells and services the Harris Corp. Model 850 LASERFAX as the EMR Model 816 Laser Facsimile Recorder for weather applications. The Model 816 is a dry process recorder which produces photographic quality images from weather satellite data. The paper or film is exposed by a low-power laser and is developed by heating the exposed medium. The complete recording and developing process is automatic and a finished picture is available within 60 seconds after signal completion, dry and ready for use. The weather photographs offer a new dimension in satellite meteorology: high quality imagery without the expense and inconvenience of wet chemicals.

The EMR Model 816 Recorder is directly compatible with standard WMO format weather data at 120 or 240 scans per minute, such as GOES-TAP or WEFAX operation. Incorporation of an EMR Model 812 SRDM provides dynamic image enhancement in these applications. The EMR Model 810 or 811 SRDM includes the required scan conversion for interface with the present NOAA satellites. Other unique SRDM features include gamma correction, temperature thresholding, isotherm annotation, "flat earth" imagery and multi-satellite operation. The 816 Recorder may be utilized in most weather imagery applications with the proper interface, if required, available from EMR.

Figure 4.1.1 Laser-Facsimile Recorder

ENHANCEMENT MB

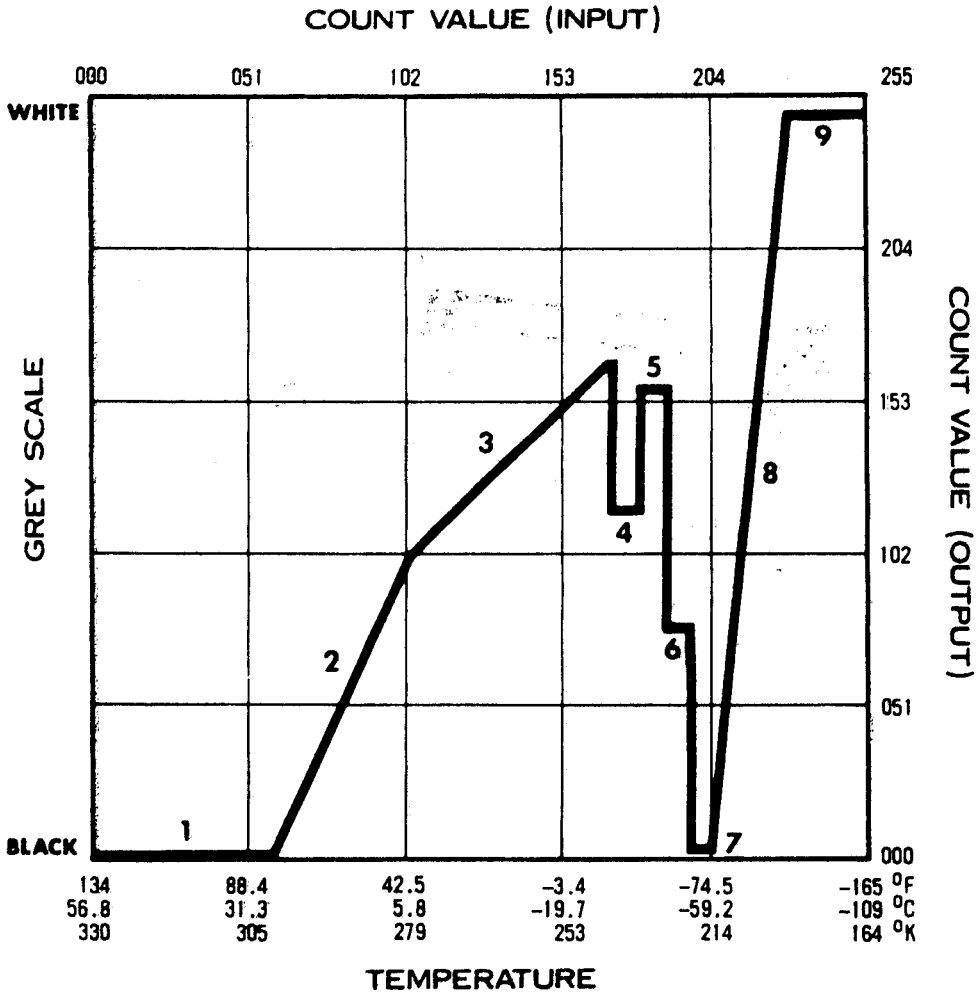

SEGMENT NUMBER	°C TEMPERATURE	COMMENTS
1	58.8 to 29.3	Little or no useful Met Data (Black)
2	28.8 to 6.8	Low Level/Sea Surface Difference
3	6.3 to -31.2	Middle Level - No Enhancement
4	-32.2 to -42.2	First Level Contour (Med Gray)
5	-43.2 to -53.2	(Light Gray)
6	-54.2 to -59.2	Thunderstorm (Dark Gray)
7	-60.2 to -63.2	Enhancement (Black)
8	-64.2 to -80.2	Overshooting Tops Enhancement
9	-81.2 to -110.2	(White)

Figure 4.1.2 Enhancement Curve used by NOAA/NESDIS for GOES Infrared Imagery (Clark, 1983)

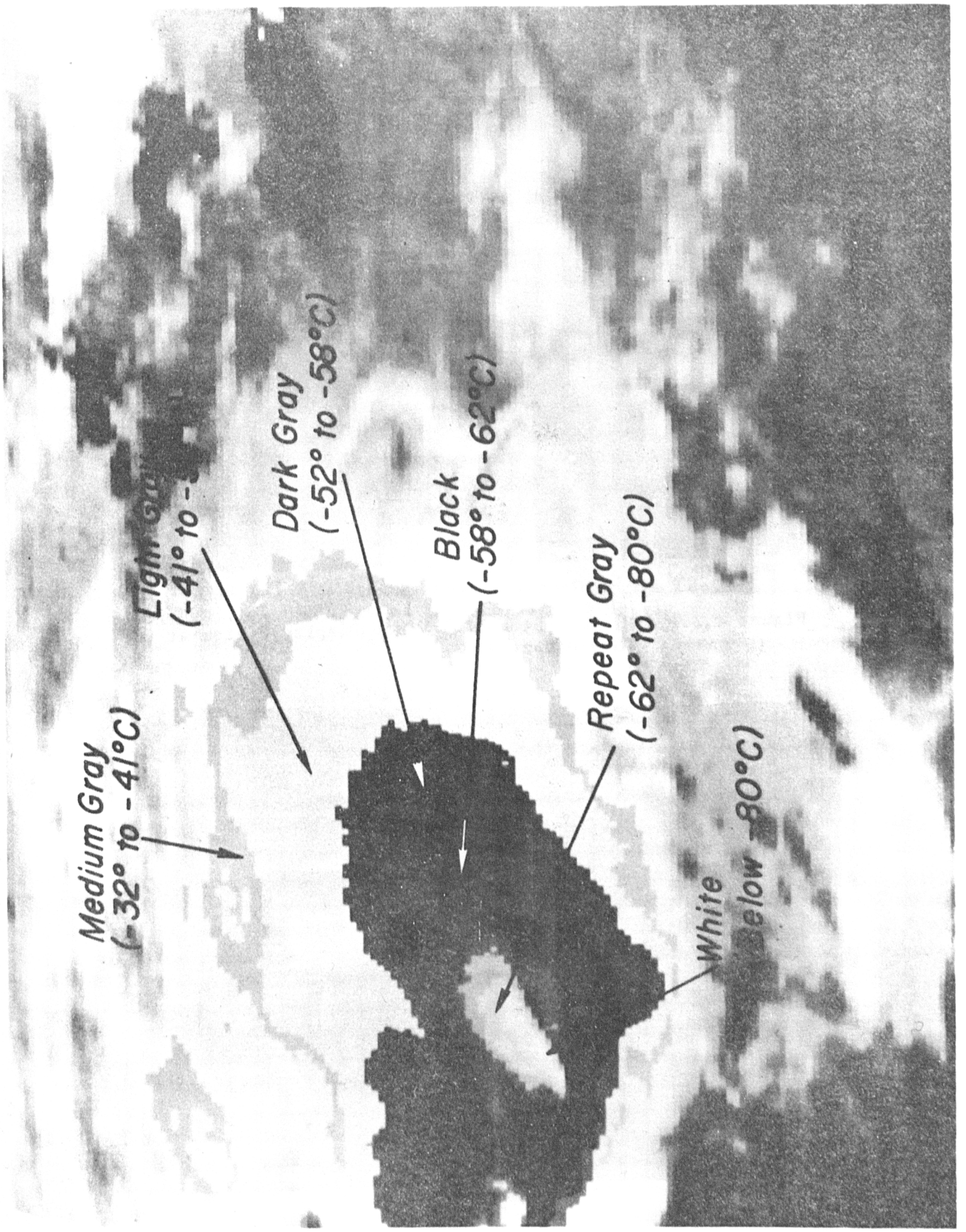

Figure 4.1.3 Example of a GOES Enhanced Infrared Image (Clark, 1983) (Slide Set #309)

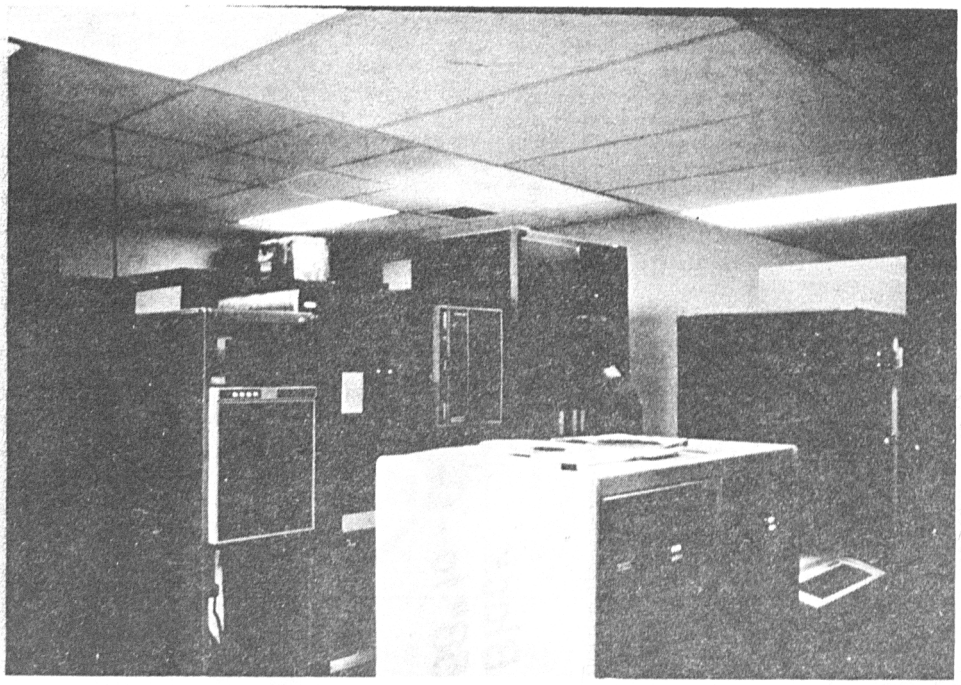

Figure 4.2.1 Minicomputers for Video Display System at CSU (Slide Set #3)

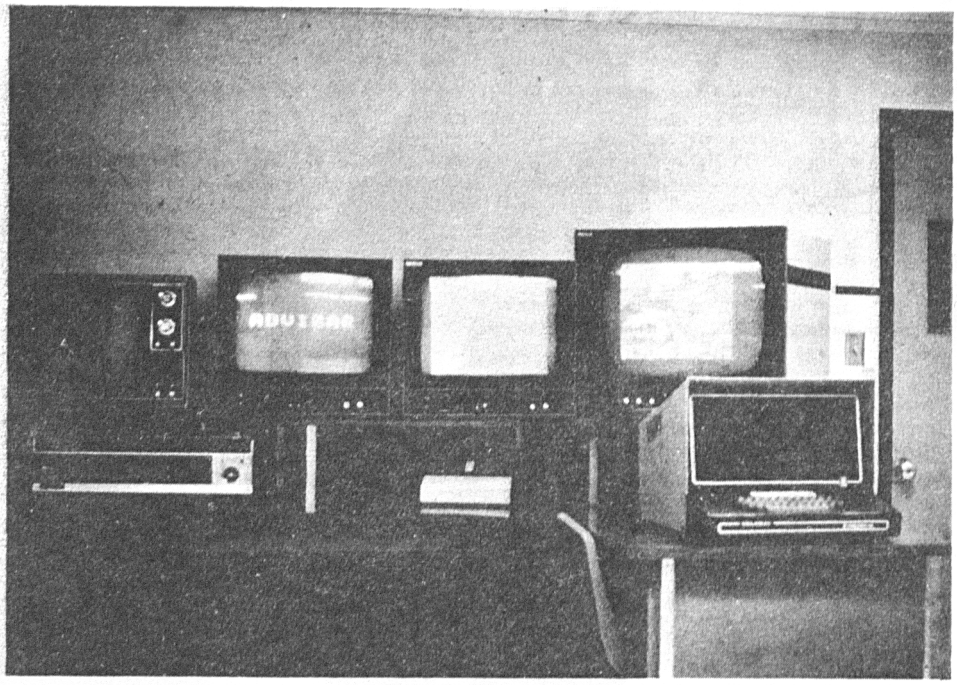

Figure 4.2.2 Terminals for Video Display System at CSU (Slide Set #4)

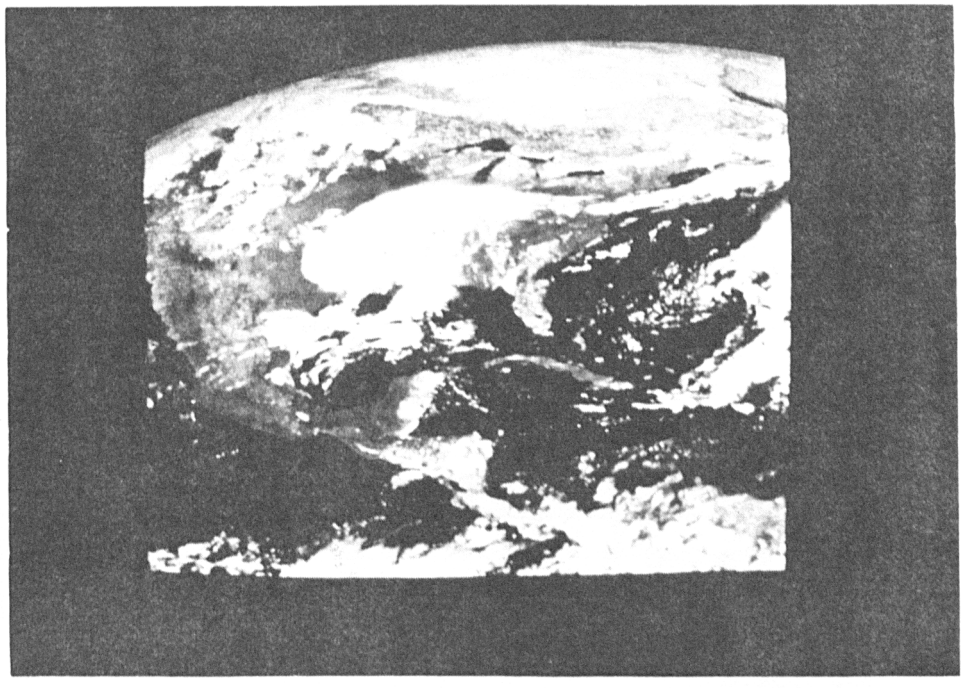

Figure 4.2.3 Strong Winter Storm Over the Central United States in GOES Visible Image (Slide Set #11)

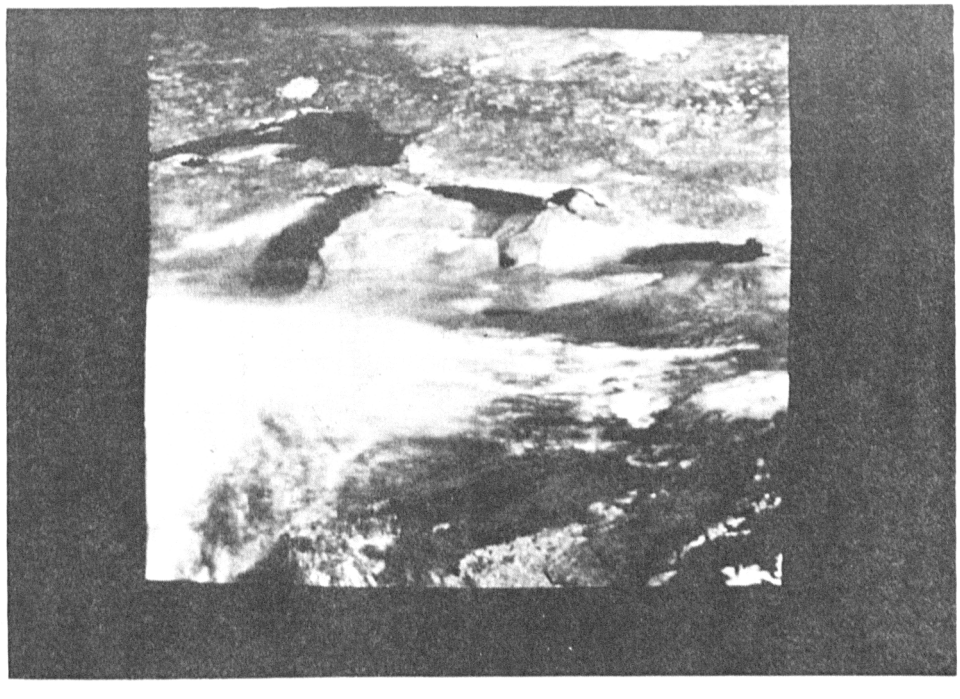

Figure 4.2.4 Zoom of Figure 4.2.3 (Slide Set #9)

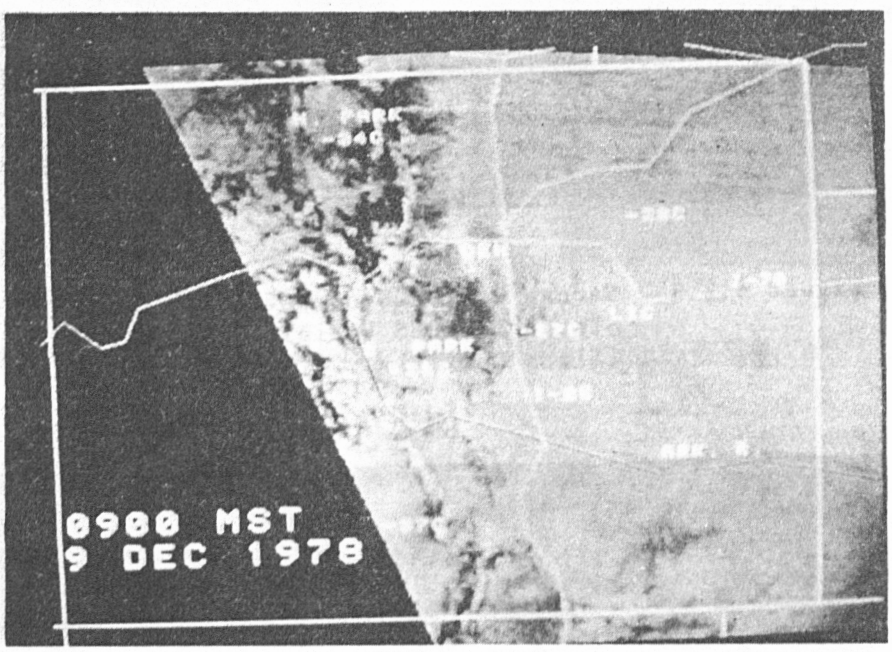

Figure 4.2.5 GOES Visible Image over Colorado with Interstate Highways Superimposed (Slide Set #14)

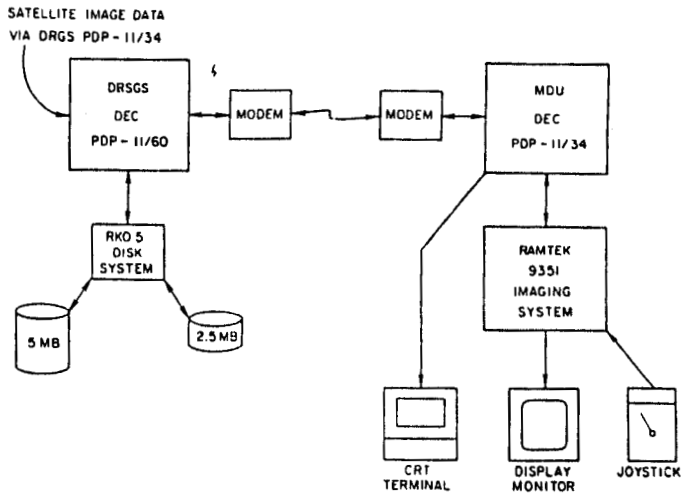

Figure 4.2.6 Block Diagram of CSU Mobile Display Unit

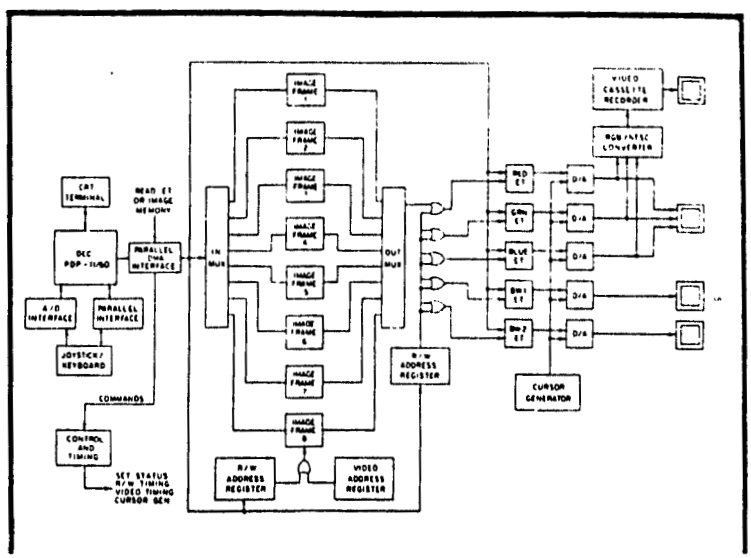

Figure 4.2.8 Schematic of the All Digital Video Imaging System for Atmospheric Research (ADVISAR) at CSU

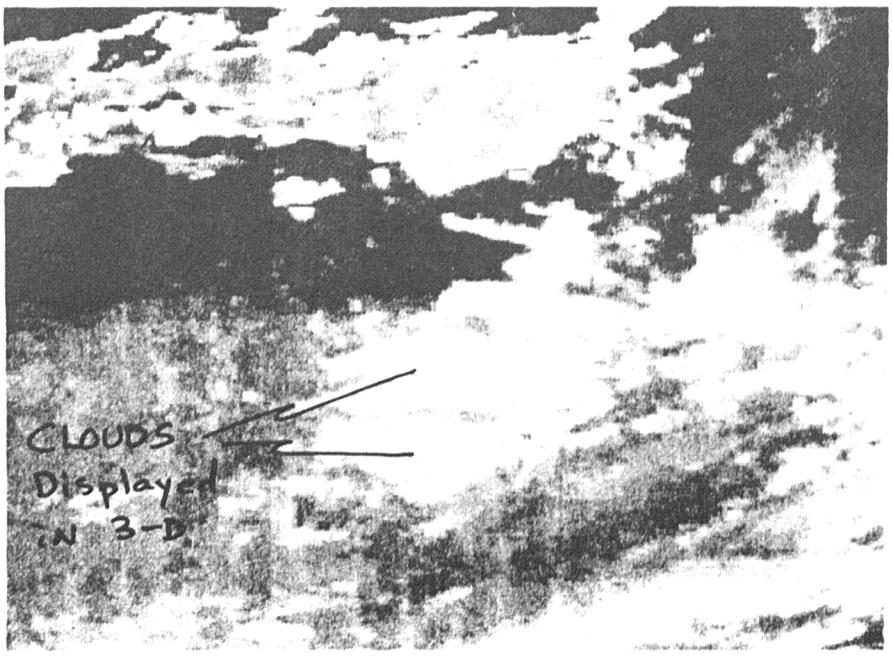

Original infrared image.

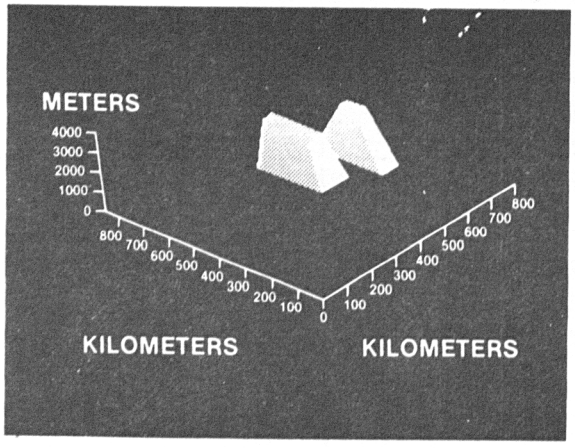

Cloud representation using a crude polygon approximation.

Three-dimensional cloud picture with dimensions.

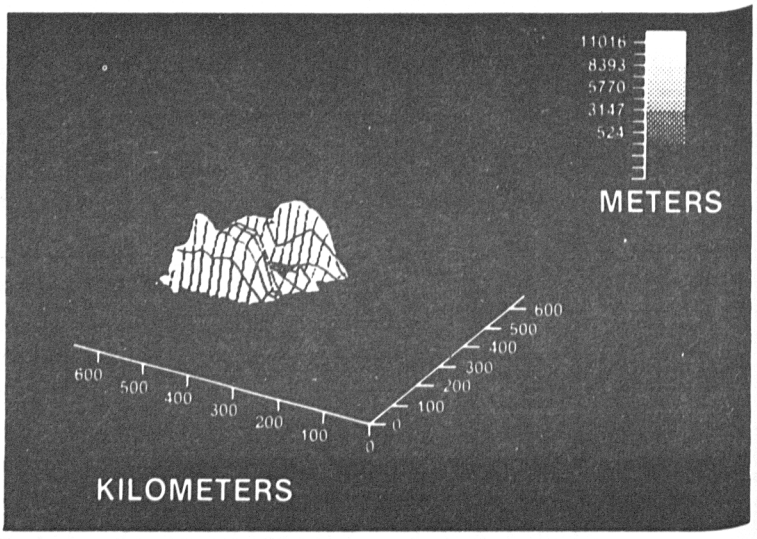

Figure 4.2.7 Three-Dimensional Display of Clouds from a GOES Infrared Image (Brubaker, 1982)

CHAPTER 5

FUNDAMENTALS OF RADIATIVE TRANSFER USED IN MEASUREMENTS FROM SATELLITES

The study of radiative transfer is basic to the understanding of satellite measurements. This chapter contains a brief description of radiative transfer quantities, definitions and some basic radiation laws. The chapter concludes with a simple formulation of the radiative transfer equation for the visible, infrared and microwave regions. The reader is urged to pursue this subject by referring to the suggested reading list.

5.1 Basic Radiometric Quantities

	Symbol	Unit	Dimensions
Radiant Energy	E,(U)	Joule	ML^2T^{-2}
Radiant Power	P	Watt	ML^2T^{-3}
Radiant Intensity	J	Watt sr^{-1}	$ML^2T^{-3}(sr^{-1})$
Radiant Exittance	W	Watt m^{-2}	MT^{-3}
Irradiance	H		
Radiance	N	Watt m^{-2} sr^{-1}	$MT^{-3}(sr^{-1})$
Wavelength	λ	cm or μm	L
Wavenumber	ν	cm^{-1}	L^{-1}
Spectral Radiant	E_λ	Joule m^{-1}	MLT^{-2}
Energy	E_ν	Joule m	ML^3T^{-2}
Spectral Radiant	P_λ	Watt m^{-1}	MLT^{-2}
Power	P_ν	Watt m	ML^3T^{-2}
Spectral Radiance	N_λ	Watt $m^{-3}sr^{-1}$	$ML^{-1}T^{-3}(sr^{-1})$
	N_ν	Watt $m^{-1}sr^{-1}$	$MLT^{-3}(sr^{-1})$

emittance - ε - ratio of emitted radiant power to that from an ideal black body at the same temperature

absorptance - a - ratio of absorbed radiant power to incident radiant power

reflectance - ρ - ratio of reflected radiant power to incident

transmittance - τ - ratio of transmitted radiant power to incident

5.2 Definitions

Solid Angle: (See Figure 5.2.1) The solid angle subtended by any surface "A" at any point "O" is equal to the area A' of the portion of a sur-

face of a sphere of unit radius, center at "O", which is cut by a conical surface with vertex at "O", passing through the perimeter of A.

Notes:

a) A sphere subtends a solid angle of 4π steradians (about point "O").

b) A hemisphere subtends a solid angle of 2π steradians (about point "O").

The reader is urged to compute the solid angle of a hemisphere by integrating the area element, $d\Omega$, where

$$\int_{2\pi} d\Omega = \int_{\phi=0}^{2\pi} \int_{\theta=0}^{\pi/2} \sin\theta d\theta d\phi = 2\pi$$

Solid angle is defined at unit radius, r=1.

<u>The Electromagnetic Spectrum:</u>

We will use the following divisions of "Radiation":

"Shortwave"	0.1 - 3.0 μm
"Longwave"	3.0 - 100.0 μm (0.1 mm)
"Microwave"	0.1 mm - 20.0 cm

($\mu m = 10^{-6} m$)

wavenumber $v = \lambda^{-1}$ with λ in cm

e.g., $\lambda = 10\ \mu m$; $v = 1000\ cm^{-1}$

Optical Mass

The optical mass of a radiatively active gas is defined as the mass of that particular gas contained in a vertical column of unit cross-section between two arbitrary reference planes.

$$u = \int_{z_1}^{z_2} \rho_v dz \qquad (5.1)$$

Optical Path (See Figure 5.2.2)

$$u^* = \int_{x_1}^{x_2} \rho_v dx \qquad (5.2)$$

$$dx = \pm dz \sec\theta$$

$$u^* = u \sec\theta$$

Note: $\sec\theta = 2$ (at $\theta = 60^o$) "air mass"

Optical Depth

Sometimes called thickness.

$$\tau = \int_{x_1}^{x_2} K\rho_v dx \qquad (5.3)$$

K = mass extinction

Generally, $K = K(v)$, so $\tau = \tau(v)$

$$\tau_v = K_v u^*$$

$$\tau_v = K_v u \sec\theta$$

Note: τ is sometimes used as a vertical coordinate; sometimes it is used to imply geometric thickness (when K and ρ are constant) .

Note: Transmittance, t related to τ by: $t = e^{-\tau}$

5.3 Basic Radiation Laws

1) Kirchhoff's Law: The spectral emittance of a substance in local thermodynamic equilibrium (L.T.E.) is equal to the spectral absorptance.

$\varepsilon_\lambda = a_\lambda$ From observation, Kirchhoff decided "good absorbers were good emitters".

Notes:

a) L.T.E. exists when the electrons, ions or molecules of a substance undergo many collisions before they recombine or have radiative transition such that a condition exists that can be characterized by a single local temperature (i.e., this implies that the state parameters p, T and ρ are homogeneous in the portion of the substance in question)

b) Kirchhoff also proposed the term BLACKBODY to apply to a substance that absorbed all incident radiant energy (According to his law, this would be the ultimate radiator.) - it would be a standard of comparison.

In 1879, Stefan (then Boltzmann in 1884) used experiments to conclude that for a BLACKBODY

$$W = kT^4 \qquad (5.4)$$

Wien in 1894 published the "Displacement Law" that fit experimental data only at short wavelengths and at low temperatures.

Also, Rayleigh in 1900 used classical physics to derive an equation to fit experimental data at long wavelengths and high temperatures (however, at short wavelengths the energy increased too much - the "Ultraviolet Catastrophe".

In view of all the above,

Planck: a) first derived a formula to interpolate between the above

b) found it verified by experiment

c) then explained his work theoretically using QUANTUM PHYSICS

2) Planck's (Most Basic) Radiation Law: A substance with $\varepsilon_\lambda = 1.0$ (a BLACKBODY) radiates according to these formulae.

$$W_\lambda = \frac{C_1 \lambda^{-5}}{\exp[C_2 \lambda^{-1} T^{-1}] - 1} \qquad (5.5)$$

$$W_\nu = \frac{C_3 \nu^{3}}{\exp[C_4 \nu T^{-1}] - 1} \qquad (5.6)$$

$$C_1 = 2hc^2 = 1.1911 \times 10^8 \text{ W m}^{-2}\mu\text{m}^4$$

$$C_2 = chk^{-1} = 1.4388 \times 10^4 \mu\text{m K}$$

$$C_3 = 2hc^2 = 1.1911 \times 10^{-8} \text{ W m}^{-2}\text{cm}^{-4}$$

$$C_4 = chk^{-1} = 1.4388 \text{ cm K}$$

where c = speed of light $\approx 3 \times 10^8$ m s^{-1}

h = Planck's constant = 6.63×10^{-34} J s^{-1}

k = Boltzmann's constant = 1.281×10^{-23} J K^{-1}

Note: If we know spectral emittance of a substance we can use Planck's Law and value of ε_λ to get W_λ from the non-BLACKBODY.

3) <u>Stefan-Boltzmann Law</u>: Integrate Planck's Law

$$W = \int_{0\lambda}^{\infty} W_\lambda \, d\lambda = \int_0^{\infty} \frac{C_1 \lambda^{-5}}{\exp[C_2 \lambda^{-1} T^{-1}] - 1.} \, d\lambda \qquad (5.7)$$

$$= \frac{2\pi^4 k^4}{15 c^2 h^3} = \sigma T^4$$

where $\sigma = 5.67 \times 10^{-8} Wm^{-2} K^{-4}$

4) <u>Wien's Displacement Law</u>:

Differentiating Plank's Law ($dW_\lambda/d\lambda$) and solving for λ_{max} at $dW_\lambda/d\lambda = 0$

$$\lambda_{max} = \frac{2897}{T} \ (\mu m \ K) \qquad (5.8)$$

for example, if T = 293 K

then, $\lambda_{max} = 9.9 \ \mu m$

5) Rayleigh-Jeans Approx.: (Large λ) Microwave applications

$$W_\lambda \approx 2kcT \cdot \lambda^{-4} \qquad (5.9)$$

since $(e^x - 1) \rightarrow x$ as $x \rightarrow 0$

5.4 The Equation of Radiative Transfer

Derivation: Consider a volume as in Figure 5.4.1.

The spectral radiance $N_v\ (P, \vec{r})$ at P_1 in the direction $\vec{r}$ is:

$$N_v(P,\vec{r}) = N_v\ (P_o,\vec{r}) + \frac{\partial N_v . ds}{\partial s} \qquad (5.10)$$

where the "source term" $\frac{dN_v}{ds} . ds = A + B + C + D$

A = Absorption of radiant energy between P_o and P_1

B = Attenuation due to scattering "out of the beam"

C = Emission from within the volume in the r direction

D = Radiant energy scattered from other direction, r, into the r direction

For any given radiative transfer case one or all "source" terms must be considered (e.g., for direct solar energy, only A + B; for thermal infrared, generally A + C).

Solar "Shortwave"

$$(N_r)_v = \int \rho(\delta,\theta,\psi) N \cos_i \, d\Omega \qquad (5.11)$$

$$\rho(\delta,\theta,\Psi) = \frac{N_r}{N_i \cos\delta \; \Delta\Omega} = \frac{N_r}{H_o \cos\delta}$$

"Albedo"

$$\text{"A"} = r(s) = \int \rho(\delta,\theta,\psi) \sin\theta\cos\theta d\theta d\psi \qquad (5.12)$$

for diffuse reflecting surface $\rho(\delta,\theta,\psi)$ = const.

$$r(s) = \pi\rho(\delta,\theta,\psi)$$

but for anisotropic surface, the factor

$$X(\delta,\theta,\psi) = \frac{r(s)}{\pi \; \rho(\delta,\theta,\psi)} \neq 1.0$$

IR and Microwave

IR source function is Planck function, B.

$$(N_r)_v = \underbrace{\varepsilon_o B(T_o)\tau(p_o)}_{\text{(surface)}} - \underbrace{\int_o^{p_o} B[T(p)] \frac{d\tau}{dp} dp}_{\text{(atmosphere)}} \qquad (5.13)$$

Approx.: Planck function at long wavelengths (Rayleigh-Jeans approx.) allows measured microwave radiance to be expressed as "brightness" temperature.

$$(T_B)_\lambda = \varepsilon_s T_s \tau_H + (1 - \varepsilon_s) T_{sky} \tau_H + \int_o^H T_A(h) \frac{d\tau}{dh} \cdot dh \qquad (5.14)$$

ε_s = surface emittance

τ = atmos transmittance = $e^{-\sec\theta \int_0^h K\rho dh}$

T_S = surface temp; T_{sky}; T_A

Typical ε_S:

Water = 0.41 (calm)

Ice = 0.97

Wet soil = 0.70

Dry soil = 0.80

$\tau \approx 1.0$ from 2 - 20 cm (window), but H_2O at 1.35 cm; O_2 at 0.6 cm.

References and Suggested Reading

Chandrasekhar, S., 1950: Radiative Transfer. Dover, New York, 393 pp.

Goody, R. M., 1964: Atmospheric Radiation. I.: Theoretical Basis. Oxford Univ. Press (Clarendon), London and New York, 430 pp.

Hudson, R. D., 1969: Infrared System Engineering. Wiley and Sons, Inc., 642 pp.

Kondratyev, K. Ya., 1969: Radiation in the Atmosphere. Academic Press, New York, 912 pp.

Liou, K-N, 1980: An Introduction to Atmospheric Radiation, Academic Press, New York, 392 pp.

Paltridge, G. W. and C. M. R. Platt, 1976: Radiative Processes in Meteorology and Climatology, Elsevier Scientific Pub. Co., New York, 318 pp.

Planck, M., 1959: The Theory of Heat Radiation. Dover (reprint of 1910 edition), New York, 224 pp.

Raschke, E. (editor), 1978: Terminology and units of radiation quantities and measurements. International Association of Meteorology and Atmospheric Physics - Radiaiton Commission, 17 pp.

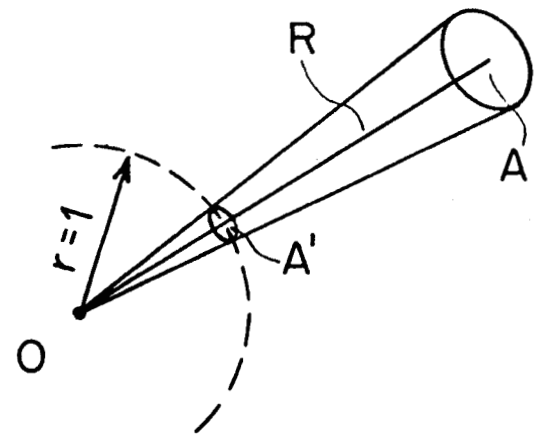

Figure 5.2.1 Solid Angle

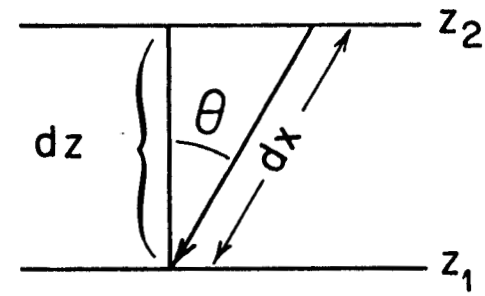

Figure 5.2.2 Optical Path

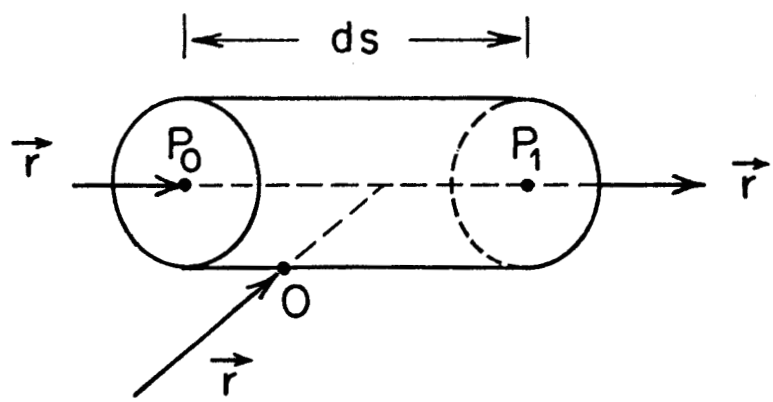

Figure 5.3.1 Radiative Transfer Volume

SECTION II

PRACTICAL APPLICATIONS

Twelve chapters comprise this section. They deal with applications of measurements from meteorological satellites to obtain information about the basic state parameters of the atmosphere, such as temperature, moisture and winds. They also discuss in Chapters 8, 9 10 and 11 the use and identification of clouds from satellites in order to obtain meteorological information about synoptic weather patterns, tropical storms and weather systems, and small-scale weather features. Chapters 12, 13 and 14 deal with severe mesoscale storms and rainfall estimation techniques. Chapter 15 covers several other atmospheric features viewed from weather satellites. Chapters 16, 17 and 18 deal with satellite applications related to weather modification and cloud physics programs, air-sea interaction and climatology studies. Because this set of lecture notes is designed as an introduction to the use of satellites by weather forecasters and those interested in research, it has been possible to cover most of the applications devoted to weather forecasting but certainly not all the ways in which satellites are used to obtain information for research projects. Thus, the reader will note the absence of sections dealing with detection of upper atmospheric density from satellites, the measurement of atmospheric constituents other than water vapor and other important research areas. Many of the documents referenced in the individual chapters lead the reader to discussion of these and other important research aspects of the satellite programs. For those interested in an overview and

summary of some of the practical applications of meteorological satellites anticipated in the 1980's and beyond, you are referred ahead to Chapter 20 in the next section.

CHAPTER 6

ATMOSPHERIC TEMPERATURE AND MOISTURE SOUNDINGS FROM SATELLITES

Since the early 1960's, satellite instruments have been measuring spectral radiances in the infrared (IR) regions. These spectral measurements are obtained in both the "strong" and "weak" absorption regions of a gas such as CO_2 or H_2O which has a known or assumed distribution. Only more recently have similar measurements been obtained in the microwave O_2 absorption band. These measurements can then be "inverted" [in reference to inverting the Radiative Transfer Equation (RTE)] to obtain estimates of atmospheric temperature and water vapor in the vertical. A better terminology would be to "retrieve" temperature and moisture profiles, since some of the methods used for this process do not directly involve the RTE.

It must be remembered that satellite soundings are inherently different than radiosonde (RAOB) measurements. The satellite measures temperatures and moisture over layers, not at levels. Measurements, therefore, are more like thicknesses. The estimated vertical profiles are smoother, but the big advantage is the better horizontal resolution (down to 15 km or less) and better horizontal gradient information. The main drawback to IR soundings has been the inability to sound below clouds. Thus, the use of microwave measurements which are largely unaffected by cloud contamination. These trade-offs will be examined.

Many satellite instruments and methods have been devised for the retrieval process. The discussion in this chapter will be limited mainly

to the use of infrared measurements taken in a downward-looking mode. The retrieval of atmospheric temperatures and water vapor will be discussed. Results using microwave measurements will be found in the references.

6.1 Fundamental Principles (Theory)

Purpose: To obtain remote measurements of the vertical temperature profile (as well as water vapor and ozone)

History: Basic approach and many methods pioneered by astronomers in their (remote) study of stellar atmospheres

Status:
a) First successful satellite experiments flown on NIMBUS-III (launched 14 April 1969)
b) Best methods of data reduction not yet finalized
c) Improved experiments planned for future sun-synchronous and geo-synchronous satellites

Physical Basis:

a) Intuitive
   1) the earth's surface (or clouds) emits IR radiation at all wavelengths
   2) the gases in the atmosphere selectively absorb (and re-emit at their characteristic temperature) the radiation of preferred wavelengths
   3) in a strongly absorbing portion of the spectrum (λ_1) the atmosphere is opaque when viewed from space; conversely, in a weakly absorbing region (λ_2) the radiation to space comes mostly from the surface (or cloud), i.e., the atmosphere is nearly transparent.

4) in a moderately absorbing part of the spectrum (λ_3) the upper part of the atmosphere is relatively transparent, but the energy reaching space will not come from the surface, rather from molecules in the middle troposphere. These molecules have absorbed the energy emitted from the surface and re-emit at their characteristic temperature (the temperature of the middle troposphere)

5) If we have a gas (i.e., CO_2) uniformly mixed through most of the atmosphere, measurements at λ_1, λ_2 and λ_3 give us information about the ambient temperature in the stratosphere, lower troposphere and middle troposphere, respectively.

6) The problem is then to choose a set of λ_N, measure the IR radiance at these wavelengths, "invert" the measurements to determine a vertical temperature profile.

The theory outlined above can be applied to several absorption bands. An an example, the wavelengths (or wavenumbers) used by the NIMBUS-4 IRIS (InfraRed Interferometer Spectrometer) are shown in Figure 6.1.1. The measurements are taken on the longer wavelength side of the 15 μm CO_2 absorption band. The other side of the band is more highly influenced by rotational water vapor absorption.

As an alternative, other absorption bands, such as the CO_2 band at 4.3 μm, can be used. CO_2 has a relatively constant mixing ratio in the atmosphere, so changes in the measured radiances can be assumed to be caused by changes in the temperature of the absorber. The layer over which

the measurements are obtained are dependent on the spectral interval that is being observed. Other regions in which spectral measurements can be obtained for sounding purposes are shown in Figure 6.1.2. The H_2O absorption bands are used to estimate atmospheric water vapor content, and the window channel regions are used to avoid most atmospheric absorption in order to measure the surface temperature. Equivalent regions in the microwave around 1 cm are also shown. These various regions have advantages and disadvantage as shown in Figure 6.1.3. The main advantage of microwave measurements is the high cloud transmission. This, however, is balanced by low relative energy at these long wavelengths.

As a note, it must also be mentioned that there is a trade-off in the use of spectral bandwidth between energy and vertical resolution. As the spectral band width is reduced, the vertical layer over which the channel measures in the atmosphere is narrowed, but that results in lower energy at the detector. Thus, the trade-off. In order to obtain sufficient energy above the noise level of the detector, the bandwidth must be wide enough, with the result that the vertical resolution of the measurement is limited to a broad region of the atmosphere. Typical band widths of 10 to 20 cm^{-1} give a vertical resolution of about 300 mb in the vertical.

6.2 Mathematical

The Equation of Radiative Transfer (for a plane - parallel atmosphere) is:

$$\mu \frac{dI_\nu(\tau_\nu,\mu)}{d\tau_\nu} - I_\nu(\tau_\nu,\mu) = - J_\nu(\tau_\nu,\mu) \qquad (6.1)$$

where I_ν = monochromatic radiance

J_v = the "source function"

τ_v = the optical depth of the atmosphere

μ = cos θ; θ = angle between the radiation stream and the surface (i.e., layer of the atmosphere)

In a <u>non-scattering</u> atmosphere in <u>local</u> <u>thermodynamic</u> <u>equilibrium:</u>

$$J_v(\tau_v) = B_v(\tau_v) \qquad \text{; the Planck function}$$

Equation 6.1 is a linear differential equation of the 1st order, for example:

$$\frac{dy}{dx} - P_y = Q$$

The integral solution for Equation 6.1 is:

$$I_v(\tau_v,\mu) = \varepsilon_v B_v(T_s)\, t_v(\tau_s) - \int_0^{\tau_s} B_v(\tau_v)\frac{dt(\tau_v,\mu)}{d\tau_v}\, d\tau_v \qquad (6.2)$$

Notes on Equation 6.2:

a) subscript (s) refers to the surface boundary (land or cloud)

b) ε_v = spectral emittance of the surface (assume ε_v = 1.0)

c) t = the fractional transmittance of the atmosphere from the level τ to the top of the atmosphere $t = e^{-\tau}$

d) variable parameters in this equation are v and μ (i.e., wavenumber and direction of measurement)

e) τ, and therefore t, is known from the knowledge of atmospheric physics

f) 1st term gives contribution to I_v from the surface (it is ZERO at

an opaque wavelength)

g) 2nd term represents the atmospheric contribution of energy to I_v; it is the average of the source function over the "weighting factor".

Use of Equation 6.2 in the atmosphere:

Since $\tau_v = \int_z^{\infty} K_v \rho dz$

with: K_v = mass absorption coefficient

ρ = density of absorbing gas

z = height

then:

$$-\int_0^{\tau_s} B_v(\tau_v) \frac{dt}{d\tau_v} d\tau_v = \int_0^{\infty} B_v(z) \frac{dt}{dz} dz = \int_0^{\infty} B_v(p) \frac{dt}{d(\log p)} d(\log p)$$

Viewing down from space ($\theta = 0^o$, $\mu = 1$) where $\tau_v = 0$, Equation 6.2 is.

$$I_v(0,1) = \varepsilon_v B_v(T_s) t_v(p_s) - \int_0^{\infty} B_v(p) \frac{dt(p)}{d(\log p)} d(\log p) \qquad (6.3)$$

For an opaque wavenumber, v, the first term is zero and:

$$I_v(0,1) = -\int_0^{\infty} B(p) \frac{dt(p)}{d(\log p)} d(\log p) \qquad (6.4)$$

which as the form of

$$R(m) = \int_0^{\infty} K(m,p) f(p) dp \qquad (6.5)$$

where: R is a measured radiance from the satellite depending on m, a parameter of measurement (e.g., wavelength <u>or</u> viewing angle)

f is an atmospheric parameter [temperature of gas (H_2O or O_3)] we want to determine

K (m,p) is the "weighting function" or KERNEL of the integral, examples of which are shown in Figure 6.2.1.

Discussion of the KERNEL:

1) K (m,p) specifies how much parameter f at p contributes to the radiance R for a particular value of m

2) In the earth's atmosphere, K (m,p) can be computed from atmospheric physics

3) In the plots of the KERNELS shown, note that:

a) the contribution at a given v can come from a broad layer of the atmosphere (i.e., 10 km thick). Thus, inversion of Equation 6.5 with such kernels can give only a coarse vertical resolution of the parameter, f.

b) a given altitude will usually contribute radiance at more than one wavelength. This shows a natural redundancy between a set of equations formed from measurements at a set of wavelengths

c) no information about the parameter, f, can be obtained (from a formal inversion) at heights that do not make a reasonable contribution to radiance at any frequency.

Solution (inversion) of Equation 6.5:

The inversion problem is essentially to obtain an optimum amount of meteorological information from the radiometric measurements.

In practice, difficulties arise because:

1) Equation 6.5 (and Equation 6.4) is a Fredholm integral equation of the 1st kind. It does not have a unique analytical solution.

2) Error in the radiance measurements means that we actually measure $[R(m) + \varepsilon(m)]$, where $\varepsilon(m)$ is the measurement error

3) We do not measure a continuous function R(m), but a set of discrete values (in separate radiometer "channels"), some of which contain redundant information.

Twomey (1966) has discussed the nature of the KERNEL, the effect of errors, and methods of solution.

Solutions may be categorized as:

1) trial and error (iterative)

2) linear or non-linear analytical

3) linear or non-linear statistical

6.3 Results

Most retrieval results have been compared to RAOBs, but as mentioned earlier, these two sets of measurements are inherently different. One is radiometric and the other is *in situ*. As a result the two sets will never match perfectly because the satellite measures over a volume and the RAOB at a series of points.

In spite of these differences, most meteorologists/users would prefer a satellite sounding to look like a RAOB as in Figure 6.2.1. This figure shows some of the first results from SIRS (Satellite InfraRed Spectrometer). The SIRS filter wheel radiometer design is similar to those which continue to be used today. Results of comparison to RAOBs have been largely unchanged throughout the history of satellite soundings with rms differences of 2 to 3°C compared to RAOB temperatures at various levels.

An alternative way of looking at the satellite soundings is in terms of thicknesses, since the satellite instrument senses over a relatively large vertical depth of the atmosphere. As a result more of the satellite-derived products are given either as geopotential thickness or in terms of integrated water vapor.

To be more radical, the radiances themselves can be interpreted in terms of their horizontal variations. The high resolution of the satellite sounder makes such gradient information easy to obtain. For example, Hillger and Vonder Haar (1979) used statistical structure function analysis of the satellite radiances alone to interpret the gradients in VTPR (Vertical Temperature Profile Radiometer) measurements.

Only recently have sounding instruments been placed in geosynchronous orbit (Smith et al., 1981). The distance (≈ 36,000 km) limits the use of microwave measurements at this time. The advantage of the view from geosynchronous orbit is the ability to observe time changes in satellite-derived products. These changes can be equal in magnitude to those observed at high-horizontal resolutions.

6.4 Impact

The impact of satellite soundings has been felt in two areas: mesoscale forecasting and numerical models. Because of the high-horizontal resolution of most satellite soundings, the ability of the satellite measurements to observe details of a resolution below that of the RAOBs (≤ 250 km) has been well documented. The observation of atmospheric moisture is especially important at the mesoscale. Hayden et al., (1981) give a good summary of methodology and results from the HIRS-2 (High-resolution InfraRed Sounder) on TIROS-N.

A second area of impact has been the result of the use of satellite soundings in numerical weather prediction models. The impact has not been fully positive or negative. A conclusion is that satellite soundings possibly add little in an area where conventional (RAOB) measurements are common. The true advantage is again the result of the use of the satellite-derived values in data-sparse or data-void regions.

6.5 Direct Sounder Broadcast

The TIROS-N/NOAA satellite series contains a Direct Sounder Broadcast (DSB) output at VHF frequencies. This capability allows a relatively low

cost receiving station to acquire sounding data from these polar-orbiting satellites. Limited detail can be found in Werbowetzki (1981) and Barnes and Smallwood (1982). It is estimated that a complete data receiving and analysis setup (via mini-computer) may be available for U.S. $10,000.

References and Additional Reading

Barnes, J. C. and M. D. Smallwood, 1982: TIROS-N series direct readout services users guide. NOAA-S/T-82-86, 122 pp.

Grody, N. C., A. Gruber and W. C. Shen, 1980: Atmospheric water content over the tropical Pacific derived from the Nimbus-6 scanning microwave spectrometer. J. Appl. Meteor., 19, 986-996.

Hayden, C. M., W. L. Smith and H. M. Woolf, 1981: Determination of moisture from NOAA polar orbiting satellite sounding radiances. J. Appl. Meteor., 20, 450-466.

Hillger, D. W. and T. H. Vonder Haar, 1979: An analysis of satellite infrared soundings at the mesoscale using statistical structure and correlation functions. J. Atmos. Sci., 36, 287-305.

Ohring, G., 1979: Impact of satellite temperature sounding data on weather forecasts. Bull. Amer. Meteor. Soc., 60, 1142-1147.

Smith, W. L., 1972: Satellite techniques for observing the temperature structure of the atmosphere. Bull. Amer. Meteor. Soc., 53, 1074-1082.

Smith, W. L, V. E. Suomi, W. P. Menzel, H. M. Woolf, L. A. Sromovsky, H. E. Revercomb, C. M. Hayden, D. N. Erickson and F. R. Mosher, 1981: First sounding results from VAS-D. Bull. Amer. Meteor. Soc., 62, 232-236.

Twomey, S., 1977: Introduction to the Mathematics of Inversion in Remote Sensing and Indirect Measurements, Elsevier Scientific Pub. Co., New York, 243 pp.

Twomey, S., 1966: Indirect measurements of atmospheric temperature profiles form satellite: II. Mathematical aspects of the inversion problem. Mon. Wea. Rev., 94, 363-366.

Werbowetzki, A. (editor), 1981: Atmospheric Sounding User's Guide. NOAA Technical Report, NESS 83, 82 pp. [NTIS Ref: PB81-230476].

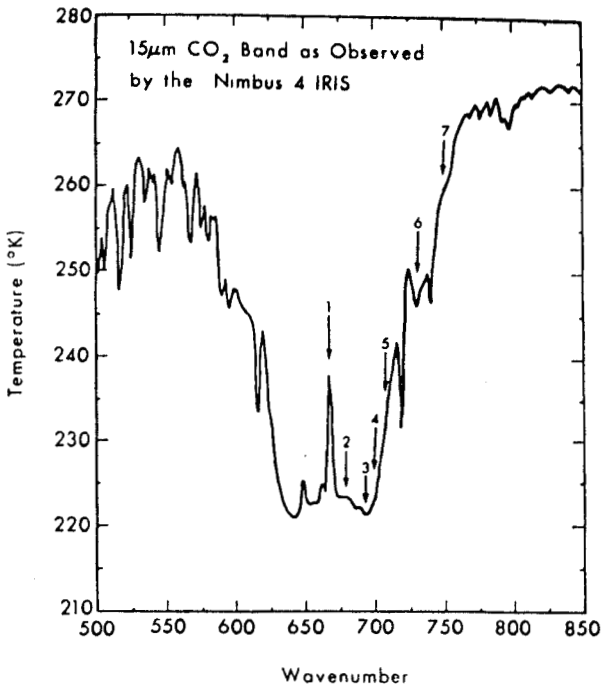

Figure 6.1.1 15 μm CO_2 Band (Smith, 1972)

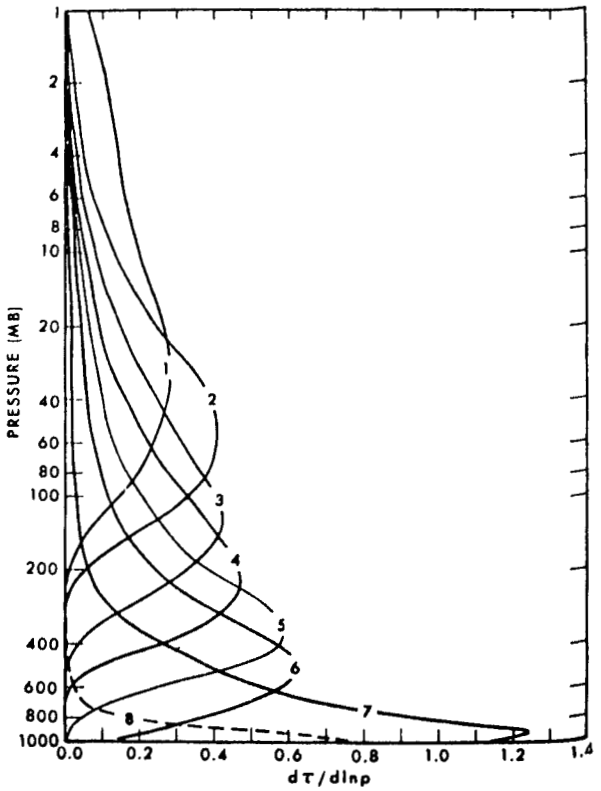

Figure 6.3.1 Weighting Functions (Smith, 1972)

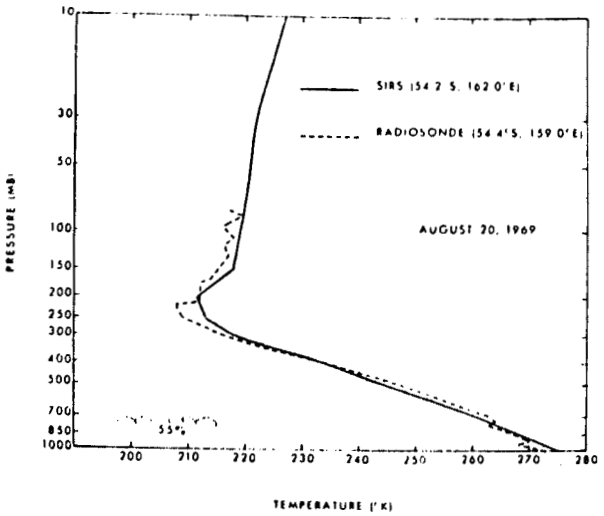

Figure 6.2.1 Radiosonde -- SIRS Comparison (Smith, 1972)

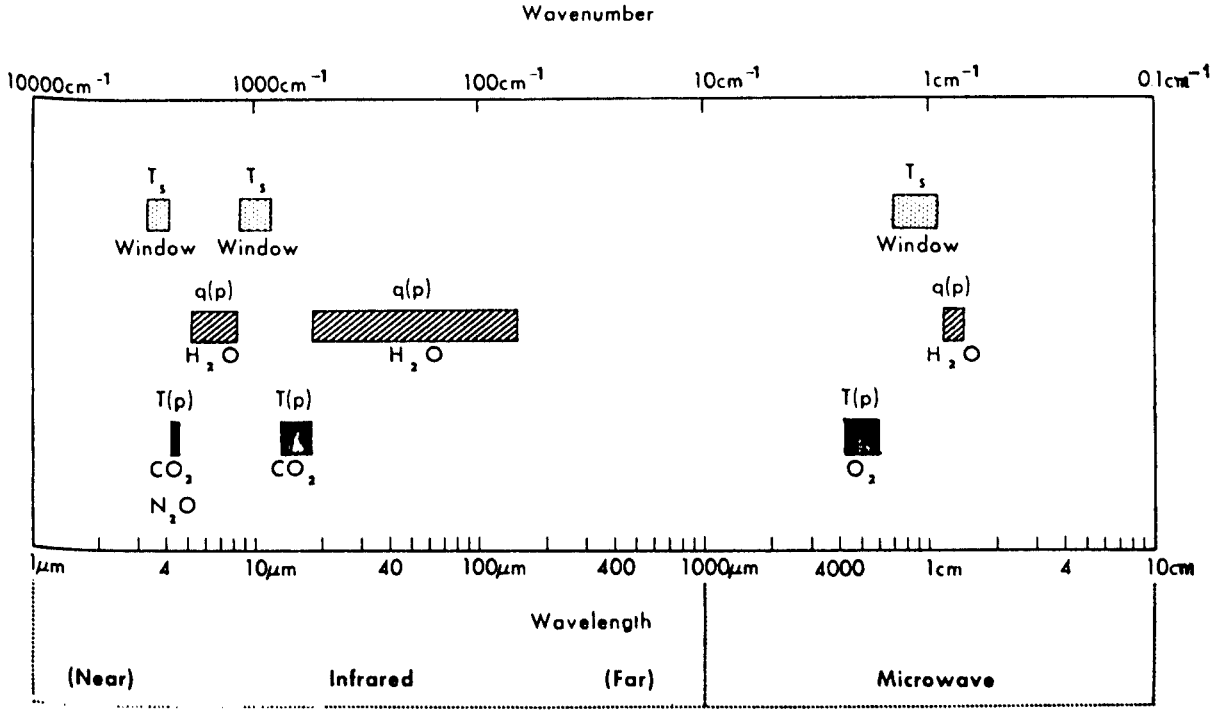

Figure 6.1.2 Spectral Bands for Indirect Sounding (Smith, 1972)

ENERGY (Relative Planck Radiance)

	200°K	300°K
4.3μm	1.25	200
15.0μm	5000	15000
5.0mm	1	1

TEMPERATURE SENSITIVITY (Relative to Detector Noise*)

	200°K	300°K
4.3μm	1	20
15.0μm	10	6
5.0mm	4	1

*(0.002, 0.2 erg/cm² s str cm⁻¹, 0.7°K)

CLOUD TRANSMISSION

	Water	Ice
4.3μm	6%	1%
15.0μm	1%	1%
5.0mm	96%	99.98%

Figure 6.1.3 Characteristics of Spectral Bands (Smith, 1972)

Blank page retained for pagination

CHAPTER 7

WIND ESTIMATION FROM CLOUD MOTION

One of the first applications of the increased time resolution of satellite images from geosynchronous orbit was in the estimation of winds (Suomi et al., 1969). The horizontal wind component is determined by using clouds as the tracers. The assumption is that the clouds follow the wind. Both manual and automatic tracking methods have been developed. Problems, however, exist with the assumption that the clouds follow the wind and in determining which level in the atmosphere is best represented by the estimated wind. Some more recent methods have used infrared sounding channels to give a vertical level assignment and water vapor images have been used to track moisture features at high levels (above 500 mb) without the need for clouds.

7.1 Methods

7.1.1 Manual Tracking

In two or more successive images an operator identifies a particular cloud feature which he feels is moving with the wind. The coordinates of the cloud are converted by a computer to distance and direction. Division by the time interval between picture yields an estimate of the wind speed. One of the "original" papers on manual cloud tracking was published by Hubert and Whitney (1971). They used visible imagery from geosynchronous orbit at 1/2 hour resolution to estimate winds from cloud

motions. Similar methods can employ slides, movie loops or a video display system. The more complex manual systems are computer intensive but still require an operator to select clouds for tracking. Such systems have been developed by the University of Wisconsin, NASA and others.

7.1.2 Automatic Tracking

These methods rely on cross-correlation techniques (Leese *et al.*, 1971) and are highly computer intensive. The method can be illustrated by the one-dimensional model in Figure 7.1.2.1. In this case the cloud brightness varies only in one dimension, L, in order to simplify the explanation.

Mathematically,

$$\text{corr} = \frac{\int_0^L B(t_0)B(t_1)\,dx}{\left[\int_0^L B^2(t_0)\,dx \cdot \int_0^L B^2(t_1)dx\right]^{1/2}} \qquad (7.1)$$

If the cloud is not changing in size or brightness, then

$$\int_0^L B^2(t_0)dx = \int_0^L B^2(t_1)dx = C \qquad (7.2)$$

and

$$\text{corr} = C^{-1} \int_0^L B(t_0)\, B(t_1)dx \qquad (7.3)$$

Converting time into distance,

$$B(t_0) = B(x)$$
$$B(t_1) = B(x + D)$$

$$\text{corr}(d) = C^{-1} \int_0^L B(x + d)\, B(X + D)dx \qquad (7.4)$$

and

$$\text{corr} = 1 \quad \text{when } d = D$$

Therefore, corr = 1 when the exact lag is found. In practice one finds maximum (non-unity) correlation when the appropriate lag is found. This is

true because the cloud seldom remains unchanged. Such changes make the method less reliable.

In two dimensions the method can be illustrated by the following explanation (See Figure 7.1.2.2):

a) Divide the first picture into reference windows (i.e., 32 x 32 pixels). The second picture is divided into search windows (i.e., 64 x 64 pixels).

The 32 x 32 reference window can move 16 pixels in each direction in the 64 x 64 search windows. Then a 2-dimensional cross-correlation is calculated for each position. Contours of cross-correlation would appear as in Figure 7.1.2.3, with the maximum value showing the wind estimate for the area.

A wind vector is assigned to the center of the 32 x 32 pixel reference window (i.e., you get a wind vector about every 256 km for 8 km IR imagery). Wind speeds up to 71 $m \cdot s^{-1}$ can be measured this way. Error is ±1/2 pixel (± 2.2 $m \cdot s^{-1}$) just from coarseness of data. There are about 3000 32 x 32 search windows on a full disk IR picture.

If the amount of computation must be decreased to fit into operational schedule, the most recent analysis can be used as a first guess to tell the computer where to start searching.

Winds can be tracked at any level there are clouds. Middle-level clouds are the rarest. Low-level clouds are the most common, and high-level clouds are usually present. Remember: No clouds; no wind estimate.

7.2 Problems

a) The human operator cannot calculate the movement of a cloud (i.e., he cannot place the cursor) as accurately as a computer can find the peak

of the cross-correlation. However, an operator can track individual clouds and thus get more wind vectors than the computer. Also, when the automatic methods do not work, often a human operator can get cloud winds, like when there are two levels of clouds.

b) Cross-correlation techniques sometimes produce:

1) All small correlations and no important maxima - clouds changed

2) All large correlations and no important maxima - stratus

3) More than one maxima - pattern in reference window is similar to more than one pattern in search window. (Tradewind cumulus, for example)

c) Clouds are not of the same shape and same brightness for 30 minutes. Small cumuli grow and die. Also, the resolution of the IR is not sufficient to track a single cloud. Cloud winds really track "blobs" of clouds ~ 20 km or more across.

d) To what level do you assign the winds? Do clouds move with the wind? Small clouds - yes; big clouds - no. Low clouds move fairly closely with the cloud-base wind. By using infrared cloud top temperature, an indication of the cloud height may be determined.

7.3 Solution

Several variations of the above methods have been used to overcome the problems. Of special concern is the cloud height or wind height determination. By using stereo images (Hasler, 1981), it is possible to assign heights to the cloud images and, therefore, to the winds determined by

cloud tracking. Using VAS sounding channels, Menzel et al. (1983) were able to assign altitudes to cloud motion vectors.

Alternatively, if there are no clouds to track, then it may be possible to follow moisture features, such as those in 6.7 μm METEOSAT water vapor imagery (Eigenvillig and Fischer, 1982).

7.4 An Application

On important application of cloud tracking is in severe weather studies (Peslen, 1980). Small cumulus may be used as tracers to determine the inflow into thunderstorms and the cirrus outflow may be used to determine the amount of mass that the cloud is processing. It is then possible to estimate vertical velocities in a cloud or cloud system.

Figure 7.4.1 shows wind vectors determined for a severe local storm case study on 24 April 1979 (Negri and Vonder Haar, 1980). Figure 7.4.2 shows the cloud imagery for the same case. These cloud-tracked winds were combined with surface mixing ratios to derive horizontal moisture convergence in the pre-storm environment.

References and Suggested Reading

Eigenwillig, N. and H. Fischer, 1982: Determination of mid-troposphere wind vectors by tracking pure water vapor structures in METEOSAT water vapor image sequences, Bull. Amer. Meteor. Soc., 63, 44-58.

Hasler, A. F., W. C. Skillman, W. E. Shenk and J. Steranka, 1979: In situ aircraft verification of the quality of satellite cloud winds over oceanic regions, J. Appl. Meteor., 18, 1481-1489.

Hasler, A. F., W. E. Shenk, and W. C. Skillman, 1977: Wind estimates from cloud motions: preliminary results of phase I, II and III of an in situ aircraft verification experiment, J. Appl. Meteor., 16, 812-815.

Hasler, A. F., 1981: Stereographic observations from geosynchronous satellites: An important new tool for the atmospheric sciences. Bull. Amer. Meteor. Soc., 62, 194-212.

Hubert, L. F. and L. F. Whitney, Jr., 1971: Wind estimation from geostationary satellite pictures. Mon. Wea. Rev., 99, 665-672.

Kastner, M., H. Fischer and H. J. Bolle, 1980: Wind determination from NIMBUS-5 observations in the 6.3 μm water vapor band. J. Appl. Meteor., 19, 409-418.

Leese, J. A., C. S. Novak and B. B. Clark, 1971: An automatic technique for obtaining cloud motion from geostationary satellite data using cross-correlation. J. Appl. Meteor., 10, 118-132.

Menzel, W. P., W. L. Smith and T. R. Stewart, 1983: Improved cloud motion wind vector and altitude assignment using VAS. J. Climate Appl. Meteor., 22, 377-384.

Negri, A. J. and T. H. Vonder Haar, 1980: Moisture convergence using satellite-derived wind fields: A severe local storm case study. Mon. Wea. Rev., 108, 1170-1182.

Peslen, C. A., 1980: Short-interval SMS wind vector determinations for a severe local storms area, Mon. Wea. Rev., 108, 1407-1418.

Smith, E. A. and D. R. Phillips, 1972: Automated cloud tracking using precisely aligned digital ATS pictures, IEEE Trans. on Computer, C-21, 715-729.

Suomi, V., T. Vonder Haar and E. Smith, 1969: [IN] Conference on the General Circulation of the Atmosphere, London, Proceedings published by the Royal Meteorological Society.

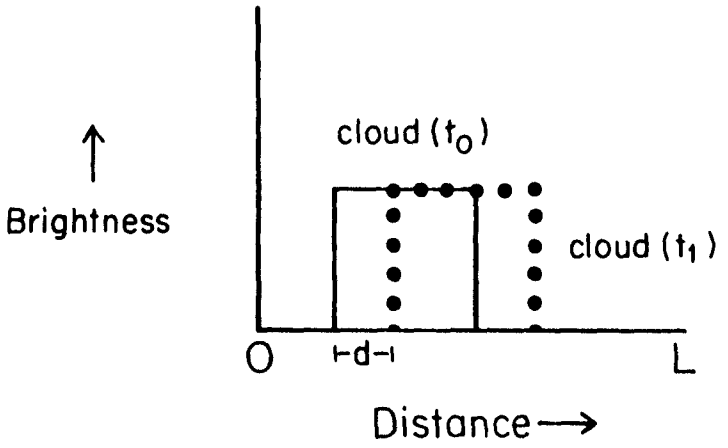

Figure 7.1.2.1 One-dimensional cloud model for automatic cloud tracking

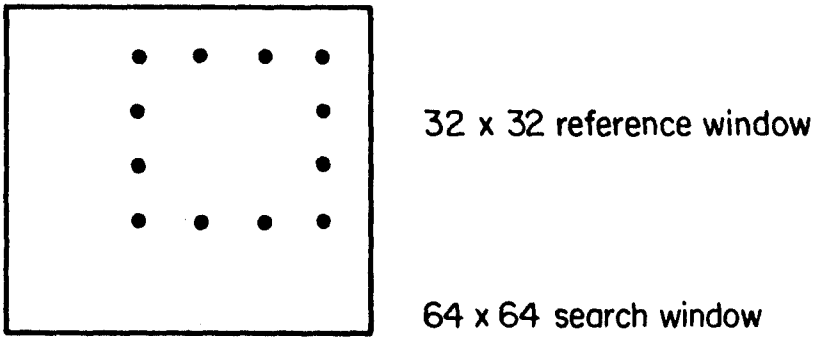

Figure 7.1.2.2 Reference and search windows

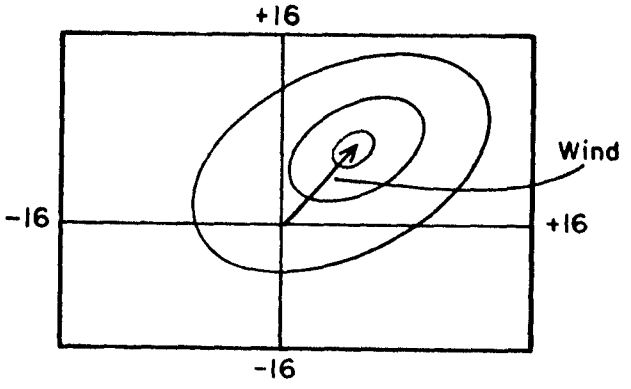

Figure 7.1.2.3 Cross-correlation output

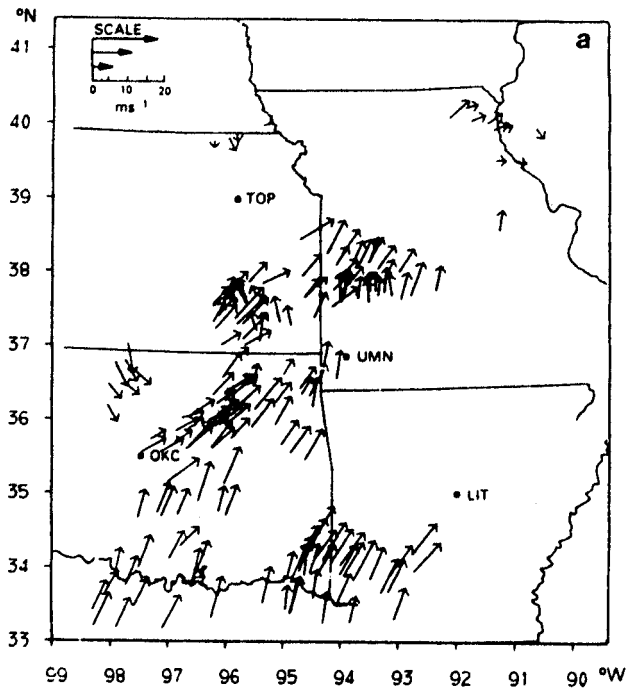

Satellite derived wind field at 2105 GMT. Inset in upper left indicates vector scaling. Locations of available rawinsonde stations are also plotted.

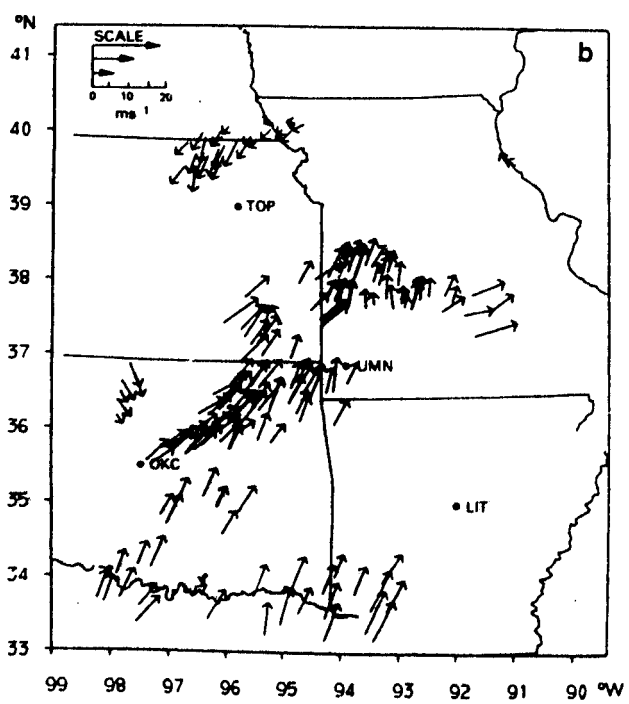

wind field at 2130 GMT

Figure 7.4.1 **Satellite-derived Wind Vectors for 24 April 1979 at 2105 and 2130 GMT (Negri and Vonder Haar, 1980)**

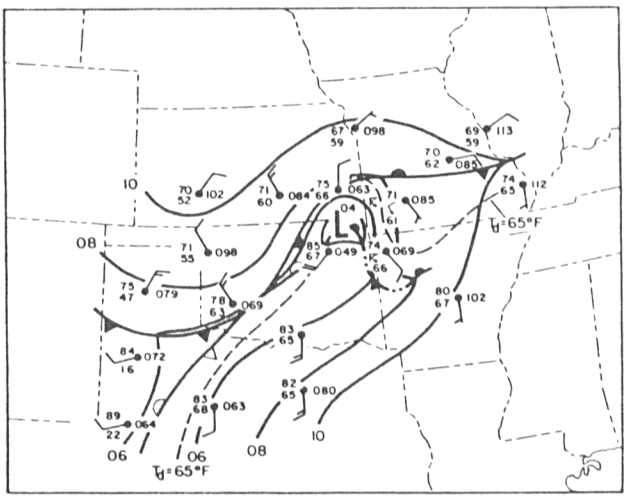

Surface analysis at 0000 GMT 25 April 1975. Wind (kt), temperature (°F), dewpoint (°F) and pressure (mb) are conventionally plotted. Dashed line represents 65°F isodrosotherm. A boundary separating warm, moist air from cooler, moist air is shown as a dissipating stationary front.

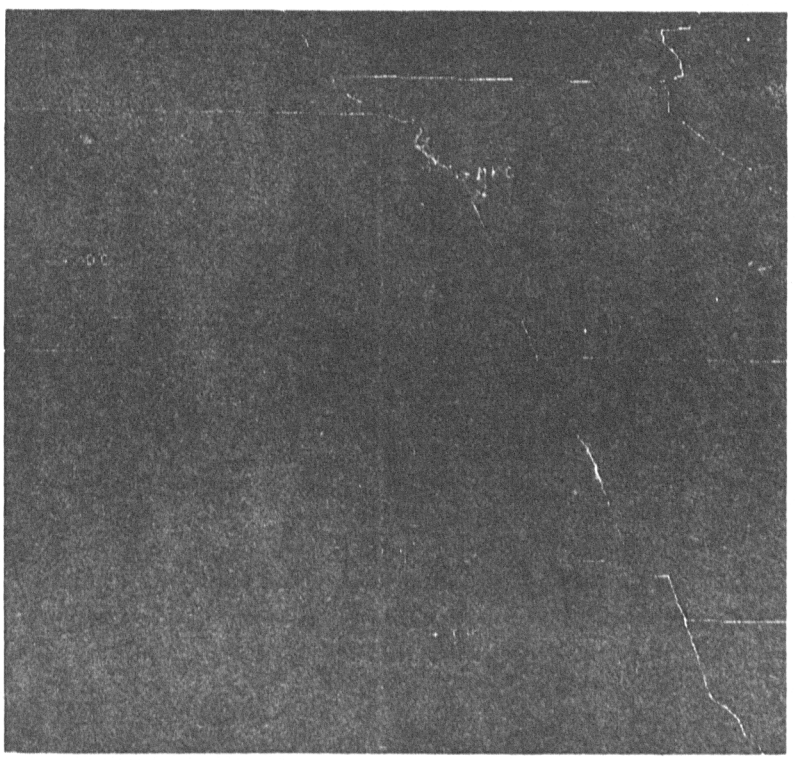

SMS-2 visible image at 2058 GMT (2 km resolution). Horizontal dimensions of the area are ~1000 km.

Figure 7.4.2 Surface Analysis and SMS-1 Visible Cloud Imagery for Case in Figure 7.4.1 (Negri and Vonder Haar, 1980)

Blank page retained for pagination

CHAPTER 8

CLOUD IDENTIFICATION FROM SATELLITES

Some definitions of basic cloud types will be given as well as the meteorology responsible for those types of clouds. The reasons for cloud determination are many and varied. Likewise, many parameters affect the satellite measurements of clouds and cause problems in the determination of cloud type, amount and height.

Methods for cloud determination range from subjective to objective and from qualitative to quantitative. Various schemes rely on either a single field-of-view (FOV) or multiple FOVs. Some limited detail will be given on a bi-spectral method as well as multiple FOV techniques.

8.1 Definition of Cloud Types

8.1.1 High Clouds

1) Cirrus - composed of ice crystals. Occurs in the form of thin fibers or filaments which may appear straight, irregularly curved or seemingly entangled in a capricious manner.

2) Cirro-stratus - composed mainly of ice crystals. Occurs in the form of a fibrous veil in which thin striations can be observed or it may be resemble a nebulous veil.

3) Cirro-cumulus - Almost exclusively ice crystals; some supercooled water may exist. Generally occurs in more or less extensive sheets, consisting of very small elements in the form of grains, ripples,

etc. Those sheets often show one or two systems of undulations. May also occur in patches in the shape of lenses or almonds often very elongated and usually with well-defined outlines.

8.1.2 Middle Clouds

1) Altocumulus - almost invariably composed of water droplets. At very low temperatures ice crystals may be present. Occurs most commonly in the form of an extensive sheet composed of elements (cloudlets) which are fairly regularly arranged. Sometimes the cloudlets take the form of elongated parallel rolls which may be separated by definite clear lanes. Can occur downwind of mountain barriers as lens or almond shaped patches (Lenticulars).

2) Altostratus - is composed of water droplets and ice crystals; also can contain raindrops and snowflakes. Altostratus is nearly always of great horizontal extent (up to hundreds of kilometers) and of fairly considerable vertical extent (up to thousands of meters). May be composed of two or more superimposed layers of slightly different levels, sometimes partly merged. Undulations or broad parallel bands are occasionally in evidence. Altostratus is a precipitating cloud, causing continuous type precipitaiton in the form of rain or snow.

8.1.3 Low Clouds

1) Stratocumulus - composed of water droplets, sometimes accompanied by raindrops or snow pellets and by snow crystals and snowflakes. Stratocumulus most often appears as a sheet or layer composed of cloudlets similar to those of altocumulus, but at a lower level. Often

occurs in a pattern of parallel rolls with clear channels in between. Stratocumulus often occur in two or more levels. Strato-cumulus is sometimes accompanied by weak precipitation.

2) Stratus - composed of small water droplets. At low temperatures it may consist of small ice particles. When dense or thick, stratus often contains drizzle droplets and sometimes ice prisms or snow crystals.

3) Cumulus - composed mainly at water droplets unless the temperatures are well below $0^{o}C$. May occur in various stages of vertical development. Cumulus clouds, usually of moderate vertical extent, are sometimes arranged in rows nearly parallel to the wind direction (cloud streets). Cumulus of great vertical extent may produce precipitation especially in the tropics, where abundant rainfall may fall due to the warm rain process.

4) Cumulonimbus - water droplets in lower layers, ice crystals in upper layers. At least part of its upper portion is usually smooth or fibrous or striated, and nearly always flattened; this part often spreads out in the shape of an anvil or vast plume. Sharp turrets may be present at the upper part of the cloud, penetrating the anvil. May appear as individual clouds or in lines or clusters.

5) Orographic Clouds - formed by mountains or terrain variations. May differ notably in shape to clouds already described. Usually of the altocumulus, altostratus or cumulus type. Usually moves very slowly as it is tied to the terrestrial relief; although wind at its level may be moving very rapidly. May appear at specific intervals or wavelengths which may allow estimation of wind speed.

8.2 Meteorology Associated with Different Cloud Types

8.2.1 High Clouds - Cirrus

1) Associated with large scale lifting - i.e., warm advection in warm sector
2) Associated with jet stream flow usually on cyclonic shear side of jet possibly 5° north of the actual wind maximum
3) Debris from earlier thunderstorm activity
4) Frontal bands

8.2.2 Middle Clouds - Altocumulus and Altostratus

1) Also with large scale lifting but in close proximity to warm front but out ahead of it. Normally over the overrunning precipitation shield
2) Cold frontal bands - may be obscurred by cirro-stratus
3) Mid-level outflow of thunderstorm activity

8.2.3 Low Clouds - Stratus

1) Radiation cooling of lower boundary
2) Condensing of lower layers by evaporation of rainfall from above
3) Advection of warm moist air over cold ground

8.2.4 Cumulus

1) Surface heating in unstable or stably stratified lower layer

2) Advection of cold air over warm surface

3) Lifting of airmass by frontal surface or surface convergence

8.2.5 Cumulonimbus

1) Surface heating

2) Lifting of lower layers by frontal surface on surface convergence

3) Enhanced by vertical wind shear

8.3 Need For Accurate Cloud Type Information

8.3.1 Aircraft

1) In route traffic control

   a) Flight altitudes for smoothest flight

   b) Allow good VFR conditions

2) Terminal forecast

   a) Landing - takeoff safety factors

8.3.2 Shipping

1) For stratus areas

2) Cloud patterns can infer wind speed and direction to help estimate sea state

3) Location of large storm clusters affecting ship safety

8.3.3 Agriculture

1) Identification of cloudiness which can affect frost or freeze warnings
2) Monitoring of convective clouds for estimation of available moisture

8.3.4 Public Forecasting

1) Identifying hazardous weather
   a) Fog to tornadoes
   b) Tropical storms
2) Potential sunshine on a given day
   a) Solar energy requirements
   b) Psychological

8.4 Parameters Affecting Satellite Measurements of Clouds

1) Thickness (albedo - IR emittance)
2) Altitude
3) Water droplet concentration
4) Ice crystal concentration
5) Horizontal width
6) Shape
7) Underlying surface - cloud, snow or ocean (See Figure 8.4.1)
8) Sun angle
9) Satellite viewing angle
10) Water vapor and aerosols, ozone in atmospheric column

8.5 Problem Areas in Cloud Type Identification

8.5.1 Visible Data

1) Equal brightness of different cloud types due to reflection properties of clouds. Does not allow good height determination.
2) Snow can appear as low clouds or fog. Usually can be discriminated by terrain features in the snow.
3) Sun glint over oceans
4) Spatial resolution of sensor (sampling on edges of image)
5) Transparency of thin clouds, especially over bright surfaces
6) Multiple layer of clouds

8.5.2 IR Data

1) Emittance of clouds - surface underlying cloud can cause serious problems
2) Multiple cloud levels
3) Snow and fog can have same temperature and appearance, spatial resolution may not allow terrain feature to be seen
4) Spatial resolution does not allow some patterns to be recognized in visible data
5) Absorption by water vapor can decrease radiance measured by the satellite

6) Temperature inversions may cause problems in estimating the altitude of clouds. This can occur both at low levels and at the tropopause level, such as in large thunderstorms.

8.6 Single FOV Techniques

As an example of a single FOV technique for determining cloud height and amount, the bi-spectral method of Reynolds and Vonder Haar (1977) will be presented. This technique relies on both a visible and an infrared measurement from the satellite for a given FOV.

The visible radiance

$$L_V = A_{clr} \cdot p_{clr} \cdot L_S + A_{cld} \cdot p_{cld} \cdot L_S \qquad (8.1)$$

is composed of two components or areas A with reflectance p. L_S is the solar radiance reaching the surface on cloud top.

For the infrared radiance

$$L_{IR} = A_{clr} \cdot L_{clr} + A_{cld} \cdot L_{cld} \cdot \varepsilon + A_{cld}(1-\varepsilon) \cdot L_{clr} \qquad (8.2)$$

where L_{clr} and L_{cld} are the spectral infrared radiances arising from the cloud-free and cloudy areas, respectively.

Assumptions required to apply this simple technique are:

1) the infrared emittance of water clouds is known (assume = 0.9).
2) the variation of cloud top within the FOV is $\leq \pm$ 500 m. (i.e., only a single cloud top exists.)

From the assumption that only two sub-areas exist in the FOV

$$A_{cld} + A_{clr} = 1. \tag{8.3}$$

This equation can then be used to join Equations 8.1 and 8.2 to solve for the cloud amount.

$$A_{cld} = \frac{L_v - p_{clr} \cdot L_s}{L_s(p_{cld} - p_{clr})} \tag{8.4}$$

and the cloud radiance

$$L_{cld} = \frac{L_v - L_{clr}}{\varepsilon \cdot A_{cld}} + L_{clr} \tag{8.5}$$

provided that certain quantities are known or can be acquired from the actual satellite measurements.

The required parameters are:

1) P_{clr} = the bi-directional reflectance of the cloud-free area (i.e., = 0.032 for ocean, = 0.064 for land)
2) P_{cld} = the bi-directional reflectance of the cloud (i.e.,0.16)
3) L_{clr} = the infrared radiance for the cloud free area (i.e., $B(T_s)$)

The cloud radiance can then be converted into a cloud temperature, T_{cld}, and then into a cloud height using a RAOB temperature profile for the height assignment.

Results of this method applied to Scanning Radiometer (SR) data from NOAA-2 are shown in Figures 8.6.1 and 8.6.2. Rms errors averaged over both cases are 0.2 in cloud amount and 0.5 km in cloud height.

A variation of the bi-spectral method can be applied to two infrared window channels, such as at 3.7 μm and 11 μm. Dozier (1980) used such a

technique to determine cloud amounts and heights by assuming that the background or surface temperature is known.

8.7 Multiple FOV Techniques

Two methods will be shown which can be used to detect cloud contamination based on multiple Fields-of-View of satellite measurements.

8.7.1 Scatter Diagrams

By plotting the infrared window channel radiance versus the visible albedo for many fields-of-view, an indication of the cloud types may be obtained. The typical effect is that higher albedos correspond to higher or thicker clouds. The infrared radiance from these thicker clouds would be low. However, various combinations of high and low albedo, and high and low infrared radiance lead to different interpretations as in Figure 8.7.1.

The distinction between groupings is neither clear nor separable; but at least an indication of the cloud type may be obtained, or whether clouds even exist in the FOV.

8.7.2 Mean Versus Standard Deviation

An alternate method may be used to categorize satellite measurements by grouping them into small sets of adjacent measurements. By comparing the standard deviation to the mean of the values in each subset, a diagram such as in Figure 8.7.2 can result. In this case, infrared measurements can be used alone.

The grouping of low standard deviations at both high and low means is significant. A low standard deviation represents uniform subareas.

Therefore, those areas with low mean values are most likely cloudy, and those areas with high mean values are most likely clear. Again, this is merely a cloud detection technique. To be more quantitative, the problem becomes more complex, especially considering all the parameters which can cause variations in the satellite-measured radiances.

References and Suggested Reading

Anderson, R. K. et al., 1974: Application of meteorological satellite data in analysis and forecasting. ESSA Technical Report NESC-51. NOAA/NESS, Washington, DC., 350 pp.

Bowen, R. A., 1982: The meteorological product: "Cloud-top height". ESA Bulletin #30, 16-20.

Dozier, J., 1980: Satellite identification of surface radiant temperature fields of subpixel resolution. NOAA Technical Memorandum, NESS-113, 11 pp.

International Cloud Atlas (1956), World Meteorological Organization.

Reynolds, D. W. and T. H. Vonder Haar, 1977: A bispectral method for cloud parameter determination. Mon. Wea. Rev., 105, 446-457.

Shenk, W. F., F. J. Hoebb and R. A. Neft, 1976: A multispectral cloud type identification method developed for tropical ocean areas with NIMBUS-3 MRIR measurements. Mon. Wea. Rev., 104, 284-291.

Weather for Aircrews, 1974. Department of the Air Force, AF Manual 51-12.

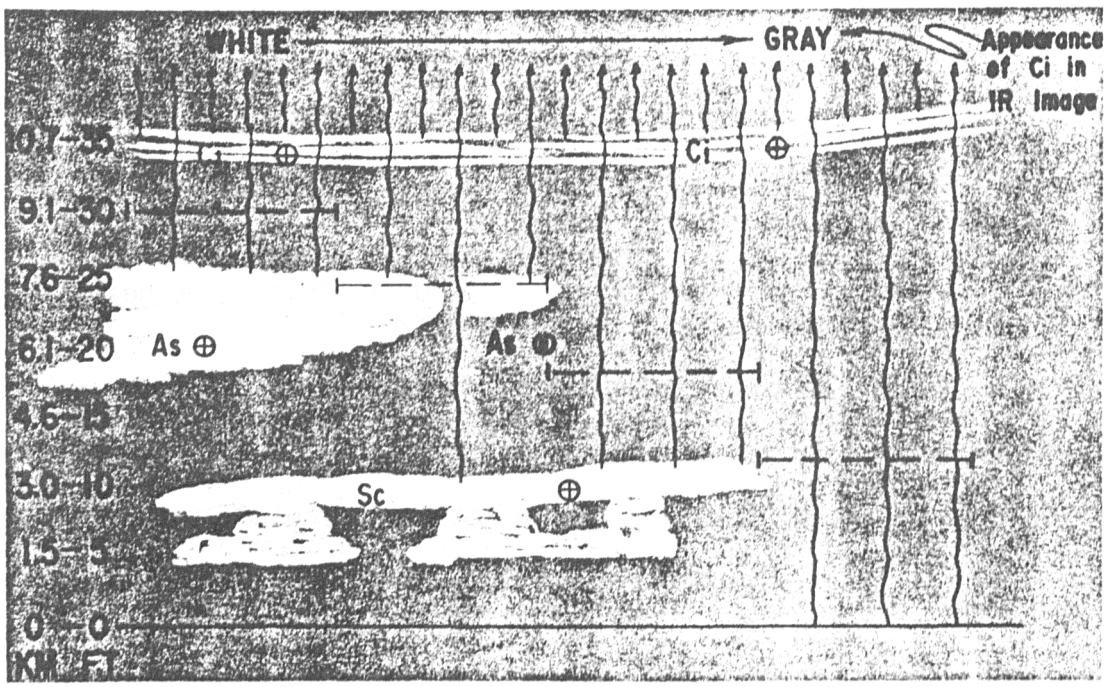

This diagram shows the effect of lower cloud on radiation emitted by a uniform layer of thin cirrus. It is assumed that no large temperature inversion is present. The vertical wavy lines represent schematically the source of the radiation reaching the satellite sensor. The horizontal dashed lines represent the height of the cirrus tops computed on the basis of the integrated temperature received by the SR. The horizontal lines are of equal length and represent the smallest distance that the IR sensor can resolve. As the clouds below the cirrus become less in amount and lower, the cirrus appears progressively grayer and warmer in an IR display. The heights and gray shades shown here are for illustration purposes only, but are considered representative of changes that actually can occur. Cirrus can appear to be as low as 10,000 feet if it is almost transparent, and occurs where the surface below is sufficiently warm.

Figure 8.4.1 Multiple Cloud Layers

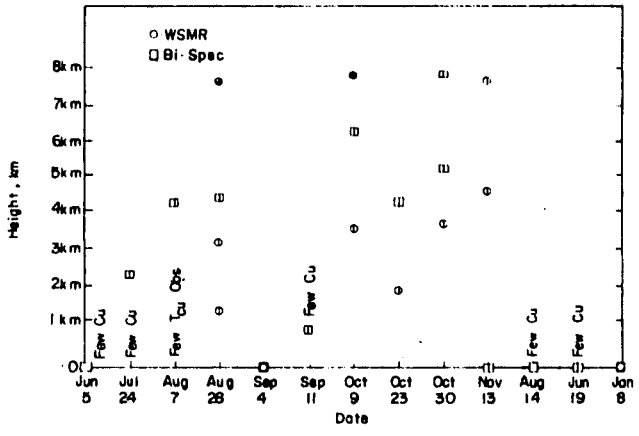

Results from the bispectral program for a 75 km×75 km area over White Sands Missile Range.

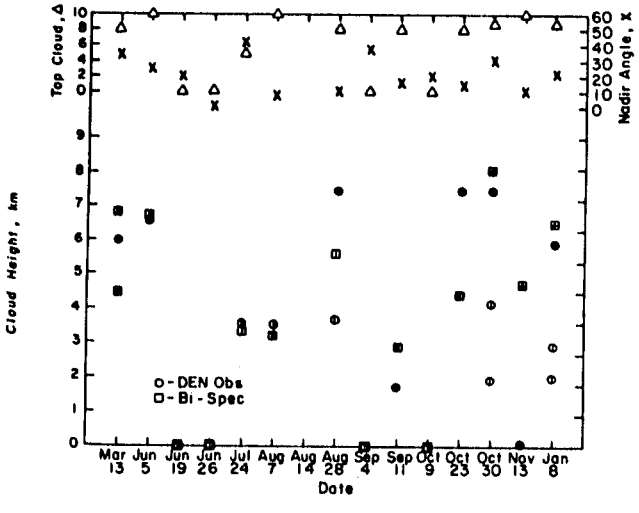

Denver, Colo. Top cloud stands for total opaque cloud amount. Where points are plotted at Z = 0, clear sky conditions were reported or calculated.

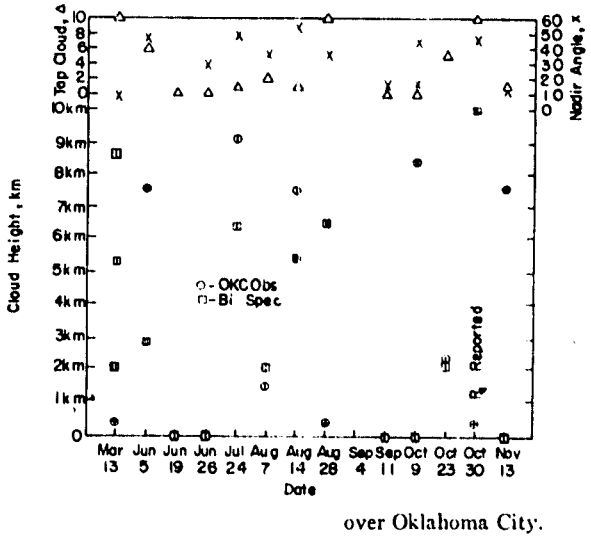

over Oklahoma City.

Figure 8.6.1 Results of Bispectral Method Using SR Data from NOAA-2 (Reynolds and Vonder Haar, 1977)

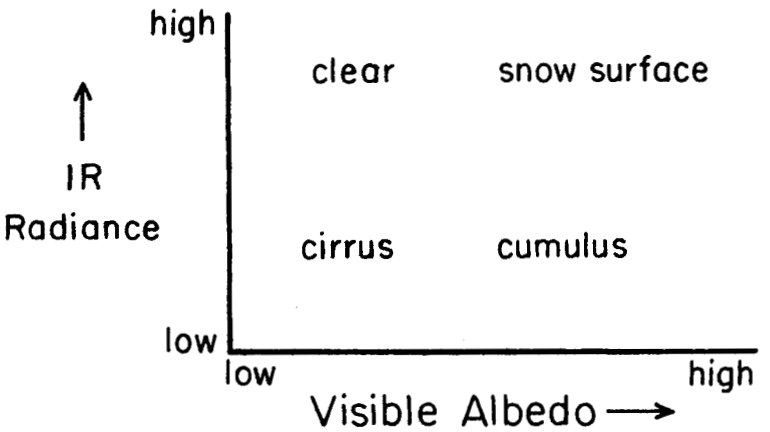

Figure 8.7.1

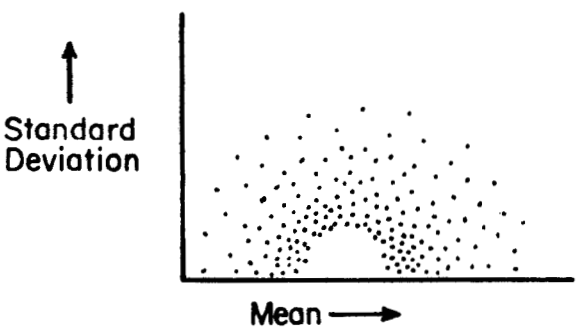

Figure 8.7.2

CHAPTER 9

MID-LATITUDE SYNOPTIC FEATURES AS SEEN FROM SATELLITES

The use of satellite photographs to locate and estimate the intensity of mid-latitude storms has been underway since 1960. In addition to the location of the gross features of the weather systems in mid-latitudes, the satellite pictures are often used to interpret the accompanying cloud situations that are important for weather forecasting. In Chapter 8 we learned about the interpretation of the cloud features from satellites and this chapter will focus more on the understanding and tracking of major weather systems in mid-latitudes with the aid of the satellite data. Today, all over the world, weather forecasters, aviation briefers, and many others are using commonly available satellite data on both television presentations and at weather forecast centers to understand and interpret the large-scale storm systems in the atmosphere. This chapter will cover the basics of identification of these storm systems and the interpretation of the systems in terms of their natural development or lifetimes. We first begin with a discussion of the storm systems, the "lows", the jetstreams, and related features and we conclude the chapter with a brief example or case study of a particular mid-latitude cyclogenesis situation that is observed with the aid of satellite photographs.

9.1 Basic Weather Features: Fronts, "Lows", Jetstreams, Blocking Features

Mid-latitude weather systems were well-defined by the conventional weather data network before the advent of satellites. However, since

satellite views have been available to weather forecasters and researchers, the information and details that have been provided have allowed an even more complete picture of the complexity of the mid-latitude cyclones or storms that represent one of the most challenging research and forecasting events in meteorology. As noted in the acknowledgements the material in this chapter is due in large part to the excellent summaries provided by Mr. Roger Weldon. His notes and lectures are well-recognized as some of the leading communications in this area in the United States. This section includes illustrations of satellite cloud photographs that allow us to define the deformation zones, jet stream structures and vorticity regions. It continues with a brief discussion of the general relationships between cloud patterns and jet stream axes. It looks at the baroclinic zone cirrus patterns and the jet stream and examines the relationships between the upper air wind field and the so-called comma cloud patterns. The section concludes with a discussion of the baroclinic "leaf" cloud systems.

As an introduction to the synoptic scale systems, Figure 9.1.1 [Note: This is slide set #43] and Figure 9.1.2 [Note: This is slide set #44] show some typical storm systems over the western hemisphere. Both extra-tropical storms over land and ocean are shown as well as several tropical storms in Figure 9.1.1. Both these images are from the GOES satellites and they are visible light images. Figure 9.1.3 [Note: This is slide set #46] shows a <u>mature</u> mid-latitude cyclone over the central portion of the United States. The figure shows a visible image with the companion infrared image shown as an inset. Note the "T" shape of the cold cloud pattern on the infrared picture. The warm frontal clouds can be seen over southeastern Canada and the State of Maine. The sharply defined cloud band on the

leading edge of the cold frontal zone is seen to extend southward over Tennessee. North of that region high cold clouds cover the frontal zone and the surface cold front crosses the rear side of the cloud frontal zone. The next figure, Figure 9.1.4 [Note: This is slide set #48] shows a "baroclinic leaf" cloud system formed over a frontal zone on the front side of a relatively high amplitude, mid-latitude trough. An enlarged version of that leaf pattern shown in both the visual and the infrared is seen in Figure 9.1.5 [Note: This is slide set #49]. We will find that this leaf pattern in the cold clouds is a characteristic feature of mid-latitude systems as was the "T" pattern mentioned in the previous set of figures.

Figure 9.1.6 shows an excellent example of mid-latitude tropical interaction as evidenced in this pair or sequence of infrared pictures taken 12 hours apart at approximately 2330 GMT on 9 September 1976 and 1130 GMT on 10 September 1976. The cirrus extends from the upstream ridge under the downstream trough [Note: This is slide set #51]. Figure 9.1 [Note: This is slide set #55] indicates an extremely well-defined edge on the equatorward side of the cirrus taken 0745 GMT 3 November 1975 in this visible light image. This picture also shows a "cut-off" low over the south central United States with a deformation zone on the northwest side and another well-defined cirrus edge.

In the next figure, Figure 9.1.8 [Note: This is slide set #56], we seen an example of the deformation zone cirrus band at a comma "head" location taken on 1200 GMT 11 January 1979. Figure 9.1.9 [Note: This is slide set #58] shows a visible light image at 1945 GMT on 10 March 1976 with an infrared insert. This is an example of a deformation zone in both high and low clouds.

The characteristic cloud system that Weldon has called the "baroclinic leaf" is the cloud pattern associated with the frontogenetic phase of system development, whereas the "comma" pattern indicates the cyclogenetic phase. Weldon says that the cloud system called the baroclinic leaf is associated with the early stage or pre-comma cloud shape. However, Weldon also notes that only about 75% of the baroclinic leaf systems evolve into comma systems. The next four figures describe various examples of the baroclinic leaf. Figure 9.1.10 [Note: This is slide set #72] is a "leaf" found over an old frontal zone south of a closed low-pressure system. This figure shows a pair of visual and infrared images taken about 2000 GMT 29 March 1979. The next figure, Figure 9.1.11 [Note: This is slide set #76], shows another baroclinic leaf in an old frontal zone over the southeast Pacific west of South America. Again, this is a VIS/IR pair taken from GOES and shows a southern hemisphere manifestation of this kind of a system. We often find the baroclinic leaf distorted into the "crescent" form as is shown in Figure 9.1.12 [Note: This is slide set #77]. This particular crescent form is found on the northeast side of a cut-off low which is just off the California coast. The infrared data was taken at 0615 GMT 22 August 1976. The cut-off low is moving toward 060° in azimuth. A final example of a baroclinic leaf over the United States, one that did not continue to develop into a comma cloud and did <u>not</u> indicate surface cyclogenesis is shown in Figure 9.1.13 [Note: This is slide set #79]. This is a visible image with an infrared inset taken at 1900 GMT 11 November 1976. Note the low clouds between the leaf system and the Rocky Mountains.

9.2 Views of Cyclogenesis or Stages of Weather Development

In addition to seeing some examples of the various characteristic clouds, it is important to relate these to the concurrent weather situations. Thus, we have prepared an example which we call a "cyclogenesis case study" wherein the satellite pictures are used to trace the development of a mid-latitude cyclone from early stages through maturity. Figure 9.2.1 [Note: This is slide set #145] shows this sequence during an approximately 42-hour period on 8 and 9 May 1979. Infrared pictures are used in this example. The next figure, Figure 9.2.2 [Note: This is slide set #146], shows a visible and infrared comparison during the early stages of the development where one of the characteristic leaf patterns is present. The next figure, Figure 9.2.3 [Note: This is slide set #147], shows a visual enlargement at 2045 GMT 8 May 1979. This figure should be contrasted with the visual and infrared comparison nearly 24 hours later wherein a rather mature and even occluding storm system is shown in Figure 9.2.4 [Note: This is slide set #148]. An enlargement of that mature situation is shown in Figure 9.2.5 [Note: This is slide set #149]. In this enlarged view of the visible light scene, we can note that the cold air is wrapped nearly completely around the low pressure center and we are in the beginning of the dissipation stages of this mature cyclone. The strong cold frontal band is evident as well as the "comma" cloud shield over the major circulation center. Suppressed convection behind the cold front over the ocean is also clearly seen.

There are many other examples of these cyclogenesis sequences to be found in almost every satellite data set taken during the wintertime over

mid-latitudes. The evolution of cyclones and their rate of development is an important forecast goal for meteorologists. Use of satellite photo graphs, particularly over data-sparse regions such as oceans, give forecasters in coastal regions a lot more information about the timing and intensity of these mid-latitude storms reaching landfall. For both forecasting and research the reader is also referred to the various time-lapse film loops which provide a dramatic representation by these evolving weather systems viewed from satellites.

References and Suggested Reading

Anderson, R. K. et al., 1974: Application of meteorological satellite data in analysis and forecasting, ESSA Technical Report NESC-51.

Brandli, Lt. Col., H. W., 1976: Satellite Meteorology, AWS-TR-76-264, Air Weather Service, USAF, Scott AFB, IL 62225, 188 pp.

Weldon, R., 1979: Cloud patterns and the upper air wind field, Satellite Training Course Notes, Applications Division NESDIS, NOAA, Washington, DC, 80 pp.

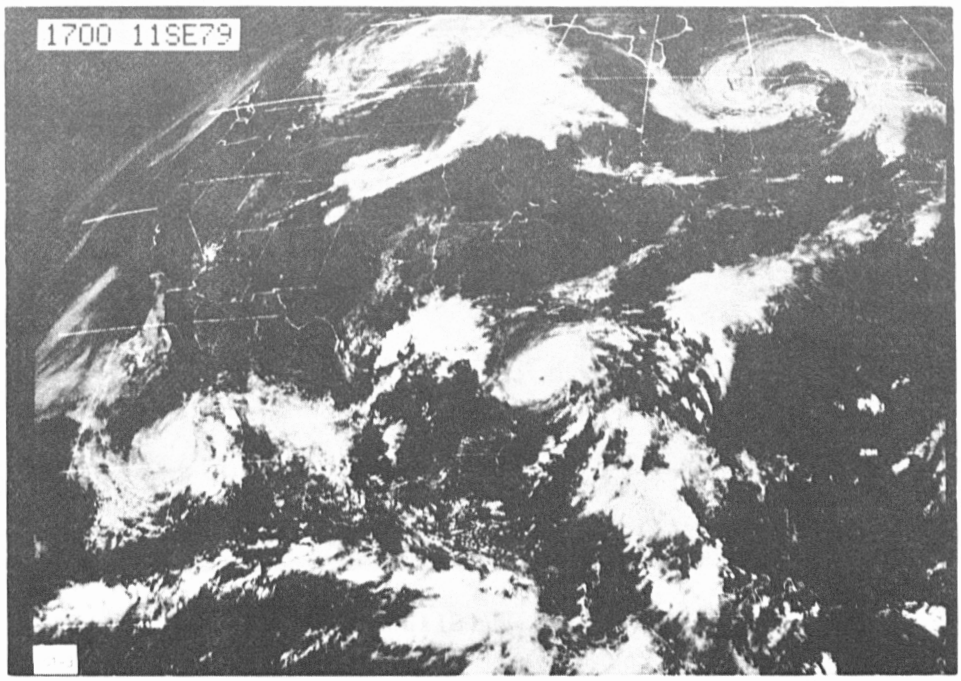

Figure 9.1.1 (Slide Set #43)

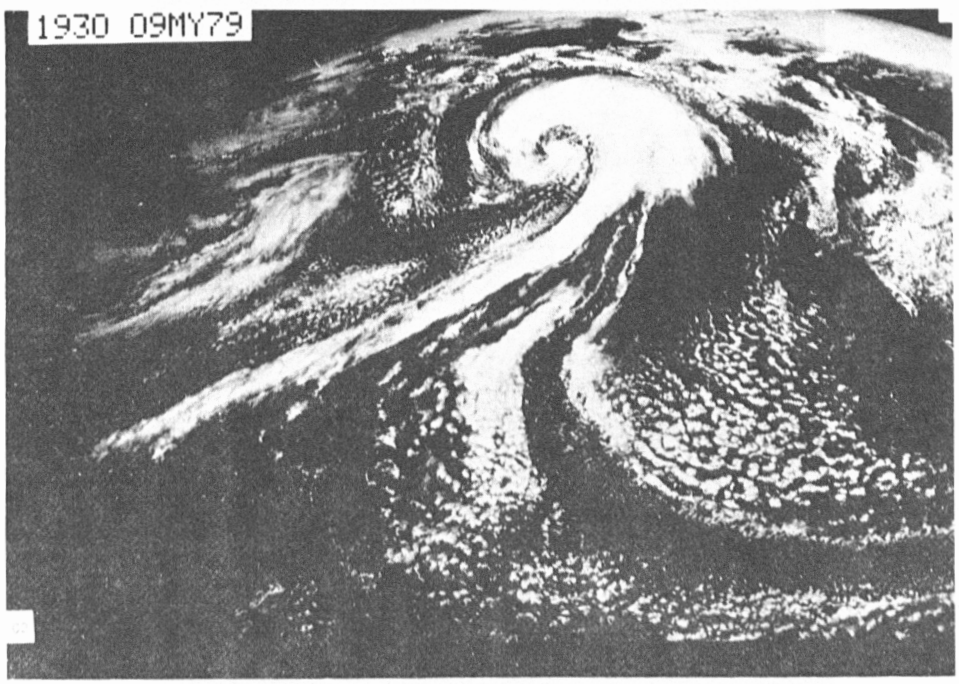

Figure 9.1.2 (Slide set #44)

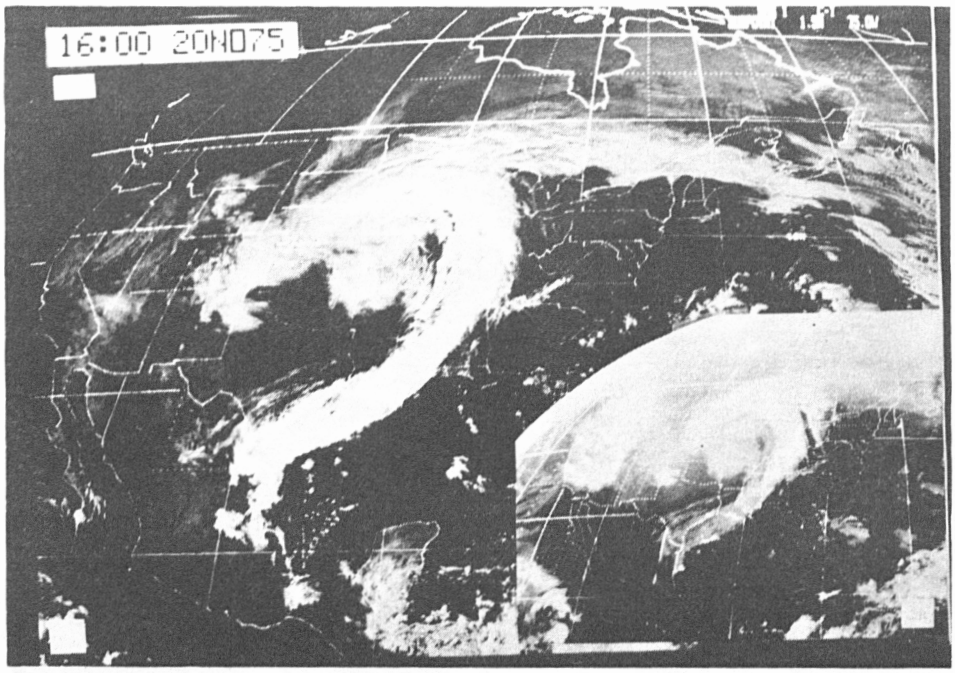

Figure 9.1.3 (Slide set #46)

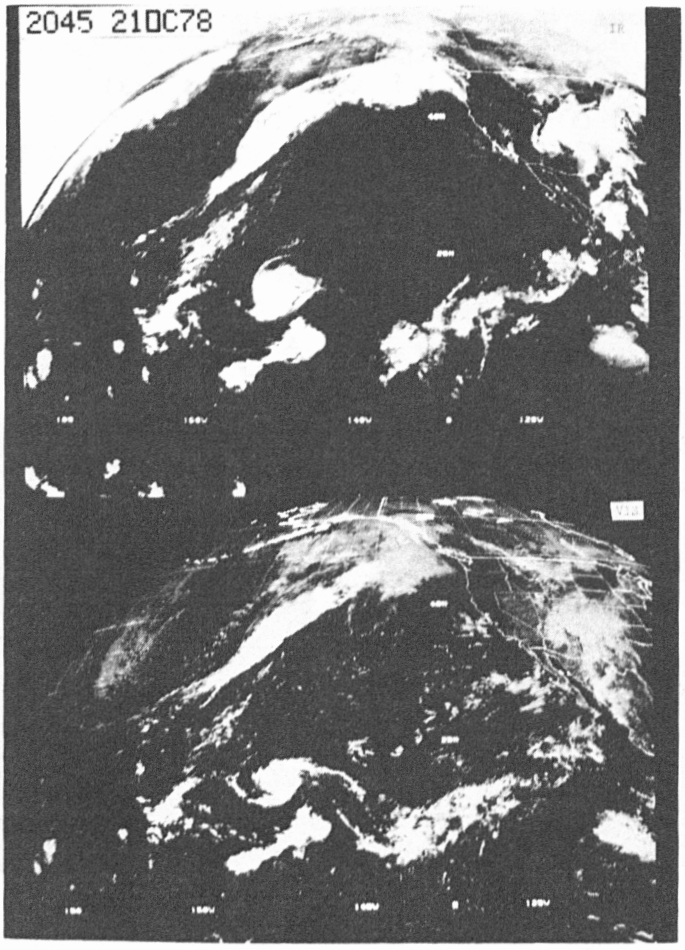

Figure 9.1.4 (Slide set #48)

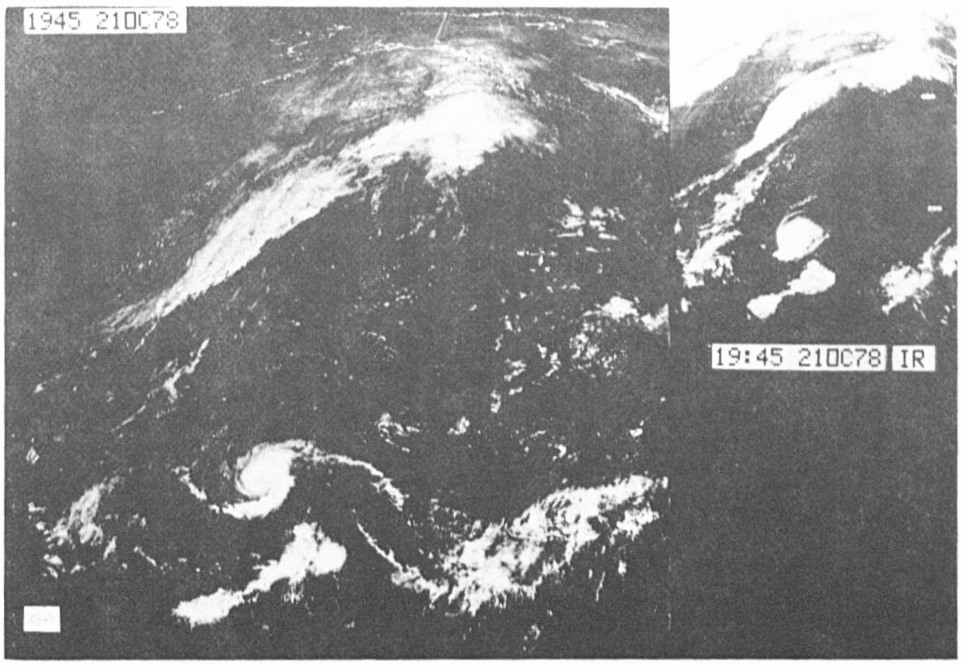

Figure 9.1.5 (Slide set #49)

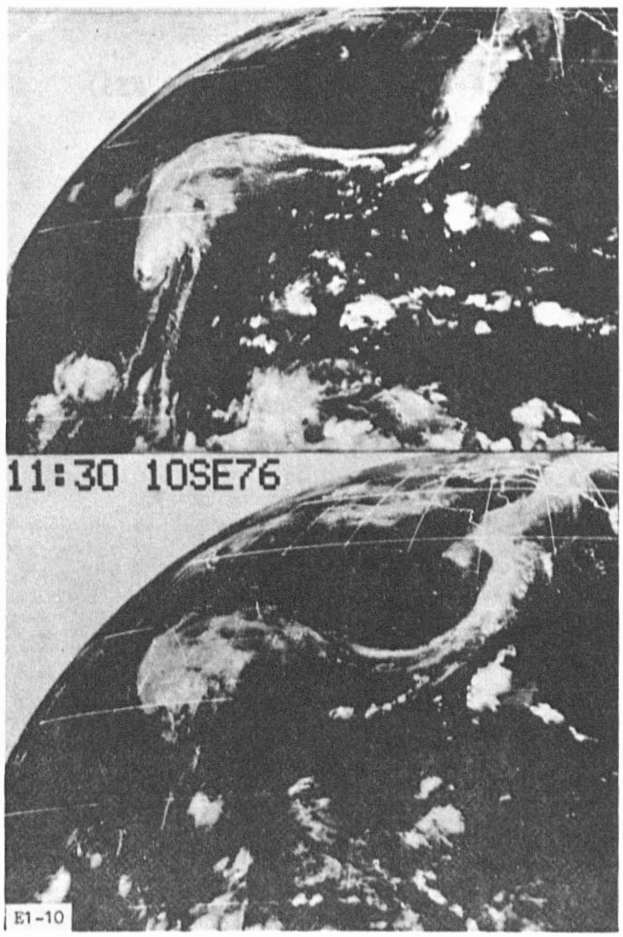

Figure 9.1.6 (Slide set #51)

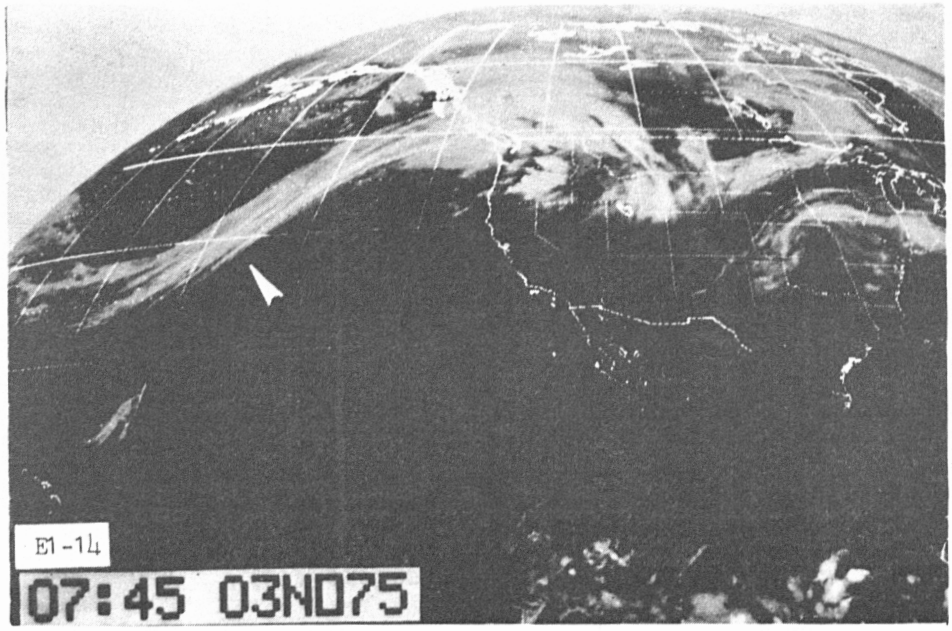

Figure 9.1.7 (Slide set #55)

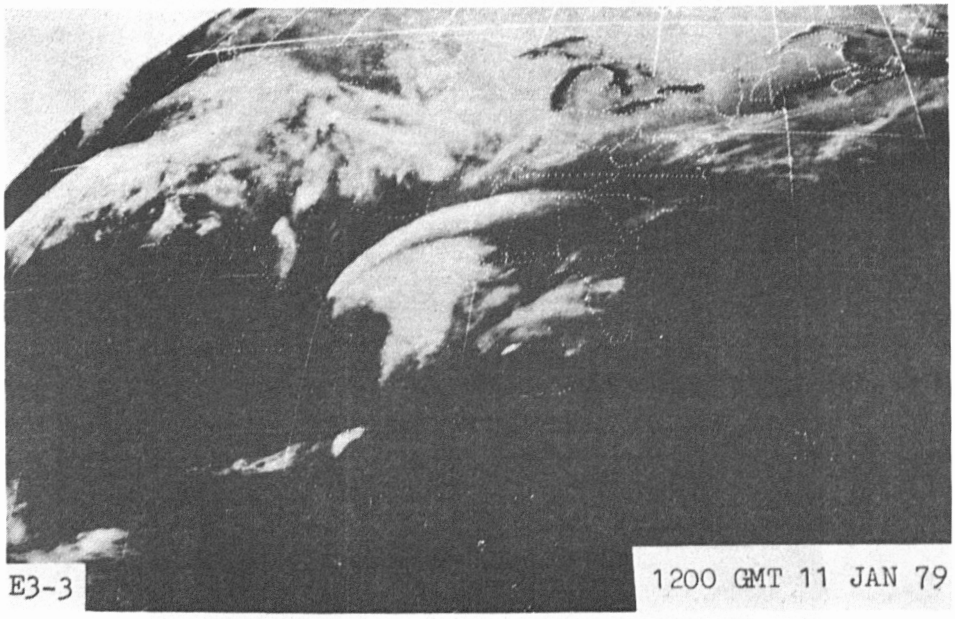

Figure 9.1.8 (Slide set #56)

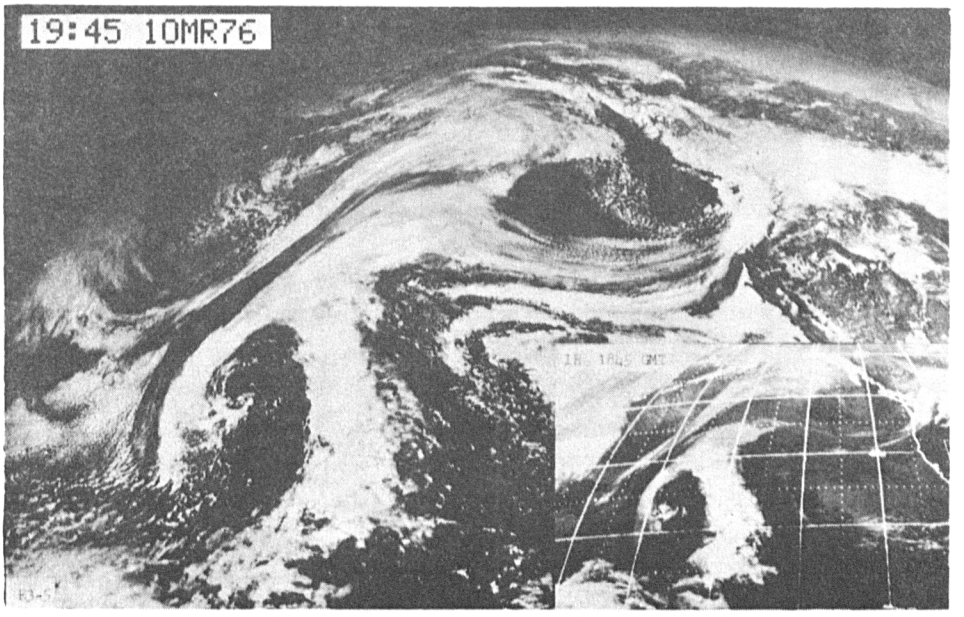

Figure 9.1.9 (Slide set #58)

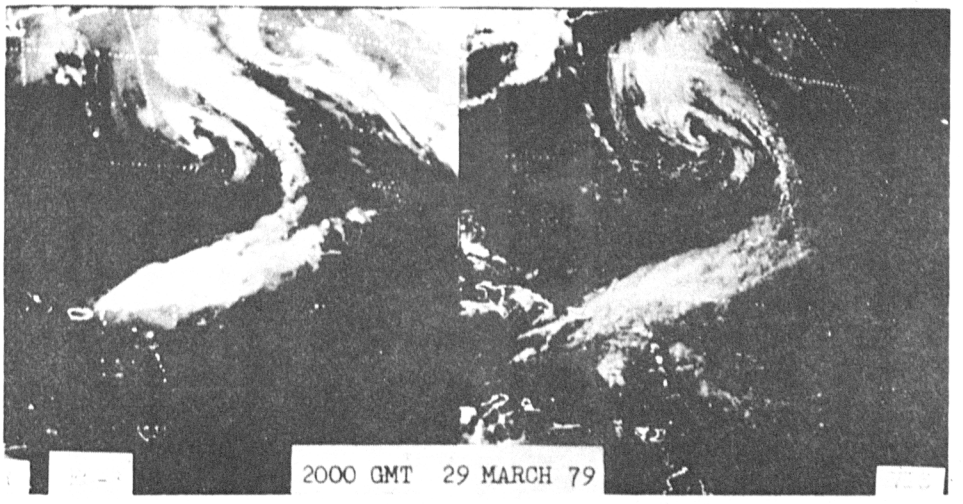

Figure 9.1.10 (Slide set #72)

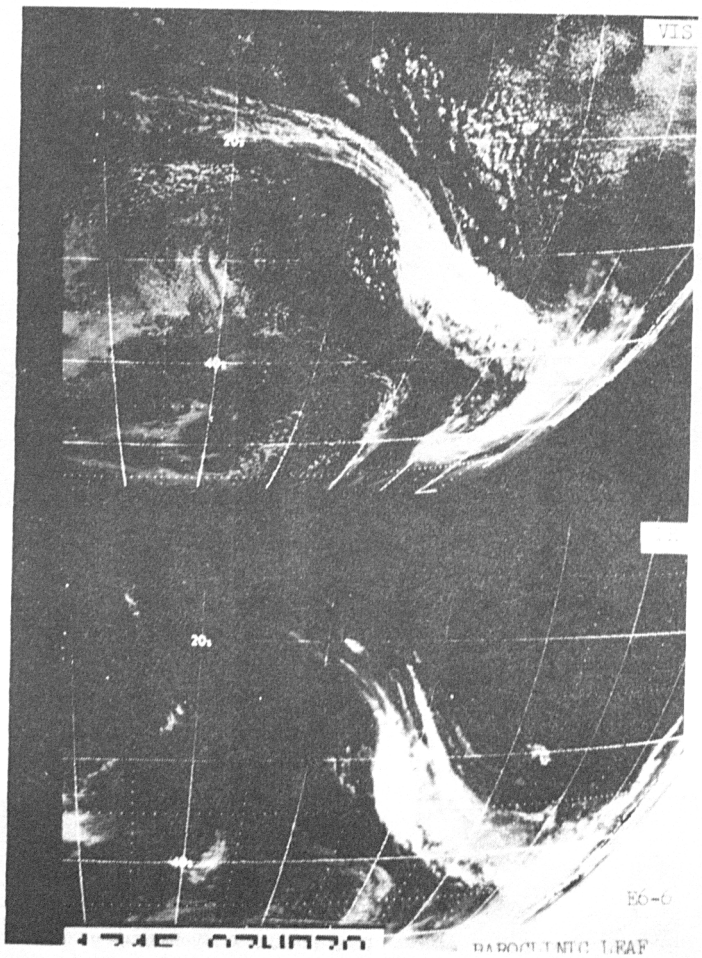

Figure 9.1.11 (Slide set #76)

Figure 9.1.12 (Slide set #77)

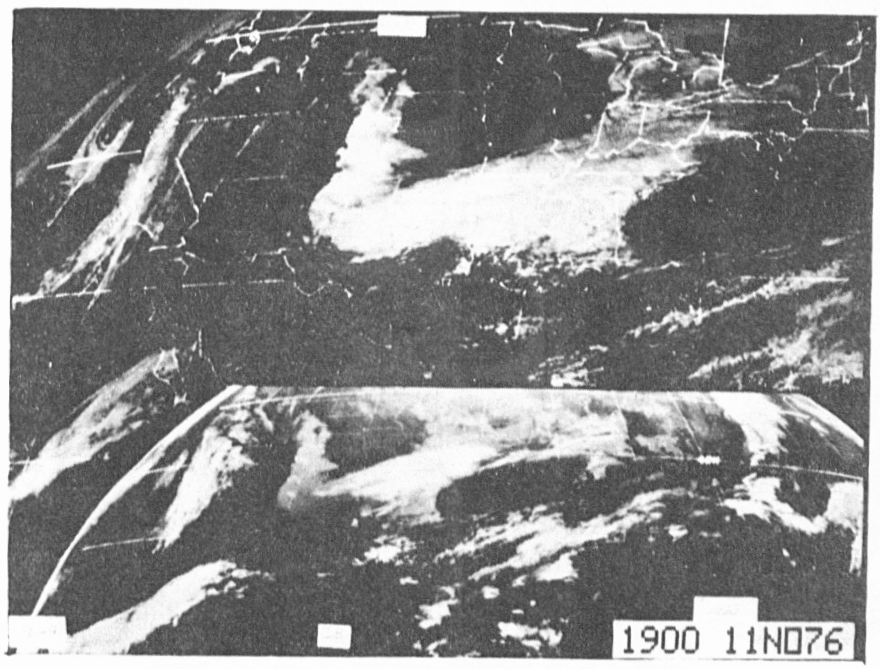

Figure 9.1.13 (Slide set #79)

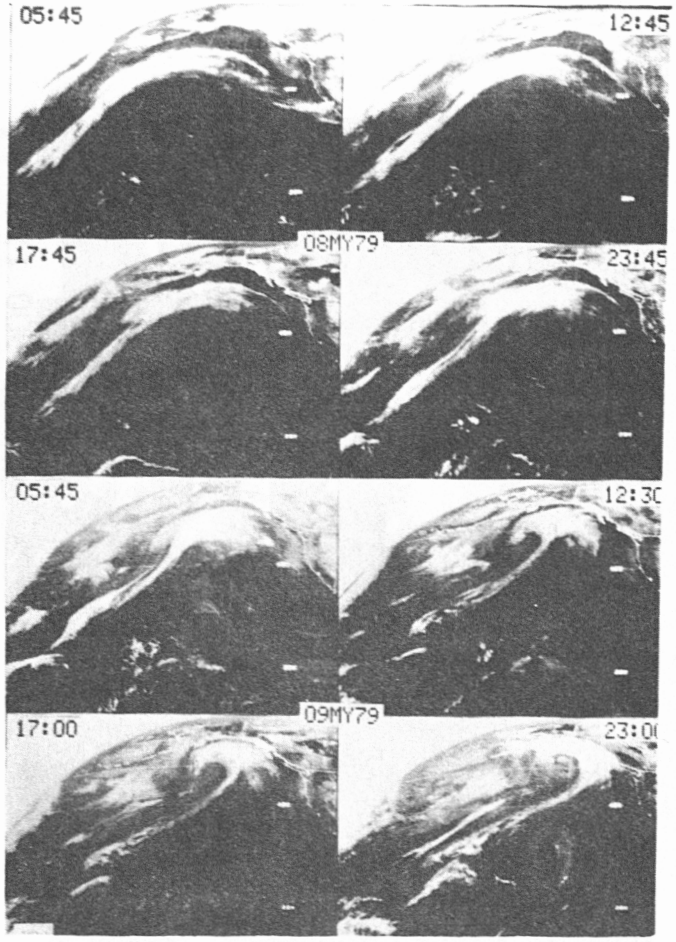

Figure 9.2.1 (Slide set #145)

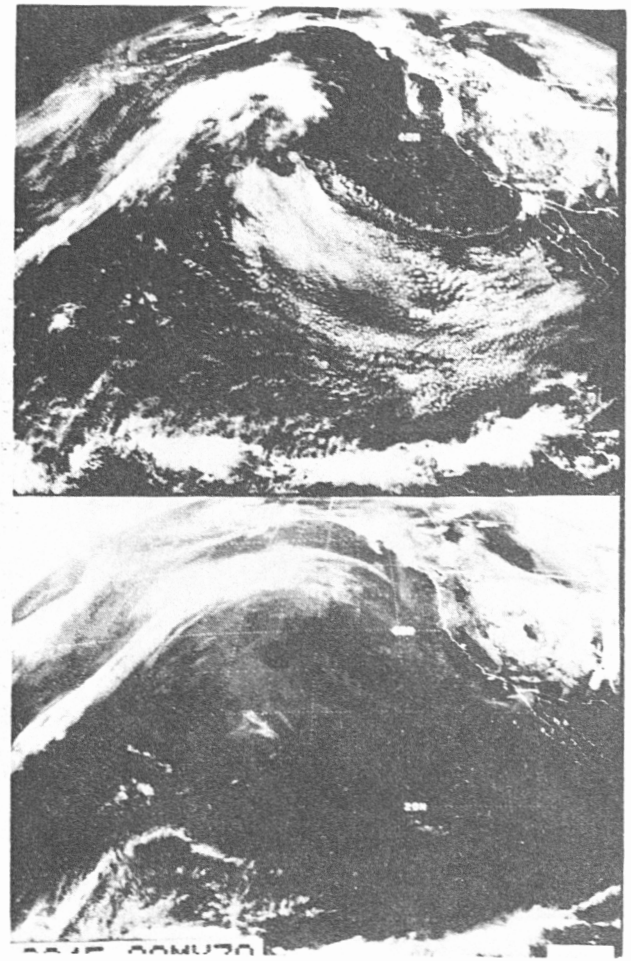

Figure 9.2.2 (Slide set #146)

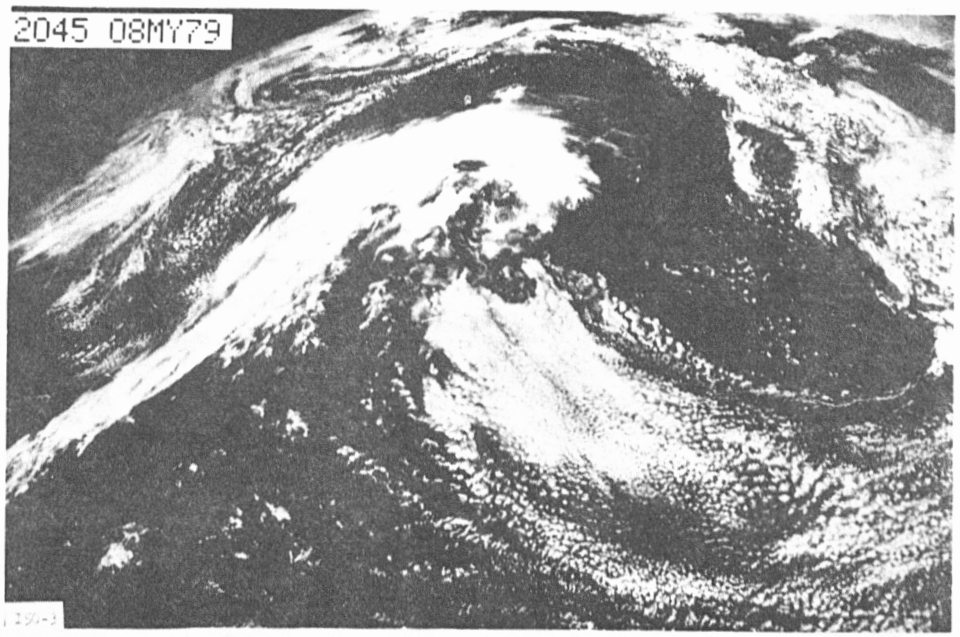

Figure 9.2.3 (Slide set #147)

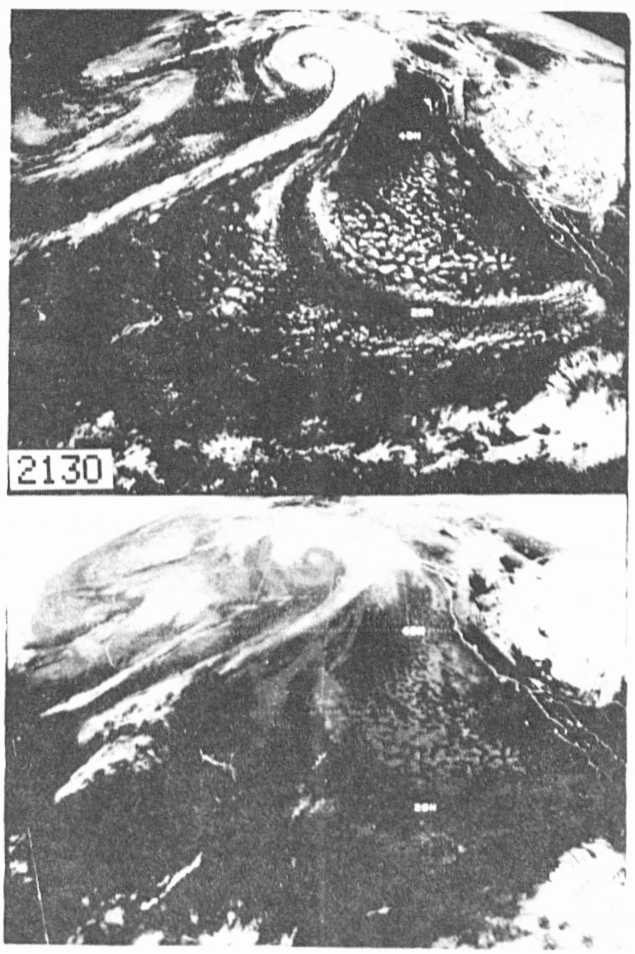

Figure 9.2.4 (Slide set #148)

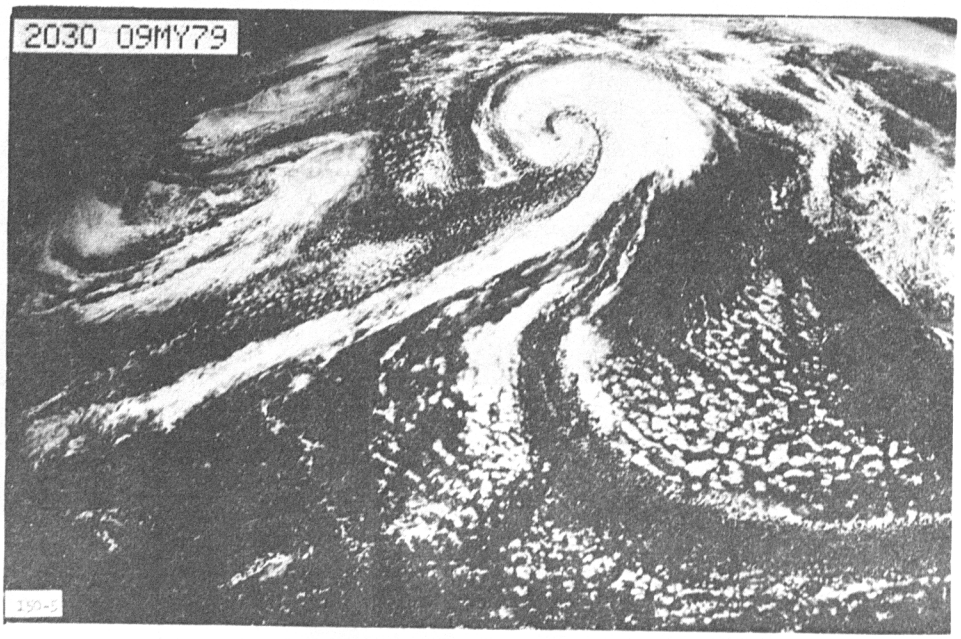

Figure 9.2.5 (Slide set #149)

CHAPTER 10

TROPICAL STORMS AND WEATHER SYSTEMS

Meteorological satellites have been used to observe the location of tropical storms for many years. In fact, one of the most well-known uses of satellite data is for the identification and tracking of these tropical storms, hurricanes and typhoons which cause so much destruction when they reach islands or major coastlines. Much remains to be done in this area of tropical storm observation from satellites because the parameters necessary to forecast the track of the storms and the intensification in the future are still important goals. This chapter will begin with a discussion of the most fundamental large-scale weather feature in the tropical belt, the InterTropical Convergence Zone (ITCZ). We will briefly examine other weather systems in the tropics which can be observed from satellites and we will conclude the chapter with a section on the observations of tropical storms, hurricanes and typhoons including an introduction to the Dvorak technique for estimating the intensity of tropical storms from satellite images.

A good portion of the notes and photographs for this chapter have been provided by Mr. Roger Weldon of NESDIS. Of course, the Dvorak method has been developed by Mr. Vern Dvorak and we acknowledge the information he provided on an up-to-date version of his technique.

10.1 The InterTropical Convergence Zone

Across the tropical oceans and most of the tropical land masses the semi-persistent convergence zone marked by converging easterly winds, a low

pressure belt and rather intensive precipitation and cloudiness has been studied by meteorologists for many years. With the advent of routine satellite observations this ITCZ came into special scrutiny and has been studied a great deal with the aid of satellite data. Forecasting the weather in tropical countries that are influenced by this zone involves careful watching of the ITCZ, and satellite pictures can be a great aid in this matter.

We will consider the following stages of ITCZ:

(a) the basic undisturbed case, no deep convection;

(b) the basic undisturbed case, deep convection;

(c) the perturbed case, with low-level developments;

(d) the perturbed case, with deep convection;

(e) the flare-up case;

(f) the double ITCZ case

In this section, we will use satellite pictures to display these various stages of the InterTropical Convergence Zone. Figure 10.1.1 [Note: This is slide set #162] shows the basic undisturbed ITCZ without deep convection. A view of this band across the central and eastern Pacific shown in both visible and infrared views displays no circulation systems imbedded in the zone. While there are a few cases of cold clouds, those in the western Pacific dissipated in 24 hours. All-in-all, this is a good example of the undisturbed case without deep convection. However, Figure 10.1.2 [Note: This is slide set #163] shows in contrast to the previous figure a basic convergence zone that is full of deep convection across most of the Pacific. The infrared view especially (in the top portion of the figure) shows that the clouds are quite cold and deep throughout a long east-west extent.

The next case or stage in development of the ITCZ is shown in Figure 10.1.3 [Note: This is slide set #164]. Here we see excellent examples of inverted "V"-waves or easterly waves, although the features are generally confined to the lower levels as evidenced by the fact that most of the cloudiness, particularly in the region around 140° West is of the warm variety. A close-up view of that region is shown in Figure 10.1.4 [Note: This is slide set #165]. This figure shows an obvious wave activity with the absence of any very deep enhanced convection.

The next view of the ITCZ in Figure 10.1.5 [Note: This is slide set #166] shows that the entire ITCZ is perturbed by three vertically deep circulation systems. The western one is of hurricane intensity and the eastern one is of tropical storm intensity. The middle one is less than tropical storm intensity and is weakening rapidly. This is an excellent example of a very perturbed condition where the circulations that have formed along the convergence zone have taken on deep vertical structures.

One of the most outstanding examples of satellite observations of tropical mid-latitude interactions came with the discovery in the late 1960's of the frequent occurrence of flare-ups from the disturbed InterTropical Convergence Zone into the mid-latitudes. Figure 10.1.6 [Note: This is slide set #167] shows what happens when a sudden surge of deep northwesterly flow occurs in the jet stream zone. Any pre-existing upper level circulation systems in the sub-tropical latitudes become deformed in an orientation transverse to the surge. Clouds form generally along the east half of the newly elongated trough and then move northeastward. When the "flare-up" is in low enough latitudes, the ITCZ clouds are affected. Usually that portion of the ITCZ band east of where the flare-up zone

intersects it becomes active with deep convection and moves poleward from its normal position. This "flare-up" condition is primarily a winter season feature. Research is still underway on these features and the role of tropical activity in their origin or support is under study. Meanwhile the "flare-up" systems are important for airline route forecasting.

During the months of March and April in the eastern Pacific we often find the occurrence of a second or double ITCZ. This double ITCZ was observed first in the late 1960's with the advent of geostationary experimental satellites viewing this area. The second convective cloud band often formed south of the equator along the gradient between the cool equatorial water and the warmer water further south at this time of year. When the double cloud bands are present the region between them is often very cloud-free. The presence or absence of the southern band is also apparently related to changes in the southern hemisphere circulation features. An example of the double band is shown in Figure 10.1.7 [Note: This is slide set #169].

10.2 Other Tropical Weather Systems

Throughout the tropics and subtropics other weather systems exist somewhat distinct from the ITCZ and from the more impressive and definitely more destructive tropical storms. These tropical weather systems can be observed from satellites and Figure 10.2.1 [Note: This is slide set #179] shows a vorticity center in the easterlies. This is a visible light picture taken on 26 August 1976. In this case there are westerly cloud motions south of the vorticity center at the time of the picture. These vorticity centers are also found in the southern hemisphere as is shown in

Figure 10.2.2 [Note: This is slide set #180]. We see these features just north of 20° South and the infrared view at the bottom of the figure shows that they are composed primarily of low, warm but bright clouds. These data were taken in September 1979.

Figure 10.2.3 [Note: This is slide set #181] shows a cut-off low system moving from east to west. Both the visual and IR pictures are shown. The system has a very deep closed circulation and has moved towards the west for several days. All comma-shaped areas of deep convection have been rotating around the center of this cut-off low in the Atlantic Ocean.

Another weather feature that is often observed and is important for forecasting is the deformation zone boundary or surge boundary that accompanies an easterly wave. Particularly when these systems approach a continental region they have the appearance as shown in Figure 10.2.4 [Note: This is slide set #183] and Figure 10.2.5 [Note: This is slide set #184]. These systems have a speed maximum in the low and middle level easterlies and frequently have a distinct deformation boundary in advance of the surge in the easterlies. This boundary is located on the northwest side of the vorticity center. Its shape depends upon whether the system is closed, how rapidly it is moving and the conditions of the environmental circulation. In the case shown here on 19 July 1975, in a visible light image, the deep cyclonic system is nearly stationary but the westerlies are pushing westward north of the system causing an east-west elongation. Such boundaries usually show as a clear band, or as a warm band on infrared images. Other characteristics vary greatly depending upon where the system is located. Over land, conditions vary diurnally. At 1400 GMT in the first figure, the band has a concentration of haze in the region to the west; the region to

the east is largely covered by stable low clouds and to the west there are patches of fog and clear to hazy conditions. The second view 7 hours later shows that the region behind the boundary to the east side now contains lines of deep convection. The western most line formed on the east side of the clear band.

10.3 Tropical Storms, Hurricanes and Typhoons

The tropical storm problem has several distinct portions. It is important to: (a) detect and track the location of the tropical storms; (b) estimate the intensity of the storm; (c) forecast its future track and (d) forecast its growth or dissipation as it moves along that future track. Satellites have been used in research work in all four of these areas. However, it is only in the first two areas, the detection/tracking and the estimate of present intensity, that operational techniques have evolved. In this section we give some examples of the tropical storms and cyclones as observed from satellites and also make use of one of the modern-day techniques for intensity estimation.

Figure 10.3.1 [Note: This is slide set #194] shows Hurricane Frederick in a high-resolution, visible light view and a hemispheric view in the infrared. These data were taken 30 minutes apart near 1800 GMT 12 September 1979. The hurricane at this point is striking the Gulf Coast of the United States and has a very well-developed circulation system as well as a large "eye". Figure 10.3.2 [Note: This is slide set #195] is a view of the same hurricane a few hours earlier. In this case the enhanced infrared data (EIR) is also used in contrast to the basic IR and visual light picture. The enhanced IR data allow special views of the top

features of the storm, particularly the region of extremely deep convection, in this case, along the southern and southwestern quadrants of the storm.

In another part of the world we see a picture of super Typhoon Bess, shown in Figure 10.3.3 [Note: This is slide set #208]. This was an especially strong typhoon and the picture was taken as the satellite passed directly over the center of the storm. Figure 10.3.4 [Note: This is slide set #207] shows one image per day for three different hurricanes during 1976. The pre-storm, the tropical storm and the hurricane stages are shown through the use of enhanced infrared (EIR). It can be seen that the variability of the tropical storms as viewed from the satellite is great, just as many of their other measurable parameters are known to vary greatly from storm to storm.

The technique by Dvorak (1975) is a method for determining tropical cyclone intensities from satellite visible or enhanced infrared (EIR) imagery. The basic premise on which the method is based is that the cloud features of a tropical disturbance can be used to determine its intensity when they are analyzed in the context of the past history of the disturbance. This means that every satellite picture of a storm's <u>cloud features</u> need not be directly related to the storm's intensity, but when a significant change in intensity occurs it will be accompanied by cloud features that are related to the new intensity. The cloud features that are observed in the satellite imagery that relate to these intensity changes of tropical disturbance are those that define the cloud system center and those that describe the banding that surrounds the center. The enhanced infrared images provide discrete boundaries (temperature levels) for

measuring the features as well as an objective estimate of their vertical depth. Because of this, the EIR imagery adds considerable objectivity to the Dvorak analysis that was not possible previously using only the visible light pictures. Thus, Dvorak has revised his paper noted above and Figure 10.3.5 [Note: This is slide set #202] shows the pattern most often observed in satellite pictures of developing tropical storms. Viewing the patterns from left to right, note that the band around the tropical disturbance curves farther around the disturbance center as the storm develops. The dense clouds making up the "cold curved bands" have temperatures of less than -30°C in the IR data. The intensity of a disturbance displaying this type of cloud pattern is related to the dense portion of the band encircling the center of the cloud system. When a storm having this type of pattern evolves to hurricane strength, the band is observed to completely encircle the storm center forming one of the "eye" patterns shown in step 4, or one of the "imbedded center" patterns in step 5. Continued intensification after hurricane or typhoon strength has been attained is indicated by the clouds encircling the "eye" becoming colder, or by the "eye" becoming warmer, smaller or more circular. The narrative above describes only a fraction of the Dvorak technique which is has refined in great detail. The reader is referred to reports issued regularly by Mr. Dvorak for the full details of the up-to-date method.

At the time of the preparation of these notes, some exciting new opportunities related to hurricane track forecasting and hurricane intensification have been produced by the research community. These new methods use the satellite temperature and moisture soundings and particularly the satellite microwave sounding data to estimate not only the intensity of the

warm core of the tropical cyclones, but also to sample the environmental mass and wind field around the periphery of the storm which plays a role in its future track. These new results are not yet available for operational use but should be adopted by some of the major tropical storm forecast centers within the next few years and should be in the hands of smaller forecast units a few years after that.

References and Further Reading

Dvorak, V. F., 1975: Tropical cyclone intensity analysis and forecasting from satellite imagery. Mon. Wea. Rev., 103, 420-430.

Grody, N. C., C. M. Hayden, W. C. C. Shen, P. W. Rosenkranz and D. H. Staelin, 1979: Typhoon June winds estimated from scanning microwave spectrometer measurements at 55.45 GHz, J. Geophys. Res., 84, 3689-3695.

Kidder, S. Q., W. M. Gray and T. H. Vonder Haar, 1978: Estimating tropical cyclone central pressure and outer winds from satellite microwave data, Mon. Wea. Rev., 106, 1458-1464.

Kidder, S. Q., W. M. Gray and T. H. Vonder Haar, 1980: Tropical cyclone outer surface winds derived from satellite microwave sounder data, Mon. Wea. Rev., 108, 144-152.

Rodenhuis, D. R. and R. A. Anthes, 1978: Hurricanes and tropical meteorology, Bull. Amer. Meteor. Soc., 59, 790-803.

Velden, C. S. and W. L. Smith, 1983: Monitoring tropical cyclone evolution with NOAA satellite microwave observations. J. Climate Appl. Meteor., 22, 714-724.

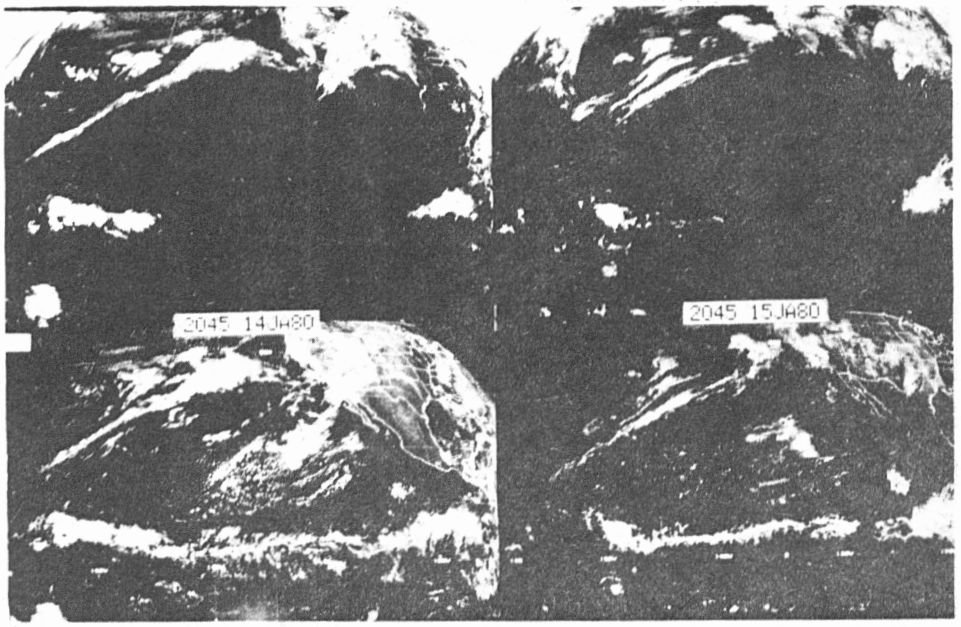

Figure 10.1.1 (Slide set #162)

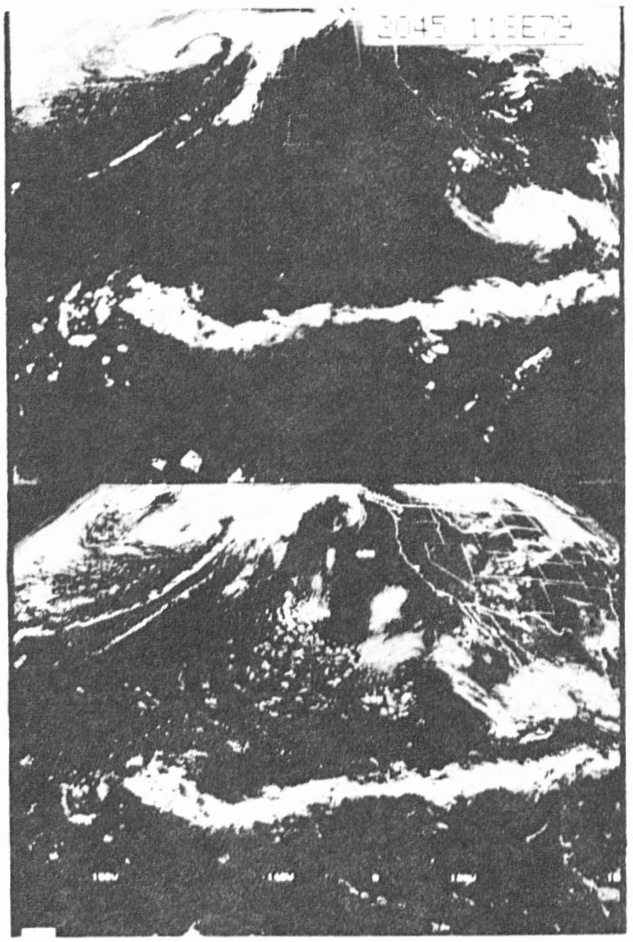

Figure 10.1.2 (Slide set #163)

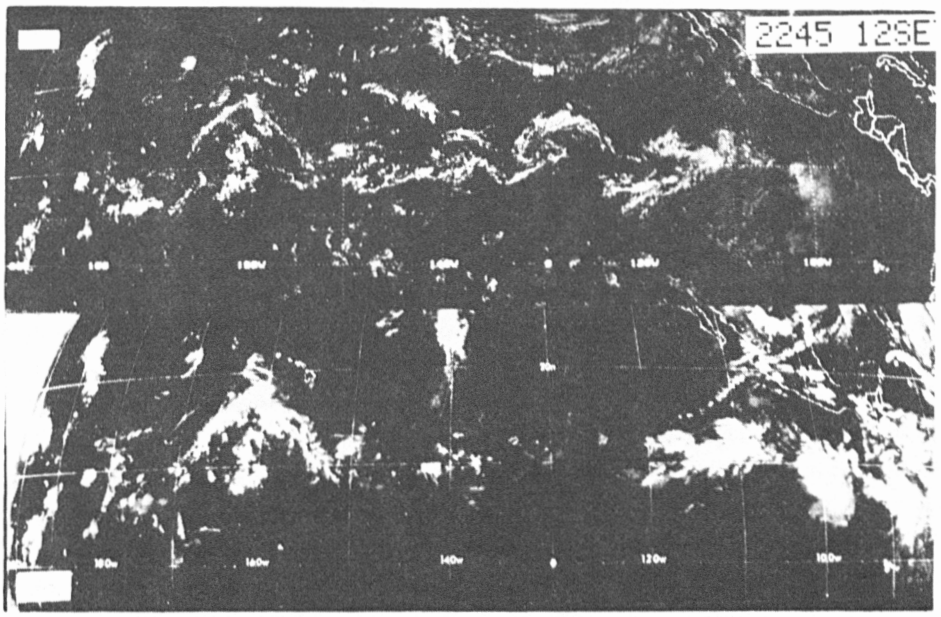

Figure 10.1.3 (Slide set #164)

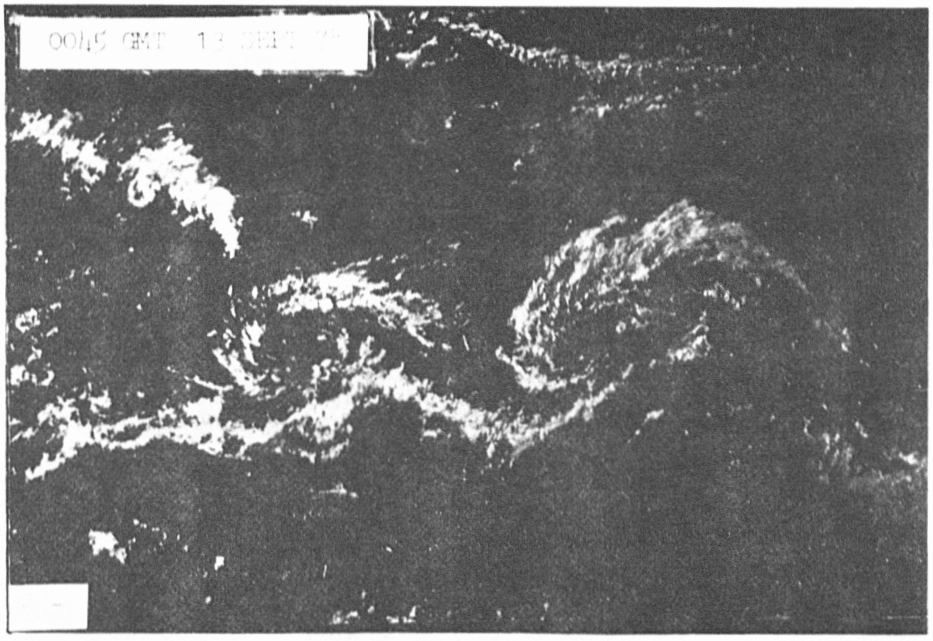

Figure 10.1.4 (Slide set #165)

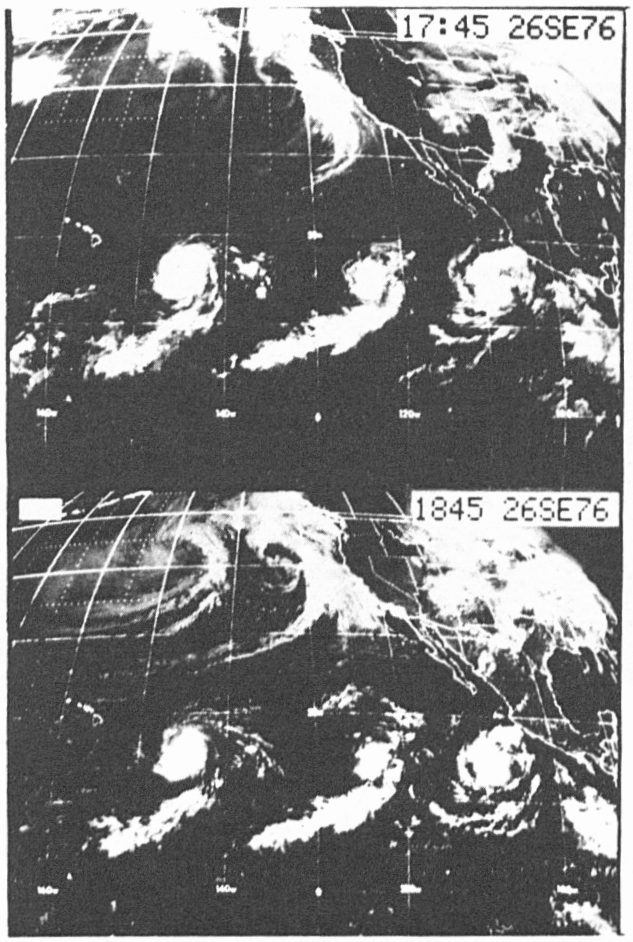

Figure 10.1.5 (Slide set #166)

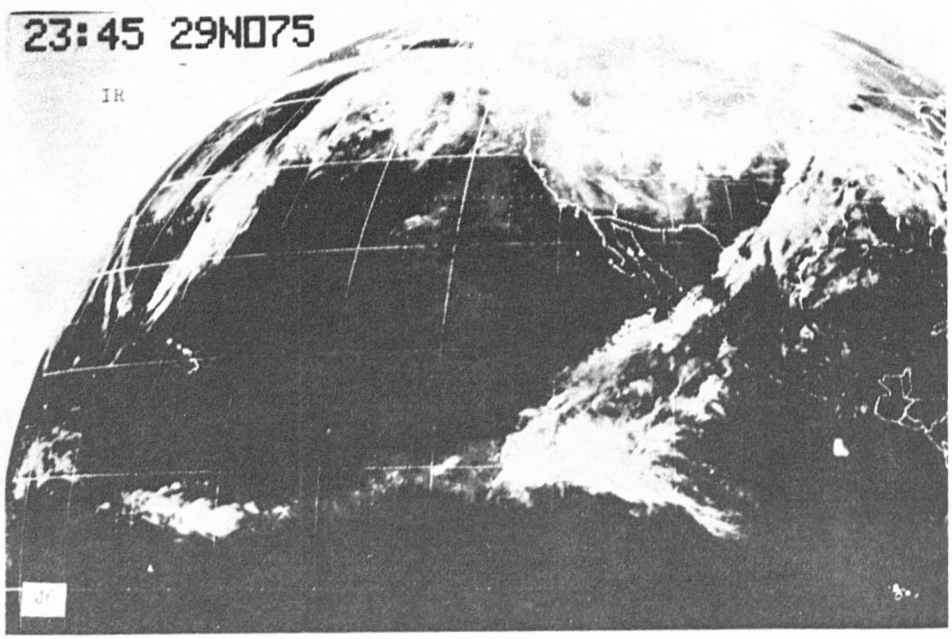

Figure 10.1.6 (Slide set #167)

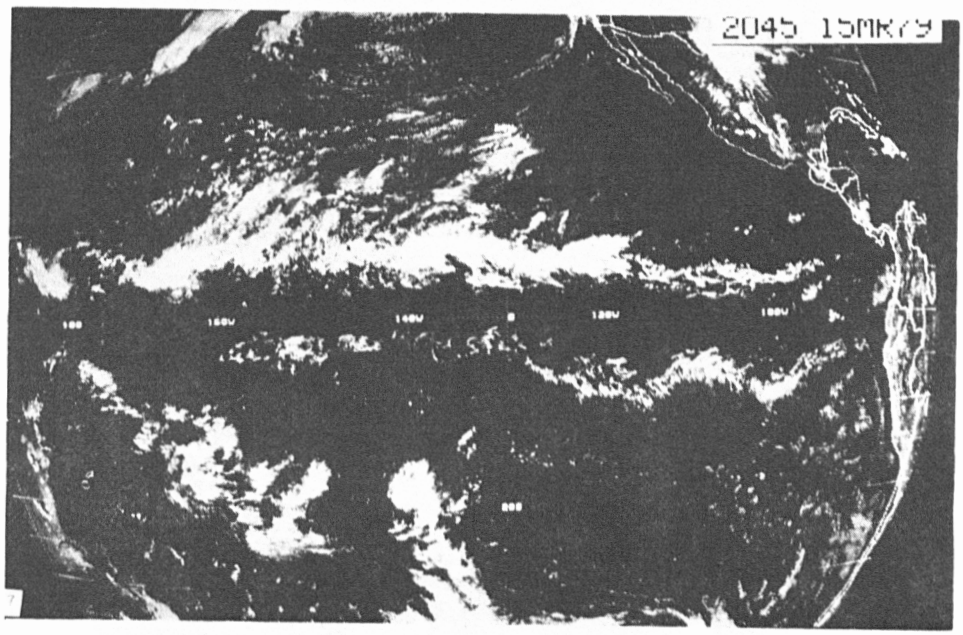

Figure 10.1.7 (Slide set #169)

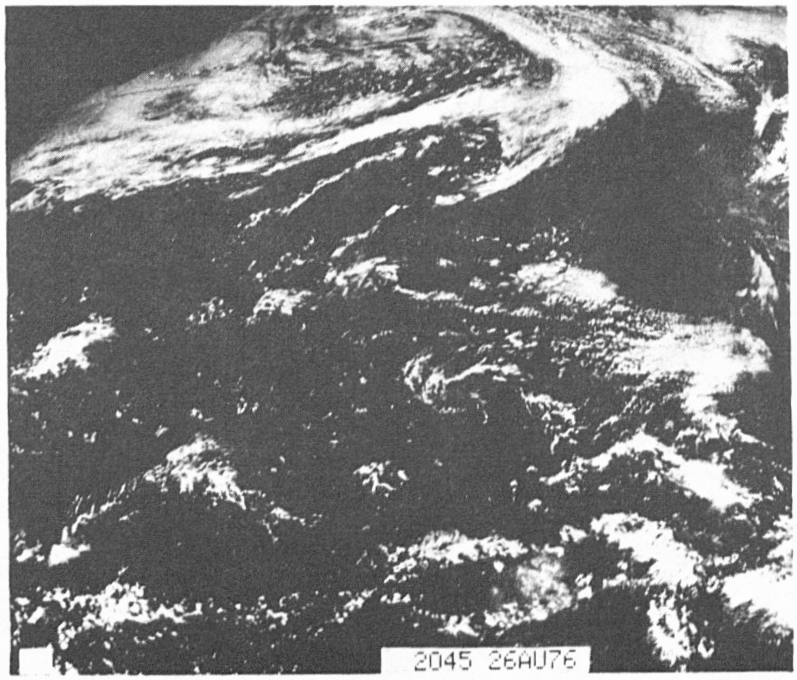

Figure 10.2.1 (Slide set #179)

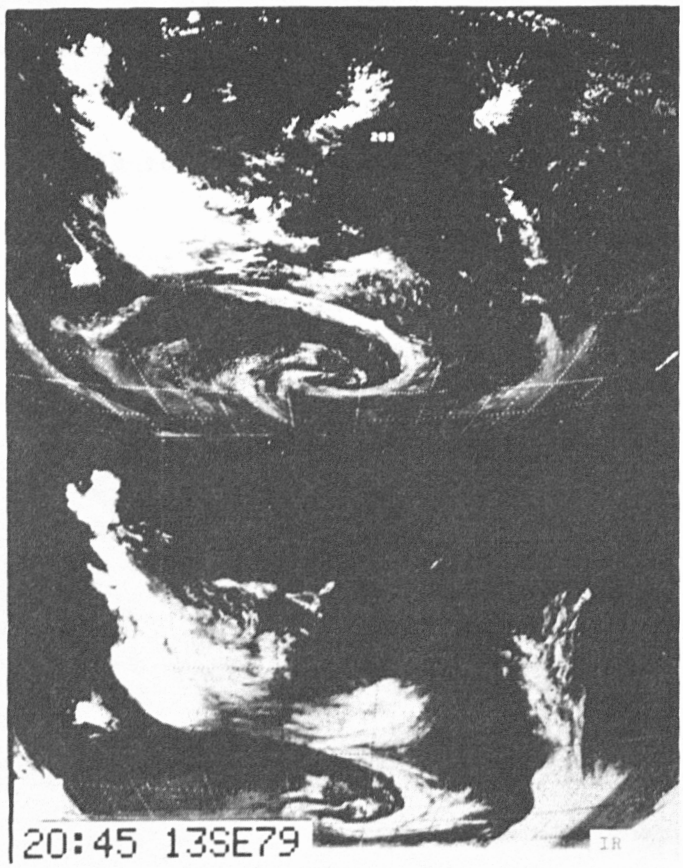

Figure 10.2.2 (Slide set #180)

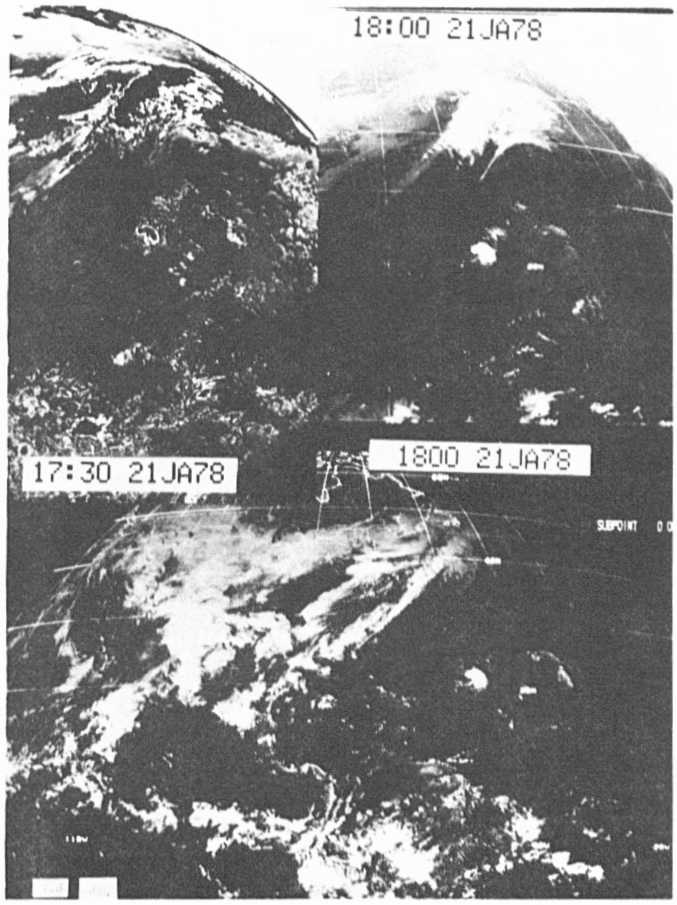

Figure 10.2.3 (Slide set #181)

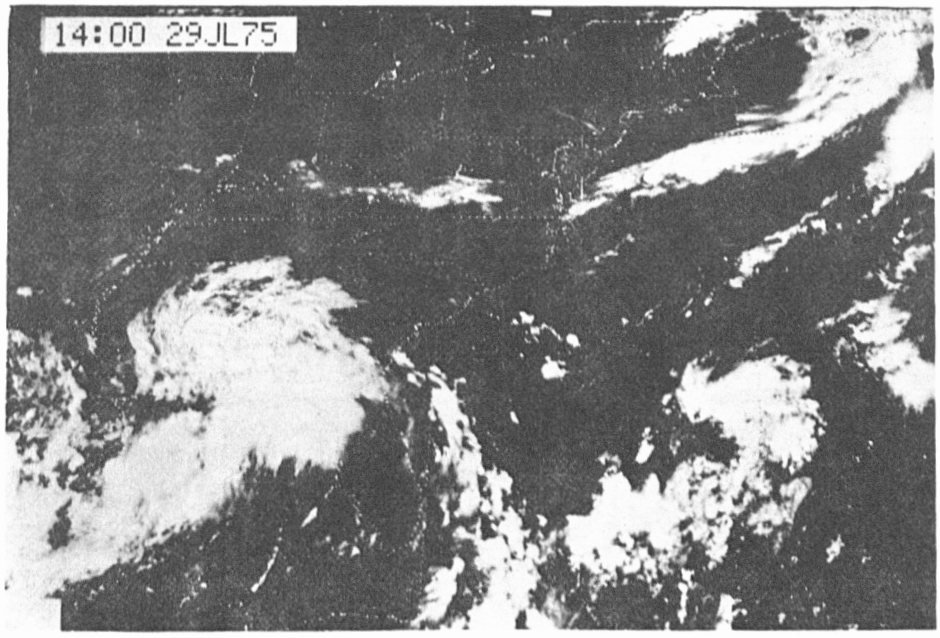

Figure 10.2.4 (Slide set #183)

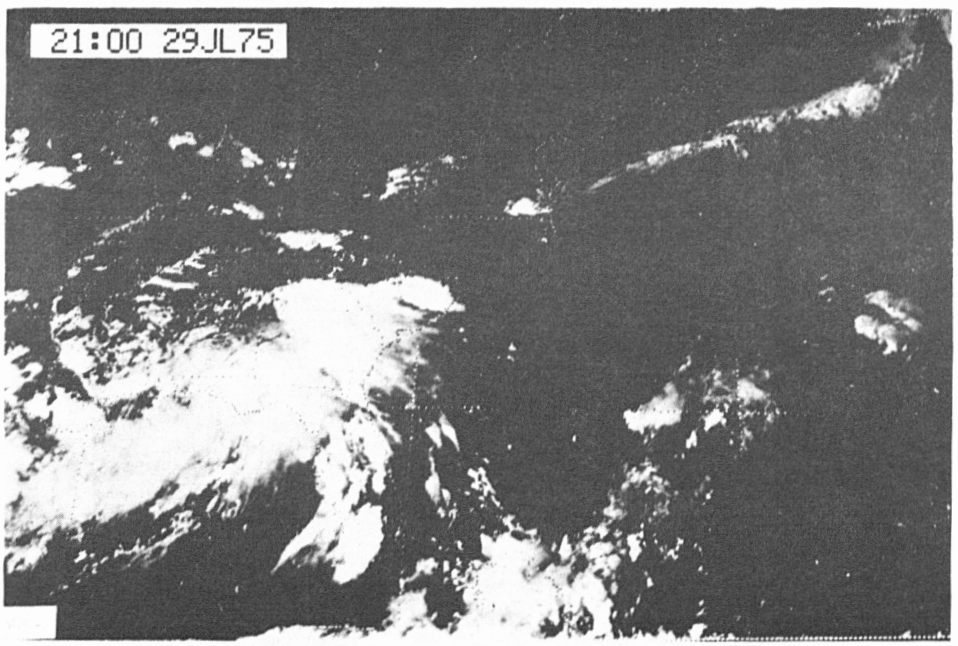

Figure 10.2.5 (Slide set #184)

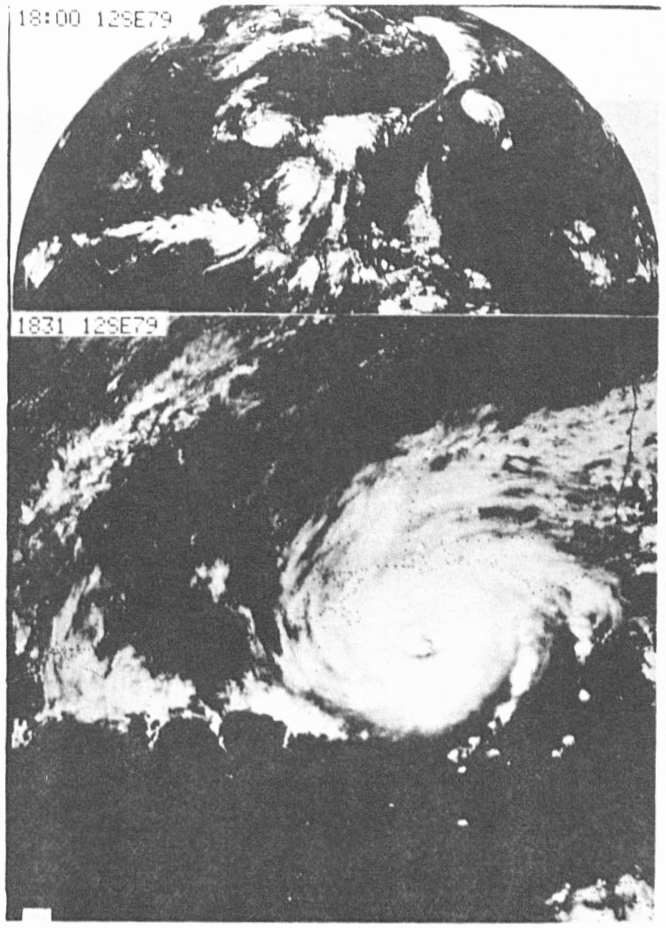

Figure 10.3.1 (Slide set #194)

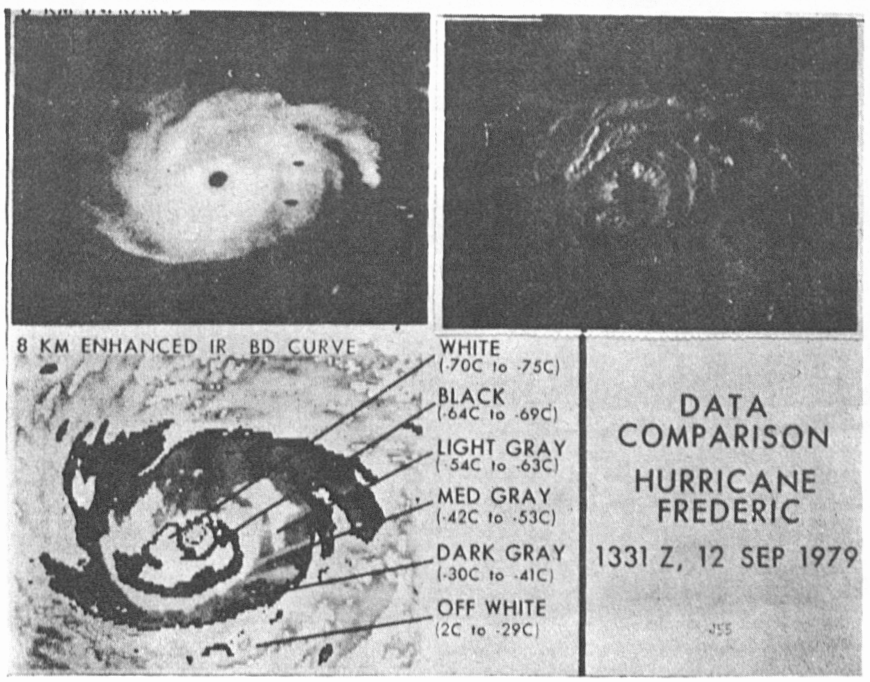

Figure 10.3.2 (Slide set #195)

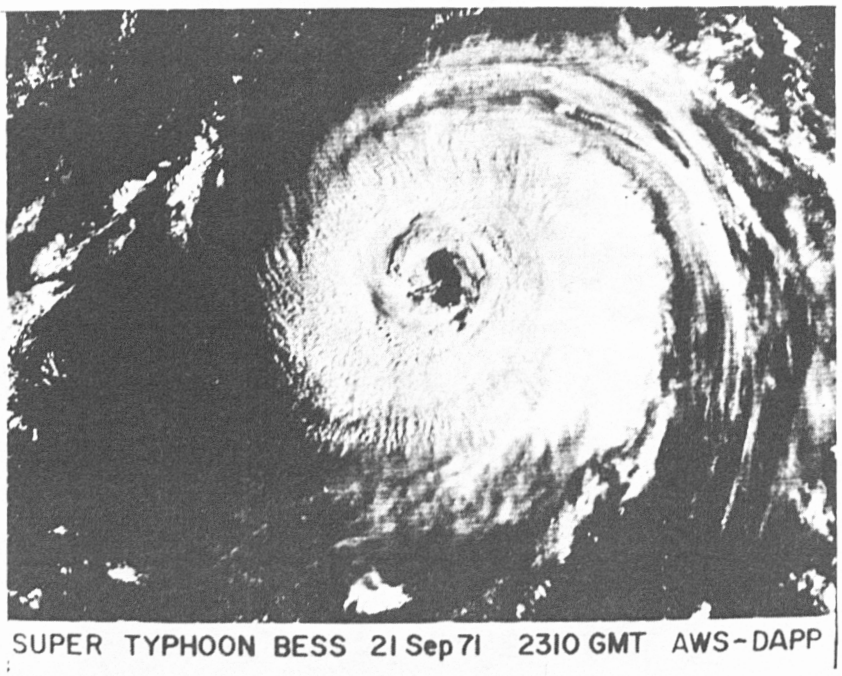

Figure 10.3.3 (Slide set #208)

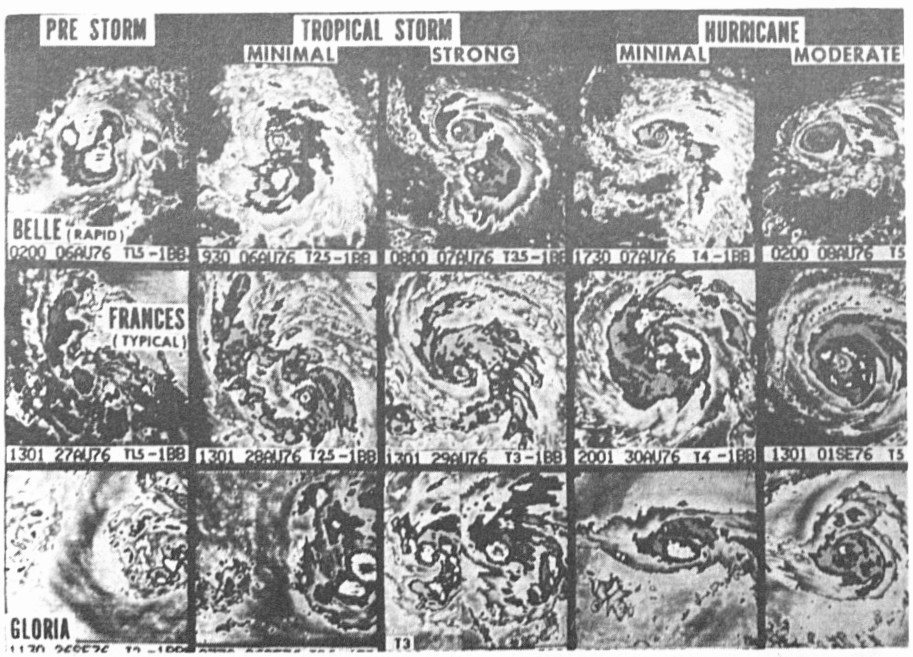

Figure 10.3.4 (Slide set #207)

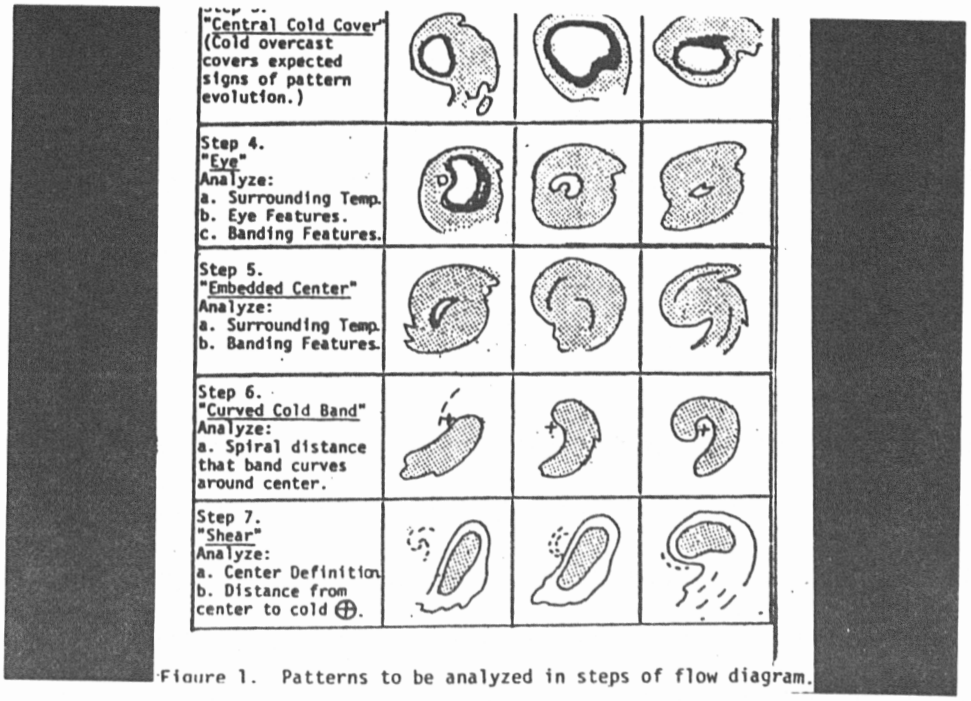

Figure 1. Patterns to be analyzed in steps of flow diagram.

Figure 10.3.5 (Slide Set #202)

Blank page retained for pagination

CHAPTER 11

SMALL-SCALE WEATHER FEATURES

Several types of small-scale features are important to weather forecasting. Satellites have the ability to observe such features in both space and time. This chapter will emphasize examples of fog as viewed from the satellite. A large number of slides in the available slide set also give good examples of fog and stratus as viewed from space. Clouds related to orography are also discussed briefly.

11.1 Fog

The formation of fog depends on the right combination of elements. In the case of radiative fog, sufficient radiative cooling must take place. Most fogs form during the night, so clear skies must exist prior to fog formation. Sufficient moisture must also exist to allow condensation. Parmenter (1976) showed that infrared imagery from satellites could be used to detect low-level moist areas. Such areas are prone to later fog development. In the infrared imagery the areas where fog and stratus are most likely to form will appear darker than surrounding areas (Gurka, 1976). Such dark areas are normally found downwind from a moisture source.

The reason for the dark appearance is not entirely straight forward. If the only difference between a potential fog area and the surroundings was due to water vapor then one would expect the moist area to appear lighter (colder) due to absorption and emission of infrared radiation at

higher (or colder) levels. However, the fact that sufficient cooling has to take place is probably the reason for the dark appearance. If a temperature inversion (temperature increase with height) were predominant over an area, as frequently occurs at night, then a moist area would appear darker due to the absorption and emission from higher (or warmer) levels.

Such keys may be used as aids in fog forecasting. The satellite view might be more important than surface observations. The higher spatial and temporal measurements from the satellite are often times helpful.

Several views of fog are given by Slides 211 through 246.

The dissipation of fog once it has formed is another forecast problem. Gurka (1978) used enhanced visible satellite imagery for this purpose. There exists a positive correlation between satellite-viewed fog brightness and fog persistence. The size of the fog area is an additional factor to be considered, since extensive areas of fog generally persist longer than smaller areas with comparable brightness.

Fog dissipation was found to occur from the outside edges of the cloudy region inward, due to differential heating along the cloud boundary and the resultant mixing (Purdom, 1982). Many times the distinction be tween fog and stratus may be apparent in satellite imagery. If the cloud appears to follow valleys and to take the shape of local terrain, then there is a better chance that it is low-level fog rather than stratus.

11.2 Orographic (Wave) Clouds

Mountain barriers have strong effects on cloud formation. Satellite pictures frequently reveal the occurrence of remarkably regular cloud bands

in the lee of mountain ranges. The cloud bands are nearly always perpendicular to the wind direction. The width and downwind extent of the area covered by cloud bands can be several hundred kilometers. These cloud bands are indicative of two-dimensional wave motion. Wavelengths are usually 10 to 30 km (Gjevik, 1980). An example of lee waves is given in Figure 11.2.1.

Lee-wave clouds occur frequently, especially in winter when the atmosphere is more stable. The cloud bands generally consist of stratocumuli (base 1 to 1.5 km, top 4 km) topped by altocumuli (6 to 7 km). A continuous cloud layer is usually distorted by wave motion to form the cloud bands. Wind speeds usually increase with height and waves will not form unless the wind speed exceeds a threshold value which depends on the mountain height and width. There is a positive correlation between wavelength and mean wind speed in the troposphere, but a negative correlation between horizontal extent and the thickness of the stable layer in which the waves form. Wind speeds of at 20 $m \cdot s^{-1}$ seem to be required at the base of the stable layer with increasing wind at higher levels. The stable layer of 0.5 to 4 km thickness is surrounded (both above and below) by less stable layers.

References

Gjevik, B., 1980: Orographic effects revealed by satellite pictures: Mesoscale flow phenomena. [IN] Orographic Effects In Planetary Flows, Chapter 9, GARP Publication Series #23, 301-316.

Gurka, J. J., 1978: The use of enhanced visible imagery for predicting the time of fog dissipation. AMS Conference on Weather Forecasting and Analysis and Aviation Meteorology. 16-19 October, Silver Spring, MD, 343-346.

Gurka, J. J., 1976: Using satellite data as an aid to forecasting fog and stratus formation. NWS/NESS Satellite Applications Information Note 3/76-1, AWS/TN-79/003 (compiled 1979), 47-51.

Gurka, J. J., V. J. Oliver and E. M. Maturi, 1982: The use of geostationary satellite imagery for observing and forecasting movement of New England sea fog, Preprints, Ninth Conference on Weather Forecasting and Analysis, Seattle, WA, 28 June - 1 July, 143-151.

Parmenter, F. C., 1976: Low-level moisture intrusion from infrared imagery. Mon. Wea. Rev., 104, 100-104.

Purdom, J. F. W., 1982: Subjective interpretation of geostationary satellite data for nowcasting, Chapter 3.1, Nowcasting, (K. A. Browning, editor). Academic Press, London, 149-166.

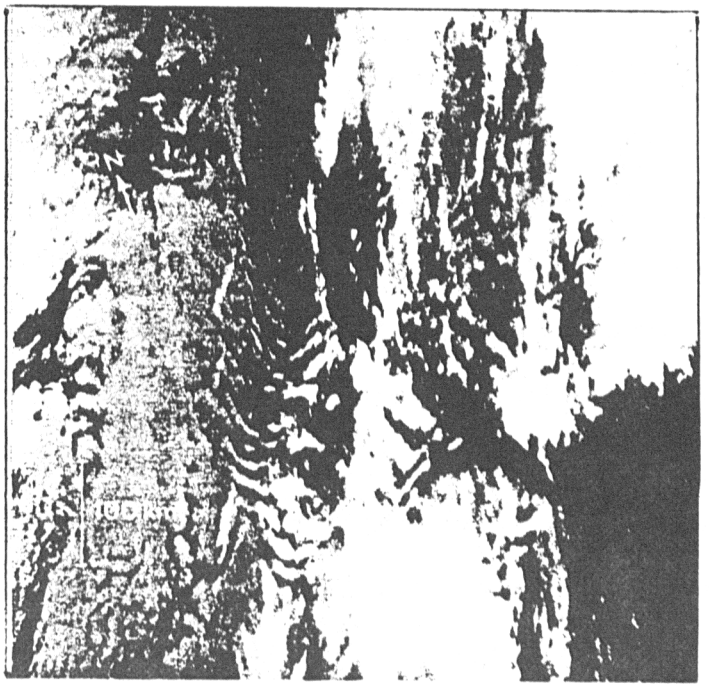

Waves over Iceland 19 November 1976, about 1130 GMT, photographed by NOAA-5. The picture shows lee-waves originated by different mountain peaks. The picture is unrectified. (See Figure 2.) (Photographed by courtesy of Tromsö satellitt-telemetristasjon, NTNF, Tromsö)

Figure 11.2.1 Orographic Wave Clouds over Iceland (Gjevik, 1980)

Blank page retained for pagination

CHAPTER 12

SEVERE MESOSCALE STORMS

12.1 Analysis and Interpretation of Thunderstorm Images

Many interesting cases have documented possible relationships between thunderstorms and their mesoscale environment. Examples of such relationship include a tendency for afternoon storms to form in regions clear during the morning or to form around the fringes of regions cloudy or foggy during the morning and a tendency for intense storms to occur where and when cloud lines intersect (Details and additional examples may be found in Purdom, 1976 and Anderson *et al.*, 1974). Specific cases demonstrating the use of satellite imagery in thunderstorm detection, monitoring and forecasting are presented in the following sections. The reader is referred to Maddox and Vonder Haar (1982) for more details.

12.1.1 Monitoring Movement and Intensity of Thunderstorm Gust Fronts

The importance of gust fronts as a hazard to aviation has been emphasized by crashes that apparently resulted when aircraft penetrated gust fronts shortly before touch down or after liftoff. Fujita (1978) feels that the shape of individual storms, as monitored in satellite and radar data, may indicate that strong outflows are present. Gurka (1976) has presented results of a more general study in which he correlated satellite-observed characteristics of thunderstorm cloud arcs with concurrent surface wind observations. Figures 12.1.1.1 and 12.1.1.2 show the southward

progression of a cloud arc across the Baltimore/Washington, D.C. area from 21 to 22 GMT on 3 July 1975. Selected surface wind observations have been superimposed on the images.

Gurka lists the following characteristics of thunderstorm gust fronts that can be identified using satellite imagery:

1. Wind gusts and wind shear occur very near to or at the leading edge of the cloud arc.
2. Strongest winds occur beneath the portion of the arc nearest to the most vigorous convection.
3. The regions of vigorous convection are pinpointed by the cloud edge brightness gradients on enhanced IR imagery.
4. Cloud arcs bounding mesohighs associated with a cloudy areas and active convection are characterized by stronger gusts than are narrow cloud arcs that are trailed by clear skies.
5. Rapidly moving cloud arcs are generally associated with strong low-level winds.

12.1.2 Severe Thunderstorm/Jetstream Relationship

Many researchers have presented both observational and theoretical studies which related positions of jetstreams, or bands of maximum wind speeds, with the development, location and orientation of severe thunderstorms. Whitney (1977), studying severe storm occurrences on 16 active days, found that severe activity rarely developed southward past the location of the sub-tropical jetstream. The positions of jetstream features were determined using both satellite photographs and conventional upper-air sounding data.

Figures 12.1.2.1 shows Whitney's analysis of the 30 April 1975 severe thunderstorm situation. The subtropical jetstream sharply delineates the southern boundary of the large area of severe storm occurrences. He found that severe thunderstorms usually develop first along the surface front very near to the polar jetstream (note that a double polar jet structure was analyzed in Figure 12.1.2.1). Activity then moves eastward ahead of the surface front while developing southward across the zone between the diverging jetstreams. Miller and McGinley (1978) have developed a technique for forecasting severe thunderstorms that integrates conventional upper-air data, surface analyses and satellite imagery to identify zones or areas having storm potential. The detection and tracking of various jetstreams and jetstream branches (utilizing both satellite imagery and upper-air reports) plays a crucial role in this innovative forecast scheme and the interested reader should refer to their extensive report for specifics.

12.1.3 Thunderstorm Boundaries and Intersection

Making use of satellite imagery, Purdom (1976) shows that the leading boundary of a thunderstorm-associated mesohigh often appears as an arc-shaped line of convective clouds. He also shows (Purdom, 1973 and 1974) that the intersection of such an arc cloud with another boundary marks a local region with a high potential for intense convective development and severe storm occurrence. These findings provide "photographic" verification of well known severe storm characteristics presented earlier by Magor (1959) and Miller (1972).

Such a convective development is presented in Figures 12.1.3.1, 12.1.3.2 and 12.1.3.3 which show the 2100 GMT GOES-1 photograph on 26 May

1975, a corresponding mesoscale surface analysis and a subsequent photograph for 2230 GMT. The impressive convective development in south central Oklahoma occurred in the favored arc line/boundary intersection zone at Point A.

The ability to locate such boundaries precisely in GOES imagery and to observe their interaction with other boundaries provides the forecaster with information which can be of use in the short range prediction of intense convective development. Likewise, such data are valuable for studies of both the climatology of such boundary effects and the dynamical reasons for their occurrences.

12.1.4 Cloud Top Tornadic Signatures

Fujita and his colleagues have tried to relate cloud top features with severe weather occurrences at the surface (see, for examples: Fujita, 1973 and Shenk, 1974). Fujita has proposed that the decay of overshooting cloud top activity may be related to tornado development. Figure 12.1.4.1 (from Fujita *et al.*, 1976) presents a correlation of overshooting cloud top activity with the occurrence of several intense tornadoes in Illinois and Indiana on the afternoon of 20 March 1976. The storm was characterized by overshooting top activity prior to and after the tornado occurrences. Figure 12.1.4.2 presents concurrent radar scope and satellite photographs at the time when the large Sadorus tornado was known to be on the ground at Point A where the satellite photograph shows a swirl in the relatively flat anvil top. Temporal and spatial satellite data of very high resolution are required if such features are to be closely monitored and many more case studies are needed before reliable forecast techniques can be developed.

12.2 Thunderstorm Research Techniques

The recent development of interactive man/machine computer systems, specifically designed for processing and analyzing satellite data, has encouraged the undertaking of more quantitative thunderstorm research. Use of digital data transmitted from the satellite and stored on magnetic tape is possible in these systems. A variety of applications, ranging from sequential looping and cloud tracking to produce a wind field, to color enhancements of specific features, to superimposed displays of differing data types, are available. Navigation (earth coordinate location of features) accuracy to within a single data element (pixel) is possible on these systems.

12.2.1 Cloud Top Temperature Fields

Sikdar *et al.* (1970) showed that convective mass fluxes could be estimated using satellite data. Adler and Fenn (1977) used infrared data and an interactive system to compute cold cloud top areas as a function of time for a large number of cloud systems that included several significant severe thunderstorms. They also used the rate of increase of cloud top area to estimate anvil divergence. Figure 12.2.1.1 shows a plot of cold top area with time for a tornadic cloud system over South Dakota on 6 May 1975.

Adler and Fenn found that the first report of tornadic activity took place during, or just after, the rapid expansion of cold cloud area, indicating rapid ascent and growth of thunderstorm tops on the scale observed by the satellite. These findings are different than the results presented

in Figure 12.1.4.1. This discrepancy may be due to the difference in resolution of the IR and visible sensors (overshooting tops must be quite large to be detected in the IR), and the need for further studies of cloud top activity as a signature of storm severity is apparent. It is possible that such studies may not only lead to improved detection and warning of tornadic storms, but also to better understanding of the dynamics and thermodynamics of tornado development.

More recent results of using advanced analysis systems include Hasler and Adler (1980) and Reynolds (1980). Maddox (1980) used enhanced, infrared satellite imagery as a basis for his definition of mesoscale convective complexes (MCC's). Several examples of MCC's as viewed in enhanced infrared satellite imagery are given in Figure 12.2.1.2.

References

Adler, R. F and D. D. Fenn, 1977: Satellite-based thunderstorm intensity parameters. Preprints 10th Conf. on Severe Local Storms, AMS, Omaha, NE, 8-15.

Anderson, R. K., et al.), 1974: Application of meteorological satellite data in analysis and forecasting. ESSA Tech. Report NESC-51, 250 pp.

Fujita, T. T., 1978: Manual of downburst identification for Project NIMROD. SMRP Paper No. 156, Univ. of Chicago, 104 pp.

Fujita, T. T., 1973: Tornado occurrences related to overshooting cloud-top heights as determined from ATS pictures. SMRP Paper No. 97, Univ. of Chicago, 32 pp.

Fujita, T. T., G. S. Forbes and T. A. Umenhofer, 1976: Close-up view of 20 March 1976 tornadoes: Sinking cloud tops to suction vortices. Weatherwise, 29, 116-131.

Gurka, J. J., 1976: Satellite and surface observations of strong wind zones accompanying thunderstorms. Mon. Wea Rev., 104, 1484-1493.

Hasler, A. F. and R. F. Adler, 1980: Cloud top structure of a tornadic thunderstorm from 3-min interval stereo satellite images compared with radar and other observations. Preprints - 19th Conf. on Radar Meteorology, AMS, 15-18 April, Miami Beach, FL, 405-412.

Maddox, R. A., 1980: Mesoscale convective complexes. Bull. Amer. Meteor. Soc., 61, 1374-1387.

Maddox, R. A. and T. H. Vonder Haar, 1982: On the use of satellite observations, Chapter 11, [IN] Thunderstorms, A Social, Scientific and Technological Documentary, Vol. 3, E. Kessler (editor), U. S. Department of Commerce, NOAA/ERL, 279-308.

Magor, B. W., 1959: Mesoanalysis: Some operational analysis techniques utilized in tornado forecasting. Bull. Amer. Meteor. Soc., 40, 499-511.

Miller, R. C., 1972: Notes on analysis and severe storm forecasting procedures of the Air Force Global Weather Central. Air Weather Service TR-200 (Rev.), 102 pp.

Miller, R. C. and J. A. McGinley, 1978: Using satellite imagery to detect and track comma clouds and the application of the zone technique in forecasting severe storms. Project Report, GE/Management and Technical Services Company, Beltsville, MD, 100 pp.

Purdom, J. F. W., 1976: Some uses of high-resolution GOES imagery in the mesoscale forecasting of convection and its behavior. Mon. Wea. Rev., 104, 1474-1483.

Purdom, J. F. W., 1974: Satellite imagery applied to the mesoscale surface analysis and forecast. Preprints of 5th Conf. on Weather Forecasting and Analysis, AMS, St. Louis, MO, 63-68.

Purdom, J. F. W., 1973: Meso-highs and satellite imagery. Mon. Wea Rev., 101, 180-181.

Reynolds, D. W., 1980: Observations of damaging hailstorms from geosynchronous satellite digital data, Mon. Wea. Rev., 108, 337-348.

Shenk, W. E., 1974: Cloud top height variability of strong convective cells. J. Appl. Meteor., 13, 917-922.

Sikdar, D. N., V. E. Suomi and C. E. Anderson, 1970: Convective transports of mass and energy in severe storms over the United States - an estimate from a geostationary altitude. Tellus, 22, 521-532.

Whitney, L. F., 1977: Relationship of the sub-tropical jet stream to severe local storms. Mon. Wea. Rev., 105, 398-412.

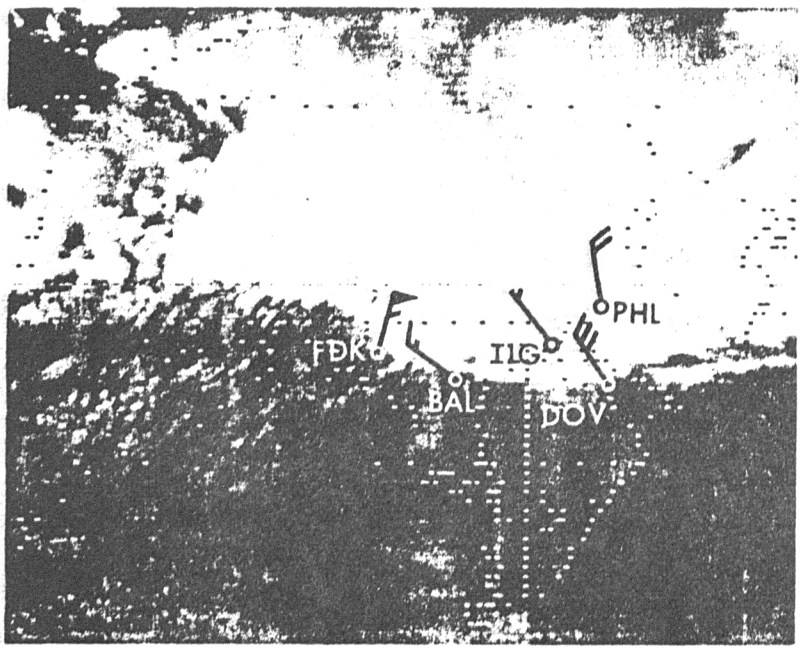

Figure 12.1.1.1

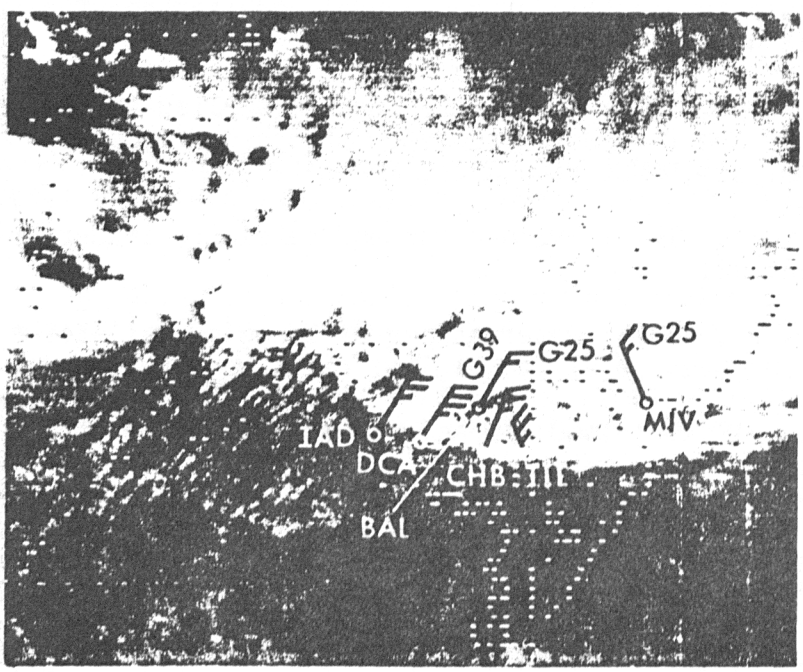

Figure 12.1.1.2 SMS-1 visible 1-km data showing surface wind observations for 2100 GMT, 3 July 1975 (above); 2200 GMT, 3 July 1975 (below) (Gurka, 1976).

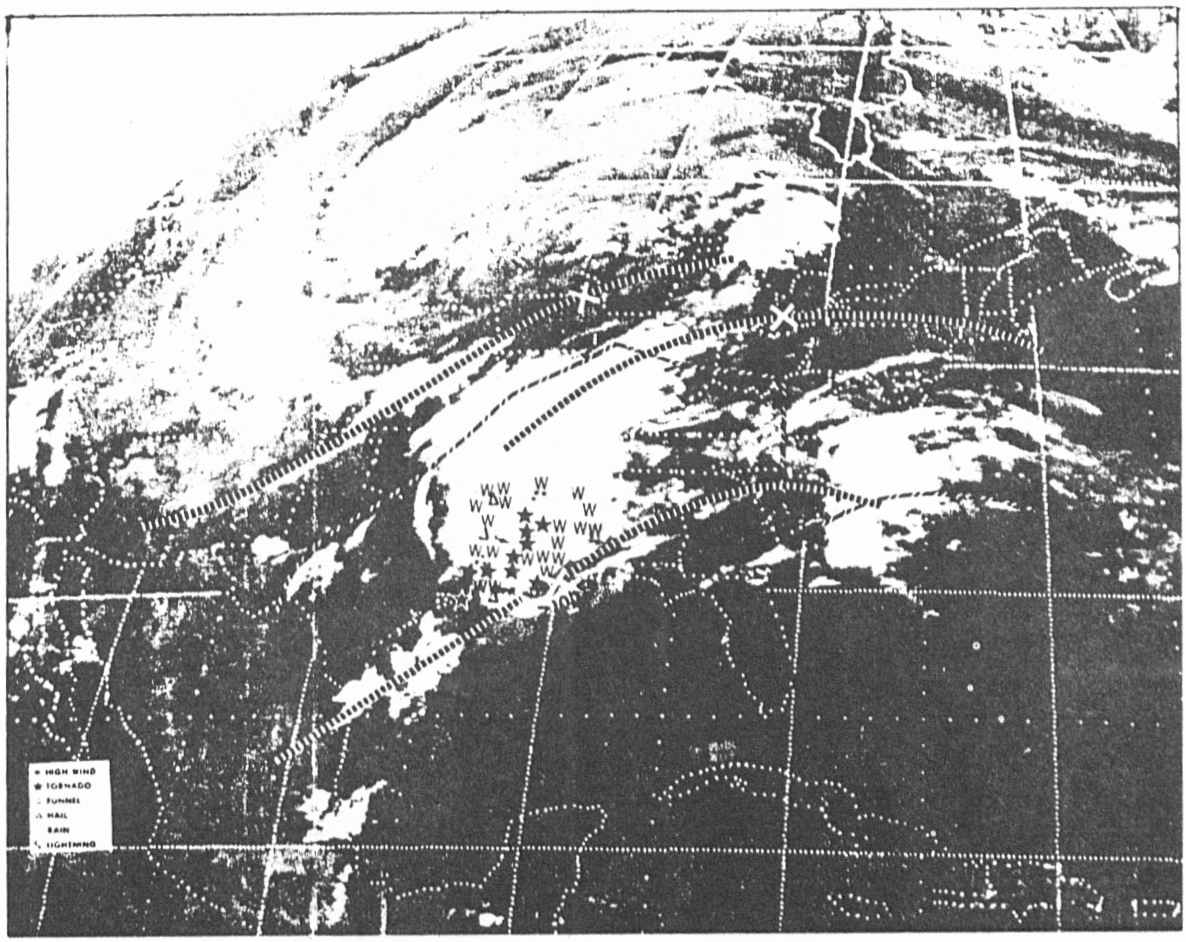

Figure 12.1.2.1 SMS infrared picture at 0000 CST, 30 April 1975 showing concurrent severe storms and the synoptic features of jetstreams and surface fronts. Bold dashed lines are the axes of the jetstreams. Heavy ×'s are positions of wind maxima. Subtropical windspeed maximum is >100 knots. Thin, candy-striped lines are surface fronts. Dotted lines are geographical and political grid overlay (Whitney, 1977).

a

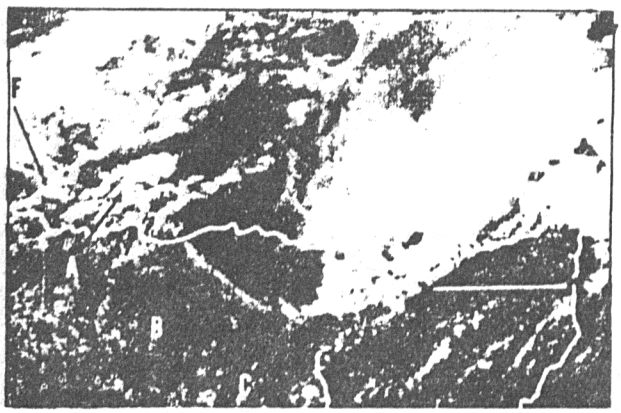

Figure 12.1.3.1

b

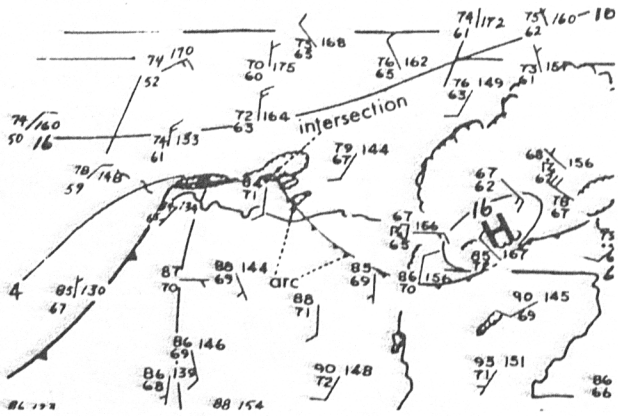

Figure 12.1.3.2

c

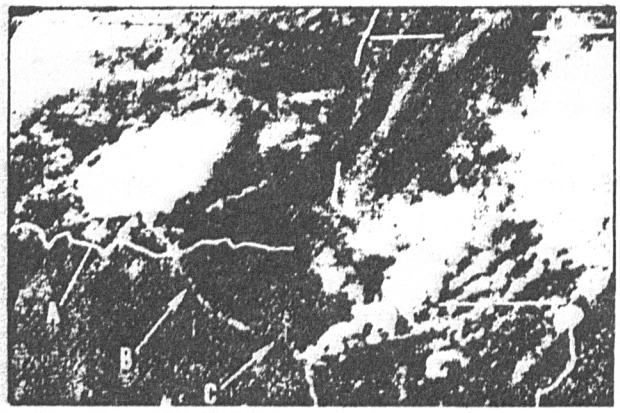

Figure 12.1.3.3 (a) GOES-1 1-km visible imagery for 2100 GMT, 26 May 1975. A cloud arc, produced by the storms over Arkansas, stretches from A to B to C. A second arc line is indicated at F. (b) Surface analysis for 2100 GMT, 26 May 1975, showing selected clouds and cloud boundaries. (c) GOES-1 1-km visible imagery for 2230 GMT, 26 May 1975 (Purdom, 1976).

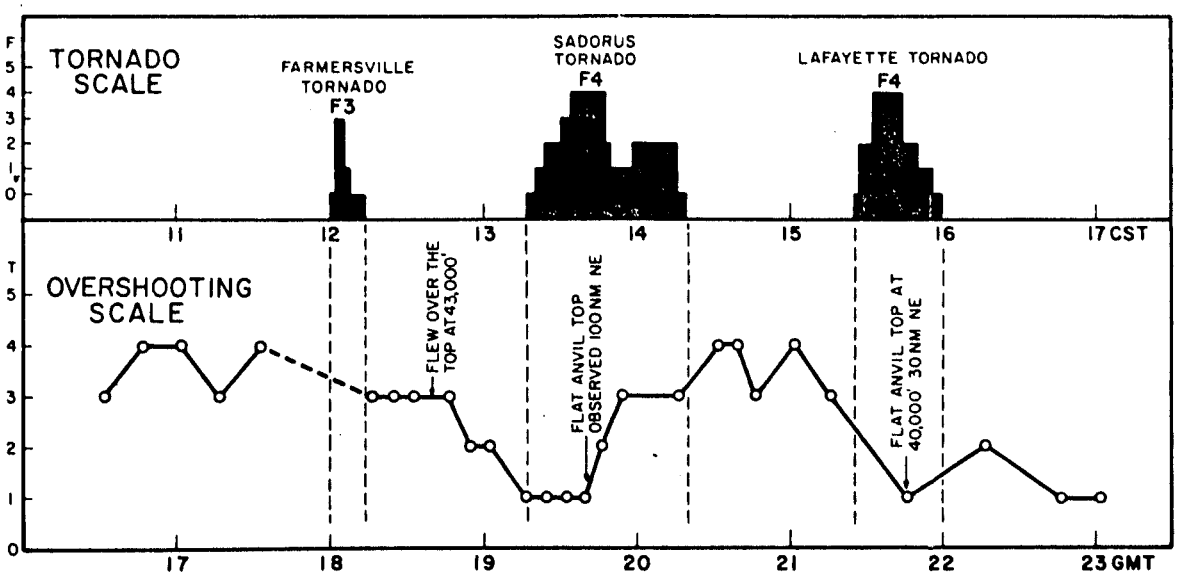

Figure 12.1.4.1 Change in overshooting scale (5 indicates intense overshooting top activity; 1 indicates very flat anvils) in relation to the intensity of tornadoes spawned by a supercell thunderstorm (Fujita et al., 1976).

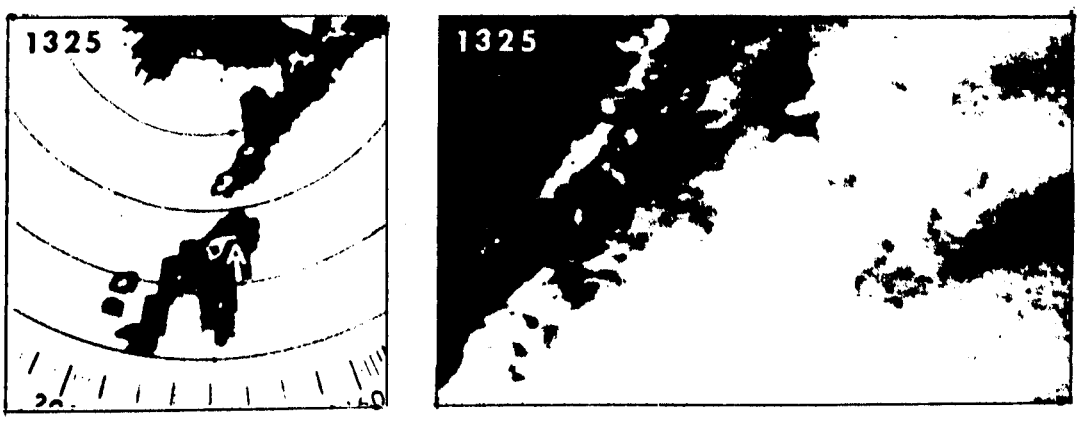

Figure 12.1.4.2 Concurrent radar PPI scope and satellite photographs of the tornadic thunderstorm (Fujita et al., 1976).

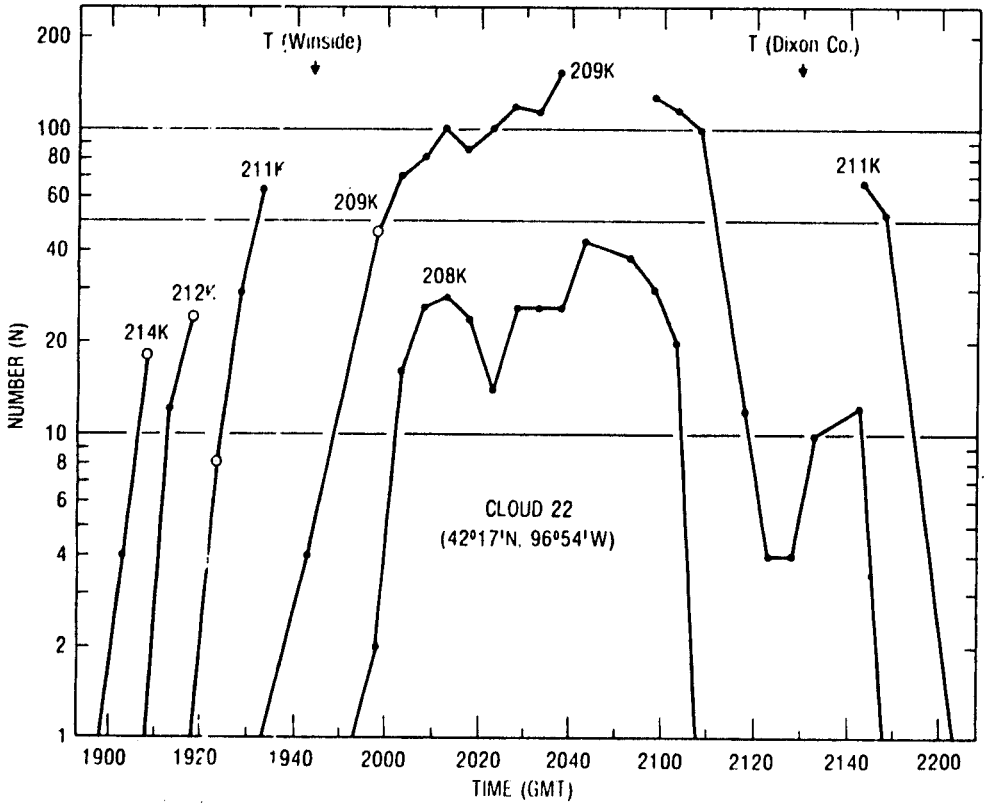

Figure 12.2.1.1 Thunderstorm growth rate diagram for a tornado over South Dakota on 6 May 1975. The number of pixels (i.e., area) having specific cold radiative temperatures is shown as a function of time. T's indicate time of tornadoes (Adler and Fenn, 1977).

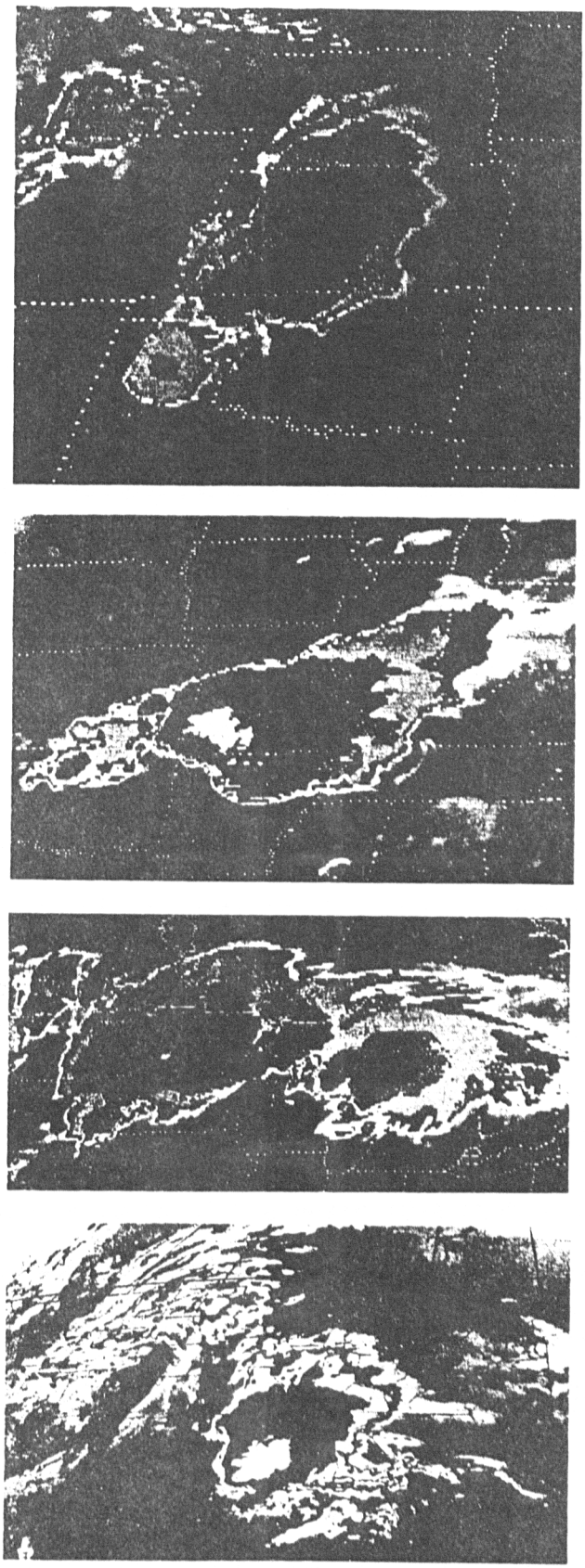

Enhanced infrared satellite image for a) 1230 GMT 4 June 1978, b) 0500 GMT 15 July 1978, c) 0730 GMT 23 August 1978, and d) 1230 GMT 7 May 1978.

Figure 12.2.1.2 Several example of MCC's as seen in enhanced infrared satellite imagery. (Maddox, 1980)

Blank page retained for pagination

CHAPTER 13

RAINFALL ESTIMATION TECHNIQUES

Techniques for estimating rainfall from satellites have typically used two types of measurements. The use of visible and infrared measurements is based on empirical relationships between cloud parameters and the resultant precipitation. Such cloud parameters include size, growth rates and cloud top temperatures. On the other hand, the use of microwave measurements has been based on theoretical relationships between rain rates and the satellite-measured values. The basis for the microwave method is somewhat similar to that behind ground-based radar reflectance measurements and rainfall, but using passive radiometers.

This chapter will only briefly cover these techniques. New multi-spectral techniques (combining visible, IR, and microwave) are presently under development. Many references will be given. Also see Chapter 14 on combined satellite/radar analyses.

13.1 Visible-IR Approach

Most schemes are variants of the basic idea that since it rains under clouds, if one knows where the clouds are, one knows where it is raining. Such precipitation information is extremely useful for crop and flood forecasting as well as for energy balance considerations in climatological studies.

Early rainfall estimation techniques are outlines in Barrett (1974) and Martin and Scherer (1973). Refinements on the system can be based on

knowledge of the fractional cloud cover, cloud type, visible brightness, IR temperature and area or areal growth rates of clouds. The accuracy of such techniques improves with increasing averaging time and with increasing averaging area.

A statistical relationship between rainfall volume and cloud properties can be established.

$$R_V = \sum_{i=1}^{m} C_{0,i} + C_{1,i}A_i + C_{2,i}(dA_i/dt) \qquad (13.1)$$

where

R_V = Rainfall volume over specified domain (x,y,z)

A_i = Areal coverage of <u>cloud type i</u>

$\frac{dA_i}{dt}$ = Growth or decay rate of cloud type i

$C_{1,i}$ = Empirical coefficients

Generally, $C_{0,i} = 0$. Only Barrett (1973) and Follansbee (1973) have allowed $m \geq 1$. Few have set $C_{2,i} \neq 0$; this term is generally small.

A notable scheme includes Scofield and Oliver (1977) in which estimates of point convective precipitation rates are based on visible and enhanced infrared GOES imagery. A decision tree process is used. The scheme "underestimates" the rainfall up to 30% in extreme rainfall situation (≥ 50 mm·h^{-1}) and overestimates rainfall up to 30% for light to heavy rainfalls (≤ 50 mm·h^{-1}).

Griffith <u>et al</u>. (1976,1978) designed a system to measure precipitation over fairly large areas by considering the rainfall from each cloud using GOES visible or infrared data at 1/2 hour resolution. The scheme uses a two-step correlation between the area of the cloud and the expected area of

the radar echo underneath the cloud. The area of the cloud is then related to the volumetric rain rate

$$R_V = I \cdot A_E \tag{13.2}$$

where

A_E = area of radar echo (km^2)

R_V = volumetric rain rate ($m^3 \cdot s^{-1}$)

I = intensity = 4.33 (echo area increasing)

= 3.27 (echo area constant)

= 2.20 (echo area decreasing)

Table 13.1.1 lists many studies which have used visible and infrared imagery to estimate precipitation from satellites. Such techniques have problems. A basic problem is the lack of a solid physical relationship between rainfall and cloud parameters.

Cheng and Rodennuis (1977) concluded that "threshhold techniques may be used with only limited success in determining the intensity of precipitation. If this is correct, the success of quantitative precipitation estimates by remote sensing reported by other authors is due more to the time-integration of a reasonable rainfall rate rather than successfully estimating intense rainfall rates."

Table 13.1.1. Classification (and associated authors) of visible and infrared based satellite precipitation estimation methods.

Method	Authors
1. Direct Correlation	Lethbridge (1967) Gerrisch (1970) Klionsky and Kamage (1976) Cheng and Kodennuis (1977a, 1977b) Silva Dias et al. (1977)
2. Nephanalysis	Barrett (1970, 1973) Follansbee (1973, 1975, 1976)
3. Radar Analog	
a. Empirical	Sherer and Hudlow (1971) Sorman (1972)
b. Parameterization	Gruber (1973)
4. Mass Transport/Radar Analog	Griffith and Woodley (sequence of reports and publications from 1971 to 1979) Martin, Sikdar and Stout (sequence of reports and publications from 1975 to 1979)
5. Hydrological Inference	Rainbird (1969) Grosch and Weinman (1973)
6. Decision Tree	Scoffield and Oliver (1977) Adler and Fenn (1976, 1977, 1978) Reynolds and Smith (1979) Schultz and Klatt (1980)

13.2 Microwave Estimates

At microwave frequencies cloud droplets are too small to interact strongly with the radiation. Raindrops, however, interact well with microwaves. Water surfaces have a very low emittance (≤ 0.5), so over the ocean the satellite-measured brightness is low and in window regions the atmosphere does not contribute much to the upwelling radiance. For example, at 19.35 GHz the transmittance of a non-raining atmosphere is $\geq 85\%$ through clouds (see Figure 13.2.1). Raindrops, however, cause the atmosphere to be more opaque, thus adding to the upwelling radiation over the cold background. Figure 13.2.2 shows that the brightness temperature, T_B increases with rainfall rate until backscattering causes T_B to decrease. Saturation occurs at ≈ 25 mm·h^{-1} at 19.35 GHz and at lower rainfall rates for higher frequencies. This technique has been used to calculate oceanic precipitation frequencies (Kidder and Vonder Haar, 1977) as shown in Figure 13.2.3. Most techniques have been based on measurements from NIMBUS-5 ESMR (19.35 GHz) and NIMBUS-6 ESMR (37.0 GHz).

For a field-of-view (FOV) composed of a clear A_D and a cloud fraction A_C, the microwave brightness temperature T_M is a linear combination of the background and cloud components.

$$T_M = \int_{A_D}^{\Gamma} R(a)T_D(a)da + \int_{A_C}^{\Gamma} R(a)T_C(a)da \qquad (13.3)$$

$$A_D = 1 - A_C \qquad \text{Let } R(a) = 1 \text{ for all } a$$

$$T_M = \int_{1-A_C}^{\Gamma} T_D(a)da + \int_{A_C}^{\Gamma} T_C(a)da$$

Assume uniform rain rate within FOV

$$T_M = \overline{T}_D \cdot (1-A_C) + \overline{T}_C \cdot A_C \qquad (15.4)$$

or

$$\overline{T}_C = T_D + A_C \cdot \Delta T$$

where $\Delta T = \overline{T}_C - \overline{T}_D$

The average cloud brightness temperature $\overline{T}_C$ can then be related to a rainfall rate by using the appropriate relationship in Figure 15.2.2 based on the known freezing level. Results of comparing satellite and radar estimates can be found in Figure 15.2.4. Table 15.2 lists many studies using microwave satellite measurements.

Table 15.2.1. Classification (and associated authors) of microwave-based satellite precipitation estimation methods.

Microwave

Radiometric

ESMR-5	ESMR-6
Allison et al. (1974)	Savage and Weinman (1978)
Wilheit et al. (1977)	Savage (1976)
Kidder (1976,1977)	Weinman and Guetter (1977)
Rao et al. (1976)	Weinman and Davies (1978)
Smith and Kidder (1978)	Durkee (1980)
Lovejoy and Austin (1979)	

Empirical

Wilheit et al. (1976)	Rodgers et al. (1970
Adler and Rodgers (1977)	
Rodgers and Adler (1980)	

19.35/37 GHz Theoretical Study	SCAMS-6
Jung (1980)	Viezee (1979)

13.3 Towards a Multi-spectral Satellite-measured Rainfall Technique

Justification

1) Need for global measurements

2) Lack of physics in the VIS-IR techniques

3) Problems with single channel passive microwave techniques

This technique developed by Smith and Vonder Haar (1982) uses radiative transfer models for microwave, visible and infrared as well as cloud microphysics for various types of clouds. The technique can be applied to data from the NOAA operational sounders, since measurements in all the required spectral bands are available.

References and Supplementary Reading

VIS-IR Techniques

Barrett, E. C., 1970: The estimation of monthly rainfall from satellite data. Mon. Wea. Rev., 98, 322-327.

Barrett, E. C., 1973: Forecasting daily rainfall from satellite data. Mon. Wea. Rev., 101, 215-222.

Barrett, E. C., 1974: Climatology From Satellites. Methuen and Co., Ltd., London, 418 pp.

Cheng, N. and D. Rodenhuis, 1977: An intercomparison of satellite images and radar rainfall rates. Postprints, 11th Technical Conference on Hurricanes and Tropical Meteorology, AMS, Boston, MA, 224-226.

Follansbee, W. A., 1973: Estimation of average daily rainfall from satellite cloud photographs. NOAA Tech. Memo NESS-44, U. S. Dept. of Commerce, Washington, DC, 39 pp.

Follansbee, W. A. and V. J. Oliver, 1975: A comparison of infrared imagery and video pictures in the estimation of daily rainfall from satellite data. NOAA Tech Memo NESS-62, U. S. Dept. of Commerce, Washington, DC, 14 pp.

Follansbee, W. A., 1976: Estimation of daily precipitation over China and the USSR using satellite imagery. NOAA Tech. Memo NESS-81, U. S. Dept. of Commerce, Washington, DC, 30 pp.

Griffith, C. G., W. L. Woodley, S. Browner, J. Teijeiro, M. Maier, D. W.

Martin, J. Stout and D. N. Sikdar, 1976: Rainfall estimation from geosynchronous satellite imagery during daylight hours. NOAA Tech Report ERL 356-WMPO 7, U. S. Dept. of Commerce, Boulder, CO, 106 pp.

Griffith, C. G., W. L. Woodley, P. G. Grube, D. W. Martin, J. Stout and D. N. Sikdar, 1978: Rain estimation from geosynchronous satellite imagery - visible infrared studies. Mon. Wea. Rev., 106, 1153-1171.

Griffith, C. G., J. A. Augustine and W. L. Woodley, 1981: Satellite rain estimation in the U.S. high plains, J. Appl. Meteor., 20, 53-66.

Martin, D. W. and W. D. Scherer, 1973: Review of satellite rainfall estimation methods. Bull. Amer. Meteor. Soc., 54, 661-674.

Reynolds, D. W. and E. A. Smith, 1979: Detailed analysis of composited digital radar and satellite data. Bull. Amer. Meteor. Soc., 60, 1024-1037.

Scofield, R. A. and V. J. Oliver, 1977: A scheme for estimating convective rainfall from satellite imagery. NOAA Tech Memo NESS-86, U. S. Dept. of Commerce, Washington, DC, 47 pp.

Stout, J. E., D. W. Martin and D. N. Sikdar, 1979: Estimating GATE rainfall with geosynchronous satellite images. Mon. Wea. Rev., 107, 585-598.

Whitney, L. F., Jr., 1982: A statistical approach to rainfall estimation using satellite and conventional data, NOAA Technical Report NESS-89, 50 pp.

Microwave Techniques

Adler, R. F. and E. B. Rodgers, 1977: Satellite-observed latent heat release in a tropical cyclone. Mon. Wea. Rev., 105, 956-963.

Allison, L. J., E. B. Rodgers, T. T. Wilheit, R. W. Fett, 1974: Bull. Amer. Meteor. Soc., 55, 1074-1089.

Kidder, S. Q., 1976: Tropical oceanic precipitation frequency from NIMBUS-5 microwave data. Atmospheric Science Paper No. 248, Dept. of Atmos. Sci., Colorado State University, Fort Collins, CO, 49 pp.

Kidder, S. Q. and T. H. Vonder Haar, 1977: Seasonal oceanic precipitation frequencies from NIMBUS-5 microwave data. J. Geophys. Res. 82, 2083-2086.

Rao, M. S. V., W. V. Abbott III and J. S. Theon, 1976: Satellite-derived global oceanic rainfall atlas (1973-1974). NASA/GSFC X-Doc 911-76-116, National Aeronautics and Space Administration, Goddard Space Flight Center, Greenbelt, MD.

Rodgers, E., H. Siddalingaiah, A. T. C. Chang and T. T. Wilheit, 1979: A

statistical technique for determining rainfall over land employing NIMBUS-6 ESMR measurements. J. Appl. Meteor., 18, 978-991.

Weinman, J. A and P. J. Guetter, 1977: Determination of rainfall distributions from microwave radiation measured by the NIMBUS-6 ESMR. J. Appl. Meteor. 16, 437-442.

Wilheit, T. T., A. T. C. Chang, M. S. V. Rao, E. B. Rodgers and J. S. Theon, 1977: A satellite technique for quantitatively mapping rainfall rates over the oceans. J. Appl. Meteor., 16, 551-560.

Multi-Spectral Techniques

Smith, E. A. and T. H. Vonder Haar, 1982: The development of a multispectral radiative signature technique for estimation of rainfall from satellites. Final Report - NASA Contract NA-80-SAC-00246, 77 pp.

General

Atlas, D and O. W. Thiele (editors), 1981: Precipitation measurements from space, Workshop Report, 28 April - 1 May, NASA-GSFC, Laboratory for Atmospheric Sciences, Greenbelt, MD.

Barrett, E. C. and D. W. Martin, 1981: The Use of Satellite Data in Rainfall Monitoring, Academic Press, New York, 340 pp.

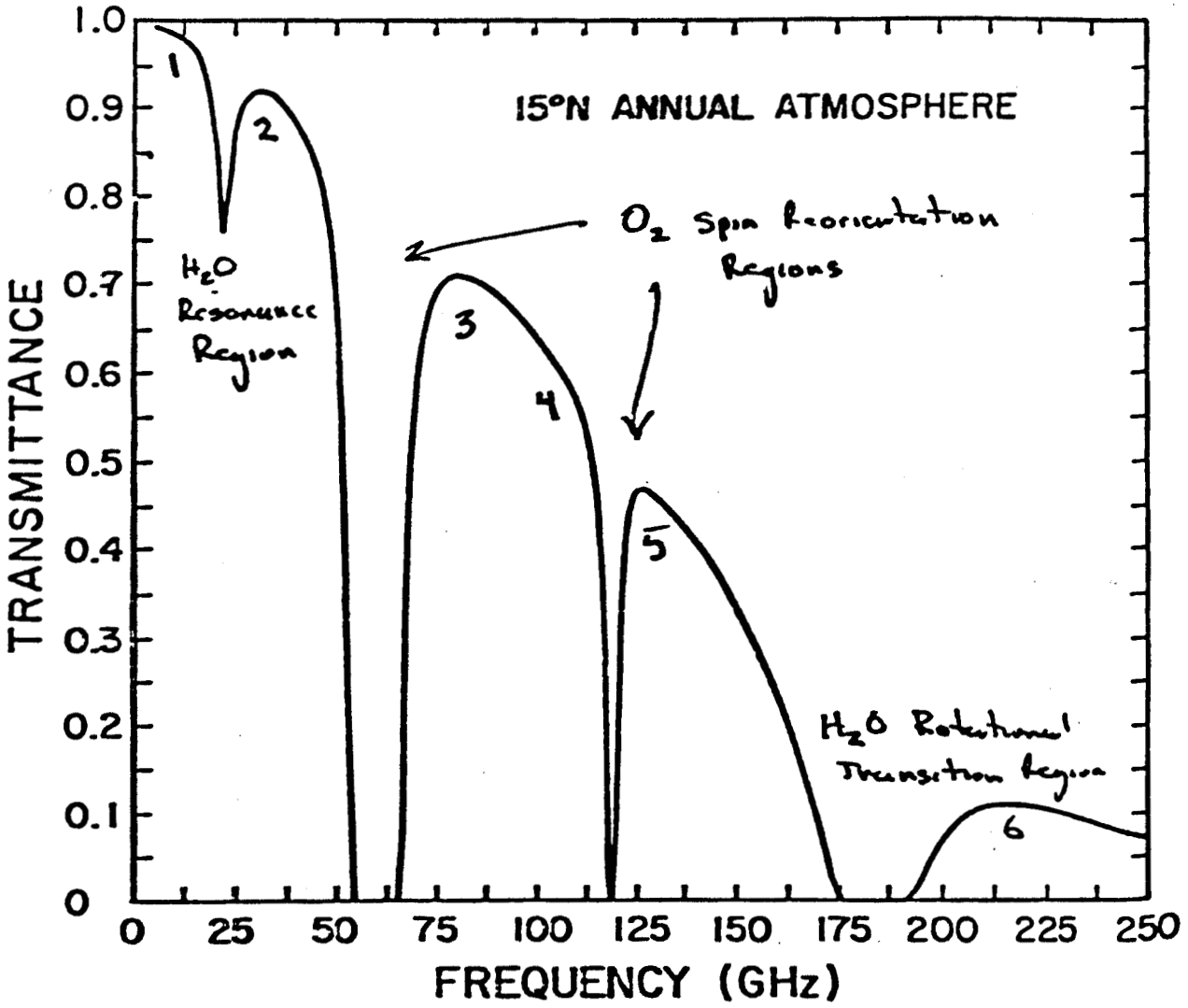

Figure 13.2.1 **Transmittance of the 15° North Annual Atmosphere**

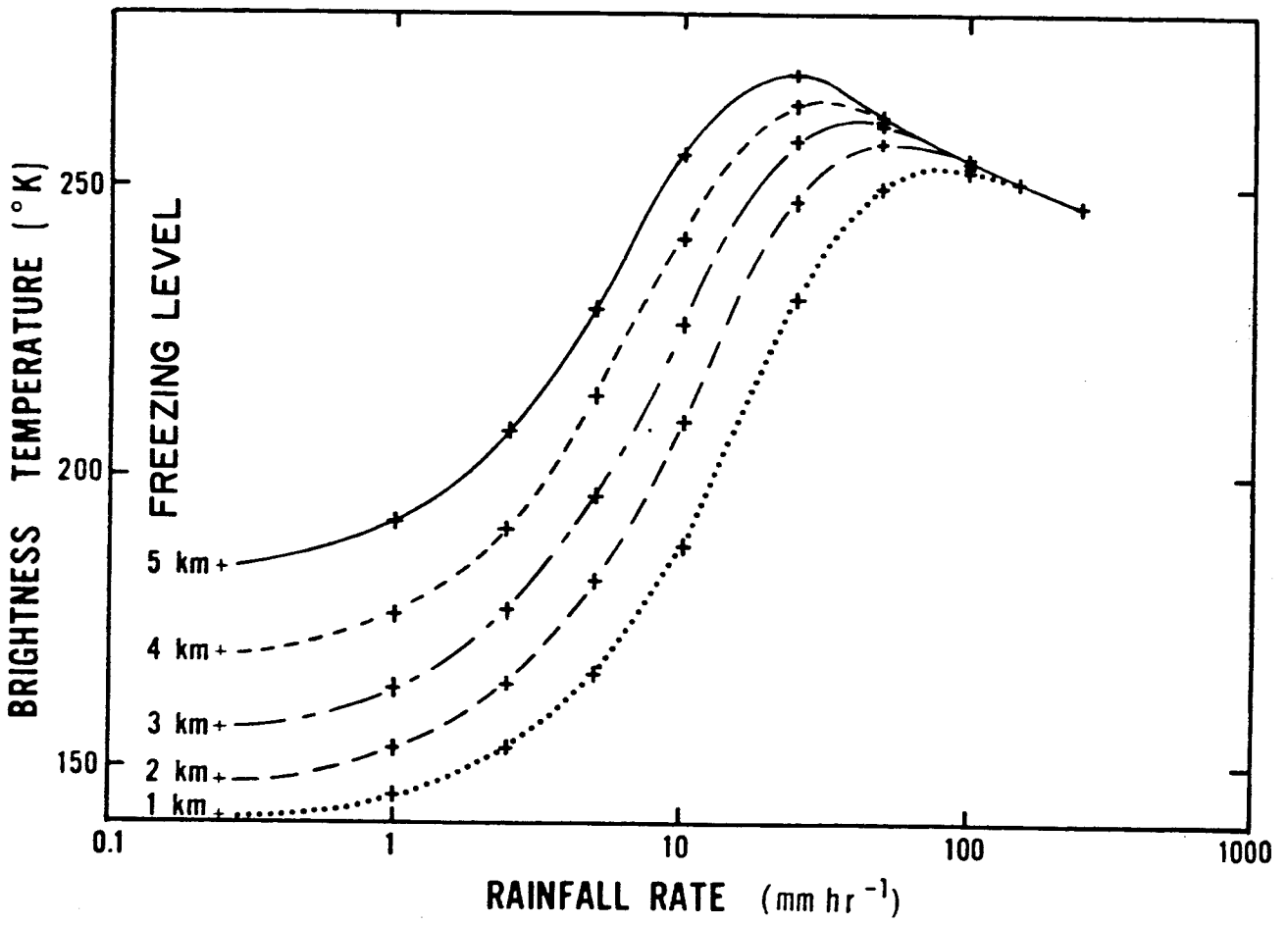

Figure 13.2.2 1.55 cm brightness temperature versus rainfall rate. (After Wilheit et al., 1975

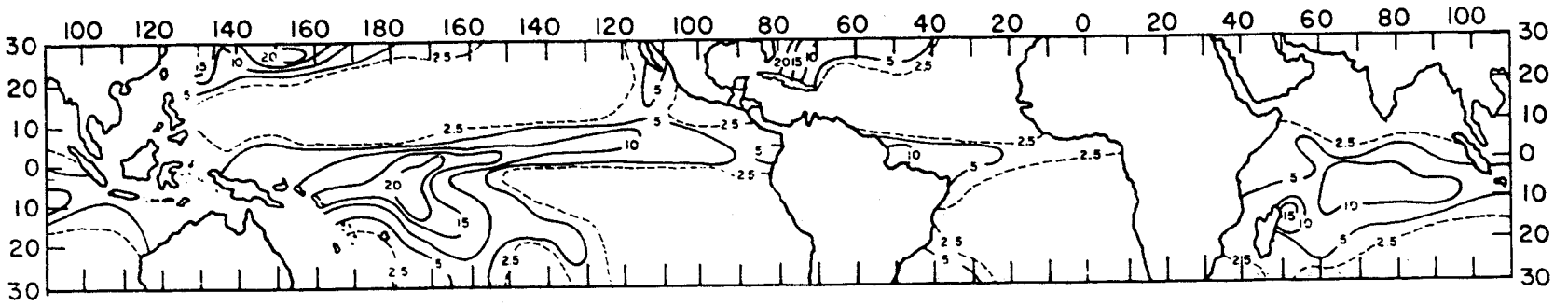

Frequency of precipitation (in percent of observations) for the season December 1972 through February 1973 as derived from Nimbus 5 ESMR data. (The noon and midnight frequencies have been averaged).

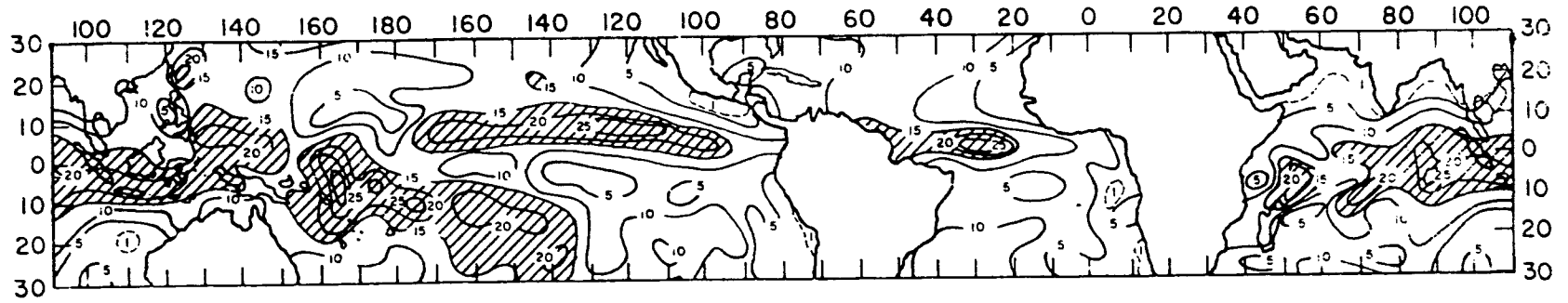

Frequency of precipitation (in percent of observations) for the season December-January-February from ship observations taken at Greenwich noon. (After McDonald, 1938).

Figure 13.2.3 Precipitation Frequency from NIMBUS-5 ESMR and from Ship Reports (Kidder and Vonder Haar, 1977)

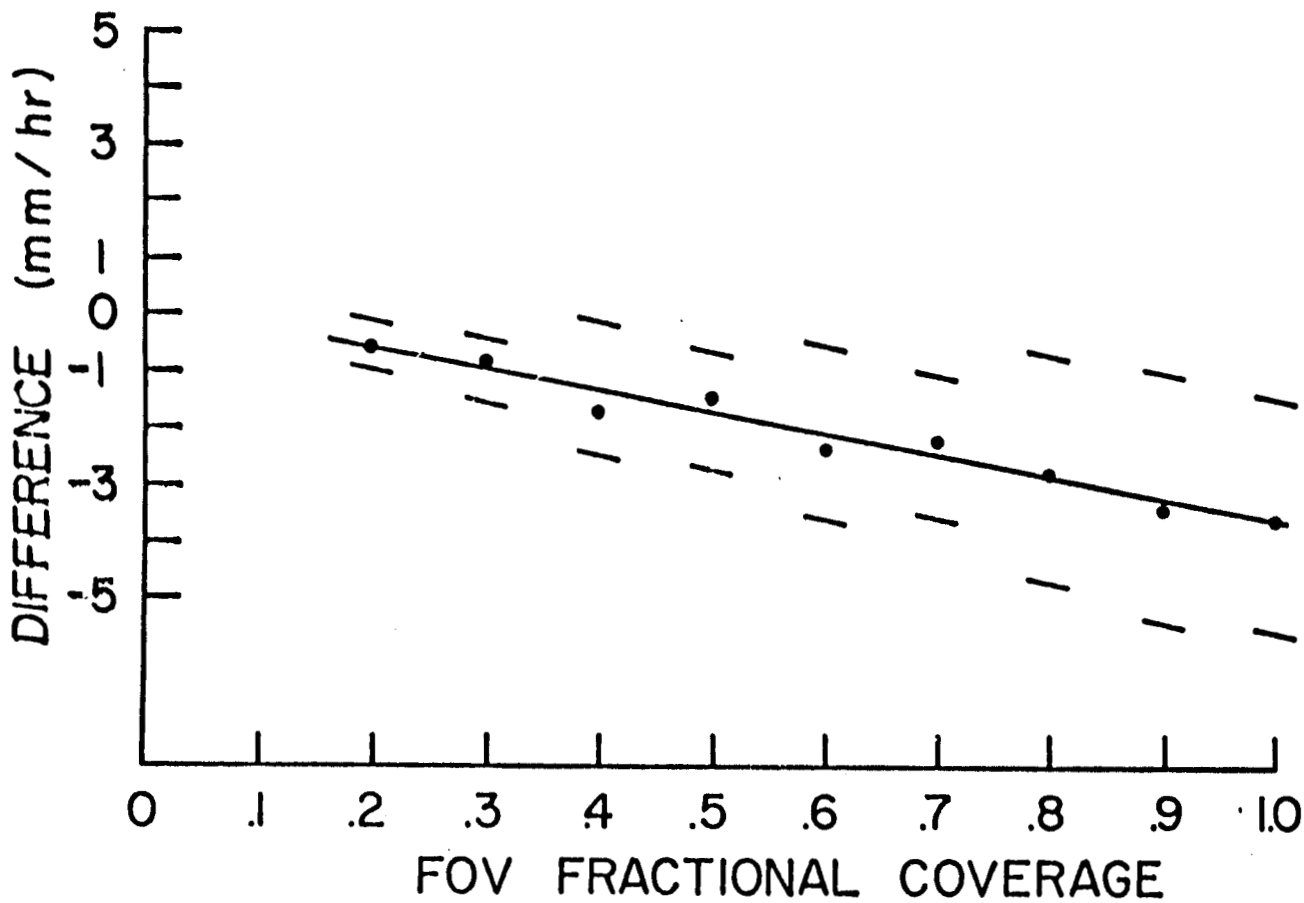

Figure 13.2.4 Microwave-Radar Rain Rate Differences as a Function of FOV Coverage

Blank page retained for pagination

CHAPTER 14

COMBINED SATELLITE/RADAR ANALYSES

Because of the remote nature of both satellite and radar measurements, several studies have used combined satellite and radar data. Most notable among the studies are those applied to convective storms, but the technique can be applied to tropical weather systems and hurricanes. In addition, combined satellite/radar data may be used to develop rainfall estimation techniques from satellite data.

14.1 Simple Satellite/Radar Comparisons

The satellite provides a good view of the cloud structure of a system and the radar reflectance provides an indication of the precipitation regions. The two systems, therefore, are complimentary.

Early techniques combining satellite and radar data to analyze a weather situation merely used both views to tell which regions of the cloud are precipitating. However, since each measurement system views the atmosphere from a different perspective, the researcher/forecaster must be careful when combining such data. A preferred technique would be to remap one set of measurements into the coordinate system of the other set (Reynolds, 1978). This requires accurate navigation of the satellite imagery. Care must also be taken to consider that the satellite view of cloud tops is also affected by the viewing angle, with increasing discrepancies at larger viewing angles.

Fujita (1978) using enhanced IR imagery from GOES noted a 21 km shift in the relative position of high altitude clouds in northern Wisconsin. He

then shifted his grid surface to compensate. Figure 14.1.1 shows examples of enhanced IR data combined with radar echoes. From Fujita and Caracena (1977) it appears that the radar data has been remapped into the satellite coordinate before combining in Figure 14.1.2. This combined image shows that only a relatively small region underneath a large anvil cloud may actually be active. The stretching of the anvil in the downwind direction is especially apparent on days with strong upper-level winds. As a result the most active areas in such storms are on the upwind side.

14.2 Satellite Rainfall Techniques Using Radar/Satellite Compositing

Because the principles of radar detection of precipitation are basically known and radar can generally cover a much larger area than raingauges, it makes an attractive measurement to combine radar with satellite data in order that one might better understand the relationship between variations in satellite brightness, cloud top temperatures and rainfall.

First, it must be understood that radar has a difficult time determining quantitative precipitation due to varying drop size distributions, presence of melting hydrometeors etc. Thus, it can only be used in a relative sense to locate areas of precipitation and areas of varying intensity unless a proven Z-R (reflectance-rainfall) relationship is derived.

In a recent paper Reynolds and Smith (1979) carried out case studies to determine the feasibility and impact of such combinations of satellite-rainfall techniques. Through case studies they illustrate the benefits of combining radar and satellite data for development of a satellite rainfall algorithm.

References

Fujita, T. T., 1978: Manual of downburst identification for project NIMROD. SMRP Research Paper No. 156, Dept. of Geophysical Sciences, The University of Chicago, 104 pp.

Fujita, T. T. and F. Caracena, 1977: An analysis of three weather-related aircraft accidents. Bull. Amer. Meteor. Soc., 58, 1164-1181.

Negri, A. J., D. W. Reynolds and R. A. Maddox, 1976: Measurements of cumulonimbus clouds using quantitative satellite and radar data. Seventh Conference on Aerospace and Aeronautical Meteorology and Symposium on Remote Sensing from Satellites, AMS, 16-19 Nov, Melbourne, FL, 119-124.

Reynolds, D. W. and E. A. Smith, 1979: Detailed analysis of composited digital radar and satellite data. Bull. Amer. Meteor. Soc., 60, 1024-1037.

Reynolds, D. W., 1978: An intense analysis of digital radar, raingauge and digital satellite data for a convective cloud system on the high plains of Montana. Preprints - 18th Conference on Radar Meteorology, AMS, 28-31 March, 310-317.

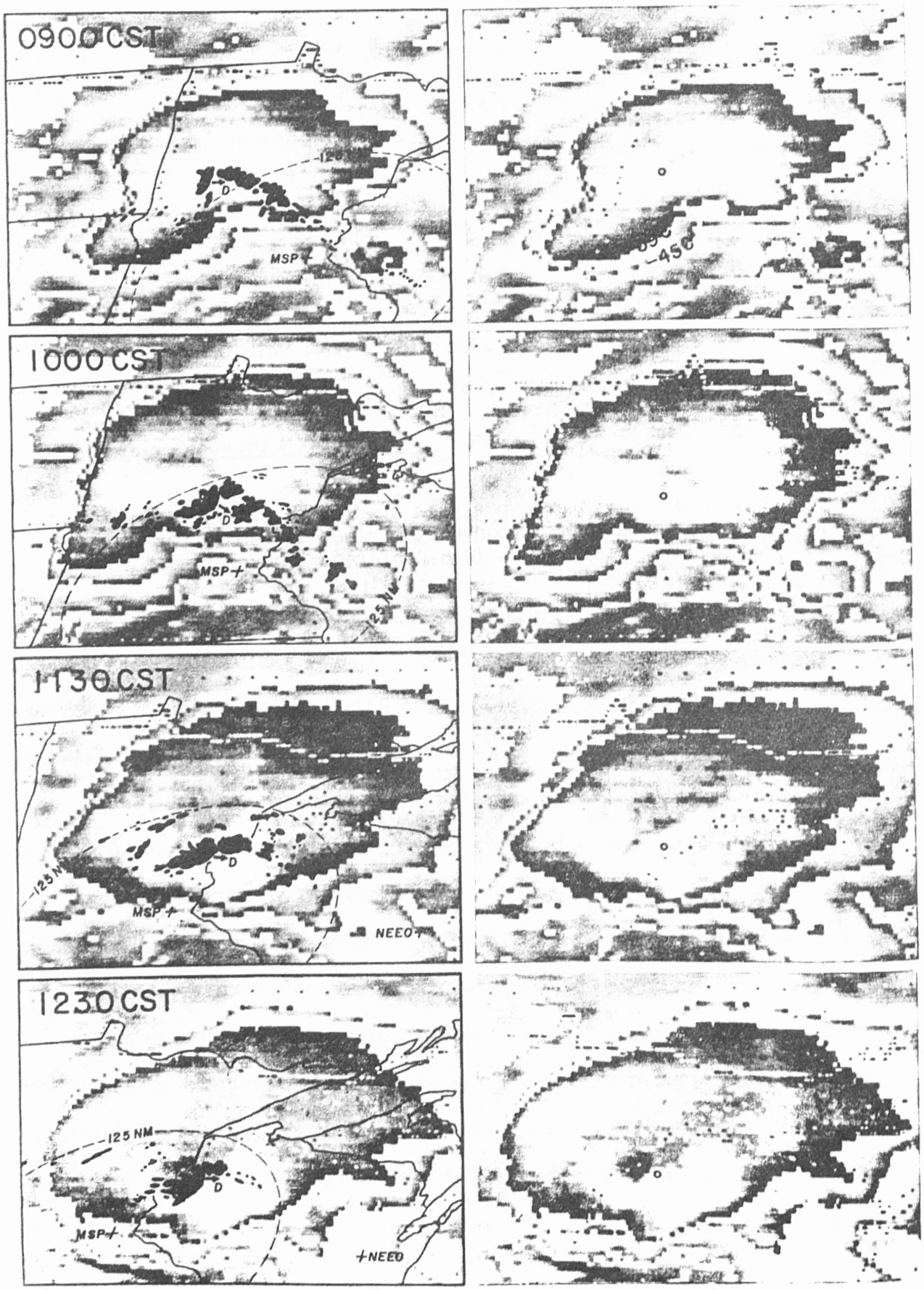

Curve 30 enhancement with radar echoes on July 4, 1977. Open circles are downburst locations.

Figure 14.1.1 Combined Radar and Enhanced IR Data (after Fujita, 1978)

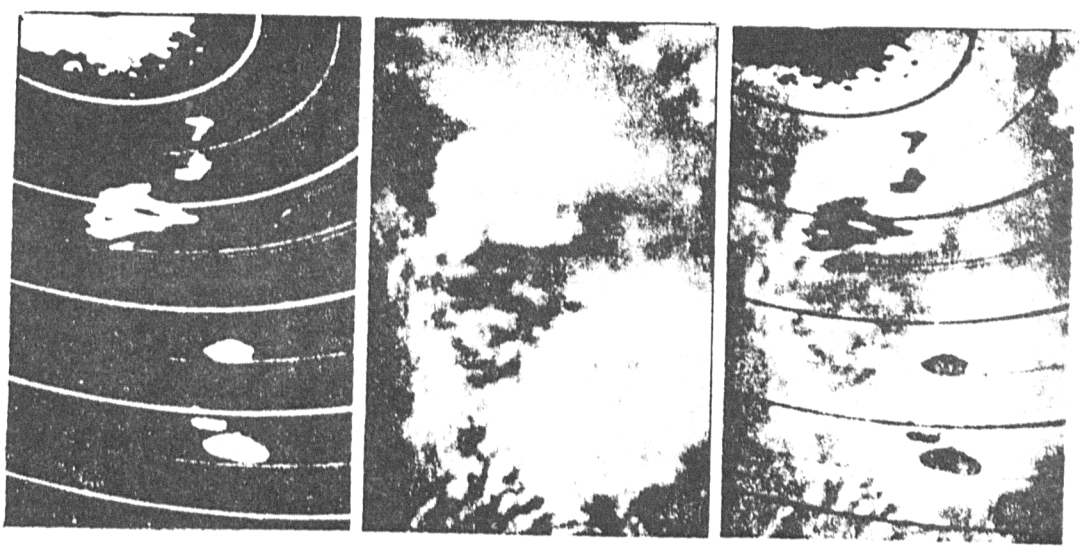

A spearhead echo of 6 May 1975. Radar echo at 1722 CDT (left), SMS/GOES picture at 1722 CDT (center), and their combination (right).

Figure 14.1.2 Remapped Radar Before Combining with GOES Imagery (after Fujita, 1977)

Blank page retained for pagination

CHAPTER 15

OTHER FEATURES VIEWED FROM WEATHER SATELLITES

A wide variety of other land, ocean and atmospheric features have been seen, sometimes occasionally, from weather satellites. Special papers have been written about the tracking and estimation of sea ice, for example. Summaries of the use of satellites for hydrological purposes have discussed the estimate of snow cover extent from satellites. Special studies have been made of the use of satellite data to understand and predict the migration of locusts. Certain experimental satellite systems have detected lightning discharges and upper atmospheric features such as the aurora. Entire satellite experiments have been designed to detect trace gases in the upper atmosphere and the important variations in ozone concentration.

Since this set of notes is focused on practical applications with a strong emphasis on forecasting the present chapter will cover:

(a) tropospheric dust outbreaks of natural origin

(b) natural maritime haze layers

(c) air pollution detection

and (d) observation of forest fires

The first two of these features are sometimes used by meteorologists as indicators of current weather. The second two features noted above are also related to current weather conditions. Fires and pollution are sometimes objects of detection or "remote sensing" as special targets.

15.1 Tropospheric Dust

Dust storms which are large enough to be detectable by meteorological satellites are primarily forced by meteorological conditions on the synoptic scale. We can generally distinguish between two types of dust outbreaks by their source regions: mid-latitude plains and subtropical deserts. The mid-latitude storm occurs in late winter and early spring, while the desert outbreak is primarily a summertime phenomenon. The examples with which we will illustrate each type are (1) for the subtropical desert case, a Saharan dust outbreak, and (2) for the mid-latitude case, a Great Plains dust storm.

15.1.1 Saharan Dust Outbreak (Rising Dust)

Intense heating of the desert surface during summer and early fall leads to a meteorological condition where dry convection and mixing form a deep layer of dust-laden heated air over the Sahara. This layer may extend upward to 5-6 km, or nearly 500 mb. In addition, the strengthening of the low-level pressure gradient and surface winds as easterly waves progress across the African continent will help to raise more dust from the surface than convection alone. The dust raised by surface winds is evidenced by the satellite images which show the dust rising from a surface source and advected by the winds. Dust emerges from the continent behind the trough followed by a large anticyclonic eddy at middle levels, 600-700 mb. The heated Saharan air may be 5-6°C warmer than the surrounding background tropical air as it moves out over the Atlantic Ocean. Since it emerges above the moist trade wind layer below, an inversion is formed at

the boundary between the two air masses, and the dusty area is relatively cloud-free. Saharan dust is observed to cross the Atlantic on occasion with a westward speed of about 7 m s^{-1}, requiring 5-6 days for the crossing. Fallout of dust into the lower moist layer can cause visibility problems as far west as the Caribbean and Florida due to haze formation.

Identification of Saharan dust outbreaks from a satellite requires either an infrared or visible image depending on whether the underlying surface is land or water. Saharan dust over land is not easily seen in visible imagery because the already high albedo of the desert surface matches the albedo of the airborne dust and therefore there is no contrast between the two on an image. However, the dust may mask certain surface features which would normally be seen on a visible image, and comparison of a dust-free image with an image where Saharan surface features are obscured would allow the location of the dust cloud to be determined. Rising dust over the Sahara is most easily identified in IR images (See Figure 15.1.1.1) [Note: This is slide set #367]. Increasing land surface temperatures due to daytime solar heating leads to a darkening of the land areas on an IR image except where rising dust decreases the surface heating and to a lesser extent, the outgoing longwave radiation. Therefore, the dust appears as a lighter area on afternoon IR images when surface heating and dust generation are at a maximum. To distinguish between dust and cloud on the IR image, the area of dust identified on the IR image is cloud-free in a corresponding visible image, which eliminates ambiguity. An area of rising dust is seen to expand rapidly in size in the downwind direction during the time when dust is rising.

A Saharan dust outbreak moving over the ocean is most easily seen in visible imagery where it appears as a widespread, milky or hazy area,

mostly free of convection and lighter than the ocean background (See Figure 15.1.1.2) [Note: This is slide set #375]. It is generally preceded in its westward travel by the curving cloud band of the low-latitude trough associated with the outbreak. Dust may be seen occasionally in IR images off the west African coast where it is still fairly dense, although low stratus which often occurs in the same area has a very similar appearance of thick dust clouds and the two may be readily confused.

15.1.2 Middle-Latitude Dust Storms

Dust storms in mid-latitudes most commonly occur in late winter or early spring in arid regions or under drought conditions. Over the Great Plains of the United States, dust storms can occur following a prolonged winter drought when the soil is dry, vegetation cover is sparse and high winds are likely. Blowing dust is caused by the strong surface winds associated with an intense, deepening cyclone and usually begins following the cold frontal passage. Great Plains dust storms are most common in the region immediately east of the Rocky Mountains in primarily agricultural areas where base soil is present.

Satellite identification of a mid-latitude dust storm is possible using either visible or infrared imagery. Dust appears in visible imagery as a lighter, milky diffuse region most likely in the cold sector of the storm. See, for example, Figure 15.1.2.1 [Note: This is slide set #395]. The land surface in mid-latitudes is generally dark enough to make the dust stand out clearly against the background. Thus, in the visible, dust may be distinguished from clouds by its lower albedo (darker than clouds) and by its smooth, homogeneous appearance. The area covered by the dust

expands with time in a downwind direction and the stationary upwind edge of the cloud reveals the surface source of the dust.

In the IR images, the dust cloud appears as a cooler area which is easiest to see in afternoon images when the land surface is warmest (darkest). Decreased surface solar heating and outgoing longwave radiation account for the colder appearance to the dust cloud. As in the visible imagery, the area covered by the dust expands rapidly downwind after the blowing dust is initiated at the surface.

15.2 Haze Layers Over the Ocean

Ocean forecasters and meteorologists in coastal regions observe not only the fogs discussed in Chapter 11 but also intense maritime hazes. Fett and Isaacs (1979) analyzed very high resolution variations of brightness over the ocean which they attributed to haze. Durkee *et al*. (1982) and Hindman *et al.* (1982) discuss the detection of maritime haze in further detail. Figure 15.2.1 shows typical haze patches seen off the California coast. Research continues on the relation of these features to marine boundary layer conditions and to the subsequent development of fogs and stratus.

15.3 Air-Pollution Observations by Weather Satellite

The types of air pollution detectable on meteorological satellite imagery are primarily in the form of aerosols, a suspension of liquid or solid particles in air. Naturally-occurring air pollution can consist of smoke and ash from forest or brush fires and volcanoes. Man-made pollution includes industrial effluent, automobile exhaust, fossil fuel combustion

and agricultural burning and dust production. In the case of fires or volcanoes, the concentration of pollutants is generally high enough that satellite detection is independent of meteorological conditions (dispersion and mixing) unless large-scale cloudiness covers the polluted area. Meteorological conditions can be responsible for natural pollution events in that lightning from dry thunderstorms may initiate forest or brush fires. The satellite can be a detection tool for fires in this type of situation.

Pollution from man-made sources becomes visible on the satellite imagery under particular meteorological conditions, where what is called a "pollution event" occurs. A stable atmosphere combined with light winds allow pollutant concentrations to increase to a level where visibility is affected. Such conditions occur near the center of anticyclones where wind speeds are low and ridging helps to stabilize the atmosphere. A dense haze forms from the pollutant aerosols when sufficient moisture is available, reducing visibility even further and making the pollution easier to see in imagery from the satellite. These conditions are common in the summer where subtropical high pressure intrudes inland, for example, over the eastern half of the United States in late summer.

Identification of air pollution from satellite is best done from visible imagery. Pollution appears as large areas of hazy or milky appearance (similar to dust clouds) which obscures surface features and landmarks and reduces the contrast between these features. Because of the forward scattering maximum of the aerosols of which the pollution is composed, pollution shows up best on imagery where the sun-earth-satellite

angle is greatest. For geosynchronous satellites, this means that pollution is most likely to be detected on an early morning or late afternoon image, using a satellite whose subpoint is farthest from the area of interest on the earth. For polar satellites it means using an image from a pass where the area of pollution is as far from the satellite subpoint as practical and is also in the direction of the sun. An orbital track to the west is desirable for morning satellites, and to the east of the area for an afternoon satellite. In this way the forward scattering and optical depth of the pollution are maximized.

Convection within the polluted region is often suppressed due to the decreased solar heating of the underlying surface and the resulting temperature contract and sea-breeze type of circulation may lead to enhanced convective activity along the boundary of the polluted region. Often in a forest fire situation, the source of the pollution may be evident on the images as in the case of a dust storm. Movement of areas of pollution is also a fairly good indicator of low-level wind flow.

Unless the pollution is dense enough, it will not be detected on IR imagery. Pollution is most likely to appear in the IR images if a layer of haze is formed with moist conditions. Haze appears as a cooler (lighter) area having diffuse edges on infrared images.

15.4 Observations of Forest Fires

Observations of the heat from forest fires has been used by groups interested in the remote sensing of the fires and their areal extent. The weather satellites carry high resolution visible and infrared sensors which, in the absence of intervening cloud cover, can be used to aid the

detection of such wildfires. An example of a high resolution infrared view of Alaskan fires in seen in Figure 15.4.1.

Using visible channels Chorowski (1980) has shown in Figure 15.4.2 a plume of smoke from an intense Colorado fire. Figure 15.4.3 [Note: This is slide set #365], also a GOES visible image, shows accumulated smoke over a large area resulting form several fires in SE Canada. The 850 mb winds plotted on the satellite image show that this smoke has been caught up in the synoptic scale wind patterns.

References and Suggested Reading

Anthony, R. W., 1978: Dust storm-severe storm characteristics of 10 March 1977. Mon. Wea. Rev., 196, 1219-1223.

Carlson, T. N. and J. M. Prospero, 1972: The large scale movement of Saharan air outbreaks over the northern equatorial Atlantic. J. Appl. Meteor., 11, 283-297.

Chorowski, L., 1980: Preprints for Symposium on Plumes and Visibility: Measurements and Model Components, 10-14 November, Grand Canyon, AZ, Sponsored by U.S. EPA, EPRI, and National Park Service.

Durkee, P. A., E. E. Hindman and T. H. Vonder Haar, 1982: The detection of marine haze with the meteorological satellites. Special Report, Research Institute of Colorado, Fort Collins, CO, 15 pp.

Ernst, J. A., 1975: A different perspective reveals air pollution. Weatherwise, 28, 215-216.

Fett, R. W. and R. G. Isaacs, 1979: Concerning causes of "anomolous grey-shades" in DMSP visible imagery. J. Appl. Meteor., 18, 1340-1351.

Hindman, E. E., P. A. Durkee, P. C. Sinclair and T. H. Vonder Haar, 1982: Detection of marine aerosol particles in coastal zones using satellite imagery. Special Report, Research Institute of Colorado, Fort Collins, CO, 21 pp.

Kondratyev, K. Ya. and Associates, 1976: Aerosol in the GATE area and its radiative properties. Atmospheric Science Paper # 247, Colorado State University, Fort Collins, CO, 109 pp.

Lushine, J. B., 1975: A dust layer in the eastern Carribean, Mon. Wea. Rev., 103, 454-455.

Mayfield, B. M., 1975: Sahara dust over the Atlantic, Mariners' Weather Log, 19, 346-347.

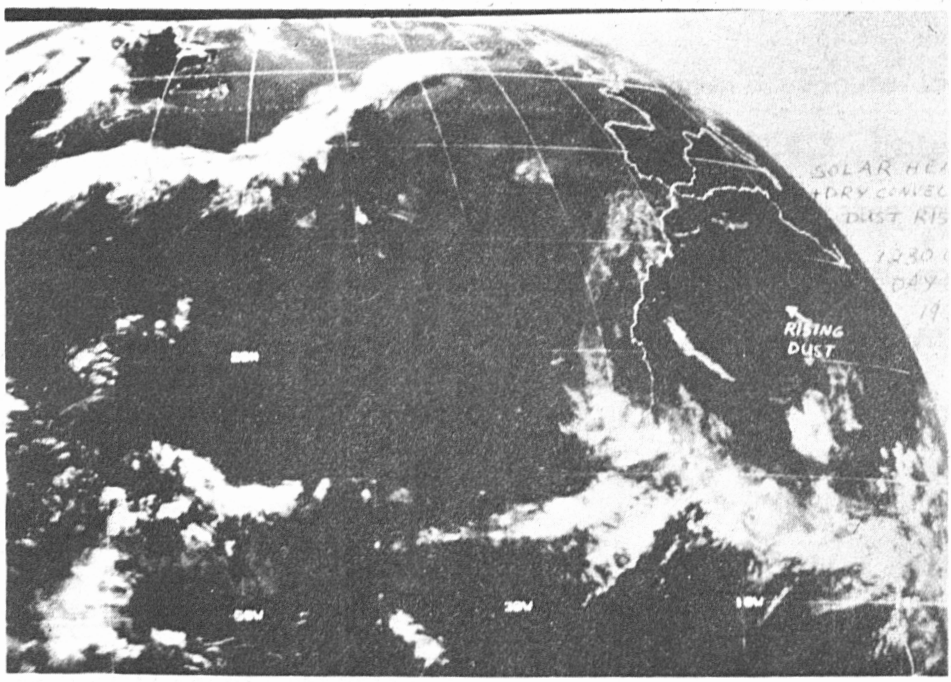

Figure 15.1.1.1 (Slide Set #367)

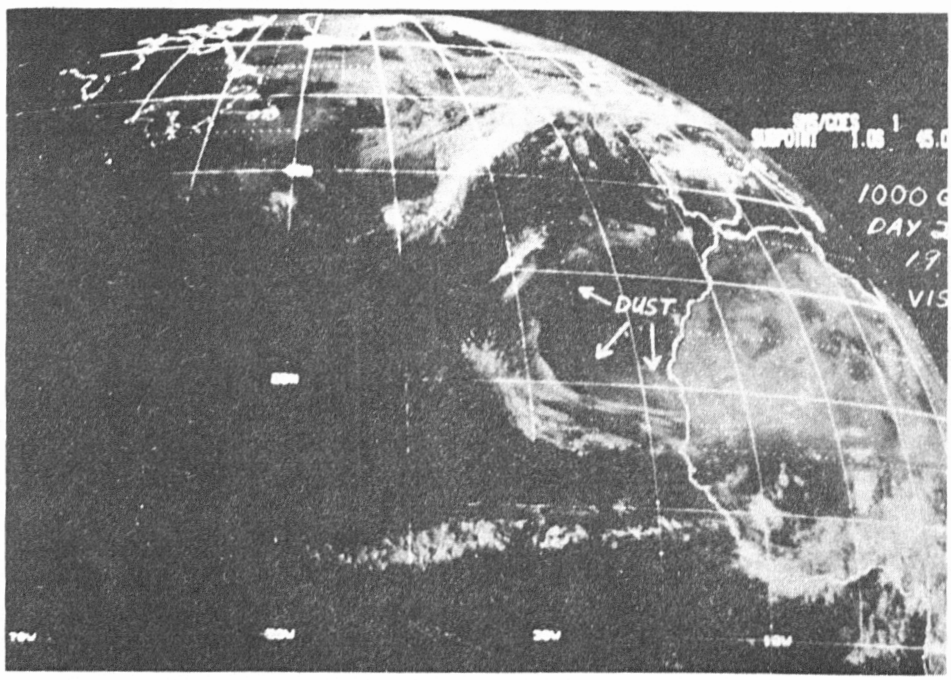

Figure 15.1.1.2 (Slide Set #375)

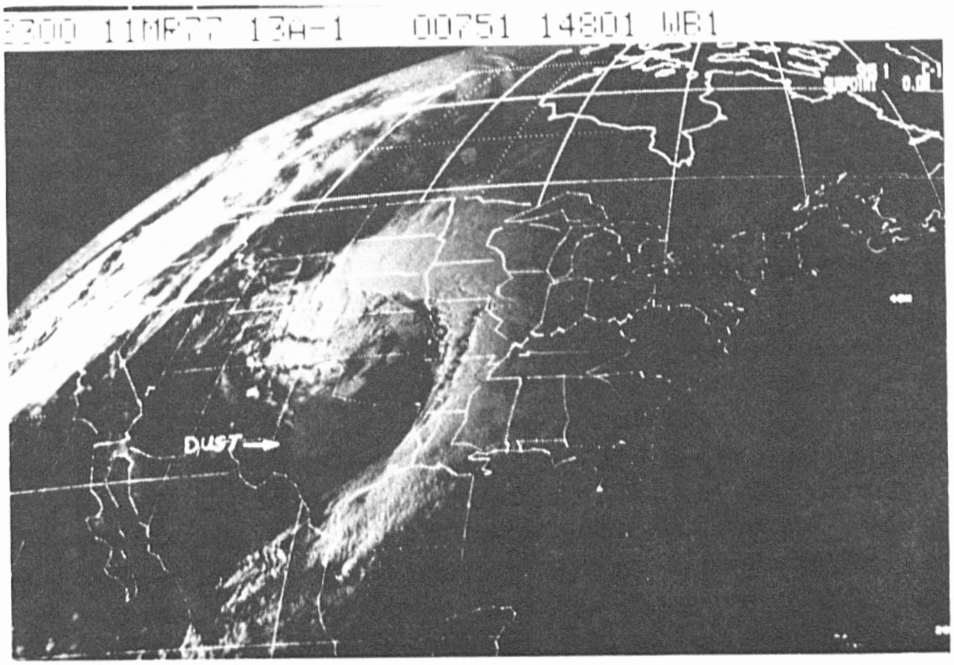

Figure 15.1.2.1 (Slide Set #395)

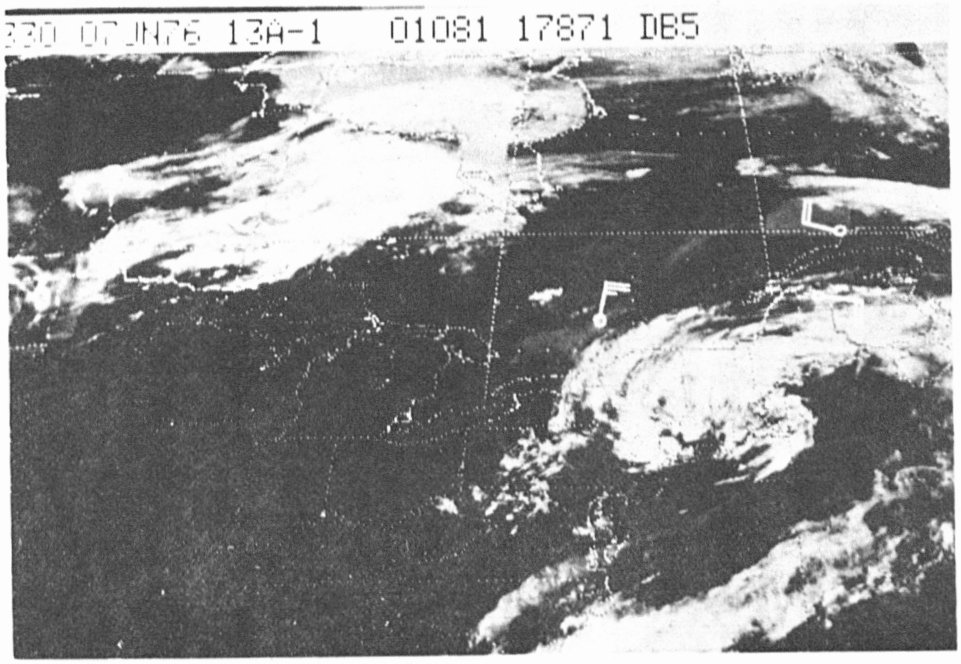

Figure 15.4.3 (Slide Set #365)

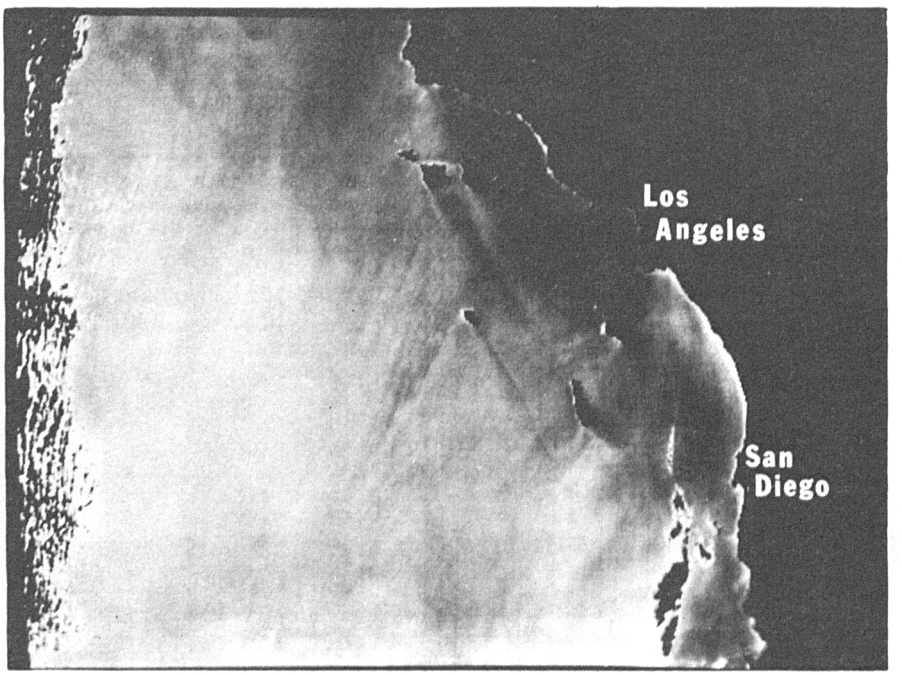

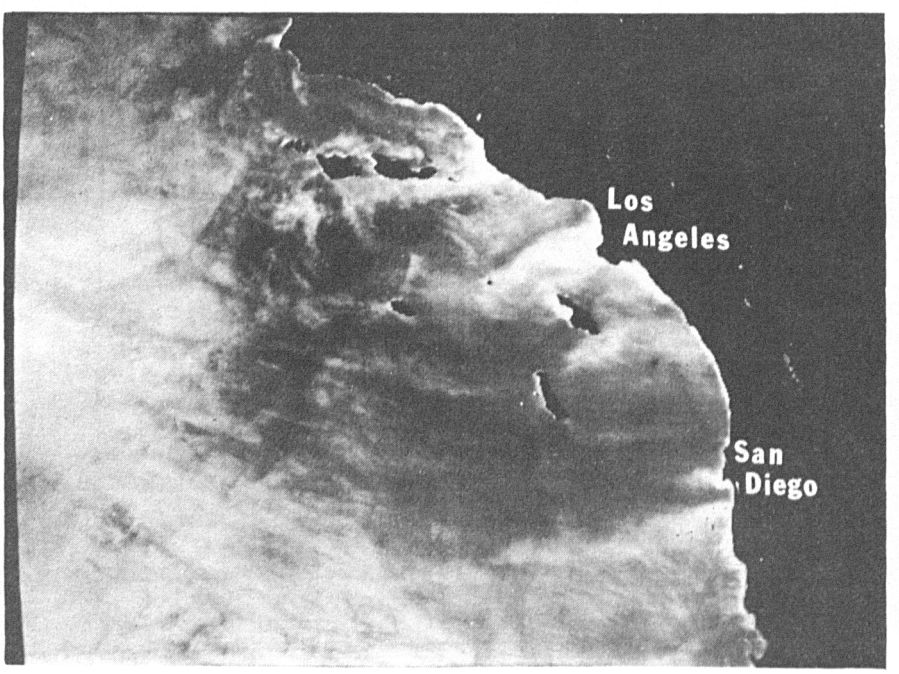

Figure 15.2.1 Haze patches off the California coast

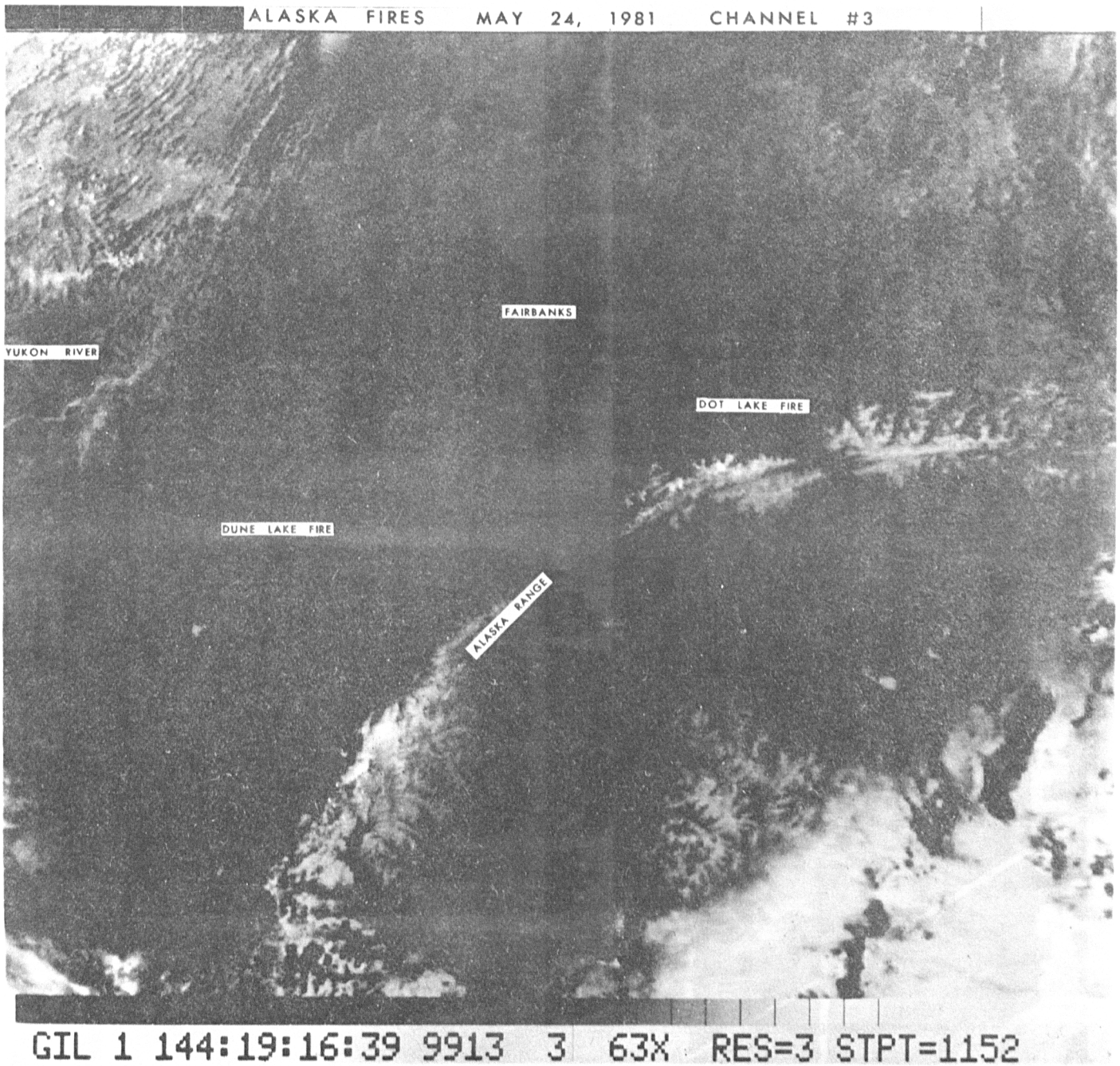

Figure 15.4.1 High-resolution infrared view of Alaskan forest fires

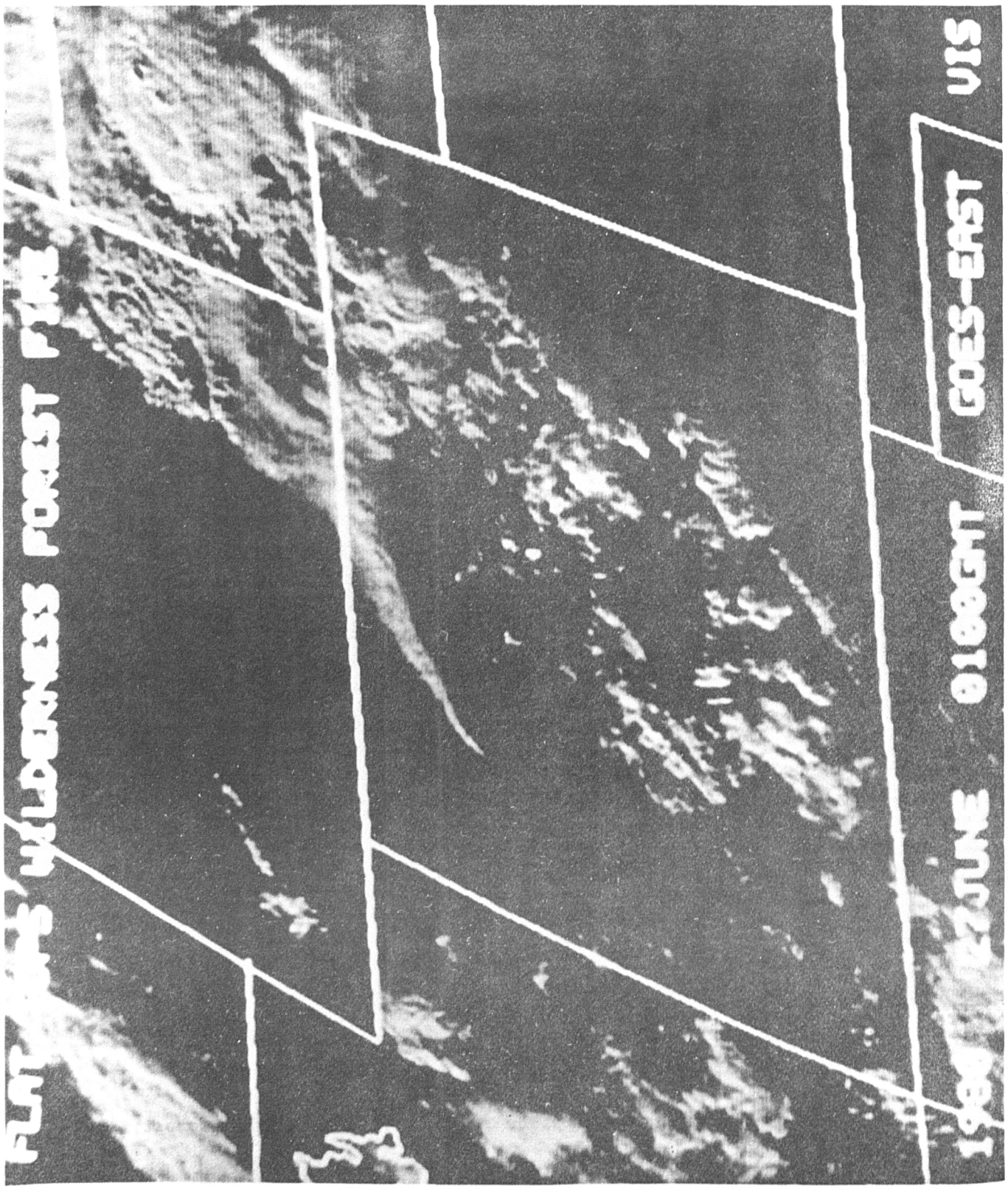

Figure 15.4.2 Plume of smoke from Flattop Wilderness Forest Fire in Colorado

CHAPTER 16

SATELLITE SUPPORT TO WEATHER MODIFICATION PROGRAMS

Satellites, just as many other observing platforms, have been used to gather data for cloud physics and weather modification research. In this chapter we discuss two of the major uses in this area: the winter orographic cloud studies and the summertime (or warm, rainy season) convective cloud case. For a discussion of satellite observation of fog, see Chapter 11.

16.1 Satellite Support to Winter Orographic Weather Modification

Visible and infrared satellite data are an important information source for both the design and operation of winter weather modification programs. Satellite-observable parameters which are desirable to be obtained include, but are not limited to (1) cloud top temperature (CTT) of clouds affecting the study area, (2) observations of mesoscale and synoptic cloud features of storms in the study area to aid in post-storm evaluation and to define storm classifications, and (3) relationships between the satellite observations and ground-based microphysical and precipitation measurements. The primary goal of the winter orographic weather modification programs to which these observations are applied is to increase the precipitation of clouds over mountain barriers during winter storms in order to augment the snowpack in the mountains and increase the water supply in the melting season.

The interest in observing cloud top temperature with the satellite IR capability stems from the reported relationship between the seedability of

a cold orographic cloud and the temperature of the top cloud (Grant and Elliott, 1974). Results from several experiments on seeding of cold (below freezing) orographic clouds have shown increases in precipitation when clouds having top temperatures between -10 and -25°C are seeded. This temperature range has been called the "seeding window" in which clouds may be deficient of enough ice nuclei, such that seeding these clouds makes them more efficient at precipitation production. Different mechanisms operating in orographic clouds at varying locations and situations can affect the validity of this seeding window criterion, such that a CTT in the seeding window range is by itself not a sufficient indicator of seedability, although it is important to consider along with other factors.

Advantages of using the satellite, particularly the geosynchronous types, to observe CTT over the method of radiosonde-derived CTT are that measurements can be made at short, half-hour intervals, and the CTT from satellite gives an area-average which may be more representative than the single-point value from a sounding. This is especially true where imbedded convection exists in the orographic cloud.

The IR and visible imagery is also used for identification of synoptic and mesoscale features that affect the taget area. Items of interest include fronts, upper-level troughs, vorticity centers, wind maxima, convective cells and banks, etc. These are easily identified in the imagery and can help classify the storm as a certain type, whose seedability characteristics have been defined. Additionally, a climatology of storm types can be produced from satellite imagery before a seeding project is undertaken to determine the suitability of an area for seeding or aid in selecting a site for the program.

Examples of the use of satellite data in winter orographic weather modification are shown in the following figures. A color-enhanced IR image produced on the CSU ADVISAR (Figure 16.1.1) shows how CTT can be determined within the target area outlined on the image. Figures 16.1.2 and 16.1.3 illustrate a major problem in using satellite data alone to determine CTT. An extensive layer of cirrus unattached to the lower preciptating clouds is observed from an aircraft between the two cloud layers (Figure 16.1.2). A visible satellite image from the same time (Figure 16.1.3) shows the extent and border of the cirrus cover, where the aircraft was west of the target area on the image. Without corresponding aircraft or sounding information, a forecaster could be misled by the satellite CTT data.

An example of the CTT information which the geosynchronous satellite can provide is shown in the CTT vs. time graph in Figure 16.1.4. The average and standard deviation of CTT in the target area is plotted for 24 hours of a Sierra Nevada winter storm, showing that only clouds in the later stages of the storm are seedable according to the CTT criterion. Figure 16.1.5 shows half-hourly precipitation totals for two stations within the target area of the preceding slide, and is useful to illustrate the relationship between cold CTT and heavier precipitation and greater precipitation efficiency when compared to the former slide for the same time period.

References

Grant, L. O. and R. E. Elliott, 1974: The cloud seeding temperature window, J. Appl. Meteor., 13, 355-363.

Reynolds, D. W., T. H. Vonder Haar and L. O. Grant, 1978: Meteorological satellites in support of weather modification, Bull, Amer. Meteor. Soc., 59, 269-281.

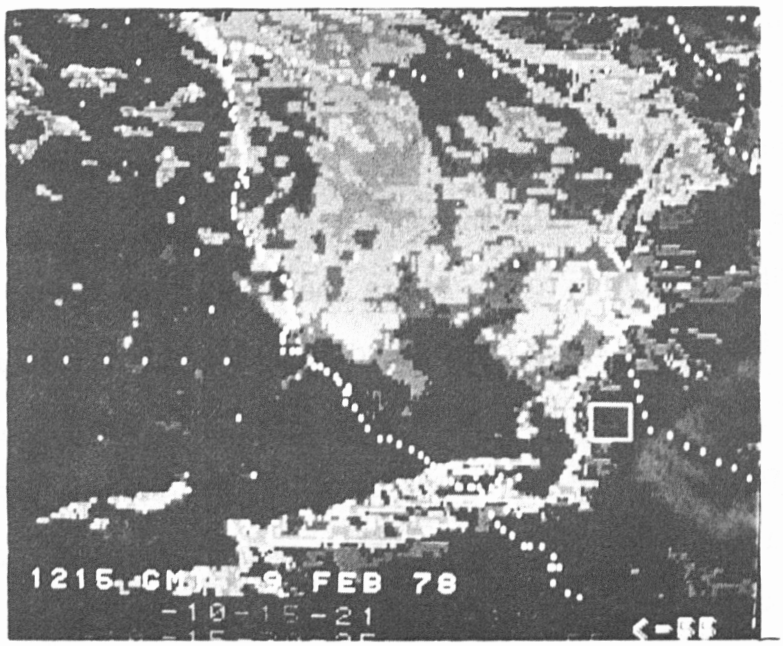

Figure 16.1.1 (Slide Set #380)

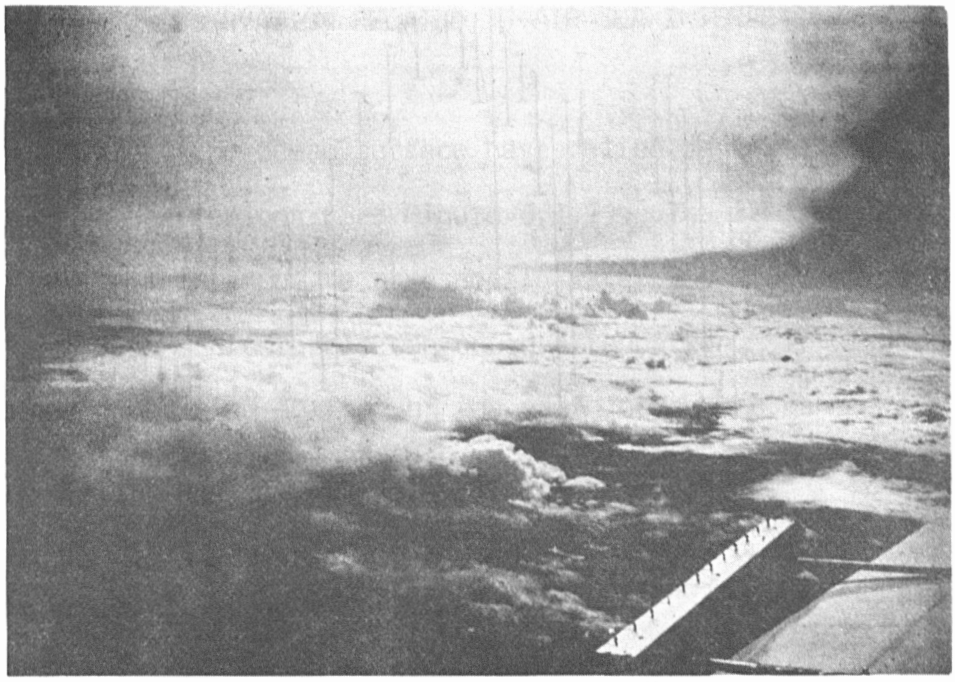

Figure 16.1.2 (Slide Set #382)

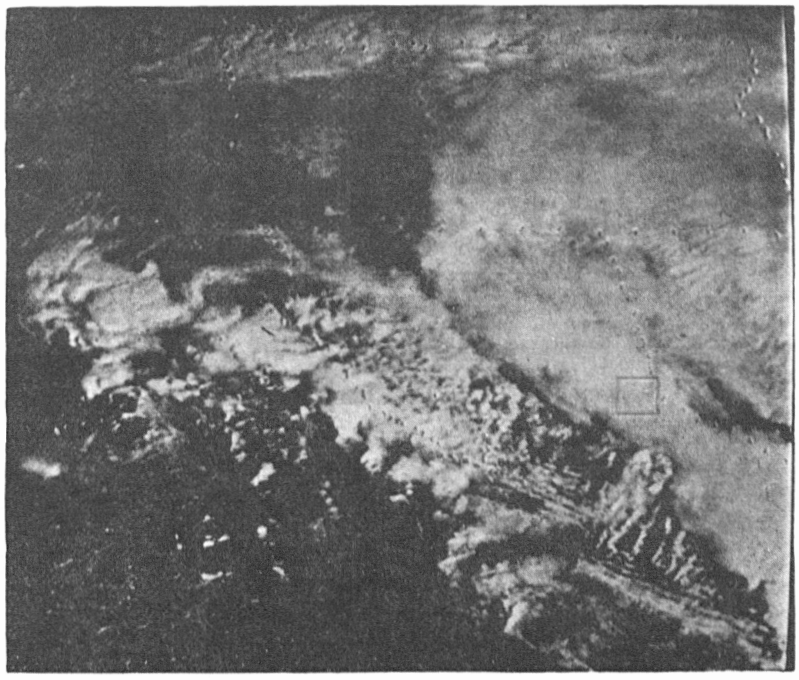

Figure 16.1.3 (Slide Set #381)

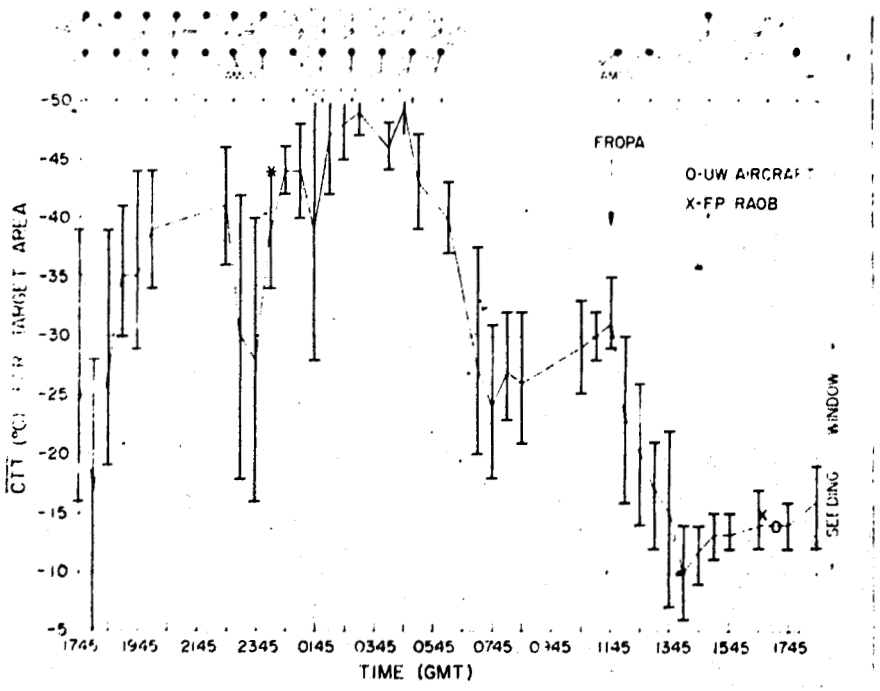

Figure 16.1.4 (Slide Set #383)

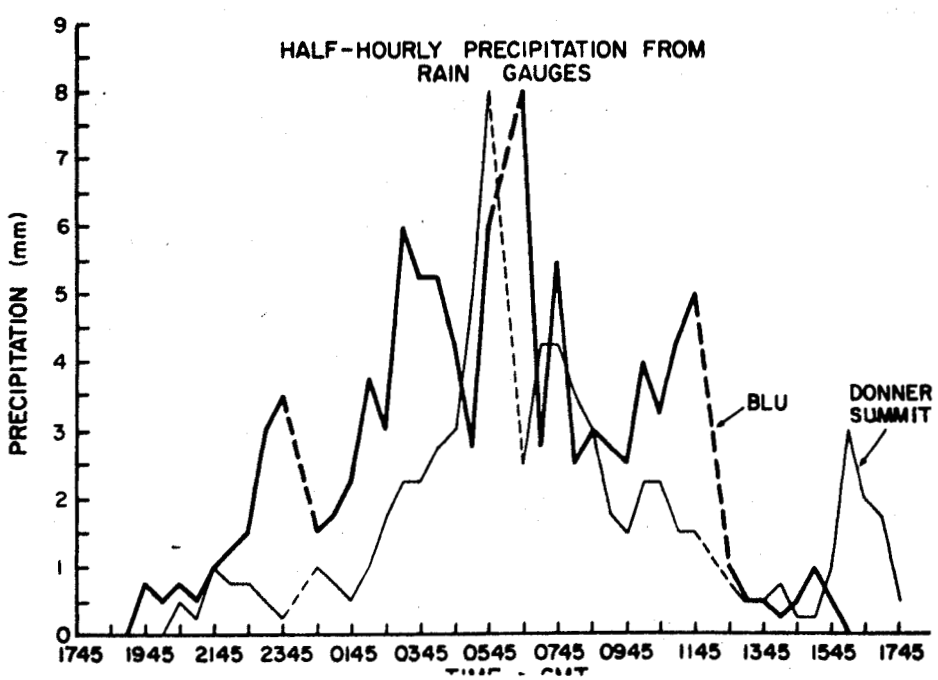

Figure 16.1.5 (Slide Set #384)

CHAPTER 17

SATELLITE OBSERVATION RELATED TO AIR-SEA INTERACTION

Attempts to study the ocean surface have relied on the of channels in the atmospheric window regions (See Figure 6.1.2). The limited absorption in these regions is mainly due to atmospheric water vapor, but other atmospheric particles and aerosols can cause attenuation. If clouds are not present, the underlying surface of the earth or oceans can be readily sensed. Many studies have focused on sea-surface temperatures by using various infrared channels. However, visible channels can also be used to sense the sea state (i.e., winds and currents).

17.1 Sea-Surface Temperature Measurements From Satellites

The ocean regions represent a large fraction of the earth's surface. However, measurements obtained over the oceans are limited in both space and time. Most, if not all, conventional (non-satellite) measurements of the ocean surface have come from ship reports. For this reason, some portions of the ocean are more frequently and densely measured, and other portions may receive few if any measurements. Until the advent of satellite measurements there was little knowledge of the global ocean surface temperatures or their variability in space and time.

Rao *et al.* (1972) derived global sea-surface temperatures with an rms difference of 2-3 K compared to conventional observations. The 10-5-12.5 μm channel of the High Resolution Infrared Radiometer (HRIR) on board ITOS 1 was used. Likewise, Smith *et al.* (1970) used the 3.8 μm channel of the

HRIR on NIMBUS-2 and -3 to determine sea-surface temperatures. Special consideration must be given to atmospheric attenuation, especially at larger zenith angles where the "limb darkening" is greater. Figure 17.1.1 shows that the amount of attenuation can be several degrees Celsius. Brandli (1977) gives an average difference between "bucket" sea-surface temperatures and emission temperatures of approximately 9°C (colder) for a region off the east coast of Florida. The rather humid atmosphere amounts for the large differences.

The possibility of reflected radiation contamination is high at these shorter wavelengths. Over land or clouds the 3.8 μm channel would contain significant amounts of reflected solar radiation. Over the oceans the albedo is lower and the problem is reduced; at night, the problem is non-existent. As a result, Rao et al. (1972) used only night-time values in their study.

Prabhakara et al. (1974) used spectral data in the 11 to 13 μm window region to determine sea-surface temperatures. Instead of using climatological data to determine the water vapor attenuation correction, the differential absorption properties of water vapor in the spectral region 775-960 cm^{-1} were used. This allows an accuracy of about 1°C to be achieved. Simple graphs of the three channel temperatures are used to extrapolate the value obtained at zero attenuation, such as in Figure 17.1.2. Although 3 channels are used, the use of 2 channels is sufficient.

The problem of cloud contamination was overcome by Smith et al. (1970) by using a histogram of values to identify the cloud-free measurements. As shown in Figure 17.1.3 the point of maximum slope on the high temperature

wing of the histogram can be used as a reference point. The assumed sea-surface temperature is that value minus the standard error of measurement. Alternately, visible or albedo values may be used to identify and eliminate cloud-contaminated values.

Many features in the sea-surface temperature structure have been observed. For example, Legeckis (1982) reports on a sea-surface temperature front in the equatorial Pacific. Such features are useful in identifying and tracking of equatorial long waves in the ocean. Examples of sea-surface temperature eddies are shown in Figures 17.1.4 and 17.1.5. These eddies are related to surface currents and vertical motions in the ocean.

On occasions an outbreak of polar continental air will extend into adjacent ocean areas. At those times the atmospheric attenuation is minimized. Figure 17.1.6 (Huh et al., 1982) shows such a cold outbreak and its associated atmospheric front extending across southern Florida.

17.2 Other Oceanographic Parameters

Many other ocean-related parameters can be measured from satellites, such as surface winds, waves, visibility, ice, currents, and altitude of the sea-surface. Each type of measurement requires special remote sensing techniques and frequencies. The requirements and users are listed in WMO-548, and should be consulted for the various satellites and instruments which can be used for such purposes.

Dismachek (1980) gives a description of oceanographic products produced by NOAA. These products include sea-surface temperatures (SST), ice charts and ocean current analyses. An example of an automated SST analysis

is given in Figure 17.2.1 as derived from NOAA polar-orbiting satellite infrared measurements. Figure 17.2.2 shows an ice chart generated manually from a combination of satellite and conventional data. The satellite measurements include those in the visible, infrared and microwave regions. Likewise, ocean current analyses are generated manually but almost exclusively from satellite visible and infrared imagery.

17.3 Non-oceanographic Products

Many other land-surface parameters can be obtained from satellite meausrements. These include land-surface temperatures, soil moisture, snow cover and vegetation indices.

To obtain land-surface temperatures using infrared measurements is a similar process to that used to obtain sea-surface temperatures. However, two additional difficulties arise. One problem is the non-unity emittance of the surface. (e.g., the surface is a grey-body). Although surface emittances in the infrared are typically near 1.0, the difference can cause an underestimation of the actual surface temperature. The second problem is the increased reflectance of land surfaces compared to sea-surfaces. The use of a visible channel to obtain the surface albedo (reflectance) is necessary when using infrared measurements which are susceptible to reflected solar contamination (Shaw, 1970).

The determination of soil moisture relies on emittance variatons detected by microwave sensors. Grody (1983) gives examples of surface emittance variations which are useful as a relative measure of surface wetness. Emittances usually lie between those for dry land (approximately 1.0) to water surfaces (approximately 0.5). Channel combinations from the

Microwave Sounding Unit (MSU) are used to eliminate the effect of air temperature variations. The Scanning Multi-channel Microwave Radiometer (SMMR) experiment on NIMBUS-7 is also designed to measure soil wetness using emittance variations.

Measurements of snow cover typically rely on the reflective properties of snow. However, the thermal properties of snow cause it to appear colder than surrounding surfaces. Therefore, both visible and infrared channels can be used, and determinations are not limited to daytime measurements. For more informaiton, see Wiesnet (1974) and McGinnis et al. (1975).

Finally, the ERTS (Earth Resources Technology Satellite)/LANDSAT series of satellite has been specifically designed to measure surface and vegetation properties using multi-spectral imaging. Sensors mainly in the visible and near-infrared are used to measure reflected and thermal radiation. Various channel combinations can be used to develop a vegetation index for various crops or natural surfaces. Coverage of these earth-sensing capabilities is beyond the scope of this set of lecture notes. To obtain LANDSAT data one should contact the Earth Resources Observation Systems (EROS) data center in Sioux Falls, South Dakota 57198. Four LANDSAT satellites have been launched so far with a sensor ground resolution as good as 30 meters. For an overview of LANDSAT capabilities, see the the special LANDSAT references at the end of the chapter.

References and Additional Reading

Barnett, T. P., W. C. Patzert, S. C. Webb and B. R. Bean, 1979: Climatological usefulness of satellite determined sea-surface temperatures in the tropical Pacific. Bull. Amer. Meteor. Soc., 60, 197-205.

Brandli, H. W., D. L. Reinke and L. E. Irvin, 1977: Sea surface emission temperatures from defense meteorological satellites. J. Phys. Ocean, 7, 302-304.

Braun, C., 1971: Limits on the accuracy of infrared radiation measurements of sea-surface temperature from a satellite. NOAA Tech. Memo. NESS-30, U. S. Dept. of Commerce, Washington, DC, 28 pp.

Breaker, L., S. Klein and M. Pitts, 1978: Quantitative measurements of sea-surface temperature at severe locations using the NOAA-3 very high resolution radiometer. NOAA Tech. Memo. NESS-98, U. S. Dept. of Commerce, Washington, DC, 28 pp.

Bretherton, F. P., 1981: Climate, the oceans and remote sensing. Oceanus, 24, 49-55.

Brower, R. L., H. S. Gohrband, W. G. Pichel, T. L. Signora and C. C. Walton, 1976: Satellite derived sea-surface temperatures from NOAA spacecraft. NOAA Tech. Memo. NESS-78, U. S. Dept. of Commerce, Washington, DC, 74 pp.

Cogan, J. L. and J. H. Will, 1976: Measurements of sea-surface temperature by the NOAA-2 satellite. J. Appl. Meteor., 15, 173-180.

Dismachek, D. C., A. L. Booth and J. A. Leese, 1980: National Environmental Satellite Service Catalog of Products, Third Edition, NOAA Technical Memorandum, NESS-109, 120 pp.

Grody, N. C., 1983: Severe storm observations using the microwave sounding unit, J. Climate Appl. Meteor., 22, 609-625.

Hamilton, G. D., 1980: Satellite data requirements for marine meteorological services, WMO-548, 46 pp.

Huh, O. K., L. J. Rouse, Jr. and P. F. Twitchell, 1982: Outbreaks of polar continental air: Windows on the mesoscale structures of the upper ocean. Naval Research Reviews, 34, 26-39.

Krishnaumurti, T. N., V. Wong, H. L. Pan, G. Van Dan and D. McClellan, 1976: Sea-surface temperatures for GATE. Dept. of Meteorology, Florida State Univ., Report 76-3, Tallahassee, FL, 268 pp.

Legeckis, R., 1978: A survey of worldwide sea surface temperatures fronts detected by environmental satellites. J. Geophys. Res., 83, 4501-4522.

Legeckis, R., 1982: Satellite infrared observations of oceanic long waves in the eastern equatorial Pacific 1975-1981. NOAA Technical Report NESS-92, 120 pp.

McGinnis, D. F., Jr., J. A. Pritchard and D. R. Wiesnet, 1975: Snow depth and snow extent using VHRR data from the NOAA-2 satellite, NOAA Technical Memorandum, NESS-63, 10 pp.

Maul, G. A., 1973: Atmospheric effects on ocean surface temperature sensing from the NOAA satellite scanning radiometer. J. Geophys. Res., 78, 1909-1916.

Prabhakara, C., G. Dalu and V. G. Kunde, 1974: Estimation of sea surface temperature form remote sensing in the 11 to 13 µm window region. J. Geophys. Res., 79, 5039-5044.

Rao, P. K., W. L. Smith and R. Koffler, 1972: Global sea surface temperature distribution determined from an environmental satellite. Mon. Wea. Rev., 100, 10-14.

Schneider, S. R., D. F. McGinnis, Jr. and J. A. Gatlin, 1981: Use of NOAA/AVHRR near-infrared data for land remote sensing. NOAA Technical Report NESS-84, 48 pp.

Shaw, J. H., 1970: Determination of the Earth's surface temperature from remote spectral radiance observations near 2600 cm^{-1}, J. Atmos. Sci., 27, 950-959.

Shenk, W. E. and V. V. Salomonson, 1972: A multispectral technique to determine sea-surface temperature using NIMBUS-2 data. J. Phys. Ocean., 2, 157-167.

Smith, W. L., P. K. Rao, R. Koffler and W. R. Curtis, 1970: The determination of sea-surface temperature from a satellite high resolution infrared window radiation measurements. Mon. Wea. Rev., 98, 604-611.

Stewart, R. H., 1982: Oceanography from space. 33rd Congress of the International Astronautical Federation, Paris, 1-14.

Vukovich, F. M., 1971: Detailed sea surface temperature analysis utilizing NIMBUS HRIR data. Mon. Wea. Rev., 99, 812-817.

Warnecke, G., L. J. Allison, L. M. McMillin and K. H. Szekielda, 1971: Remote sensing of ocean currents and sea-surface temperature changes derived from the Nimbus II satellite. J. Phys. Ocean, 1, 45-60.

Wiesnet, D. R., 1974: The role of satellites in snow and ice measurments. NOAA Technical Memorandum, NESS-58, 12 pp.

LANDSAT

Estes, J. E. (editor), 1983: Manual of Remote Sensing, Volume 2: Interpretation and Applications, American Society of Photogrammetry, (210 Little Falls St., Falls Church, VA 22046), 1208 pp.

LANDSAT, 1979: Landsat Data Users' Handbook, United States Geological Survey (For sale by USGS, Eastern Distribution Branch, Text Products Section, 604 S. Pickett St., Alexandria, VA 22304, $16.50).

Rundquist, D. C., 1983: Satellite view shows crop "signatures". Farm, Ranch and Home Quarterly, 29/4, 12-17. Published by University of Nebraska (Lincoln, NE), Institute of Agriculture and Natural Resources, Department of Agricultural Communications.

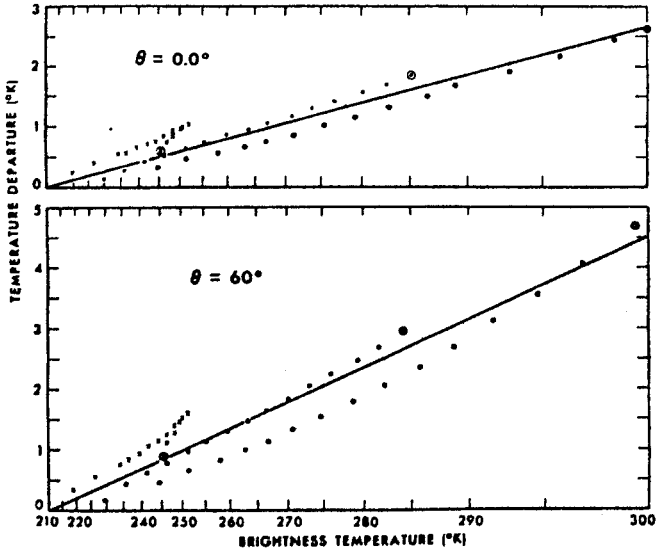

Figure 17.1.1 Atmospheric Attenuation of Sea-Surface Temperature at 3.8 μm (Smith et al., 1970)

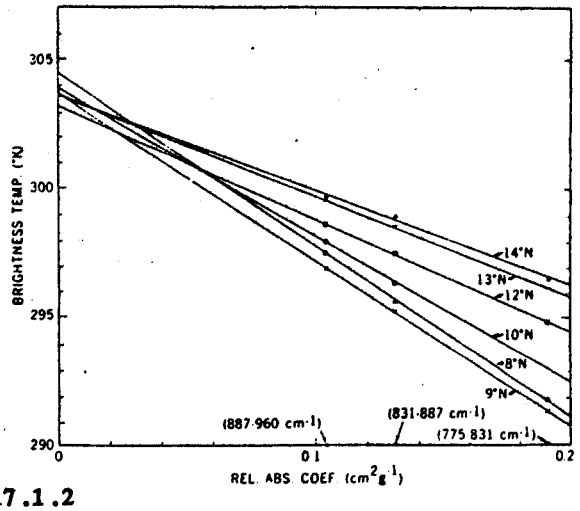

Figure 17.1.2
Extrapolation of Brightness Temperature to Zero Attenuation (Prabhakara et al., 1974)

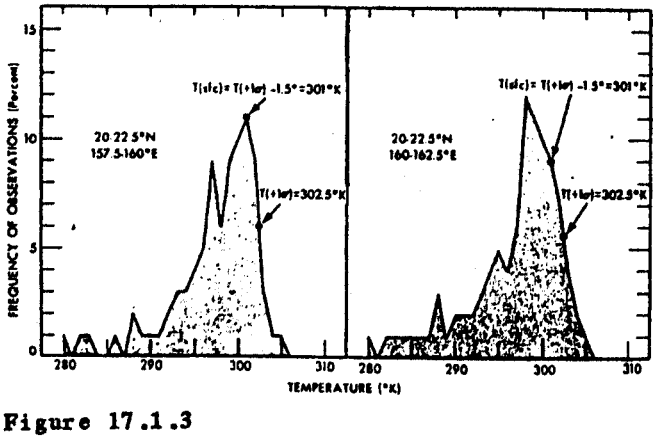

Figure 17.1.3
Histograms of Satellite Measurements to Identify Cloud-Free, Sea-Surface Temperature (Smith et al., 1970)

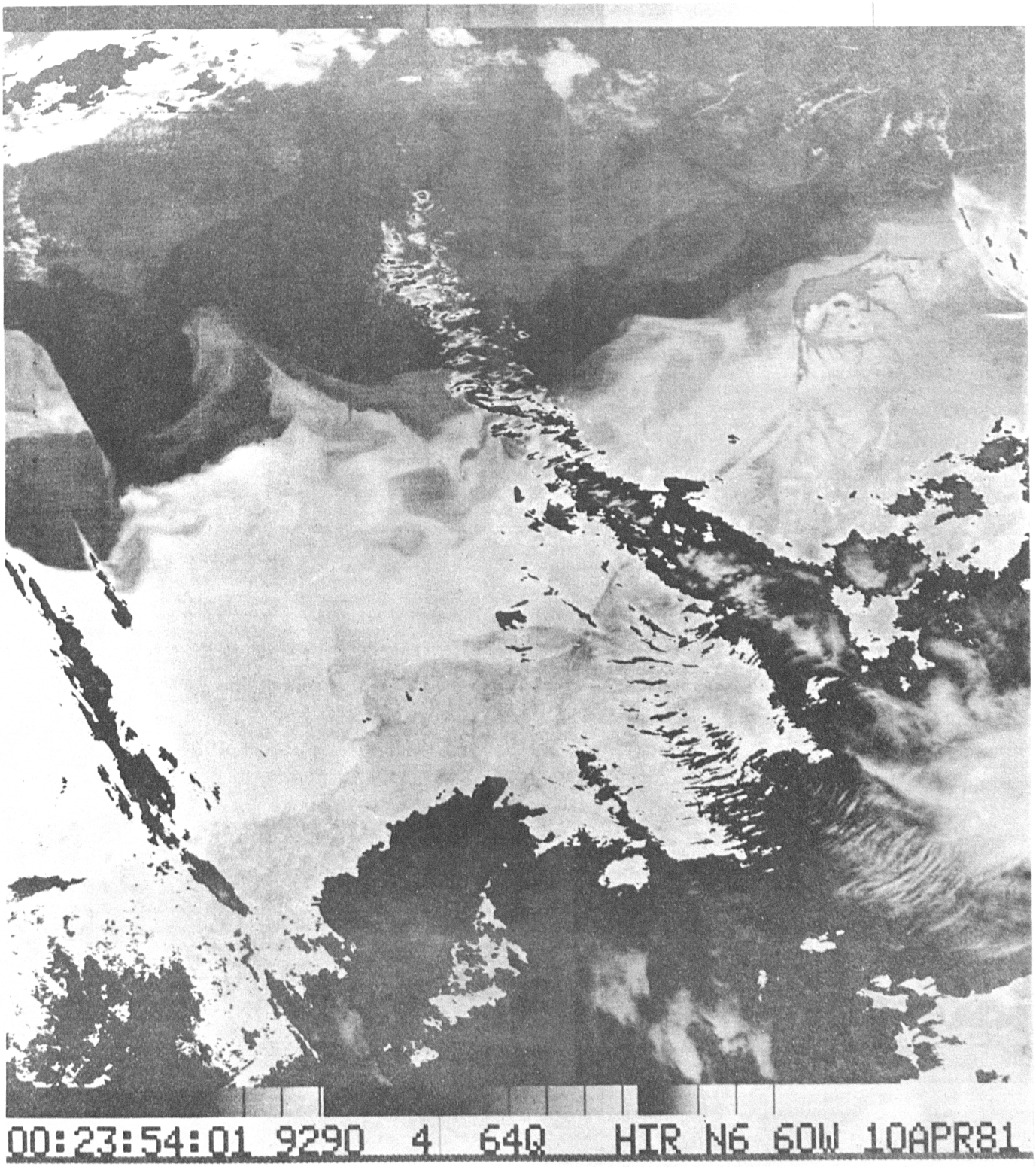

Figure 17.1.4 Sea-Surface Temperature Eddies as seen in infrared imagery from NOAA-6.

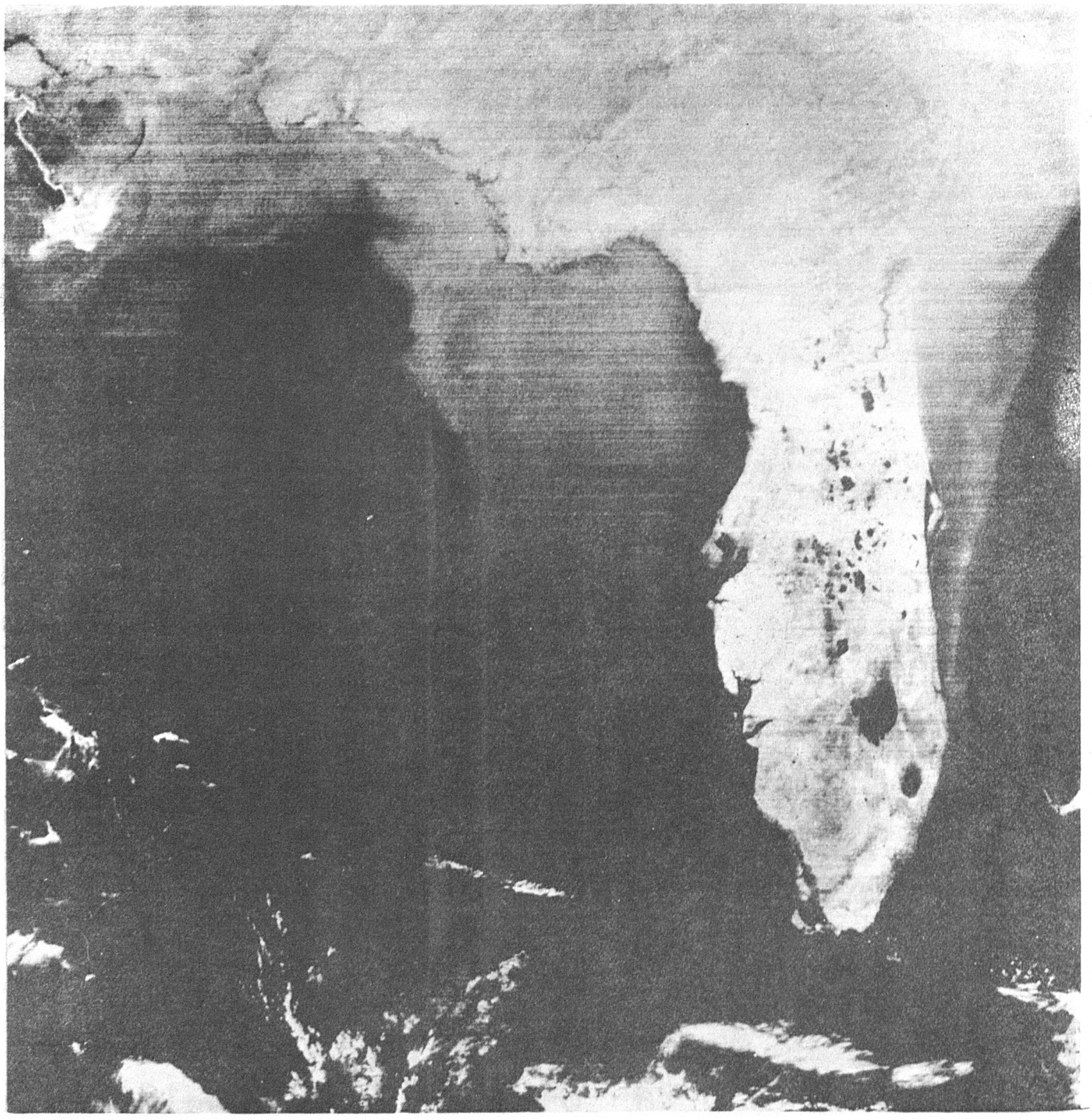

Figure 17.1.5 Sea-Surface Temperature Eddies in the Gulf of Mexico as seen in a VHRR infrared image from NOAA-3.

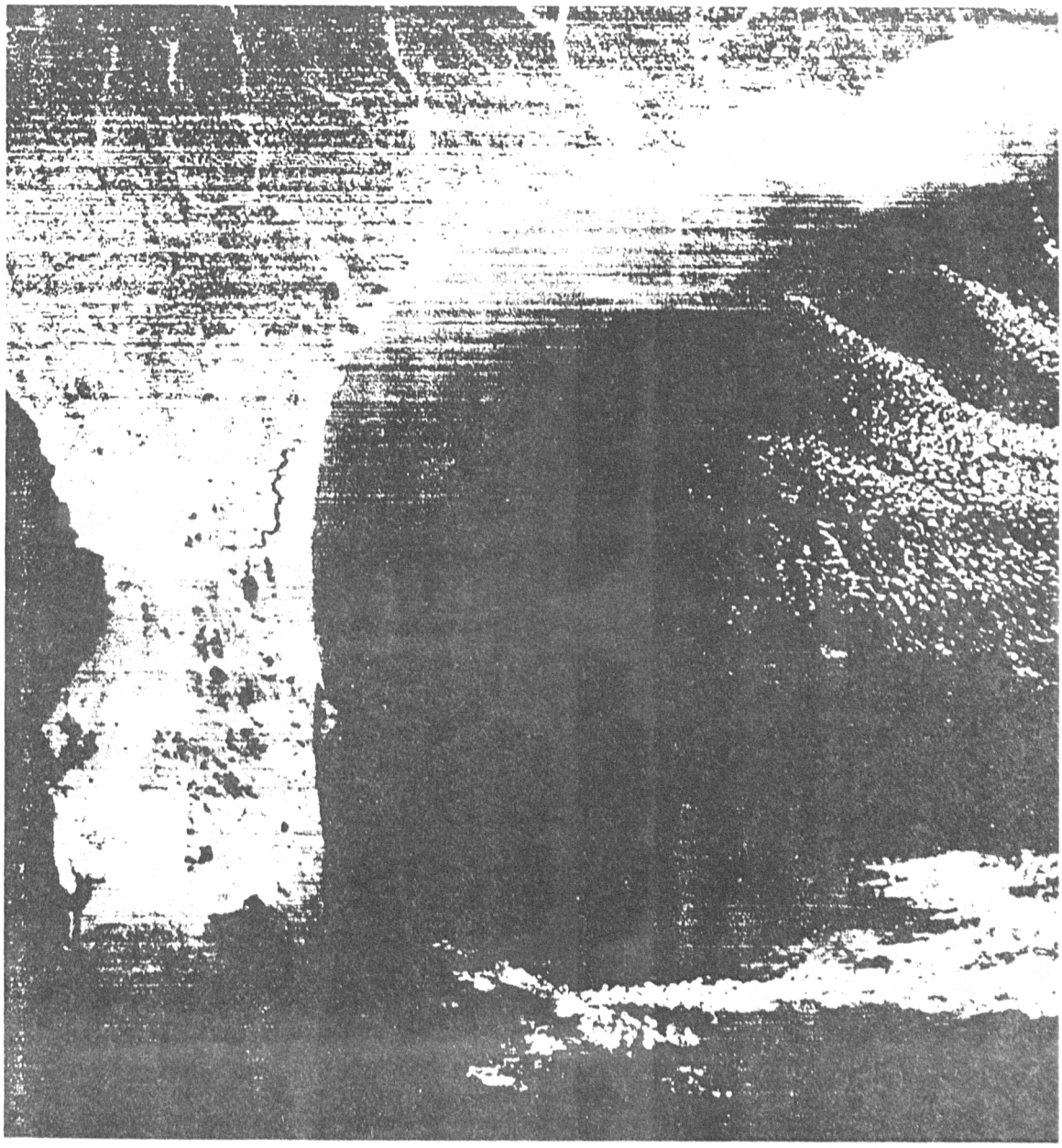

Figure 17.1.6 Polar Continential Air Outbreak Giving Minimum Atmospheric Attenuation. Note the Atmospheric Front Across Southern Florida. (Huh et al., 1982)

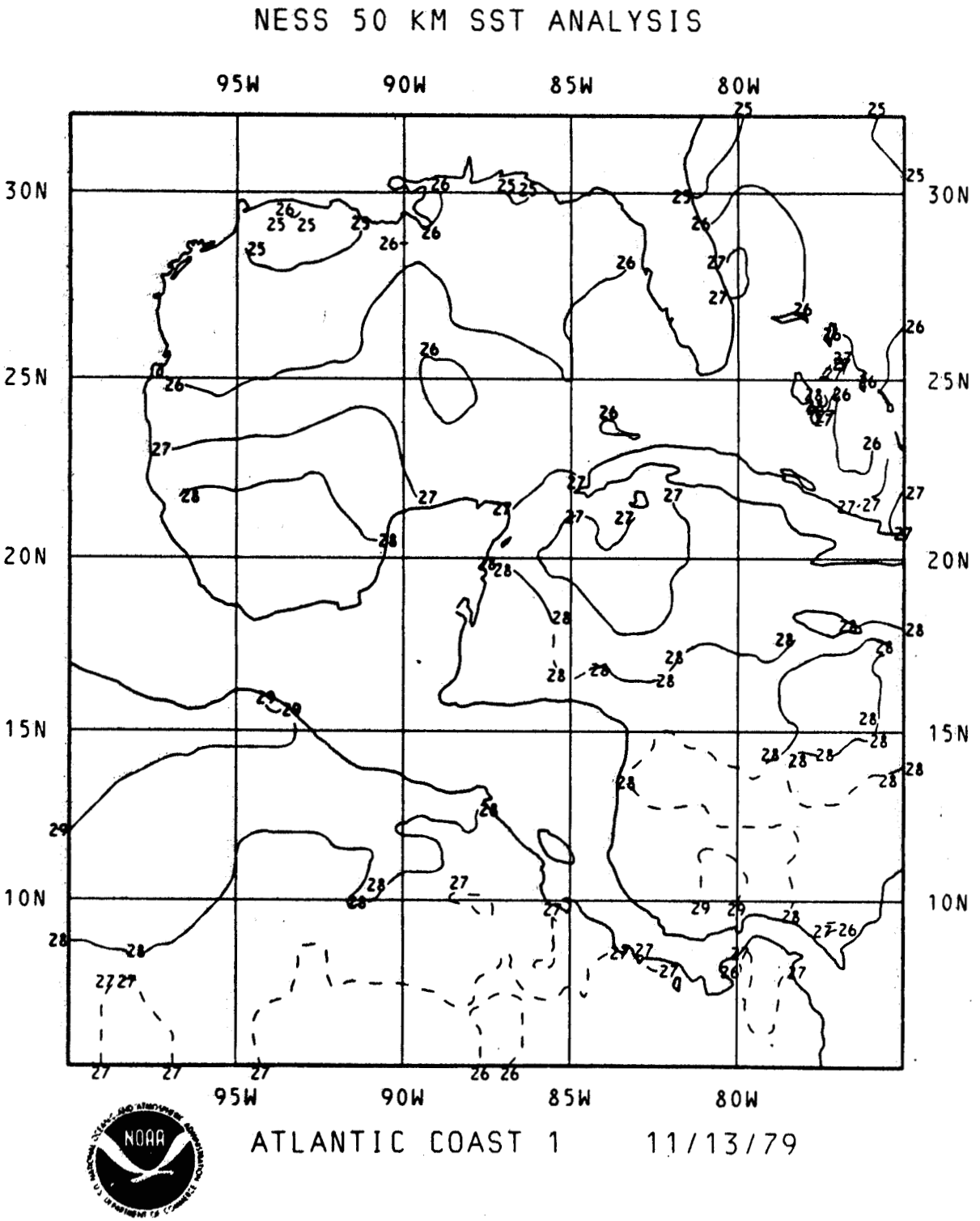

Figure 17.2.1 NOAA Operational Sea-surface Temperature Analysts for 13 November 1979 for Carribean Region. (Dismachek et al., 1980)

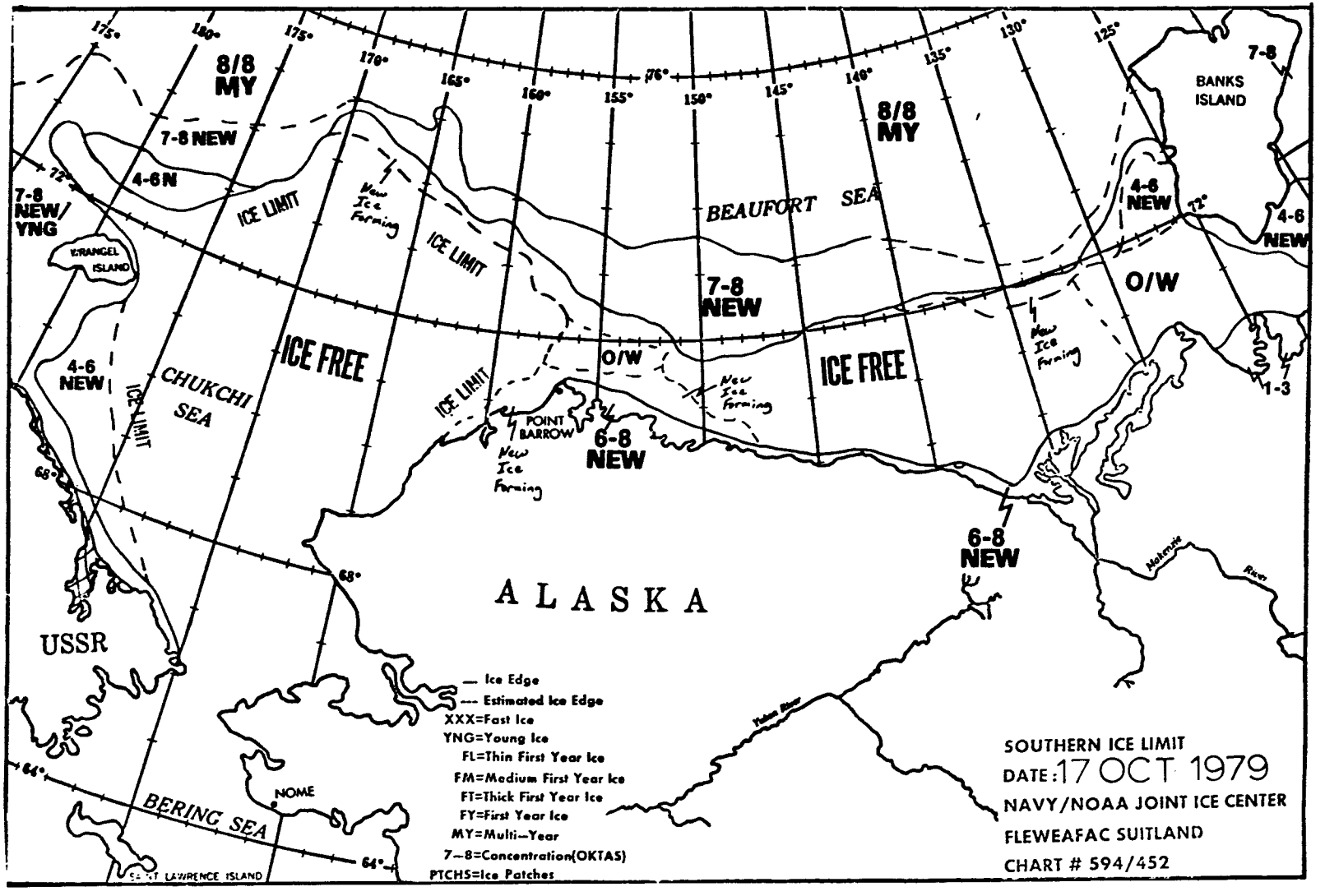

Figure 17.2.2 NOAA Operational Ice Chart for 17 October 1979 for Alaska-north slope region. (Dismachek et al., 1980)

Blank page retained for pagination

CHAPTER 18

ASPECTS OF CLIMATOLOGY STUDIES FROM SATELLITE DATA

18.1 Radiation Budgets

The earth's radiation balance has been a subject of a number of studies for many years. Crucial to the question of climate research is the knowledge of the solar radiation input and the longwave radiation output at the top of the atmosphere and the exchange of heat, momentum and material (especially water vapor) at the bottom. Furthermore, it is necessary to know the size and scale of interannual variations in the components of the energy budget. It is particularly important to assess the role of oceans in climatic variations and the extent and variability of the partitioning of the heat transport between the atmosphere and the oceans. It is evident that accurate and extensive measurements of the earth's radiation budget are required particularly over a period of several years to provide insight as to the extent of the interannual variabilities. Satellite measurements presently provide the best estimate of the earth radiation budget with sufficient temporal and spatial resolution over the entire globe. Further, from a combination of such data with conventional measurements of atmospheric and oceanic variables, the heat transports within the ocean and atmosphere can be deduced (e.g., Oort and Vonder Haar, 1976).

A number of studies have been presented over the last 10-15 years regarding the mean steady state magnitudes of the energy exchange between earth and space. For example, Vonder Haar and Suomi (1971) presented

results for the mean annual and seasonal cases based on measurements during 5 years (1962-1966). Others, including Winston (1967) and Raschke and Bandeen (1970) discussed short spans of data (weeks and seasons). Raschke et al. (1973) reported on budget results from measurements obtained from an experiment on the NIMBUS-3 satellite. In Stephens et al. (1981) the earth atmospheric radiation budgets are presented for a composite of 48 months over an intermittent period spanning 14 years (1964-1977) including 24 months of the more recent NIMBUS-6 data obtained from the continuing earth radiation budget (ERB) experiment. The reported data are a result of a continuing compilation of radiation budget measurements that were first reported by Ellis and Vonder Haar (1976) (29 months of selected radiation budget measurements).

The determination of the radiative balance at the earth's surface is also essential to atmospheric modeling, and, in particular, surface radiation budgets may provide insight into the possible atmospheric and oceanic partitioning of the heat transport. Satellite-based observations of the components of the radiation budget currently serve as one of the important tests of radiation modeling validity.

18.1.1 Satellite Data Sources

There is an increasing amount of information on the planetary radiation budget being provided by satellite measurements. Thus, the possibility arises for misunderstnading the different measurements as a source of data for energy budget studies. It is important for scientists who use the data to understand the nature of the measured or estimated quantities before the data can be interpreted for energy budget and

climate-related studies. Ideally, radiation budget studies require measurements at the "top of the atmosphere" of the total upwelling radiant energy from the earth atmosphere system, that is, the total radiant energy in both the solar and IR spectra integrated over all directions. No satellite measurement system yet developed can completely accommodate these rather fundamental requirements, but some provide better approximations than others. Furthermore, quantitative estimates of the uncertainties associated with the different systems vary in detail.

There are basically two fundamentally different sensors employed to measure the upwelling solar and IR radiation leaving the earth atmosphere system: radiometers that employ flat plate sensors and scanning radiometers. The measured quantities derived from these instruments are as fundamentally different as the instruments themselves. This point is evident from Figure 18.1.1, which schematically depicts the nature of the measurement and of the region sampled by the instrument.

The flat plate sensor measures the upwelling radiant flux density (exittance) reaching the plate and includes the earth atmosphere signal from a well-defined cone (SAB). The object is to convert this measurement at the satellite altitude (S) to an equivalent flux measurement at height H (the top of the atmosphere). The upwelling radiation at S, while composed of radiation from within cone SAB, originates largely within the smaller cone SCD. This more confined sampling region is a consequence of the instrument weighting radiation received about the subsatellite point (SS) more heavily that radiation received from those regions toward the limb. This feature is one of the determinants of the practical instrument resolution ($\sim 10^{o}$ ground coverage area for the flat plate sensors in orbits of height $\sim$ 600 km).

The satellite-based detector at S measures not only the radiant energy through the "equivalent detector" at S' but also radiation received from the surrounding regions of the atmosphere. Thus, some correction is strictly required to eliminate this radiation so that the exittance measured at S represents the exittance at S'. However, since the radiation through S' accounts for a large amount of the total upwelling radiant energy detected at the satellite, this correction is likely to be small. Finally, since spatial gradients or time rates of change of the radiation budget are often the important parameters under consideration and the spatial and temporal differences of measurements of the radiation through S are very similar to those through S', the data at satellite altitude are often employed without adjustment.

The scanning radiometer, on the other hand, measures the radiant energy (analogous to radiance) confined to a particular direction and to a small but finite solid angle (Figure 18.1.2b). Thus, while the reinterpretation of this measurement at S' is trivial, such a measurement does not represent the total upwelling radiant energy, but is rather the energy sampled in a confined but small set of solid angles.

It is obvious from the comparisons shown in Figures 18.1.1a and 18.1.1b that the flat plate sensor, while encompassing a majority of the total upwelling radiation, does so at the expense of ground resolution. The full field-of-view is $\sim 60^{\circ}$ but the effective resolution is of the order of 10° (or $\sim$ 1000 km) resulting in a smoothing of the data. Scanning radiometers, by contrast, have far better resolution (often $\leq 2^{\circ}$ with averaging) but at the expense of losing representation of the total radiant exittance from the earth-atmosphere.

The angular variation of the radiation field measured with a scanner is most severe when applied to the determination of planetary albedo. While the problem still exists for IR measurements, it is generally assumed that the emitted radiation has approximate black body characteristics and is therefore more nearly isotropic.

The performance, in terms of applicability to radiation budget estimates, of the various satellite measuring systems is summarized in Table 18.1.1. Five major systems are reviewed, the sun-synchronous polar orbiter like NIMBUS-6 and -7 and NOAA satellites, geosynchronous satellites (e.g., GOES, SMS), and the proposed ERBE program (1984), which is to implement three polar orbiting satellites. The local times of sampling are also shown in parentheses in the section labeled diurnal variation.

The flat plate sensors associated with the NIMBUS-6 and -7 satellites have significant advantages in that measurements are broad band (i.e., they measure the upwelling solar radiation in the spectral region form 0.2 to 3.8 μm and the IR emitted flux for the spectral region 3.8 to ≥ 50 μm) and also measure radiant energy integrated over a broad variation of angles. Unfortunately, the satellite sun-synchronous orbits do not pass directly over the polar regions, and the earth's radiation viewed from those regions by flat plate sensors is at some oblique angle. Therefore, the determination of planetary albedo in the polar region (poleward of about 70° latitude) is subject to some uncertainty since it requires large angular correction, the validity of which remains uncertain. The chief disadvantages of these measurements are their inherent coarse resolution and the possibility of diurnal bias. Possible diurnal biases in reflectance by varying solar elevation can be corrected. However, it must be recognized

that this data processing cannot remove possible diurnal effects that arise from variations in the state of the atmosphere (such as cloud cover). In particular, the tropics that constitute roughly half of the surface area of the earth and account for more than half of the radiative interaction with space, exhibit some fairly regular variations in temperature and cloudiness over the diurnal cycle (Riehl and Miller, 1978; Short and Wallace, 1980).

The scanning radiometers (SR) employed on the NOAA and geosynchronous satellites measure the upwelling radiation in narrow spectral regions (0.5-0.7 μm in the visible and 10.5-12.5 μm in the IR). The disadvantage of such measurements is the need to correct empirically these narrow spectral band values to broad band total shortwave and longwave radiant energies. A regression approach is employed to the IR measurements from the NOAA scanning radiometer (Gruber and Winston, 1978), which provides representative values of emitted flux. A similar correction is needed for the shortwave measurements, but it is not performed for the current scanning radiometer "albedo" estimates. Another significant disadvantage is the need to correct the measurements for angular variation of the radiance fields. Again, this correction is not employed to the currently available scanning radiometer data.

The advantages associated with the scanning radiometer data reside in the high resolution of the data that are available over a longer "continuous" period than are the flat plate measurements. Future TIROS and NOAA SR data will be available at 0730, 1500, 1930, and 0300 (local time), which may eliminate diurnal biases. Studies of any diurnal cycle evident in the radiation budget data, however, are best suited to geosynchronous satellite data, and such studies are required to test the extent of

possible diurnal biases that may occur in the sun-synchronous polar orbiting satellites. Unfortunately, the measurements from geosynchronous satellites are not global in extent, and the data also require the difficult angular and spectral corrections described above for the SR.

In addition to the flat plate sensors, the NIMBUS-7 satellite has a multi-axis broad band scanning radiometer that not only measures the upwelling radiance field across the entire spectrum but also scans for a number of different angles. This data may offer significant advances to our present qualitative understanding of the bi-directional reflectance function. Data from the existing single axis scanning radiometers can also be employed to study this function but for a more restricted variation of the dependent angles. The proposed ERBE program will employ two near polar-orbiting sun-synchronous satellites and another with orbital inclination of 48° as an attempt to overcome the possible diurnal biases associated with the current measurements. The program will continue its use of the flat plate sensors as well as employing a broad band single axis scanning radiometer. It is hoped by the time of those measurements that the current scanning radiometer data from NIMBUS-7 as well as the current single axis scanner measurements will lead to a workable understanding of the bi-directional reflectance function. Such a reflectance model may then be coupled to the scanning radiometer data to provide high resolution radiation budget estimates.

18.1.2 Radiation Budget Measurements

The planetary net radiation budget is composed of incoming solar flux, reflected solar flux to space, and the emitted terrestrial

flux. At the top of the earth atmosphere boundary, the net radiation budget is defined as

$$N = (1 - \alpha)Q - I \qquad (18.1)$$

where α is the planetary albedo, Q is the incoming solar flux based on the solar constant of 1376 $W \cdot m^{-2}$ (Hickey et al., 1980) and corrected for variations in sun earth distance, day length, and solar declination and I is the emitted flux (IR) by the earth atmosphere system.

The latitudinal distribution of the annual and seasonal net radiative energy input into the earth atmospheric system, the planetary albedo, and the outgoing (emitted) longwave radiation are shown in Figure 18.1.2.1 for the 48-month composite data set as a function of latitude. (The abscissa scale is non-linear with respect to latitude but linear with respect to area.) In the annual profiles, approximate symmetry in N, α, and I prevails between the northern and southern hemispheres. The minimum in emitted flux near the equator (5°N) is a result of the high topped clouds associated with the ITCZ. It is apparent from the seasonal profiles how this minimum migrates about the equator. The high emission around 25°S and 25°N are indicative of the subtropical dry zones (both over land and over ocean). The annual profile of planetary albedo, on the other hand, displays a maximum at 5°N in concert with the minimum in the emitted flux. In the tropical region, the planetary albedo variation is influenced more by weather disturbances and their attendant cloud distributions. In the polar regions, the major ice sheets are regions of large negative net radiation due to the high albedo of snow and ice. The general increase of albedo poleward of the subtropics is also particularly attributable to the decreasing mean solar elevation angle with latitude.

There is a significant amount of month-to-month variation in the radiation budget quantities. This is exemplified in Figure 18.1.2.2 which shows the annual variation of the mean values of emitted flux, planetary albedo, and net flux. These values are area means from 70°N to 80°S. Global integrations were not performed in this case because some data were missing poleward of 70°N and S for individual months. The annual cycle in the globally integrated net flux, previously reported by Ellis et al. (1978) has an amplitude (peak-to-peak) of about 26 $W \cdot m^{-2}$. The credibility of such a cycle can be qualitatively assessed from the heat budget studies of Ellis et al. who showed that the change of heat content (storage) of the earth possessed similar amplitudes and phases to the planetary net flux. Their global heat storage estimates were computed by independent in situ measurements of temperature.

Shown on Figure 18.1.2.2 as a dashed curve is the annual cycle in the globally-averaged integrated solar flux that has a peak-to-peak amplitude of about 22 $W \cdot m^{-2}$. This variation is a result only of external forcings associated with variations in the earth sun geometry. It is likely that the observed annual variation of the globally-averaged net flux at the top of the atmosphere (solid curve in Figure 18.1.2.2) is largely a result of this external forcing. The residual of the cycle is likely to be a result of the hemispheric differences in land-ocean extent, but cloud cover differences between the hemispheres cannot be ruled out. Specifically, the annual cycle of planetary albedo is also likely to be determined by the hemispheric differences of snow ice extent that provides large albedos (particularly in the polar regions). Further, the annual variation in the longwave emission to space occurs in part because of unequal temperature

responses between the land and the water surfaces and the assymetrical distribution of these between the northern and the southern hemisphere.

Figure 18.1.2.3 presents the interannual variations of the hemispherically averaged net flux that are presented for the seasonal intervals specified above. For both hemisphere, the largest changes in the net flux from one season to another occur for the transition from solstice to equinox. This marked variation is also evident in the global maps of net flux discussed below.

Figure 18.1.2.4 shows the global distributions of emitted flux, planetary albedo and net flux averaged for the mean annual period. The annual albedo maps reveal a distinct ocean-continent contrast equatorward of 30°N and 30°S and the high reaching convective clouds associated with the Asian monsoon are particularly apparent especially when related to the low emission (less than 230 $W \cdot m^{-2}$) evident in Figure 18.1.2.4 for that region. Generally, a net radiation gain prevails over ocean regions that may be directly attributed to the lower albedo over oceans compared to the zonal average. Poleward of 30°N and S, the albedo is zonally uniform except for some slight continental influence (e.g., over North America) in the northern hemisphere.

A distinct feature of the net flux distribution is the relatively high input of net radiative energy in the southeast Asian region and regions of relative low energy input particularly west of South America and southern Africa (associated with the presence of low persistent stratus clouds) and a minimum over the desert regions.

The maps presented in Figure 18.1.2.4 are for the mean annual case, and thus all daily and even seasonal anomalies are smoothed. Even so, at

lower latitudes in particular, regions of relative gain and loss of energy are evident within a given zone. For example, distinct variations are evident in the net fluxes in the tropical zones where the deserts of Africa and Arabia appear as negative or small positive anomalies and the convective regions near Asia are large positive anomalies in net flux. Thus, numerical simulations of the atmospheric or oceanic circulation cannot include forcing functions only as a function of latitude (i.e., of solar declination). Stephens and Webster (1979), for example, indicated that zonal variations in the radiative forcing cannot be simulated without zonal variations in cloud cover.

The albedos are generally negatively correlated with the emitted flux except over the desert regions discussed above. This reciprocity between emitted flux and albedo is a direct result of the effect of cloud on these components. Simply, the increased loss of energy to space by reflection from the cloud is offset by the decreased emission from the (colder) cloud tops. This reciprocity is evident in each of the seasonal maps producing net flux distributions that are more zonal in structure than either the maps of the two components α or I.

18.2 Clouds

Very little is known about the global coverage and distribution of clouds. However, with the availability of satellite measurements which cover almost the entire earth and which can make frequent measurements, the capability to determine global cloud cover is to be attempted.

Using 3-hourly measurements from 5 geosynchronous and the NOAA polar-orbiting satellites, for the polar regions (see Figure 18.2.1), a 5-year

cloud data set (or global cloud climatology), will be collected starting in 1983 for the International Satellite Cloud Climatology Project (ISCCP). This ambitious project will require the participation of many international agencies as well as government and academic research institutions throughout the world. These institutions will collect, process and analyze the satellite data. A goal will be the study of cloud-radiation processes. Much new information should be forthcoming as the ISCCP progresses.

18.3 Other Parameters

18.3.1 Estimates of Integrated Liquid Water, Cloud Water Concentrations and Integrated Water Vapor in the Atmosphere Over the Oceans

Variations in the hydrologic cycle, especially through the storage, transport and release of energy by water vapor/liquid water, are exceedingly important to interannual variations of weather and climate. Rawinsondes and radars over land networks, and satellites on a global scale, contribute to the understanding of the H_2O variables. (New satellite experiments, VAS on GOES and WV on METEOSAT, can now trace atmospheric water vapor patterns over land and ocean on an experimental basis). There definitely is a need to better map the H_2O vapor and liquid variations over the oceans.

It is important to note that mapping of integrated atmospheric water vapor and liquid would be very important climate measurements. (Ocean ship or buoy data would be aggregated into monthly and seasonal data sets.) In addition, if the cloud tops are estimated (e.g., by concurrent IR measure-

ments from GOES or other satellites) then actual cloud liquid water concentrations can be estimated using this new data.

18.3.2 Estimates of Precipitation Over the Ocean

For many years the weather observations from ships (the synoptic code data) have been used to estimate the climatological distribution of precipitation over the oceans. This is a very important climate data set because of what it tells us about the time and space variation of latent heat release in the atmosphere. All major national and international climate study groups have recommended that special effort be placed upon improvement of the knowledge of oceanic precipitation.

Despite the fact that the ship (and island) data are limited in areal distribution, Reed and Elliott (1979) optimistically state that random error in midlatitudes is only ± 10% for mean annual and seasonal estimates with a greater uncertainty in the tropics. They also believe that systematic bias in the precipitation estimates has been eliminated. Frequency of precipitation can be estimated by satellites based on several methods already tested (e.g., Kidder and Vonder Haar, 1977). Both infrared and microwave methods have been described in Chapter 13.

References and Suggested Reading

Barrett, E. C., 1974: Climatology from Satellites. Methuen, London, 418 pp.

Ellis, J. S. and T. H. Vonder Haar, 1976: Zonal average earth radiation budget measurements from satellites for climate studies. Atmos. Sci. Paper #240, Colorado State University, Fort Collins, CO, 57 pp.

Ellis, J. S., T. H. Vonder Haar, S. Levitus and A. H. Oort, 1978: The annual variation in the global heat balance of the earth. J. Geophys. Res., 84, 1958-1962.

Flanders, D. H. and W. L. Smith, 1975: Radiation budget data from the meteorological satellites, ITOS 1 and NOAA 1. NOAA Technical Report NESS-72, U. S. Dept. of Commerce, 20 pp.

Gruber, A. and J. S. Winston, 1978: Earth-atmosphere radiative heating based on NOAA scanning radiometer measurements. Bull. Am. Meteor. Soc., 59, 1570-1573.

Hickey, J., L. Stowe, H. Jacobowitz, P. Pelegrino, R. Maschhoff, A. Arking, J. House, A. Ingersoll and T. H. Vonder Haar, 1980: Initial solar irradiance determination from Nimbus-7 cavity radiometer measurements, Science, 208, 281-283.

Kidder, S. K. and T. H. Vonder Haar, 1977: Seasonal oceanic precipitation frequencies from NIMBUS-5 microwave data. J. Geophys. Res., 82, 2083-2086.

Oort, A. H. and T. H. Vonder Haar, 1976: On the observed annual cycle in the ocean-atmosphere heat balance over the North Hemisphere, J. Phys. Ocean, 6, 781-800.

Raschke, E. and W. R. Bandeen, 1970: The radiation balance of the planet Earth from radiation measurements of the satellite Nimbus-2, J. Appl. Meteor., 9, 215-238.

Raschke, E., T. H. Vonder Haar, W. R. Bandeen and M. Pasternak, 1973: The annual radiation balance of the earth-atmosphere system during 1969-70 from Nimbus-3 measurements, J. Atmos. Sci., 30, 341-364.

Reed, R. K. and W. P. Elliot, 1979: New precipitation maps for the North Atlantic and North Pacific Oceans. J. Geophys. Res., 84, 7839-7846.

Riehl, H. and A. Miller, 1978: Differences between morning and evening temperatures of cloud tops over tropical continents and oceans, Q. J. R. Meteor. Soc. 104, 757-764.

Short, D. A. and W. M. Wallace, 1980: Satellite inferred morning to evening cloudiness changes, Mon. Wea. Rev., 108, 1160-1169.

Stephens, G. L. and P. J. Webster, 1979: Sensitivity of radiative forcing to variable cloud and moisture, J. Atmos. Sci., 36, 1542-1556.

Stephens, G. L., G. G. Campbell and T. H. Vonder Haar, 1981: Earth radiation budgets, J. Geophys. Res., 86, 9739-9760.

Tarpley, J. D., S. R. Schneider, J. E. Brag and M. P. Waters III, 1978: Satellite data set for solar incoming radiation studies, NOAA Technical Report NESS-96, U. S. Dept. of Commerce, 36 pp.

Vonder Haar, T. H. and V. Suomi, 1971: Measurements of the Earth's radiation budget from satellites during a 5-year period, I, Extended time and space means, J. Atmos. Sci., 28, 305-314.

Wiesnet, D. R., V. G. Konovalov and S. I. Solomon, 1979: Applications of remote sensing to hydrology. WMO-No.513, 52 pp.

Winston, J. S., 1967: Planetary scale characteristics of monthly mean

long-wave radiation and albedo and some year to year variations, Mon. Wea. Rev., 95, 235-256.

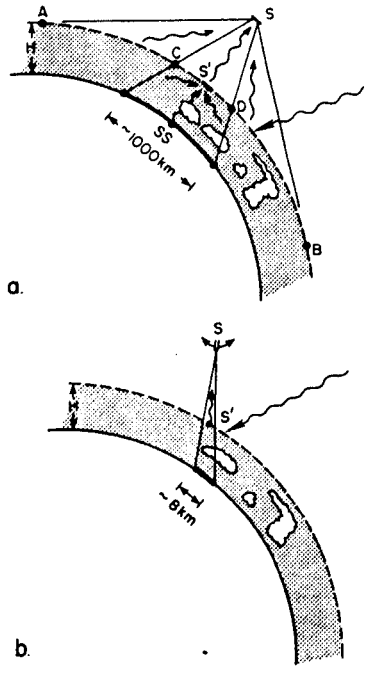

Figure 18.1.1 Schematic of (a) Flat Plate and (b) Scanning Detector Views (Stephens, et al., 1981)

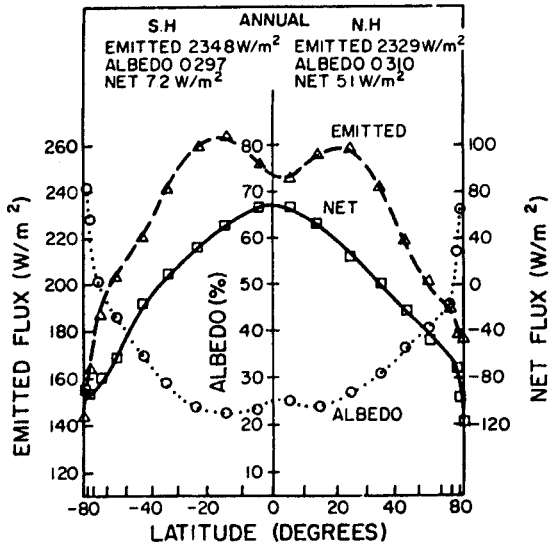

Figure 18.1.2.1 Zonally-Averaged and Annually-Averaged Emitted Flux, Net Flux, and Planetary Albedo (Stephens, et al., 1981)

Table 18.1.1 Satellite Systems for Radiation Budget Estimates (Stephens, et al., 1981)

COMMENT	NIMBUS 6	NOAA (TIROS N)	GOES, SMS	NIMBUS 7	ERBE (1983)
ORBIT	← Sun-synchronous polar orbiting →		Geosynchronous orbit	← Polar orbiting → Sun synchronous	2 sun synchronous 1 Drifter orbiter
DETECTOR	Flat Plate	← Single axis scanners →		← Flat Plate → Multi axis scanner	Single axis scanner
INTEGRATION OVER DIRECTION	Largely eliminated (except in polar regions)	← Requires a ρ model →		By scanning in more directions, ρ may be explicitly determined	Requires a ρ model (hopefully from Nimbus 7 for example
INTEGRATION OVER WAVELENGTH	Broadband detectors solar (0.2-0.38) IR (3.8->50)	← Requires empirical corrections to broadband values →		← Both radiometers are broadband instruments →	
RESOLUTION	Coarse resolution (∿10° x 10°) with smoothing	← High Resolution (∿2° x 2°) or higher →		← Flat Plate have coarse resolution → Scanner (∿4° x 4°)	Scanner (∿2° x 2°)
DIURNAL SAMPLING	Measurement at single daylight hour (∿OZ, 12Z)	Measurement twice daily (0900, 2100 local time)	Continuous temporal sampling	As for Nimbus 6 (OZ, 12Z)	Improved temporal sampling with 3 polar orbiting satellites six times a day

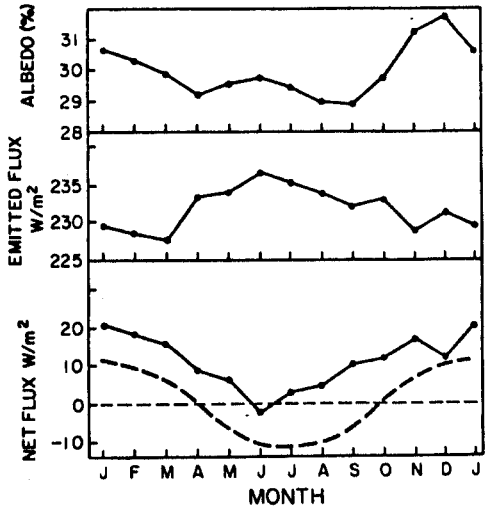

Figure 18.1.2.2
Annual Variation in Global Radiation Balance (Stephens, et al., 1981)

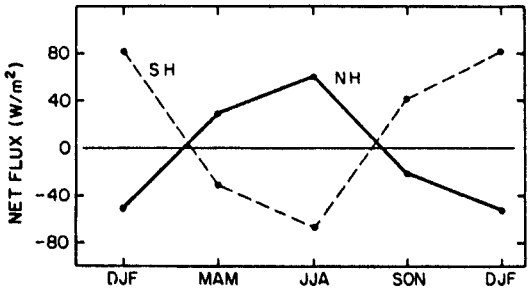

Figure 18.1.2.3
Mean Seasonal Hemisphere Net Fluxes (Stephens, et al., 1981)

ANNUAL EMITTED

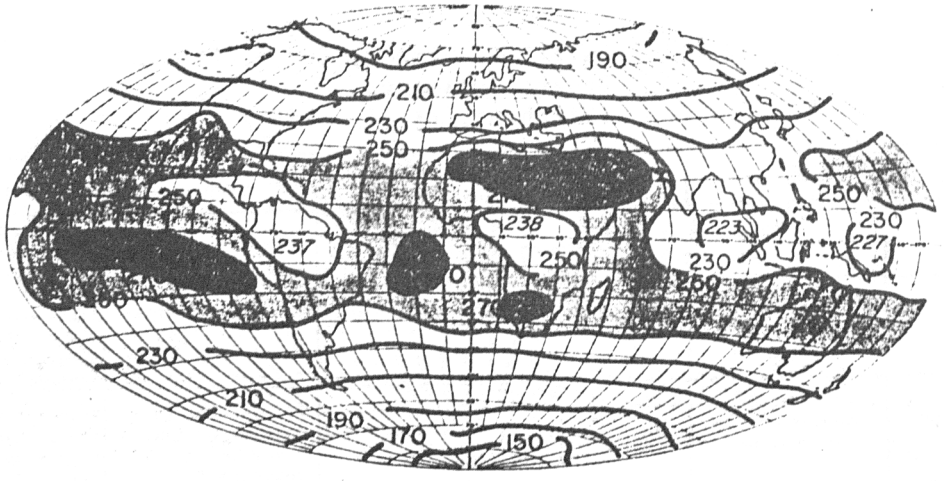

ANNUAL ALBEDO

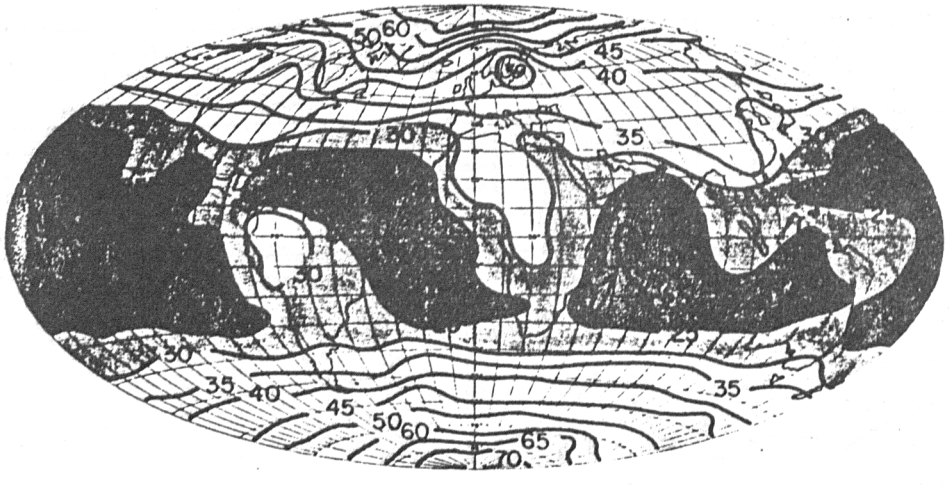

ANNUAL NET

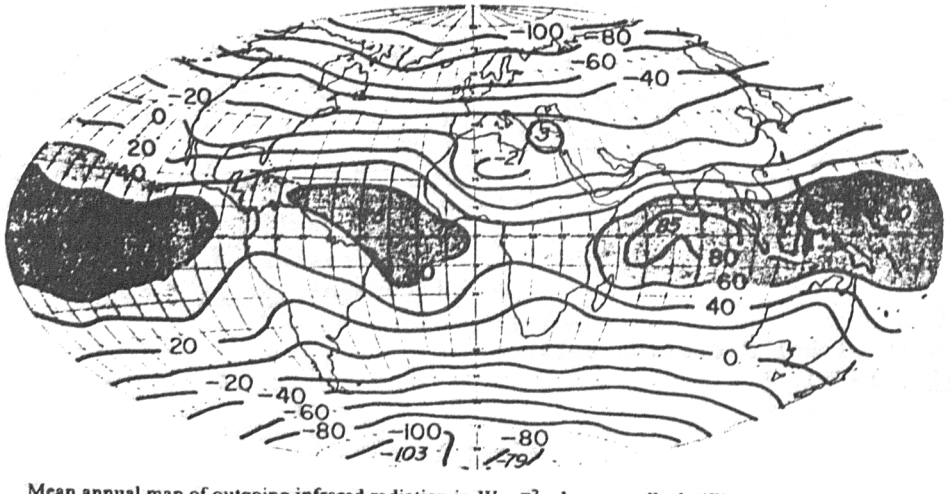

Mean annual map of outgoing infrared radiation in W m^{-2}, planetary albedo (%), and net radiation (W m^{-2}) for the 48-month period.

Figure 18.1.2.4 Global Distribution of Radiation Budget for 48 Months (Stephens, et al., 1981)

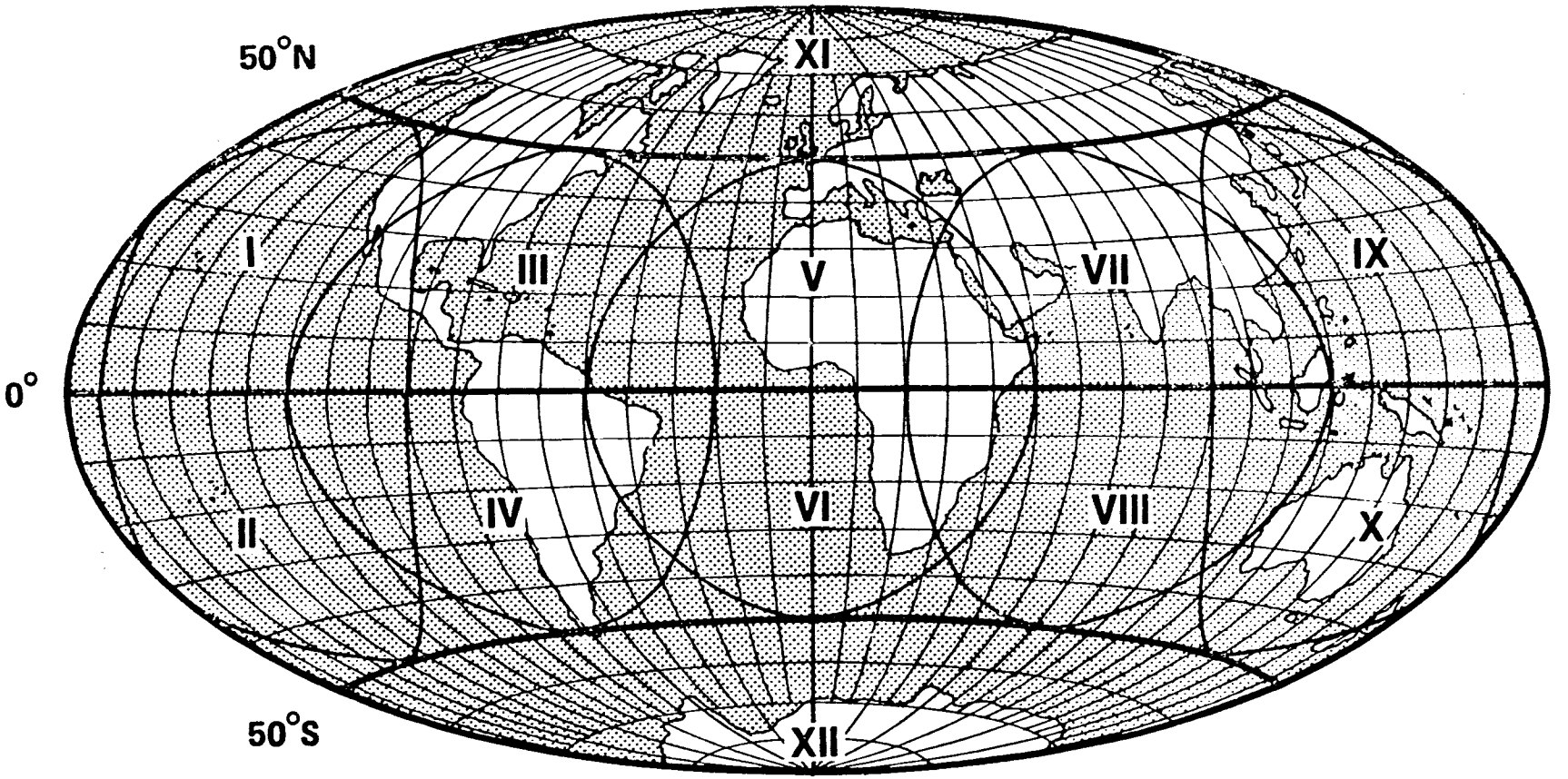

I GOES-W
II GOES-W
III GOES-E
IV GOES-E
V METEOSAT
VI METEOSAT
VII INSAT
VIII INSAT
IX GMS
X GMS
XI NOAA
XII NOAA

Figure 18.2.1 Satellite Coverage for the ISCCP

Blank page retained for pagination

SECTION III

FUTURE DEVELOPMENTS

The preceding sections in this set of lecture notes have discussed the basic operating principles and many practical applications of the present-day meteorological satellites. Throughout the last 20 years and continuing we expect through the 1980's, the development of capabilities in the meteorological satellite and data processing areas will provide an even greater spectrum of uses for weather satellite data. With an eye toward the future, this section is intended to remind the reader of some of the most recent developments that have not yet reached the full application stage. It is also intended to look ahead during at least the next ten year period to the improved satellite systems that the readers of this set of notes will undoubtedly encounter.

Blank page retained for pagination

CHAPTER 19

FUTURE DEVELOPMENTS IN METEOROLOGICAL SATELLITES AND DATA-PROCESSING SYSTEMS

19.1 Future Satellite Capabilities

It appears that improvements in satellite technology will lead to new instruments, as well as improvements in both space and time sampling of existing sensors. Some goals for improvement and additions to the geosynchronous satellite system include:

a) Increased spatial resolution (0.5 km visible and 1-2 km infrared) and decreased full disk imaging time (15 minutes or less for limited sectors) as well as an increased number of multispectral images

b) Increased vertical resolution (1-5 km) and horizontal resolution (to 10 km) for atmospheric sounding products

c) Improved Data Collection Systems (DCS) while maintaining existing platforms

d) Additional ability to monitor solar x-rays, electron flux density and low energy plasma

e) Simultaneous imaging and WEFAX functions (not presently possible)

19.2 New Instruments

Among the new instruments that will be available in polar orbit are:

a) AMSU (Advanced Microwave Sounding Unit) with up to 20 microwave channels to provide "all weather" atmospheric temperature and moisture soundings

b) LIDAR doppler sounder for wind determination by doppler measurements of aerosols

c) LAMMR (Large Antenna Multi-frequency Microwave Radiometer) to determine sea-surface temperatures, wind speed and ice cover

d) SCAT (Scatterometer) to determine wind speed and direction at the sea surface by measuring radar backscatter

The "GOES-Next" systems will have as a goal the ability to provide both images and soundings simultaneously. Other sensors include:

a) Higher-resolution VIS/IR imager/sounder

b) Microwave sounder

c) Lightning mapper

d) Solar x-ray imager

These new systems are dependent upon both feasible technology and favorable budgetary considerations. The reusable space shuttle of NASA Space Transportation System (STS) will be employed to launch future meteorological satellites. This, however, may require system design changes but may also allow new capabilities not before possible. The shuttle has already been used to carry experimental instruments such as the SIR-A (Shuttle Imaging Radar-A), an active microwave device used to gather information about the earth's surface properties (Elachi, 1982). This active microwave system can obtain images day or night and through clouds, to measure ocean currents, ice flows, and vegetation patterns. Soil water content also affects the backscattered signal. Swamps and wetlands appear as very bright features as in Figure 19.2.1.

19.3 Data-processing Systems and Communications

To keep up with the increased amount of data that will be provided, new or updated ground station and data analysis sytems will be required. The key will be the ability to quickly analyze the data and to provide it to the user in an acceptable format. The ability to combine various data sets (satellite plus satellite, or satellite plus ground-based) will also be required. This is now becoming a reality with experimental analysis systems scattered around the U.S. However, the vital link to the user is not as well developed and has only seen limited use, such as in the Prototype Regional Observing and Forecast System (PROFS). This system is a testing ground for bringing the quantitative data to the users and to determine the value of various products (Reynolds, 1983).

References and Further Reading

Canby, T. Y., 1983: Satellites that serve us. National Geographic, 164, 281-335.

Denaro, R. P., 1981: Navstar: The all-purpose satellite. IEEE Spectrum, 18, 35-40.

Elachi, C., 1982: Radar images of the earth from space. Scientific American, 247, 54-61.

Miller, D. B. and J. R. Silverman, 1982: User needs and the future of operational meteorological satellites. Meteorological Satellites - Past, Present and Future, NASA Conference Publication 2227, 63 pp.

Reynolds, D. W., 1983: Prototype workstation for mesoscale forecasting, Bull. Amer. Meteor. Soc., 64, 264-273.

SIR-A IMAGE FROM SECOND SHUTTLE FLIGHT

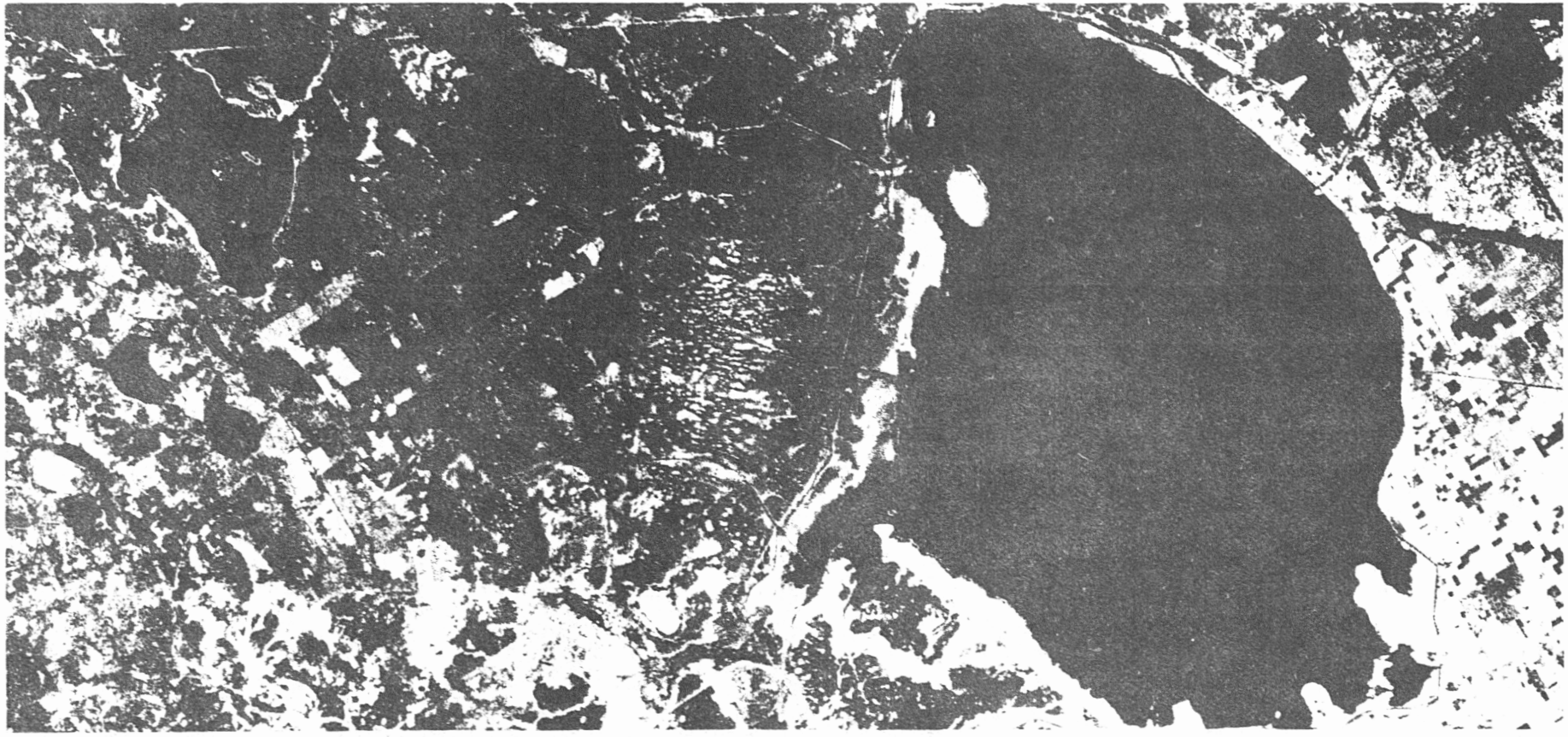

LAKE OKEECHOBEE AND SURROUNDING AREA IN CENTRAL FLORIDA

Figure 19.2.1 Image from the SIR-A (Shuttle Imaging Radar-A) carried on board the Columbia. Bright areas denote wet or swampy ground.

Chapter 20

SPECIAL DISCUSSION OF PRACTICAL APPLICATIONS FOR METEOROLOGICAL SATELLITES IN THE 1980's

Meteorological satellites, more commonly called weather satellites, rival communications satellites for ranking as the most useful and practical applications of our space program. While many are familiar with the relay of telephone conversations, business communications and even television signals by communication satellites, the meteorological satellites, which began even earlier in our space program, are not as well known to the general public. However, in recent years the accelerating use of weather satellite data in the transportation industries, in agri-business and in many other facets of our economy has demonstrated the continuing economic value of observations of the earth's weather from a space platform.

Based on more than 20 years of actual experience, the weather satellites have now been honed into efficient tools for both observing and communicating weather data in a timely fashion. An entire fleet of weather satellites fly above us every day. Figure 20.0.1 shows an example of this fleet and it can be said that every portion of the earth's surface and the weather above that surface are now observed by weather satellites at least every hour and many times with a frequency of only a few minutes. While the United States has taken the lead, it is an international program with weather satellites now operated by countries forming the European Space Agency, India, Japan and the Soviet Union as well as the United States. The United Kingdom, Canada and France also contribute major components to

the U.S. weather satellite program much in the way that Canada is collaborating in the space shuttle activity. Based on these 20 years of experience, operational weather satellites are a necessary and integral part of the weather services of the nations of the world. For this reason, they are solidly built into the future plans and can be depended upon to be observing platforms of the future. It is this dependability, often called their "operational nature", that makes the weather satellites attractive to those in the business community. Business can now depend upon weather satellites and the data from them just as they can depend upon business information compiled routinely by the Department of Commerce.

So, you may ask, now that the spaceborne weather satellites have become a useful tool to the specialists and can be depended upon to be launched regularly through the 1980's and 1990's, how can those in the business community take advantage of this new activity? Well, first of all, we are well aware of the rising industry of data communications. Weather data or <u>information</u> extracted from the weather data is perishable and must be delivered in a timely fashion. Thus, the first aspect of the practical use of weather satellite data is coupling its availability with the new mass communications systems that are available throughout the business community. Computers talking to computers, terminals connected to large computers, data flow and relay by satellite are all part of the 1980's business world. Weather data, including that from satellites, is then another stream that allows one to obtain the information needed to make business decisions in either a short-term or long-term basis. New weather data allow a business manager to be a bit more free than in the past from uncertainties and vagaries surrounding the weather impact on

various industries. Thus, as in many other areas, communication is a key. We shall see that the meteorological satellite platforms are not only excellent observation platforms from which to view the weather, but many of them are in the same orbits as communication satellites and thus can relay weather data from point to point and give us a major start towards the communications problem as well.

Secondly, improved use of weather satellite data involves collaboration with the satellite data researchers and producers to insure that practical information is extracted from the data. During the remainder of this section we will demonstrate some practical examples of weather satellite use today. These examples will be drawn from the (a) agri-business community, (b) the transportation industry including both land and ocean transportation, (c) the construction industry, (d) the retail marketing industries and (e) the commercial fishing industry. In each case we will dwell upon those aspects of the meteorological satellite systems that have advanced beyond the experimental stage and into the realm of practical usefulness. We will not discuss those new applications still in a research mode. Our approach is to prepare specific examples of both the new satellite technology and applications of its use in industry. Furthermore, it is the intent of this short paper and discussion to focus upon those aspects of scientific/industrial cooperation which could move the present application even further into the economically useful categories. Finally, in the chapter on future activities in our space program, especially the weather satellite program, we noted the promise of even more expanded application of the weather satellite information to practical problems here on Earth.

20.1 Examples of Practical Applications

20.1.1 Use of Satellite Data in Agri-Business.

During the last 15 years the use of satellite data by selected segments of the agricultural industry has rapidly increased. Major consortia of agricultural interests, such as the Canadian Wheat Board, as well as individual groups such as companies interested in the cocoa market, have employed staffs or individual consultants in the meteorological data area. Timely information about the crops and the forecasts of crop output over not only your own production areas but the production areas of your competitors have been the ultimate goal of this use of new weather data. Satellite data of interest to agri-business falls into the following categories: (a) frost/freeze situations, (b) precipitation, (c) cloud cover (which influences solar insolation) and (d) indications of extensive drought (namely, a drought index which combines the lack of precipitation with the amount of solar energy).

The satellite information on an experimental basis has also been gathered by NASA and NOAA as part of a program entitled AGRISTARS. This experimental program has been superseded, in many cases, by individual corporate applications. The meteorological satellite data can easily provide inferences regarding the cloud cover. Cloud cover heavily influences frost and also is an important variable in the estimate of local precipitation.

Groups such as the Canadian Wheat Board headquartered in Winnipeg, Canada, bring together data from around the world and attempt to provide more timely estimates than their competitors of the crop situations in wheat and other commodities on an international basis. The satellite data

on cloud cover and precipitation estimates are augmented by the use of infrared measurements from the satellites that estimate the surface temperature. From such estimates, one can deduce the diurnal range of temperature, and thus, the possibility of damaging frost at the low end of the temperature scale or excessive heat at the other extreme. A frost or too much heat inhibits development of cash crops and may be interpreted by agricultural market analysts in terms of commodity futures. Weather satellites also provide information about moisture conditions that are important for crop growth and the amount of solar energy reaching the surface. Of course, sunshine is a very important variable for crop growth and it is one of the factors that is entered into the crop models that are popular with the agri-business community.

In a related area, satellite temperature and cloud information is combined with surface weather data to estimate the Evapotranspiration Index (ET) that is important for the determination of the need to irrigate crops in the western part of the United States and in many other parts of the world. This Evapotranspiration Index is also dependent upon the low-level wind speed which can be estimated from tracking cloud motion from geostationary satellites. It is very important to the local agricultural economies.

The value of water resources should be noted at this point because one of the aspects of satellite support to the agricultural community arises with respect to monitoring the water supply. Meteorological satellites have been used to estimate not only the amount of precipitation in the form of rainfall but also in terms of snowfall. After skies clear following a snow episode, the extent and the approximate thickness of snow cover can be

monitored from satellites to provide a valuable input measure to water shed managers. The amount of such water available for potential irrigation in the upcoming growing season is an important factor in deducing the potential of the local crop production.

20.1.2 The Transportation Industry.

Both land and ocean-going transportation systems are heavily dependent upon weather. Ocean ships can encounter tremendous storms enroute and, in fact, the damage to and loss of ships each year is greater than commonly assumed. Over land, massive snowstorms and blizzards can immobilize transportation both by truck and rail. In terms of heavy cargo carried by river-going barges the early freezing of the rivers can have severe economic consequences. Thus, for many years, satellites have been used to observe the weather related to the routing of transportation. Hurricane and tropical storm tracking are noteworthy examples. Long-haul transportation services are dependent upon a weather warning that reaches out days in advance. Tankers, cargo ships, long-haul railroad transportation (such as those bringing citrus fruits from California to eastern states) and long-range trucking operations require timely information about the weather as well as forecasts. Weather satellites can observe newly developed storms that may have escaped the normal forecasting network. Ships and trucks, particularly, are amenable to routing around these storms which may allow them to reach their destination much more efficiently Thus, in the area of transportation it is not surprising that meteorological satellite data have been used for several years in this area and that a good number of small specialized consulting companies have arisen to provide such information to the transportation industries.

Of course, the aviation industry has always been a heavy user of weather data. Now, as competition has increased, special satellite data are being used to dispatch and plan the "flow" of equipment into economically important metropolitan areas. As always, safety issues involving weather are of equal concern. Trans-oceanic routes to conserve fuel require enroute winds and temperatures. Satellite sensors can estimate both these parameters. In addition, enroute data obtained by aircraft can be relayed via satellite as was noted in Section 2.3.

The routing of electrical power is a less well-recognized use of transportation. The power grid system in the United States has the flexibility of routing around adverse weather. It has become an important aspect of the operations of electric power companies to understand the rapidly developing severe weather that can cause damage and disruption to their power transportation. The dislocation of lines and the subsequent labor intensive repairs of a damaged transportation system is an area of special concern. For the same reason as noted above, several small companies are now in the business of providing these special forecasts needed by the electric power industry. They depend heavily on weather satellite data to tell them of the severe weather that is moving across particular areas and use their meteorological knowledge to interpret satellite images in terms of the severe weather that will disrupt power situations.

20.1.3 The Construction Industry in the United States is Extremely Weather Sensitive

We know that the planning and implementation of the construction of major highway systems as well as the special activities associated with the raising of major buildings and even small homes are dependent upon the wind and adverse weather. Cold weather and freezing temperatures will damage and sometimes make unacceptable extensive activities in the highway construction industry. In the same manner, the severe weather that might accompany a major storm can delay and even damage construction if proper precautions are not made.

Of special concern to those construction industries in our eastern-southeastern seaboard and Gulf States are the advent of hurricanes and tropical storms. Weather satellites for many years have allowed extensive monitoring of the progress of these storms which appear through the August-October time frame. Thanks to the satellite observations, the prediction of the time and occurrence of the landfall of these storms can be estimated with great precision. In this area alone, meteorological satellites have provided extensive information that has already had great economic impact.

20.1.4 The Fishing Industry

Commercial fishing in the United States, both in the Great Lakes and off each coast, is heavily dependent upon weather information. Weather satellites not only allow a forecast of the occurrence of major storms that can disrupt the fishing industry and the fishing fleet but also

provide special information about the temperature of the ocean. The temperature sensors from the weather satellites use the principle of infrared radiation emission. They allow us to map temperature patterns in the ocean which can be interpreted by fishing specialists in terms of the potential of these areas for a particular catch.

20.1.5 The Retail Sales Industry

Numerous studies have shown that the irregular portion of retail sales is heavily influenced by weather. Shopping patterns as well as response by the general public to certain kinds of advertising are definitely weather related. Meteorological satellites allow a particular retail sales organization to monitor approaching weather patterns, such as extensive cloudy regions or conversely, periods of exceedingly good weather, and target advertising in the very short term to those particular kinds of products to which the public will respond better in view of the weather. A number of private consulting agencies serve the retail industries. They combine not only the advertising-marketing weather related advisories but also the transportation related advisories that have such an influence on inventories of particular seasonal items. For example, it is wise to have a good supply of snow tires in stock when the first major snowstorm of the season hits a major metropolitan area. The use of weather observations from satellites can allow a particular retail group to be better prepared than its competition if such a snowstorm or other event approaches at an abnormally early time of the year.

In addition to the facts noted above regarding retail sales, the vacation industries such as the ski industry, the summer resort industry, and

certain vacation complexes which depend heavily on weather favorable for hunting or fishing are other examples of retail sales operations that are heavily influenced by the weather. Many times the timely observation of cloud patterns, snowstorms, or periods of particularly balmy weather from satellites will be of prime interest to the operators of this portion of the retailing industry. Extensive periods of inclement weather on one particular coast or in one area may provide information to owners of competing resort regions to prepare for an influx of visitors.

20.2 Examples of Scientific/Industry Cooperation

One of the most obvious opportunities in this area of weather satellites for scientific/industrial collaboration is in the aerospace industry and related research. Obviously, with more than 20 years of weather satellite experience behind us there is a solid foundation for research into improvements in both spacecraft and the instrumentation flown on them. The opportunities to jointly develop this fertile area for more practical and directed applications to economic problems is timely. With the example of the communication satellites again before us, it seems most reasonable that a joint university-industry collaboration in the area of applications of weather satellites and indeed even the launch of specifically oriented satellites is a viable option for the late 80's and early 90's.

In the introduction of this section, the arising data and information industry was mentioned. Weather data and information extracted from weather data represent new activities for many companies. For example, Control Data Corporation has developed a special product line that provides

specialized information extracted from weather and other data sets. There is an opportunity before us for the communications, data processing and data packaging industries to collaborate with the information processors, the remote sensing community and the meteorological scientists in the universities to provide new and better products extracted from the weather satellite data. This information must also be communicated in a timely fashion. In this regard, there will be a very great upsurge in the use of weather satellite data relay systems to communicate the results of data taken by the remote data collection platforms scattered in various areas. Combining these data together with the imagery from the satellites will be a packaging and information distribution problem that is just beginning to be attacked.

As mentioned in earlier sections, the specific use of weather satellite data in the agri-business, the transportation, the fishing and retail industries, and other areas of economic activity have already begun, based on the solid foundation of weather satellite data during the last 20 years. These activities have by no means peaked and there is much room for joint scientific-industry collaboration in developing these products further.

Finally, the microelectronics industries which provide the foundation for much of the spacecraft and instrument technology are playing increasingly large roles in the data processing and communications technologies. There is an opportunity for a joint-university cooperation on special forms of microelectronic devices which will enhance and greatly reduce the price of the use of weather satellite data once it reaches the ground. In this regard, special "chips" can be developed which combine the

talents of the scientific meteorologist familiar with weather satellite information and the microelectronic specialists. Such collaboration would produce a tailored "chip" that extracts information from the weather satellite data stream (presently more than five million bits of data per second reaching the ground!) and speeds it to the user in the economic sector.

References and Further Reading

Maunder, W. J. , 1970: The Value of the Weather, Methuen, London, 388 pp.

Suchman, D., B. Auvine and B. Hinton, 1981: Determining economic benefits of satellite data in short-range forecasting. Bull. Amer. Meteor. Soc., 62, 1458-1465.

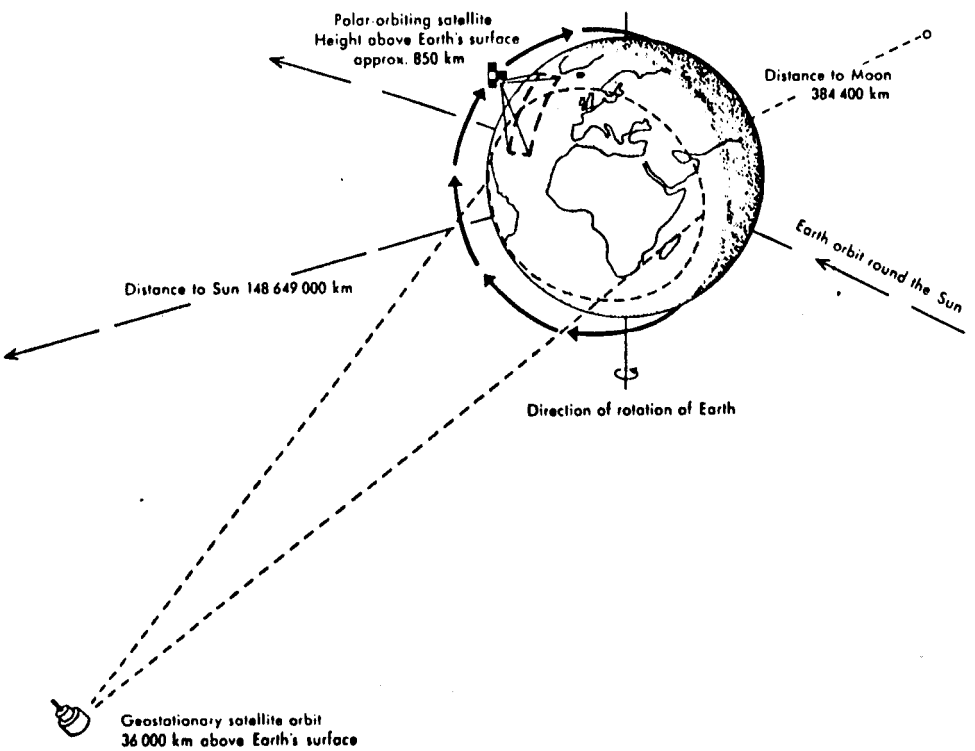

Figure 20.0.1 Schematic illustration showing how the Earth is viewed from a polar-orbiting satellite and from a geostationary satellite.

LIST OF ABBREVIATED TITLES OF SLIDES ON SOME APPLICATIONS OF METEOROLOGICAL SATELLITE DATA

Slide Number	Title
	INTRODUCTION AND BACKGROUND
	Course Introduction; Present State-of-Art
1,2	GOES Groundstation Antennae
3,4	ADVISAR Equipment
5,6	ADVISAR Displays
7-12	Digital Zoom Sequence
13,14	Remapped GOES Images
15-20	Digital METEOSAT Images
	Satellites and Instruments
21	TIROS-N AVHRR
22	TIROS-N Layout
23	TIROS-N Spacecraft
24	SMS-1 VISSR Cutaway
25	SMS-GOES Spacecraft
26	Scanning Radiometer Cutaway
27	ITOS Spacecraft
28	NIMBUS-4 ESMR
29	TIROS-1 Vidicon Camera
	Data Collection Platform Systems
30-32	Data Collection Platforms
33	DCP Electronics
34	DCP Solar Cells
35	DCP Batteries
36	GOES Ground Station Antennae
37	Downlink Receiver
38	DCP Demodulator
39	DCP Minicomputer and Disks
40	DCP Printout
	SYNOPTIC SCALE SYSTEMS
	General Example
41	GOES-W Full Disk VIS, IR
42	GOES-E Full Disk VIS, IR
43	General Example Cyclone Systems

44	Winter Storm
45	Winter Storm
46	Winter Storm Over Land
47	Same Image, Darker
48	Baroclinic Zone
49	Enlargement of 48
50	Tropical Systems

Jet Streams

51	Jet Stream Cirrus
52	Advection Type Jet Cirrus
53	Baroclinic Zone Cirrus
54	Baroclinic Zone Cirrus
55	Well-defined Cirrus Edge

Deformation Zones

56	Comma Head Deformation Zone
57	Deformation Zones
58	High/Low Cloud Deformation Zones
59	Same Slide, Darker
60	Cutoff Low Deformation Zones
61	VIS & IR of same
62	Same Slide, Darker
63	Fountain Type Deformation
64	Same Slide, Darker
65	Low Level Deformation Zones
66	Connecting Band Deformation Zone
67	Connecting Band in Tropics
68	Same Slide, Lighter
69	Clear Area Deformation Zone

"Leaf" Type Cloud Systems

70	VIS & IR Baroclinic Leaf
71	VIS & IR Baroclinic Leaf
72	Old Frontal Zone Leaf
73	VIS, IR, EIR Leaf
74	Same Slide, Lighter
75	Leaf on Trailing Front
76	Leaf over Pacific
77	Crescent Leaf
78	Arch Baroclinic Leaf
79	Non-developing Leaf
80	Low Cloud Leaf

Extratropical Cloud Systems

81	Mature Storm System
82	Same Slide, Lighter
83	Rapidly Deepening Storm, VIS
84	Same Image, IR
85	Southern Hemisphere Mature Storm
86	Same Slide, Lighter
87	Cutoff Low Sequence
88	"Popcorn" Type Cold Low
89	Cold Low Blocking Pattern
90	Winter Storm with Jet Stream
91	Tau-shaped Pattern
92	Tau Pattern Over U.S.
93	Mature U.S. Winter Storm
94	Atlantic Cutoff Low
95	Mature Storm with Smaller System
96	Same Slide, Darker
97	"T" Perturbation in Mature Storm, VIS
98	IR of above
99	Short Wave in Ridge
100	Mature Storm with Perturbations
101	Cold Low over Land, IR
102	VIS of Same Low
103	Cutoff Low, VIS, IR, EIR
104	VIS Enlargement of Same
105	IR EIR Enlargement of Same

Jet Stream Cirrus Examples

106	Jet Cirrus Over Lower Perturbations, IR & VIS
107	Close-up VIS of Same
108	Same Slide, Lighter
109	Extended area VIS of Same
110	Cirrus-Low Cloud Interface
111	Enlargement of Same
112	1-km VIS of Same
113	"Wire" Convection Under Jet

Frontal Systems

114	Rapidly Deepening Storm
115	Same Slide, Darker
116	Differing Frontal Zones
117	Cutoff Low with Front
118	Frontal Zone-Upper Flow Relation
119	IR Image of Same
120	Same Slide, Darker
121	Jet Axis-Cellular Convection Relation
122	Similar Example
123	Subsidence Surge with Jet
124	Frontal Clouds - Jet Stream Effect

125	Similar Situation
126	Frontal Zone - Upper Air Relations
127	Warm Frontal Zone
128	Frontal Breakdown Sequence
129-134	Enlargements of Same
135	Warm Front Formation
136-139	Comma Development from Leaf
140	Shifting Precipitation Patterns
141	Heavy Frontal Convection
142	Vertically Deep Storm
143	"Shearing Out" of Same Storm
144	Shear-Out Sequence

Cyclogenesis

145	Type 1 Cyclogenesis Sequence
146	VIS-IR Comparison, Early Stages
147	VIS Enlargement
148	VIS-IR Comparison, Later Stages
149	VIS Enlargement
150	Cyclogenesis - Base Cutoff Sequence
151	Enlargements, Early Stages
152	Enlargements, Early Stages

Tropical Cloud Systems

153	Winter Storm, Tropical
154	Composite of 155, 156, 157, 158
155	Tropical Cyclone
156	Comma Pattern Winter Storm
157	Hybrid Storm Pattern
158	Cold Low
159	General Example VIS
160	General Example VIS
161	General Example VIS & IR
162	Undisturbed ITCZ
163	ITCZ with Deep Convection
164	ITCZ Perturbed Low Level
165	VIS Enlargement
166	ITCZ, Deeply Perturbed
167	ITCZ Flare-up
168	ITCZ FLare-up
169	Dual ITCZ Bands
170	Interrupted ITCZ
171	Common ITCZ Clouds
172-175	4-day ITCZ Sequence
176	VIS Enlargement, Day 3
177	VIS Enlargement, Day 4
178	Low Level in Easterlies
179	Vorticity Center in Easterlies
180	Vorticity in Southern Hemisphere Easterlies
181	Westward Moving Cutoff Low

182	Deformation Zone Boundary
183	Same Slide, Darker
184	Convection in Surge Boundary
185	VIS & IR Intermediate View
186	Warm Zone/Surge Boundary
187	Same Slide, Lighter
188	Tropical Trough-Ridge Couple
189	Development of Trough-Ridge
190	Tropical Cyclones, IR
191	Smaller Tropical Cyclone, IR
192	Tropical Cyclone, VIS & IR
193	Tropical Cyclone Asymmetry
194	Hurricane Frederick VIS & IR
195	"Frederick" VIS-IR-EIR Comparison
196-200	(Not missing slides, just a mistake in numbering)

SPECIAL CLOUD SYSTEMS

Hurricane Intensity Technique

201	"BB" IR Hurricane Enhancement
202	Dvorak Technique Patterns for EIR
203	Enhance IR Banding Features
204	Dvorak Technique Flow Chart
205	Eye Distinctness Adjustments for EIR
206	Hurricane "Belle" Development
207	3 Hurricane Life Cycles (1 image/day)
208	Super Typhoon "Bess"
209	VIS-IR Color Overlay
210	Hurricane Interaction

Fog and Stratus

211	Fog Over Pennsylvania
212	Sacramento Valley Fog - VIS
213	Sacramento Valley Fog - IR
214	Fog Terrain Influences
215	River Valley Fog
216	Gulf Coast Fog - VIS
217	Gulf Coast Fog - IR
218	Satellite & Surface Observations, Fog
219	Fog and Stratus, Satellite & Surface
220	Sacramento Valley Fog, Satellite & Surface
221	Fog and Stratus
222	Fog and Stratus
223	Snow Cover & Surface Observations
224	North Atlantic Fog
225-231	Visible Enhancement for Fog
232-237	Fog Dissipation Examples
238	Fog VIS Enlargement Curve
239	Sunrise VIS Image

240	Enhanced VIS Image
241	Dissipation Time vs. Brightness
242	Dissipation Time vs. Adjusted Brightness
243	IR Fog Image
244	Corresponding Ceilings & Visibilities
245	Corresponding Temperatures & Dewpoints
246	Corresponding VIS Image
247	Blowing Dust
248	Forest Fire Smoke
249	Agricultural Burning Smoke
250	Sun Glint

Thunderstorm Gust Fronts

251	Arc Speed vs. TRW Max Gust
252	TRW Gusts - VIS & Surface Winds
253	Corresponding Enhanced IR
254	TRW Gust - VIS & Surface
255	Corresponding Enhanced IR
256-264	Arc Cloud & Surface Winds
265	TRW Enhanced IR
266	TRW Line - VIS & Surface Winds
267-269	Enhanced IR Continuation

Sea Breeze and Lake Effects

270-272	Great Lake Effects - Cloud Plumes
273	Lake Breeze Effect
274	Sea Breeze
275-276	Sea Breeze Peninsular Effect
277	Cumulus Over Pavement
278	Enhanced Sea Breeze
279	Island Effects

Thunderstorm Analysis

280	Schematic TRW Gust
281-282	Gust Front Thermodynamics
283	Gemini Photo - Intersecting Outflows
284	Surface Data
285	Surface-Satellite Overlay of TRW's
286	Satellite with Analyzed Dewpoints
287	Satellite with Analyzed Dewpoints
288	Satellite with Analyzed Streamlines
289	Satellite with Meso-Analyzed Pressures
290	Arc-Initiated TRW
291	TRW Arc VIS Image
292	Corresponding Surface Analysis
293-294	Subsequent VIS Images
295	Corresponding Surface Analysis
296	Initiated TRW's

297	Corresponding Surface Analysis
298	Line Intersection Initiation
299	Meso-Analysis with Satellite (Fujita)
300-305	Orographic TRW Initiation Sequence
306	Blank

Thunderstorm Rainfall

307	IR Image of TRW
308	Mb Enhancement Curve
309	Corresponding Enhanced IR Image
310	Aircraft-viewed Overshooting Top
311	EIR of TRW
312	Corresponding RADAR Display
313	Aircraft-viewed Overshooting Top
314	EIR of TRW
315	EIR-D/RADEX Overlay
316	VIS of TRW Overshoots
317	Corresponding RADAR Display
318	Subsequent EIR
319	Corresponding VIS
320	Radar Analysis
321-322	TRW Anvil Growth
323	Corresponding 300 mb Analysis
324	Schematic Anvil Expansion
325-326	TRW Anvil Growth
327	Kansas City Radar Analysis
328-329	Corresponding EIR Images
330	Corresponding Satellite-Isohyet Analysis
331	Radar from Big Thompson Flood
332-333	Corresponding EIR Images
334	Subsequent Radar Display
335	VIS of TRW
336-337	EIR of Growing TRW
338	Radar of Frontal TRW
339	Corresponding EIR Image
340-343	Thunderstorm Growth Cycles

SPECIAL TOPICS

Satellite/Synoptic Comparisons

344	Radar of Winter Storm
345	Corresponding VIS
346	Corresponding IR
347	VIS + Surface of Cyclone
348	VIS + Radar for Cyclone
349	EIR + Radar for Cyclone
350	EIR + 850mb for Cyclone
351	EIR + 500mb for Cyclone
352	Blank

Radar-Satellite Combination

353	VIS-IR APT Image
354	GOES Raw VIS Image
355	Radar-remap VIS
356	Radar-remap IR
357	Radar Image
358-360	VIS-IR Radar Overlays
361	Digital VIS of Tornadic Storm
362	Corresponding Color IR

Air Pollution

363-364	Air Pollution from Forest Fires in Southeast Canada
365	VIS of Smoke with 850 mb Winds

Saharan Dust Outbreak

366-379	Saharan Dust Outbreak Sequence

Wintertime Weather Modification

380	Color IR Winter Orographic Cloud
381	VIS of Winter Storm
382	Corresponding Aircraft View
383	Cloud Top Temperature vs. Time
384	Precipitation vs. Time

Cyclogenesis/Mid-Latitude Dust Storm

385-395	Cyclogenesis - Dust Storm Development